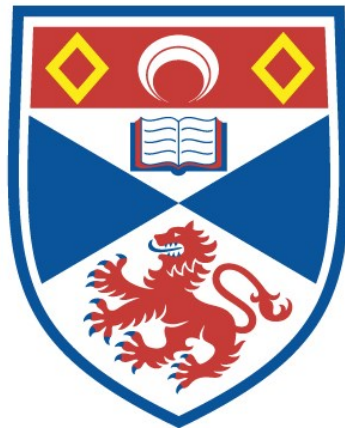# UNIAXIAL STRESS TECHNIQUE AND INVESTIGATIONS INTO CORRELATED ELECTRON SYSTEMS

Mark E. Barber

A Thesis Submitted for the Degree of PhD
at the
University of St Andrews

2017

Uniaxial Stress Technique and Investigations into Correlated Electron Systems

Mark E. Barber
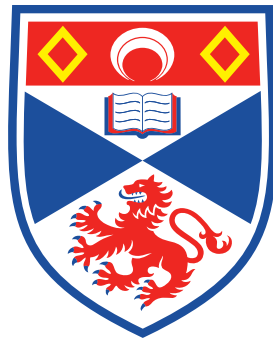
University of
St Andrews

This thesis is submitted in partial fulfilment for the degree of
Doctor of Philosophy at the University of St Andrews

March 2017

Declarations

1. Candidate's declarations:

I, Mark Barber, hereby certify that this thesis, which is approximately 50,000 words in length, has been written by me, and that it is the record of work carried out by me, or principally by myself in collaboration with others as acknowledged, and that it has not been submitted in any previous application for a higher degree.

I was admitted as a research student in September 2012 and as a candidate for the degree of Doctor of Philosophy in September 2012; the higher study for which this is a record was carried out in the University of St Andrews between 2012 and 2016.

Date: .... *signature of candidate:* ....

2. Supervisor's declaration:

I hereby certify that the candidate has fulfilled the conditions of the Resolution and Regulations appropriate for the degree of Doctor of Philosophy in the University of St Andrews and that the candidate is qualified to submit this thesis in application for that degree.

Date: .... *signature of supervisor:* ....

3. Permission for publication:

In submitting this thesis to the University of St Andrews I understand that I am giving permission for it to be made available for use in accordance with the regulations of the University Library for the time being in force, subject to any copyright vested in the work not being affected thereby. I also understand that the title and the abstract will be published, and that a copy of the work may be made and supplied to any bona fide library or research worker, that my thesis will be electronically accessible for personal or research use unless exempt by award of an embargo as requested

below, and that the library has the right to migrate my thesis into new electronic forms as required to ensure continued access to the thesis. I have obtained any third-party copyright permissions that may be required in order to allow such access and migration, or have requested the appropriate embargo below.

The following is an agreed request by candidate and supervisor regarding the publication of this thesis:

PRINTED COPY
Embargo on all of print copy for a period of two years on the following ground: publication would preclude future publication in the research literature.

ELECTRONIC COPY
Embargo on all of electronic copy for a period of two years on the following ground: publication would preclude future publication in the research literature.

Date: .... *signature of candidate:* ....

Date: .... *signature of supervisor:* ....

This thesis is best viewed in Adobe Reader, version ≥ 9, or Foxit Reader.

Abstract

In the repertoire of an experimental condensed matter physicist, the ability to tune continuously through features in the electronic structure and to selectively break point-group symmetries are both valuable techniques. The experimental technique at the heart of this dissertation, uniaxial stress, can do both such things.

The thesis will start with a thorough discussion of our new technique, which was continually developed over the course of this work, presenting both its unique capabilities and also some guidance on the best working practices, before moving on to describe results obtained on two different strongly correlated electron materials.

The first, Sr_2RuO_4, is an unconventional superconductor, whose order parameter has long been speculated to be odd-parity. Of interest to us is the close proximity of one of its three Fermi surfaces to a Van Hove singularity (VHs). Our results strongly suggest that we have been able to traverse the VHs, inducing a topological Lifshitz transition. T_c is enhanced by a factor ~ 2.3 and measurements of H_{c2} open the possibility that optimally strained Sr_2RuO_4 has an even-parity, rather than odd-parity, order parameter. Measurements of the normal state properties show that quasiparticle scattering is increased across all the bands and in all directions, and effects of quantum criticality are observed around the suspected Lifshitz transition.

$Sr_3Ru_2O_7$ has a metamagnetic quantum critical endpoint, which in highly pure samples is masked by a novel phase. Weak in-plane magnetic fields are well-known to induce strong resistive anisotropy in the novel phase, leading to speculation that a spontaneous, electronically driven lowering of symmetry occurs. Using magnetic susceptibility and resistivity measurements we can show that in-plane anisotropic strain also reveals the strong susceptibility to electronic anisotropy. However, the phase diagram that these pressure measurements reveal is consistent only with large but finite susceptibility, and not with spontaneous symmetry reduction.

Acknowledgements

The work this thesis represents amounts to almost four years of study, spanning two different institutions, all of which would not have been possible had it not been for the great number of colleagues and friends alike who have helped and supported me throughout.

First and foremost I would like to thank Andy Mackenzie, my supervisor, for his guidance and support along the way. His unique perspective on physics has been incredibly enlightening and I have learnt a great deal. I am also particularly grateful that Andy gave me the time to explore these new ideas in my own way.

None of the work in this thesis would have been possible without the ingenuity of Clifford Hicks and to him I would like to express my sincere gratitude. Not only did he instigate the whole the uniaxial stress project but he has also provided invaluable support, physical insight and supervision throughout my measurements.

During my PhD I have been fortunate enough to spend time at the University of St. Andrews and the Max Planck Institute for Chemical Physics of Solids where I have benefited in different ways from a great number of people. There are too many to thank explicitly here, but I would like to mention just a few in particular. The technical staff of the mechanical workshops and Ulrike Ließ who built the devices were pivotal in the success of this technique, and so too were the cryogenics staff. As part of the Condensed Matter Centre for Doctoral Training I am particularly indebted to the administrative staff, Christine Edwards, Julie Massey and Wendy Clark, who made everything run so smoothly and were especially accommodating with my move to the MPI.

From the lab I am thankful to Dan Brodsky and Jan Bruin who first introduced me to the adiabatic demagnetization refrigerator. I did not ultimately use this cryostat for my final measurements, but it is the one on which I got to work on the strain project for the first time, in collaboration with Dan.

During the middle of my PhD I worked on a series of measurements on the cuprates with Nabhanila Nandi and Chufo Borzi. Despite these measurements not making the final cut for inclusion in this thesis I am particularly grateful for the useful discussions we had together and for making my time in the lab, and Dresden, especially enjoyable. I would also like to thank Veronika Sunko who helped out at the start of the $Sr_3Ru_2O_7$ measurements.

Finally, I would like to thank my family who have always been supportive of my studies and have helped me to reach where I am today.

Contents

Introduction

<div style="text-align: right">**1**</div>

The interactions between particles in nature can present a bewildering array of exotic states and phenomena, each fascinating in their own right, but also in terms of their potential applications. Condensed matter systems with as many as 10^{22} atoms in a single cubic centimetre are a prime example. Of interest for this thesis are a group of materials in which the interactions between electrons are particularly strong, such that one must consider the behaviour of the electrons as correlated. These interactions can drive the formation of states such as superconductors, strange metals and a variety of different magnetic states, to name just a few.

To understand the behaviour of a complex system one often turns to the individual building blocks. In condensed matter physics these are the atoms making up the solid. When considering metals we are concerned with the positive ions which form the crystal lattice and the conduction electrons that move through it. The positive ions comprise the nuclei of the constituent atoms plus the core electrons. The conduction electrons are the outer most electrons which can lower their kinetic energy by travelling through the lattice. This energy benefit is key to the cohesion of atoms in metals [1].

It is simple to account for the motion of each of the individual building blocks and the Coulomb interactions between them but this fully reductionist approach runs into complications [2]. The equations can describe a vast number of properties in condensed matter but the interaction terms put exact solutions for all but the simplest systems out of reach. Instead we must simplify the situation and look for 'emergent' phenomena. As experimentalists we can try to understand these emergent states by measuring their physical properties, but given the ability to perturb the systems we can play with the underlying interactions and make the best tests of theories.

In this thesis I will present measurements on two materials, the first Sr_2RuO_4, known for its unconventional superconductivity, and the second $Sr_3Ru_2O_7$, for its quantum critical behaviour and large nematic-like susceptibility, and show how their properties can be manipulated through carefully applied uniaxial stress. Both materials are exquisitely clean, so to perturb them without destroying the fragile nature of the emergent phenomena a suitably clean tuning parameter is required. Significant technical development was needed to be able to apply a sufficiently homogeneous uniaxial

$$\mathcal{H} = \mathcal{H}_i + \mathcal{H}_e + \mathcal{H}_{e-i}$$

$$\mathcal{H}_i = \sum_i \frac{\mathbf{P}_i^2}{2M_i} + \frac{1}{2} \sum_{i \neq j} \frac{Z_i Z_j e^2}{|\mathbf{R}_i - \mathbf{R}_j|}$$

$$\mathcal{H}_e = \sum_i \frac{\mathbf{p}_i^2}{2m_e} + \frac{1}{2} \sum_{i \neq j} \frac{e^2}{|\mathbf{r}_i - \mathbf{r}_j|}$$

$$\mathcal{H}_{e-i} = -\sum_i \sum_j \frac{Z_j e^2}{|\mathbf{r}_i - \mathbf{R}_j|}$$

Hamiltonian describing simple metals. $\mathcal{H}_i$ describes the positive ion subsystem with masses M_i and charges Z_i. $\mathbf{P}_i$ is the momentum of ion i. $\mathcal{H}_e$ similarly describes the electron subsystem and $\mathcal{H}_{e-i}$ accounts for the coulomb potential between the electrons and positive ions at positions $\mathbf{r}$ and $\mathbf{R}$, respectively.

pressure, so as well as the results a thorough discussion on the improvements to the technique that made this work possible will be given. Before this, though, I will start by briefly introducing how we describe the behaviour of electrons in metals, which will later form the basis for the specific discussions of each material presented in their respective chapters.

1.1 Electrons in metals

To start the discussion of electron correlations in metals it is intuitive to begin with the free non-interacting case and then slowly introduce the correlations. In adopting this procedure, one must trust that reintroducing electron correlations later will not render the insights from the non-interacting case meaningless. In fact there are good reasons for this and a proper justification will be given in the section on Fermi liquids. Now also leaving the lattice of ions behind briefly, or better assuming a uniform positive background charge to maintain charge neutrality, we begin with the free Fermi gas and follow the Sommerfeld model. Conduction electron densities in metals are typically of the order 10^{22} cm^{-3} at room temperature [3]. At these densities the interparticle separations are less than the thermal de Broglie wavelength of the electrons. So to correctly describe the nature of this gas of electrons, quantum effects must be included and the electron gas will obey Fermi-Dirac statistics. Electrons occupy quantised energy states and obey the Pauli exclusion principle. Imagining a gas of electrons in a box of side L with periodic boundary conditions, the wave-functions of the electrons are plane waves with energy

$$\varepsilon_k = \frac{\hbar^2 k^2}{2m_e} \tag{1.1}$$

with quantised values of the wave-vector **k** in units of $(2\pi/L)$. The ground state is built up by filling up from the lowest energy state to the Nth lowest state where N is the number of electrons. The highest occupied energy is called the Fermi energy ε_F with the corresponding Fermi wave-number k_F. In reciprocal space the surface separating the volume containing all the filled states from the unoccupied states is called the Fermi surface, see figure 1.1 [3–5].

At non-zero temperature the population of states follows the Fermi-Dirac distribution. Thermal energy can excite an electron from within the filled Fermi surface to a state just outside creating an electron-hole pair. In a 'free electron metal' the typical Fermi temperature, $\varepsilon_F/k_B \sim 3 \times 10^4$ K, is much much higher than ambient temperature so only a small number of states within an energy of $\sim k_B T$ of the Fermi energy are ever excited. The Pauli

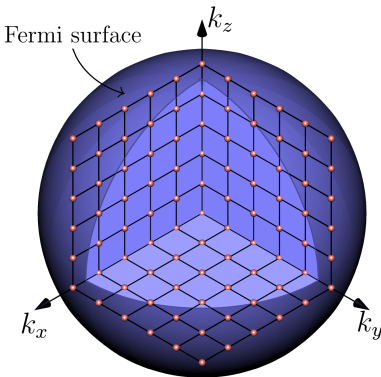Fig. 1.1: **Free electron Fermi surface.** Each **k** point within the sphere is occupied by one up- and one down-spin electron.

exclusion principle prevents the excitation of the lower states since there are no unoccupied final states within $\sim k_{\mathrm{B}}T$. This leads to a T linear specific heat, unlike the constant value for a classical gas, and a temperature independent magnetic susceptibility unlike the Curie-Weiss behaviour of the classical gas, both of which can be observed in real materials.

Reintroducing the periodic lattice, the wave-functions for the electrons are no longer plane waves but instead are described by Bloch waves [5]. The wave-vector or momentum used in the free electron picture no longer makes sense for the Bloch states because of the translational symmetry breaking. Instead, the electron states can be described by a quantity called crystal momentum.

The real space crystal structure is completely defined within the definition of the primitive unit cell. This irreducible volume can map out the whole structure by copying it along each of the translation vectors of the lattice. The same periodicity must exist in reciprocal space where the irreducible volume is now called the Brillouin zone. All momentum states can be mapped back to the first Brillouin zone through the reciprocal lattice vectors giving us the first idea of an electronic band structure, i.e. multiple bands of the electron dispersion, each at higher energy, within the first Brillouin zone. Each band has its own dispersion relationship, $E = E(\mathbf{k})$, but the number of possible states in each band is always equal to the number of allowed crystal momenta in the first Brillouin zone. This is always two times the number of primitive unit cells in the crystal, with the factor of two for spin degeneracy. Filling the allowed states proceeds as in the free electron gas and Sommerfeld model; starting from the lowest energy but now filling a new band when it is the next lowest in energy.

Between each of the bands an energy gap develops, i.e. there are regions of energy where no Bloch wave solutions exist [4]. At wave-vectors satisfying the Bragg reflection condition of the lattice, the two left and right travelling wave-functions combine to form two different standing waves. The two standing waves have different probability densities, with one having higher probability at the lattice sites, and the other between lattice sites. There is therefore a difference in potential energy between the two solutions and this is the origin of the energy gap.

From the idea of Bloch waves we can extract a mean velocity for each of the electron states. At the Fermi energy we define the Fermi velocity

$$\boldsymbol{v}_{\mathrm{F}} = \frac{1}{\hbar}\left.\nabla_{\mathbf{k}}\varepsilon\right|_{k_{\mathrm{F}}} , \tag{1.2}$$

and from this we can identity a band mass

$$m^{*} = \left(\frac{1}{\hbar^{2}k_{\mathrm{F}}}\left.\nabla_{\mathbf{k}}\varepsilon\right|_{k_{\mathrm{F}}}\right)^{-1} . \tag{1.3}$$
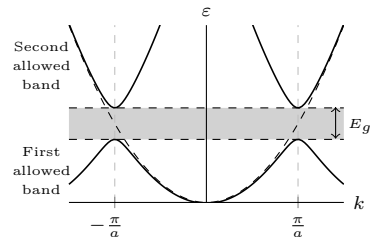

Fig. 1.2: **Nearly-free electron dispersion.** The free electron dispersion, dashed line, transforms into a set of discrete bands with energy gaps in between when a periodic potential with lattice constant a is weakly introduced. Adapted from [4].

This measures the impact of the lattice on the motion of the electrons by how much it differs from the bare electron mass m_e. We will see later that electron correlations can also enhance the effective mass further above the band mass.

When filling up states up to the Fermi level we can think of filling up to a surface with electrons but if only a few empty states remain close to the top of the band it is equally sensible to describe the band in terms of only the unoccupied states, or holes, at the top of the band. A hole is the absence of an electron so carries opposite charge and momenta to the electron states they are replacing.

There are two common limiting cases when continuing this discussion further; the periodic potential can be added to the free electron gas as a weak perturbation in a model called the nearly-free electron model, or we can start with atomic orbitals and slowly bring the lattice closer together allowing the electrons to hop between atomic sites described by the tight-binding model [5]. In this case, the itineracy is a perturbation on the atomic limit. The nearly-free electron model works very well for the alkali metals [5]. Although the Coulomb attraction to the lattice should at first sight be large, the Pauli exclusion principle keeps the conduction electrons in higher orbitals, further away from the ion cores on average, where the interaction is lower and the core electrons can additionally screen the ion's charge. So in some scenarios the nearly-free electron model is entirely valid. For the alkali metals, with only one valence electron per atom, it is particularly good, because the Fermi surface fills only half of the first Brillouin zone, well away from the zone boundaries, thus avoiding the distortions of the band due to the band gaps [3].

For the materials we will be discussing later, Sr_2RuO_4 and $Sr_3Ru_2O_7$, both transition metal oxides, we are mainly concerned with the d-electron shell. For example, at the normal valencies for strontium and oxygen in Sr_2RuO_4, Sr^{2+} and O^{2-}, the ruthenium ion with a valency of Ru^{4+} is left in a $4d^4$ electronic configuration [6]. The d-electron shells have small orbital radii meaning the interatomic overlap of the orbitals will be small and there will be a large potential penalty for double occupancy [7]. These factors take us away from the nearly-free electron limit. Many d-electron systems remain localized, forming a magnetic insulating state as opposed to a metallic one, especially in the 3d series [7]. The strontium ruthenate series is an exception and each remains metallic, but it is constructive to view them in a tight-binding fashion. I will now continue with a more formal description of the tight-binding model which will be useful for the derivations of the Fermi surfaces for both materials later.

In the tight-binding description we build the Bloch wavefunctions for the electrons from the atomic orbitals [3]. We assume

the extent of the atomic orbitals, $\phi(\mathbf{r})$, is close to or smaller than the interatomic separation so they are mostly unperturbed when assembled into the lattice. The tight-binding wavefunction is a linear combination of approximately atomic orbitals [5]

$$\Psi_{\mathbf{k}}(\mathbf{r}) = \sum_{\mathbf{R}} e^{i\mathbf{k}\cdot\mathbf{R}}\phi(\mathbf{r} - \mathbf{R})\,. \tag{1.4}$$

The real space positions of the atoms determine how the bands develop. To illustrate this I will start with a simple cubic lattice, lattice constant a, of s states. We take a small perturbation, $V(\mathbf{r})$, to the atomic Hamiltonian which captures the periodicity of the lattice and look for the first-order corrections to the energy.[1]

$$\Delta E = \langle\Psi_{\mathbf{k}}|V|\Psi_{\mathbf{k}}\rangle \tag{1.5}$$

$$= \sum_n \sum_m e^{i\mathbf{k}\cdot(\mathbf{R}_n - \mathbf{R}_m)} \int \phi^*(\mathbf{r} - \mathbf{R}_m)V\phi(\mathbf{r} - \mathbf{R}_n)dV \tag{1.6}$$

$$= \sum_m e^{-i\mathbf{k}\cdot\mathbf{a}_m} \int \phi^*(\mathbf{r} - \mathbf{a}_m)V\phi(\mathbf{r})dV \tag{1.7}$$

where $\mathbf{a}_m = \mathbf{R}_m - \mathbf{R}_n$. The integral is dominated by the on-site terms, $\mathbf{a}_m = 0$, and the six nearest neighbour terms, $\mathbf{a}_m = \pm a\hat{\mathbf{x}}$, $\pm a\hat{\mathbf{y}}$, $\pm a\hat{\mathbf{z}}$. We can drop all other terms because the atomic orbital overlap will be negligible. Thus we end up with

$$E(\mathbf{k}) = E_\phi - B - 2t(cos(k_x a) + cos(k_y a) + cos(k_z a))\,, \tag{1.8}$$

where

$$B = -\int \phi^*(\mathbf{r})V\phi(\mathbf{r})dV \tag{1.9}$$

$$t = -\int \phi^*(\mathbf{r} - \mathbf{a})V\phi(\mathbf{r})dV\,. \tag{1.10}$$

The parameter t is known as the transfer integral, a measure of the ease of hopping from one atom to the next. In general, starting from n atomic levels on each atom, these will combine to form n separate bands. The bandwidth of the band is directly related to the transfer integral. A smaller atomic overlap, with a correspondingly smaller transfer integral, has a narrower bandwidth and a higher effective mass. In this way the effects of the real-space crystal structure are seen in the band structure; if in a certain direction the atoms are further apart, the bandwidth will be narrower for motion along that direction as is expected. The shape of the bands will also reflect the character of atomic orbitals they are made up from [5].

We have just seen two extreme cases for electrons in a metal; a scenario where the periodic potential is only a very weak perturbation to otherwise free electrons and the opposite extreme where the potential is so strong the electrons can hardly hop from one atom

to the next. Both cases give rise to bands with corresponding gaps between them but crucially they are qualitatively similar. This implies that real materials, which will fall somewhere in between these two extremes, must also have qualitatively similar band structures.

1.2   Landau's Fermi liquid

Up until now we have been ignoring the electron-electron Coulomb interaction but without foresight this should not have seemed like a sensible thing to do. By no means is the Coulomb interaction weak. Just making a quick back of the envelope calculation we can compare the scale of the Coulomb interaction with the kinetic energy of the electrons, which is the other important energy scale. From the electron density we can define a characteristic length, the radius of a sphere occupied by one electron, which sets the approximate kinetic energy $E_K \approx \hbar^2/8m_e r_s^2$ and the Coulomb repulsion between two electrons $E_C \approx e^2/8\pi\varepsilon_0 r_s$. The ratio gives us the importance of the electron-electron Coulomb interaction $E_C/E_K \approx r_s m_e e^2/\pi\varepsilon_0\hbar^2 = 4r_s/a_0$, where a_0 is the Bohr radius. For typical metallic densities r_s is order Ångströms [3] whereas a_0 is half an Ångström. The electron-electron Coulomb interaction is not weak so how did we get on so well when we ignored it? The answer comes from Landau and his notion of a Fermi liquid [8–10]. If we start from a Fermi gas and turn on a mutual repulsion between all the electrons the Fermi gas turns into a Fermi liquid. The naming is in analogy to classical gases and liquids whereby introducing inter-particle interactions condenses the gas to a liquid. The beauty is that the Fermi liquid retains some of the key properties of the Fermi gas.

By allowing the electrons to interact and exchange momentum the Fermi surface, in its original state, is no longer stable [11]. The insight of Landau was rather than caring about the individual electron states, to instead see what happens to the excitations of the Fermi gas as the electron-electron interaction is 'turned on'. An electron excited above the Fermi level can now Coulomb scatter with another below the Fermi level resulting in an additional electron-hole pair. This process can continue creating additional electron-hole pairs until some equilibrium is reached. This original excitation can now be described as the superposition of the bare electron, the bare electron and an electron-hole pair, the bare electron and two electron-hole pairs, and so forth [12].

$$|\Psi_{qp}\rangle = \sqrt{Z}|\phi_{el}\rangle + |\text{particle-hole excitations}\rangle + \dots \qquad (1.11)$$

The insight of Landau was that if we turn on the interaction slowly enough we can evolve smoothly from one picture to the other as

the strength of the Coulomb interaction is increased. This concept is referred to as adiabatic continuity and we call the excited states of the interacting system Landau quasiparticles to remind us that the wavefunctions and energies are different from the corresponding electrons in the non-interacting problem. The quasiparticles do however retain the same charge and spin as the bare electron but neither the mass nor the interactions between quasiparticles need to remain the same. This one-to-one mapping of the interacting states with those of the non-interacting Fermi gas retains the picture of Fermi particles and a Fermi surface but one that is now stable since the Coulomb interaction has already been taken into account.

By producing the quasiparticles in this way they are made out of states which are no longer exact eigenstates of the system. Thus they cannot be infinitely long lived and the quasiparticles can scatter off one another. Their inverse lifetime can be calculated from Fermi's golden rule. Making reference to figure 1.3, a quasiparticle at energy ε scatters off one in the Fermi sea and looses energy ω. The total decay rate $1/\tau_\varepsilon$ for these processes is

$$\frac{1}{\tau_\varepsilon} = \frac{2\pi}{\hbar} \sum_f |V_{if}|^2 \, \delta(\varepsilon - \varepsilon_f) \tag{1.12}$$

Fig. 1.3: **Quasiparticle Scattering.** A quasiparticle with energy ε above the Fermi surface can scatter off another from within the Fermi sea to create an additional particle-hole pair. Reproduced from [12].

where the sum is over all possible final states. We assume the scattering matrix elements $|V_{if}|$ are constant and make use of conservation of energy and momentum to restrict the possible final states. The Pauli exclusion principle also puts strict phase space restraints on the possible scatterings. There must be an unoccupied final state for the electron to scatter into so ω must be less than ε and the second electron must be within ω of the Fermi energy such that is can also reach an unoccupied state with the promotion of energy ω. Using the density of states at the Fermi level, g_{F}, to turn this into an integral

$$\frac{1}{\tau_\varepsilon} \sim \frac{2\pi}{\hbar} \, |V|^2 \int_0^\varepsilon g_{\mathrm{F}} d\omega \int_0^\omega g_{\mathrm{F}} d\varepsilon' \int_{-\infty}^\infty \delta(\varepsilon - \omega - \varepsilon' + \varepsilon'') g_{\mathrm{F}} d\varepsilon'' \tag{1.13}$$

$$\frac{1}{\tau_\varepsilon} \propto g_{\mathrm{F}}^3 \varepsilon^2 \, . \tag{1.14}$$

We can now see that at sufficiently small energies close to the Fermi surface the quasiparticle is well defined. Here the quasiparticle's decay rate, $\propto \varepsilon^2$, is much less than its excitation energy ε. Further from the Fermi surface adiabatic continuity no longer holds, i.e. the quasiparticles scatter before the interaction can be completely turned on. Quasiparticles are therefore only well defined around the Fermi energy.

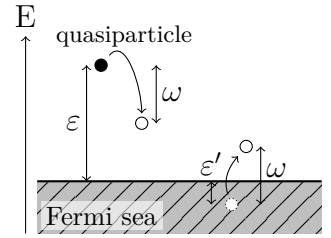We are now in a position to see why the non-interacting case

A $n_{\mathbf{k},e}$

1

k_F $\quad$ $|\mathbf{k}|$

B $n_{\mathbf{k},e}$

1

Z

k_F $\quad$ $|\mathbf{k}|$

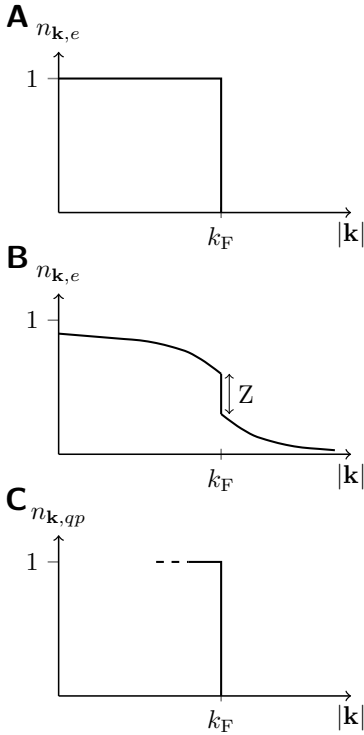**C** $n_{\mathbf{k},qp}$

1

k_F $\quad$ $|\mathbf{k}|$

Fig. 1.4: **Particle probability distributions. A.** The probability that any given energy state is occupied by an electron at $T = 0$ in a Fermi gas, the Fermi-Dirac distribution. **B.** The probability distribution of electrons at $T = 0$ in a Fermi liquid, the discontinuity at k_F remains. **C.** The probability distribution of quasiparticles in the Fermi liquid recovers the Fermi-Dirac distribution. Reproduced from [12].

worked so well. The same phenomenology of electron-hole excitations from an electron Fermi sea applies for the Fermi liquid, but now the excitations are quasiparticle-quasihole excitations from the quasiparticle Fermi sea, and we recover the same qualitative predictions as those of the Sommerfeld model. Figure 1.4 shows how we can schematically think of this transformation. The electron probability distribution is modified under the presence of a weak mutual interaction but the sharp discontinuity at the Fermi wavevector survives. If instead we talk of the quasiparticles we recover the ordinary Fermi-Dirac distribution but as the quasiparticles are only well defined near the Fermi surface, we can only talk of small excitations from the Fermi energy.

Calculating the total energy of the interacting system by just summing up the contributions from each of the individual excitations will not now in general yield the total energy of the system. A quasiparticle's energy will also depend on the distribution of the other quasiparticles. The energy can be written as a function of the quasiparticle distribution $\delta n_{\mathbf{k},\sigma}$ [12]

$$E = \sum_{\mathbf{k}\sigma} \frac{\hbar k_\mathrm{F}}{m^*}(|\mathbf{k}| - k_\mathrm{F})\delta n_{\mathbf{k}\sigma} + \sum_{\mathbf{k}\sigma,\mathbf{k}'\sigma'} f_{\mathbf{k}\sigma,\mathbf{k}'\sigma'}\delta n_{\mathbf{k}\sigma}\delta n_{\mathbf{k}'\sigma'}. \quad (1.15)$$

The Fermi liquid is described by a number of parameters. Its effective mass m^*, a measure of how easily quasiparticles can move, and Landau's f functions. In an isotropic system, a circular Fermi surface in 2D or a spherical Fermi surface in 3D, these can be expanded as Legendre polynomials and quantify the angular dependence of the interactions of the quasiparticle system. Using this terminology the specific heat and magnetic susceptibility can be re-expressed as [12]

$$C_\mathrm{V} = \frac{m^* k_\mathrm{F}}{3\hbar^2}k_\mathrm{B}^2 T = \frac{m^*}{m_e}C_{\mathrm{V,Fermi\ gas}} \quad (1.16)$$

^{2} F_0^a is a Landau parameter.

$$\chi = \frac{m^* k_\mathrm{F}}{\pi^2}\frac{1}{1+F_0^a}\mu_\mathrm{B}^2 = \frac{m^*}{m_e}\frac{1}{1+F_0^a}\chi_{\mathrm{Fermi\ gas}}.^2 \quad (1.17)$$

The Fermi liquid's specific heat and susceptibility are both enhanced over the Fermi gas values by the effective mass, and for the susceptibility also the Wilson ratio $1/(1 + F_0^a)$. Both these are measures of the strength of the correlations.

The electrical resistivity of a Fermi liquid has a characteristic T^2 dependence [13, 14]. We saw from equation 1.14 that the decay rate of quasiparticles goes like the square of their energy measured from the Fermi energy. At finite temperature the excitations are of order $k_\mathrm{B}T$ so the decay rate is proportional to the temperature squared. However in equation 1.14 we originally discussed

normal quasiparticle-quasiparticle interactions that conserve momentum so do not produce a finite resistivity, but the decay rate for quasiparticle-quasiparticle umklapp scattering, which can relax the momentum to the lattice, has similar phase space constraints so produces the same T^2 dependence of the decay rate and the T^2 resistivity in the simplest picture.

Although it is a phenomenological theory, Landau's Fermi liquid theory works remarkably well. Experimental verification has been seen in a whole variety of systems, including those where you might suspect interactions to be too strong. An example is UPt_3 which shows particularly strong correlations with effective masses enhanced in the range 10 to 30 above the band mass, yet still follows the predictions from Landau's Fermi liquid theory [15–18]. However, Fermi liquid theory does not always work and because of the robustness of the theory the cases where it fails are all the more interesting.

If the interparticle interactions are long range the idea of adiabatic continuity breaks down; a finite speed of propagation means the interaction takes infinite time to 'turn on' so there can be no stable quasiparticles. The bare Coulomb interaction is long range but in metals the Fermi liquid is saved by screening. Electron screening means that at large distances, greater than the Thomas-Fermi screening length $k_{TF}^2 = 4\pi e^2 N_0$, only the background charge level is felt. In special cases long range interactions can still be observed which break apart the Fermi liquid. Near to a continuous phase transition order parameter fluctuations slow down and become increasingly long range. One quasiparticle can then quite easily affect a large number of other quasiparticles increasing the scattering cross section. If the continuous phase transition can be suppressed to zero temperature by a non-thermal tuning parameter such as pressure or chemical doping, the quasiparticle interaction range can grow without limit. We call such a zero temperature continuous phase transition a quantum critical point and in the vicinity of the quantum critical point the quantum fluctuations cause a break-down of the Landau Fermi liquid phenomenology.

Weakly repulsive interactions in the metallic phase are well accounted for by Fermi liquid theory, but if the interparticle interactions are attractive Fermi liquid theory can become invalid as bound states of quasiparticles can be stabilised. An example is the retarded electron-phonon interaction which is attractive and below a critical temperature the Fermi surface is unstable to forming bound states of electrons. These bound states of two fermions can then condense into a new ground state, namely superconductivity.

The materials being studied in this thesis both have well characterised Fermi liquid phases but are unstable to different instabilities. Sr_2RuO_4 develops an unconventional superconducting state at low

temperatures but one where the paring symmetry has not yet been unambiguously determined. $Sr_3Ru_2O_7$ can be tuned to a quantum critical end point with applied magnetic field and there a novel phase with suspected spontaneous C_4 to C_2 symmetry breaking develops. Further discussions of the physics of both systems is presented in their respective chapters, 3 and 4, but in the next chapter I will switch gears and first discuss the experimental technique that my research so heavily relied on.

Uniaxial Stress Technique

<div style="text-align:right">**2**</div>

2.1 Introduction

Advances in condensed matter physics come, often, from new material discoveries. The field of superconductivity is one such example, marked by the discovery of each new family of superconductors. Since the first observation of superconductivity in mercury by Onnes in 1911 [19] there was a gradual increase in the highest critical temperature for over 50 years, up to what was thought at the time to be a theoretical limit of ∼30 K [20]. These superconductors are now termed conventional superconductors. Then in 1986 the first high temperature cuprate was discovered [21] leading to a flurry of material discoveries bringing T_c at ambient pressure up to ∼133 K [22]. Similar developments occurred when the families of heavy fermion superconductors [23, 24, 16] and iron-based superconductors were found [25–28]. In parallel to these material discoveries, experimental techniques were continually improving and new techniques developed. For instance stronger magnetic fields allowed the Fermi surface of the underdoped high temperature cuprate superconductors to be seen with quantum oscillations measurements for the first time [29–31] and ever increasing hydrostatic pressures have produced superconductivity at 203 K in H_2S at a pressure of ∼150 GPa [32]. These advances in experimental techniques allow us to probe deeper into the physics of both new and old materials, guiding the way for future developments.

Here I will discuss one such development. The technique of uniaxial pressure has been employed in condensed matter physics for a long time but it appears to be wholly underused, especially in comparison to its hydrostatic counterpart. This could chiefly be due to the extreme technical challenges associated with traditional methods for applying uniaxial pressure. However this technique was recently reenvisioned by Clifford Hicks *et al.* in a landmark experiment on Sr_2RuO_4 [33, 34]. By moving away from the typical sample measurement geometries and instead shaping samples into long thin bars, that are fixed across the jaws of a vice, exceptional homogeneity, tunability and precision of the applied strain can be achieved.

Uniaxial strain or pressure can be a powerful tool for investigating the electronic properties of correlated matter. In the simplest picture the crystal lattice is deformed anisotropically influencing

the overlap between atomic orbitals on neighbouring sites. For a correlated electron system the effect can be particularly strong since the overlap integral is very important for electron hoppings between neighbouring sites.

This effect can be much larger in uniaxial pressure compared to equal hydrostatic pressures. Uniaxial pressure is also a directional technique so different lattice distortions can be selected and compared. It can also be used to lift point-group symmetries of the crystal and perturb finely balanced systems. In this sense it is a combination between an experimental technique and something that creates new materials that are not available to equilibrium chemistry under ambient conditions.

In this chapter I will start by introducing the stress and strain formalism then describe the finite element method (FEM) used for carrying out realistic simulations. In the next section I will describe existing uniaxial stress and strain techniques before introducing our new uniaxial pressure cell. I will use simple analytic expressions accompanied by in-depth finite element simulations to highlight the improvements of this technique and provide readily achievable guidelines for experiments.

2.2   Stress and strain

The deformation an object undergoes when subject to a load can be described in terms of two quantities; the stress and the strain within the object. These are both tensor fields over the extent of the object. Stress is a measure of how the force is distributed internally throughout the object in units of N/m^2 and strain is a dimensionless quantity that measures the relative displacements within the object referenced to the original size. Stress and strain are in a way analogous to pressure and volume, a thermodynamic conjugate pair for a non-viscous fluid, but are applicable for viscous fluids and elastic solids where the stress tensor can be thought of as a generalisation of the pressure and the strain tensor as a generalisation of the change in volume.
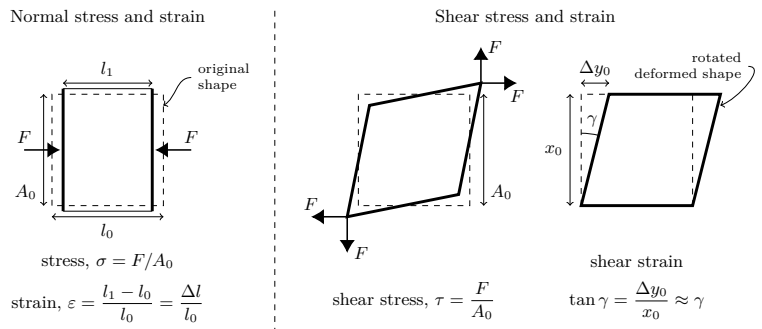
Fig. 2.1: **Stress and Strain** Definitions of engineering normal stress and strain, and engineering shear stress and strain.

Normal stress and strain

stress, $\sigma = F/A_0$

strain, $\varepsilon = \dfrac{l_1 - l_0}{l_0} = \dfrac{\Delta l}{l_0}$

Shear stress and strain

shear stress, $\tau = \dfrac{F}{A_0}$

shear strain

$\tan\gamma = \dfrac{\Delta y_0}{x_0} \approx \gamma$

For any given plane in the object the internal forces acting on that plane can be decomposed into a normal component and two in-plane components. These forces, divided by the original area of the plane, define the engineering normal and shear stresses respectively (see figure 2.1 for a schematic representation). Engineering strain is defined in a similar manner; displacement divided by original object size. A more general representation of the strain field can be obtained from the displacement field $\boldsymbol{u}$, where $\boldsymbol{u}$ is a three component vector field defining the displacement at any point within the object. The different components of the strain tensor are given by,

$$\varepsilon_{ij} = \frac{1}{2}\left(\frac{\partial u_i}{\partial x_j} + \frac{\partial u_j}{\partial x_i}\right),\tag{2.1}$$

where $\boldsymbol{x}$ is the coordinate and the two indices label the three orthogonal coordinate directions.

The six components of the strain tensor explicitly are:

$$\begin{aligned}
\varepsilon_{xx} &= \frac{\partial u}{\partial x} & \varepsilon_{yz} &= \frac{1}{2}\left(\frac{\partial w}{\partial y} + \frac{\partial v}{\partial z}\right) = \frac{1}{2}\gamma_{yz} \\
\varepsilon_{yy} &= \frac{\partial v}{\partial y} & \varepsilon_{zx} &= \frac{1}{2}\left(\frac{\partial u}{\partial z} + \frac{\partial w}{\partial x}\right) = \frac{1}{2}\gamma_{zx} \\
\varepsilon_{zz} &= \frac{\partial w}{\partial z} & \varepsilon_{xy} &= \frac{1}{2}\left(\frac{\partial v}{\partial x} + \frac{\partial u}{\partial y}\right) = \frac{1}{2}\gamma_{xy}
\end{aligned}\tag{2.2}$$

where u, v and w are the three components of the displacement field $\boldsymbol{u}$ in the x, y and z directions respectively.

The full tensor is given by:

$$\boldsymbol{\varepsilon} = \begin{pmatrix} \varepsilon_{xx} & \varepsilon_{xy} & \varepsilon_{xz} \\ \varepsilon_{yx} & \varepsilon_{yy} & \varepsilon_{yz} \\ \varepsilon_{zx} & \varepsilon_{zy} & \varepsilon_{zz} \end{pmatrix},\tag{2.3}$$

in which, by symmetry, the off-diagonal components $\varepsilon_{ij} = \varepsilon_{ji}$.
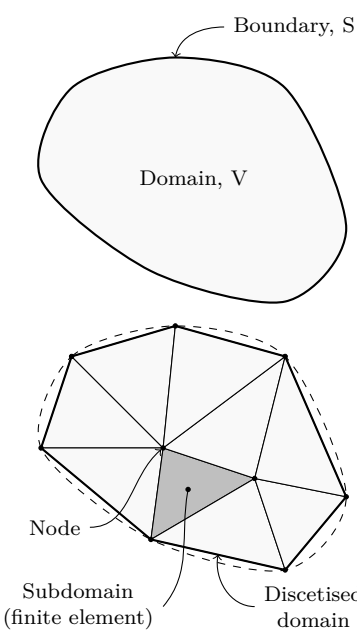
Stress and strain are intimately linked. At low strains where the response is still elastic, stress and strain are directly proportional. For a uniaxially loaded object the relationship is

$$\sigma = E\varepsilon.\tag{2.4}$$

This is just Hooke's Law where E is the Young's Modulus of the material. The analogous equation for shear stress and strain is $\tau = G\gamma$ where G is the shear modulus. In three dimensions E and G generalise to a 6 by 6 tensor, $\boldsymbol{C}$, called the stiffness tensor; $\sigma_i = C_{ij}\varepsilon_j$. The stiffness tensor is symmetric so at most there can be 21 independent components, but if the material possess further symmetries this number is reduced. One example, for instance, is the tetragonal lattice

$$
\begin{pmatrix} \sigma_{xx} \\ \sigma_{yy} \\ \sigma_{zz} \\ \sigma_{yz} \\ \sigma_{zx} \\ \sigma_{xy} \end{pmatrix} = \begin{pmatrix} C_{11} & C_{12} & C_{13} & 0 & 0 & 0 \\ C_{12} & C_{11} & C_{13} & 0 & 0 & 0 \\ C_{13} & C_{13} & C_{33} & 0 & 0 & 0 \\ 0 & 0 & 0 & C_{44} & 0 & 0 \\ 0 & 0 & 0 & 0 & C_{44} & 0 \\ 0 & 0 & 0 & 0 & 0 & \frac{1}{2}(C_{11} - C_{12}) \end{pmatrix} \begin{pmatrix} \varepsilon_{xx} \\ \varepsilon_{yy} \\ \varepsilon_{zz} \\ 2\varepsilon_{yz} \\ 2\varepsilon_{zx} \\ 2\varepsilon_{xy} \end{pmatrix} . \tag{2.5}
$$

Since this is no longer an isotropic system, the Young's modulus is direction-dependent and takes on a different value along each of the high-symmetry directions; $E_x = \sigma_{xx}/\varepsilon_{xx}$ and $E_z = \sigma_{zz}/\varepsilon_{zz}$. Poisson's ratio must be defined in a similar manner. Poisson's ratio is the coefficient of transverse expansion, i.e. it is the ratio of transverse strain to longitudinal strain for a longitudinal loading. In the tetragonal lattice Poisson's ratio is defined along the high symmetry directions as $\nu_{xy} = -\varepsilon_{yy}/\varepsilon_{xx}$ and $\nu_{zx} = -\varepsilon_{zz}/\varepsilon_{xx}$ when $\sigma_{xx} \neq 0$ and all other $\sigma_{ij} = 0$. The Young's moduli and Poisson's ratios are included in the stiffness tensor in the following way:

$$
\boldsymbol{C}^{-1} = \begin{pmatrix} \dfrac{1}{E_x} & -\dfrac{\nu_{yx}}{E_x} & -\dfrac{\nu_{zx}}{E_z} & 0 & 0 & 0 \\[2mm] -\dfrac{\nu_{xy}}{E_x} & \dfrac{1}{E_x} & -\dfrac{\nu_{zx}}{E_z} & 0 & 0 & 0 \\[2mm] -\dfrac{\nu_{xz}}{E_x} & -\dfrac{\nu_{xz}}{E_x} & \dfrac{1}{E_z} & 0 & 0 & 0 \\[2mm] 0 & 0 & 0 & \dfrac{1}{G_{yz}} & 0 & 0 \\[2mm] 0 & 0 & 0 & 0 & \dfrac{1}{G_{yz}} & 0 \\[2mm] 0 & 0 & 0 & 0 & 0 & \dfrac{2(1 + \nu_{xy})}{E_x} \end{pmatrix} . \tag{2.6}
$$

When applying these ideas to real life models the analytical equations introduced above quickly become very complex. In all but only the very simplest cases approximations must be made. I will show later on in this chapter some ways a model can be simplified but more often than not it is necessary to move away from analytics and turn to numerical simulations. In the next section I will introduce one such method for numerical simulations and outline how to use it to solve for the stress and strain of a complex geometry.

2.3   Finite element method

In its most general form, the finite element method is a framework for calculating approximate numerical solutions to boundary value problems for partial differential equations. A key feature

Fig. 2.2: **Discretisation of a domain.** The domain V is discretised by tessellating triangular elements. Reproduced from [35].

is the subdivision of the problem into simpler parts called finite elements [35]. By doing this we can easily represent a complex geometry with simple standardised building blocks, see figure 2.2. It also allows us to keep track of different material properties for different parts of the geometry. For each finite element an approximate solution to the global differential equation is found, built from linear combinations of the nodal values using approximating functions. The relationships between the nodes are then used to assemble all the elemental solutions into a solution over the whole domain.

I will now outline briefly how this procedure works for linear elasticity and calculating stresses and strains for objects under load. See Reddy [35] or Cook [36] for a more in-depth discussion of the theory behind this technique.

The potential energy associated with elastic deformation is

$$U = \frac{1}{2} \int_V \boldsymbol{\varepsilon}^T \boldsymbol{\sigma} dV \,, \tag{2.7}$$

where $\boldsymbol{\varepsilon}$ and $\boldsymbol{\sigma}$ are the strain and stress vectors, respectively, and the integral is over the volume of the object. When the deformation is due to external forces acting on the surfaces of the object the contribution to the total potential energy due to the work done by the external forces $\boldsymbol{F}$ is given by

$$U = - \int_S \boldsymbol{u}^T \boldsymbol{F} dS \,, \tag{2.8}$$

where this time the integration is over the surfaces of the object and $\boldsymbol{u}$ is the displacement. The stationary solution for the unknown displacements is found by minimising the total potential energy with respect to the displacements.

As per the FEM formalism we represent the displacement at any given point by interpolating from the nodal displacements for each element. Within a given element the displacement vector, $\boldsymbol{u}^e$, is calculated by

$$\boldsymbol{u}^e(x,y,z) \approx \boldsymbol{N}\boldsymbol{q}^e$$

$$= \begin{pmatrix} \sum_{i=1}^{n} N_i^e(x,y,z)\, q_{i,x}^e \\ \sum_{i=1}^{n} N_i^e(x,y,z)\, q_{i,y}^e \\ \sum_{i=1}^{n} N_i^e(x,y,z)\, q_{i,z}^e \end{pmatrix} \tag{2.9}$$

$$= \begin{pmatrix} N_1^e & 0 & 0 & N_2^e & & 0 \\ 0 & N_1^e & 0 & 0 & \cdots & 0 \\ 0 & 0 & N_1^e & 0 & & N_n^e \end{pmatrix} \boldsymbol{q}^e \,.$$
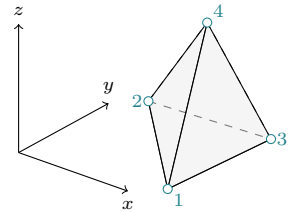
Global coordinates
$(x,\ y,\ z)$

Natural coordinates
$(\xi,\ \eta,\ \zeta)$

$$N_1(\xi,\eta,\zeta) = 1 - \xi - \eta - \zeta$$
$$N_2(\xi,\eta,\zeta) = \xi$$
$$N_3(\xi,\eta,\zeta) = \eta$$
$$N_4(\xi,\eta,\zeta) = \zeta$$
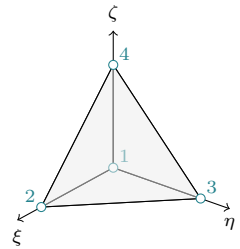
Fig. 2.3: **Natural coordinates and shape functions.** Natural coordinates of a linear tetrahedral element and the shape functions for this element.

N_i are the shape functions for the element and they specify how to interpolate between the nodal displacements $\boldsymbol{q}^e$. The shape functions depend on the type of element used; see figure 2.3 for an example using tetrahedral elements. Figure 2.3 also shows the transformation to the natural coordinates of the element which makes processing easier.

Turning back to the equations for potential energy we can now represent $\boldsymbol{\varepsilon}$ in terms of the nodal displacements

$$\boldsymbol{\varepsilon}^e = \boldsymbol{D}\boldsymbol{u}^e$$

$$= \begin{pmatrix} \dfrac{\partial}{\partial x} & 0 & 0 \\ 0 & \dfrac{\partial}{\partial y} & 0 \\ 0 & 0 & \dfrac{\partial}{\partial z} \\ 0 & \dfrac{\partial}{\partial z} & \dfrac{\partial}{\partial y} \\ \dfrac{\partial}{\partial z} & 0 & \dfrac{\partial}{\partial x} \\ \dfrac{\partial}{\partial y} & \dfrac{\partial}{\partial x} & 0 \end{pmatrix} \boldsymbol{u}^e \tag{2.10}$$

$$= \boldsymbol{D}\boldsymbol{N}\boldsymbol{q}^e = \boldsymbol{B}\boldsymbol{q}^e \,,$$

from which we can then minimise the total potential energy with respect to displacement to find the equilibrium equation

$$U_T^e = \frac{1}{2} \int_{V^e} \boldsymbol{\varepsilon}^T \boldsymbol{\sigma} \, dV^e - \int_{S^e} \boldsymbol{u}^T \boldsymbol{F}^e dS^e$$

$$U_T^e = \frac{1}{2} \int_{V^e} (\boldsymbol{q}^e)^T \boldsymbol{B}^T C \boldsymbol{B}\boldsymbol{q}^e dV^e - \int_{S^e} (\boldsymbol{q}^e)^T \boldsymbol{N}^T \boldsymbol{F}^e dS^e$$

$$\frac{\partial U_T^e}{\partial \boldsymbol{q}^e} = \int_{V^e} \boldsymbol{B}^T C \boldsymbol{B}\boldsymbol{q}^e dV^e - \int_{S^e} \boldsymbol{N}^T \boldsymbol{F}^e dS^e = 0 \tag{2.11}$$

$$0 = \boldsymbol{k}^e \boldsymbol{q}^e - \boldsymbol{f}^e \,.$$

$\boldsymbol{k}^e$ is known as the element stiffness matrix

$$\boldsymbol{k}^e = \int_{V^e} \boldsymbol{B}^T C \boldsymbol{B} dV^e \,. \tag{2.12}$$

The global stiffness matrix, $\boldsymbol{K}$, is obtained by adding the individual coefficients in the elemental stiffness matrices $\boldsymbol{k}_{ij}^e$ to $\boldsymbol{K}_{kl}$ in such a way that that the subscripts ij, indicating the nodal displacements $\boldsymbol{q}_i^e$ and $\boldsymbol{q}_j^e$, match with the global nodal displacement indices. The components of the force vector are added in a similar way and this

leads the the final equation

$$\boldsymbol{K}\boldsymbol{q} = \boldsymbol{f} \, . \tag{2.13}$$

So in practice the first step is to divide the object up into small elements, then calculate the stiffness matrix for each. The integration can be performed efficiently by making use of Gaussian quadrature rules and the Jacobian to perform the integration in the natural coordinates. The elemental stiffness matrices are combined to form the global stiffness matrix and the boundary conditions are applied to the problem by generating the force vector before solving equation 2.13 for $\boldsymbol{q}$ with any of the variety of suitable algorithms.

Commercial software is available for finite element analysis, but it is either too restrictive to be applied to the full range of problems relevant to the research described in this thesis, or prohibitively expensive. I therefore wrote a program to perform the calculation myself with the desired level of flexibility. Using MATLAB® [37] this could be achieved in under 500 lines of code.

2.4 Uniaxial stress and strain techniques

Uniaxial pressure studies have presented themselves in many forms. Here I will outline some of the techniques that have been developed as well as their accomplishments and pitfalls that motivated the development of a new technique.

2.4.1 Indirect determination using Ehrenfest relations

The fragile nature of some materials makes direct uniaxial pressure measurements challenging. Fortunately information about the pressure derivatives of transition temperatures can be obtained indirectly from thermal expansion and heat capacity measurements combined with the thermodynamic Ehrenfest relation. In the Ehrenfest classification of phase transitions a first-order transition exhibits a discontinuity in the first derivative of the free energy. An example is the liquid-gas transition, which has a discontinuity in the density between the liquid and gas phases. The density relates to the first derivative of free energy with respect to pressure, $\rho = m(\partial G/\partial p)_T^{-1}$ [3]. A second order phase transition shows no discontinuity in the first derivative of free energy. The order parameter of the transition, which is related to the first derivative of free energy, is continuous across the transition. However quantities that depend on the second derivatives of the free energy show discontinuities. The differential form of the Gibbs free energy is

[3] Where m is the mass, G the Gibbs free energy, p pressure and T temperature.

$$dG = V dp - S dT \tag{2.14}$$

so at a second-order phase transition

$$dG_1 = V_1 dp - S_1 dT = V_2 dp - S_2 dT = dG_2 \tag{2.15}$$

were 1 and 2 indicate the two phases. Substituting in the values for the volume thermal expansion coefficient, β, and the heat capacity, C_P,

$$\beta = \frac{1}{V} \left(\frac{\partial V}{\partial T} \right)_p, \quad C_P = T \left(\frac{\partial S}{\partial T} \right)_p \tag{2.16}$$

this can be written

$$\left(\frac{\partial V_1}{\partial T} \right)_p dp - \left(\frac{\partial S_1}{\partial T} \right)_p dT = \left(\frac{\partial V_2}{\partial T} \right)_p dp - \left(\frac{\partial S_2}{\partial T} \right)_p dT \tag{2.17}$$

$$V_1 \beta_1 dp - \frac{C_{P,1}}{T_1} dT = V_2 \beta_2 dp - \frac{C_{P,2}}{T_2} dT \tag{2.18}$$

$$\frac{\Delta C_P}{T} dT = V \Delta \beta dp. \tag{2.19}$$

At the transition temperature, where there is a jump in β and C_P,

$$\frac{dT_c}{dp} = \frac{\Delta \beta T_c V}{\Delta C_P}, \tag{2.20}$$

or for uniaxial pressure

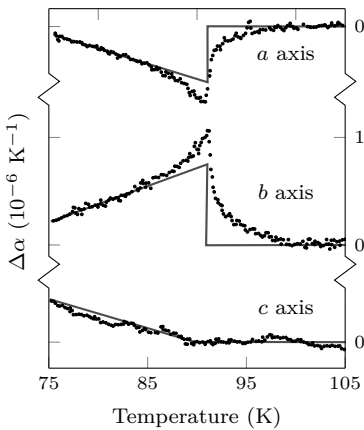$$\frac{dT_c}{dp_i} = \frac{\Delta \alpha_i T_c V}{\Delta C_P} \tag{2.21}$$

were p_i now denotes a uniaxial pressure direction and α_i is the linear thermal expansion coefficient along that direction. These are the Ehrenfest relations which can be used to calculate the zero-pressure limit of the derivative of T_c with pressure from the the size of the discontinuities in thermal expansion and heat capacity.

One example where this technique has been put to good use is cuprate high-temperature superconductors. Meingast *et al.* [38, 39] used an ultrahigh resolution capacitive dilatometer to measure the lattice response as superconductivity sets in, in the $YBa_2Cu_3O_{7\text{-}\delta}$ system. They found a highly anisotropic response of the expansivities in the CuO_2 plane, and very little effect out of plane. $YBa_2Cu_3O_{7\text{-}\delta}$ has an orthorhombic crystal structure and the derived pressure derivatives of T_c suggest a more tetragonal lattice is favourable for superconductivity. The uniaxial pressure dependence has opposite sign along the two in-plane crystal axes, $dT_c/dp_a = -1.9$ K/GPa and $dT_c/dp_b = +2.2$ K/GPa, and almost no response along the c-axis, $dT_c/dp_c \approx 0$ K/GPa. The a- and b-uniaxial pressure dependences almost cancel out for hydrostatic

Fig. 2.4: **Temperature dependence of thermal expansivities.** Change in expansivities for $YBa_2Cu_3O_{7\text{-}\delta}$ near the superconducting transition temperature. Reproduced from [38].

pressure, which is in good agreement with measurements [40].

Thermal expansion measurements are relatively simple to carry out, especially once the infrastructure has been built up, and sample turn around time can be very quick [41]. The sample also remains intact and can be reused but direct observation of any changes in T_c cannot be seen. This makes for a good first indication of whether uniaxial pressure might have an interesting effect, except for systems where a possible nonlinear response would be missed in this zero-pressure limit, and so to actually influence the material, and make changes to its properties, pressure needs to be applied.

2.4.2 Anvil-based pressure cells

The most obvious way to uniaxially pressurise a sample is to just squeeze it between two anvils, and hence this is also the most common way to apply uniaxial pressure. However, this technique does need to be performed with care if the pressure is to be homogeneously distributed across the sample. The sample faces are in direct contact with the anvil faces. A typical sample might have a Young's modulus of 100-200 GPa and a thickness of hundreds of microns to millimetres. Typically achieved pressures are in the kbar range, so for a 0.5 mm thick sample with a Young's modulus of 200 GPa pressurised to 1 kbar the anvils should be compressed 250 nm. In order for the pressure to be equally distributed across the sample the sample faces and the anvil faces must both be parallel, smooth, and flat on a scale well below this displacement. Some surface irregularities can be smoothed out by using soft interface layers between the sample and anvil but this is still no easy feat, and for many interesting materials these constraints are especially challenging to achieve because of small or irregularly shaped samples, and or poor mechanical properties for fine polishing.

However, even when this can be achieved it does not solve the homogeneity problem completely. When the sample is compressed it will try to expand transversely according to its own Poisson's ratio, but the faces of the sample will be frictionally locked to the anvils introducing a strain inhomogeneity once more. The strain homogeneity is improved if samples with either a large or small aspect ratio are used. For small aspect ratio samples the transverse expansion will be locked to the anvils and for large aspect ratio samples the effect of the sample-anvil locking will die away towards the centre giving a homogeneous centre. The soft metal films that can be added between the sample and anvils to reduce the effect of surface defects can also help to reduce frictional locking to some extent. Despite these efforts the effects of strain inhomogeneity are still apparent in many experimental studies; some typical results are shown in figures 2.5, 2.6 and 2.7. The role of inhomogeneity is
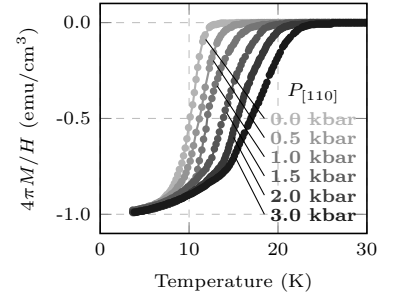
Fig. 2.5: **La$_{1.64}$Eu$_{0.2}$Sr$_{0.16}$CuO$_4$ temperature dependence of magnetization under [110] uniaxial pressures.** [110] oriented pressure destabilises stipe order relieving the competition with superconductivity and a strong T_c enhancement is seen. Reproduced from [42].
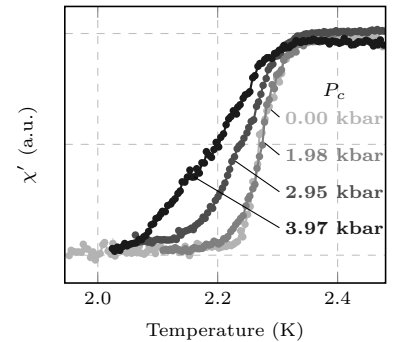
Fig. 2.6: **Susceptibility against temperature for CeCoIn$_5$ under *c*-axis uniaxial pressure.** The transition width ΔT_c is strongly pressure dependent, whereas the onset temperature T_c is not. Reproduced from [43].

[4] There are a few honourable exceptions achieving less broadening than the typical examples I reproduced here, for instance the work of Welp *et al.* [44].
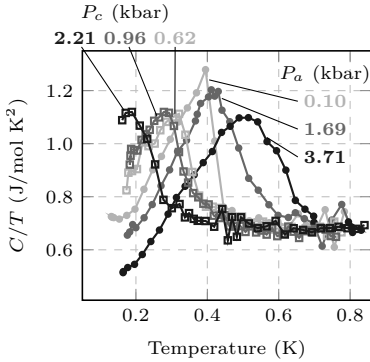
Fig. 2.7: **Heat capacity for CeIrIn$_5$ under a- and c-axis uniaxial pressure.** Uniaxial pressure causes a linear change in T_c with opposite slope for a- and c-axis pressures. Reproduced from [45].

[5] Part number P-885.51 from PI Ceramic GmbH, taken from the specification sheet [52] and checked with an interferometer.

not particularly emphasised by the respective authors. However, the increasing transition widths, at least in part, allow us to infer inhomogeneity is a problem.[4]

In a typical uniaxial pressure cell the pressure is set at room temperature and locked in place with a nut. The pressure is then fixed for the duration of the measurement and the experiment must be thermal cycled to make adjustments. Implementations that offer *in situ* adjustment have been achieved by using helium-activated bellows to set the pressure [45] but this adds additional complications.

Despite the complications of anvil based uniaxial pressure cells they have been successfully incorporated with a wide range of measurement techniques. To name just a few: AC magnetic susceptibility and DC magnetisation are possible when the device is made from a material with a suitably low magnetic background signal [42, 43]; electrical resistivity is possible with access to the sides of the sample [46]; heat capacity when the sample is thermally isolated from the pressure cell, for instance by making some or all of the cell from a superconductor [45, 47]; and neutron scattering when the pressure cell is made from a material sufficiently transparent to neutrons [48, 49].

2.4.3   Sample on piezo stack

Another common technique to apply uniaxial pressure, or more strictly in this case anisotropic biaxial strain, is to fix the sample directly to a piezoelectric actuator. This offers a much simpler route for *in situ* strain adjustment. This technique was originally developed for low temperature strain tuning of semiconductors [50] but has also been used with great success for correlated electron systems after the work of Fisher *et al.* [51].

In this technique samples are prepared as thin slabs and glued to the side wall of a piezoelectric lead zirconate titanate (PZT) stack, in Fisher *et al.*'s work with a 5-minute epoxy. Strain is applied to the sample as the piezo actuator deforms when subjected to a bias voltage. For a positive bias voltage the stack extends along its poling direction and contracts in the transverse direction. The strain in the sample is typically measured by affixing a resistive strain gauge to the upper surface of the sample or estimated from a strain gauge on the piezoelectric stack itself. The achievable strain range with this technique is not very large. For a typical PZT stack at room temperature the strain within the stack can reach $\sim$0.1 %[5]. However, as the temperature is lowered the displacement per volt is severely reduced and at cryogenic temperatures these piezoelectric actuators can only achieve 10–15 % of the room temperature value. The coercive field strength does however increase with cooling, so

it is possible to operate the stacks at higher voltages and against the poling direction without depoling the stack [53]. For a stack with the manufacturer's recommended voltage limits of -20 to 120 V we found we could repeatably and reliably operate between -400 and 600 V at 1 K.

Another concern for measurements with the sample fixed directly on the piezo stack is differential thermal expansion. The thermal expansion coefficient of PZT along its poling direction is approximately $-2.5 \ 10^{-6} \ \mathrm{K}^{-1}$, i.e. the stack lengthens as it is cooled [53,54]. This is in contrast to typical materials which contract by 0.1 - 0.5 % between room temperature and 4 K. If there is no plastic deformation of the epoxy layer, a typical sample will be severely tensioned as it is cooled down, and beyond the range that could be brought back to zero strain by operating the piezo stack. In reality plastic deformation with 5-minute epoxy is observed and the strain is not well transmitted above about 100 K [50,51].

By fixing the sample to the piezo's surface the sample is constrained to follow the deformation of the stack, but in reality the epoxy is nearly always softer than the sample and stack, so significant strain can be lost in the epoxy layer. A typical measurement for this apparatus is differential longitudinal elastoresistance. For this two separate samples, cut into bars for transport measurements, are mounted perpendicularly to one another on the stack [55]. This allows the longitudinal elastoresistivities to be measured in both directions, parallel and perpendicular to the applied stress, and the differential longitudinal elastoresistance to be determined from the difference. However, an accurate measurement relies on equal strain transmission, which is not trivial to achieve. A simulation of the strain transmission is shown in figure 2.9 for a bar sample mounted parallel and perpendicular to the poling direction of the stack. The strain is not transmitted over the full area of the sample. For instance with the specific dimensions and parameters used in this simulation, the strain builds up over about the first 20% of the ends of the sample mounted parallel to the poling direction but is homogeneous in the middle portion. However the sample mounted perpendicular to the poling direction is much shorter along the strained direction and not long enough to give a homogeneous region in the middle.

This technique is therefore best suited for making measurements where the resistive response is linear with strain and can be measured with small strain perturbations. Strain offsets due to differential thermal expansion are not important when the derivative with strain is taken and the response is linear. Strain homogeneity is always an issue, however, particularly for bar shaped samples such as those shown in figure 2.9. An alternative mounting method is to use a square shaped sample and measure using the Mont-
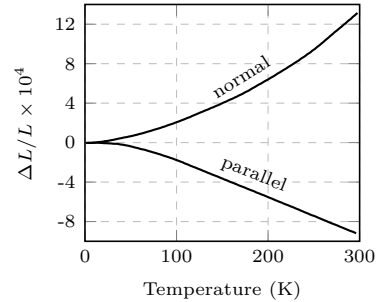
Fig. 2.8: **PZT thermal expansion.** The thermal expansion of PZT measured both parallel and normal to the poling direction. Reproduced from [54].
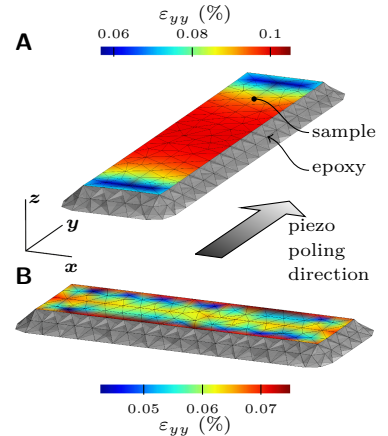
Fig. 2.9: **Sample on piezo stack finite element simulations.** Finite element simulations of the strain transmitted to samples mounted parallel and perpendicular to the poling direction of the piezo stack. Samples are $800 \times 200 \times 20 \ \mu m$ with a Young's modulus of 50 GPa and Poisson's ratio of 0.35. The epoxy is 20 μm thick and has a Young's modulus and Poisson's ratio of 10 GPa and 0.3, respectively. The stack is strained to $+0.1$ % and has a Poisson's ratio of 0.45. Deformations are exaggerated $200\times$.

gomery method [56]. This gives the same strain transmission in both directions but neither would be as homogeneous as that in a parallel-mounted bar sample. Information about the nematic susceptibility can also be obtain more directly using a single sample and a transverse resistivity configuration as set out by Shapiro *et al.* in [57].

The simplicity and compactness of this technique mean it is particular straightforward to implement. Overall this technique has proved particularly fruitful for the Fe-based superconductors. Ubiquitous nematic behaviour has been seen and nematic quantum criticality has been observed in the optimal doping regime of these materials [56].

2.4.4   Other techniques

There are still other techniques for applying uniaxial or biaxial strain and I will mention just two more here. Thin film samples are nearly always prepared on a substrate. This gives the opportunity to strain the sample by first straining the substrate either by stretching or bending. Since the sample is very thin the strain homogeneity can be very high. One such example is graphene prepared on a PET substrate where $\sim$0.8 % tensile strains were achieved and provided a way to experimentally tune the band gap of single-layer graphene [58, 59].

Another way to achieve strain for thin films is to grow the film using molecular beam epitaxy on a substrate with a mismatched lattice constant. By choosing the right substrate a certain amount of strain can be selected, however, usually only biaxial. This technique was used to double the superconducting critical temperature of $La_{1.9}Sr_{0.1}CuO_4$ [60]. By growing the sample on $SrLaAlO_4$ the sample is compressed in-plane and expanded out of plane, providing the largest T_c enhancement.

2.5   New uniaxial stress cell

I have shown there are a large variety of techniques for applying uniaxial stress and strain. However, to test a specific hypothesis for the material Sr_2RuO_4, Clifford Hicks was motivated to propose a new technique. Sr_2RuO_4 is an unconventional superconductor but of particular significance since it may host a unique superconducting state. A body of accumulated evidence has led to the proposal that the pairing in Sr_2RuO_4 is spin-triplet with an odd-parity chiral order parameter, $p_x \pm ip_y$ [61]. This would be a superconducting analog of the A-phase of superfluid ^{3}He. Sr_2RuO_4 has a tetragonal lattice so the two components p_x and p_y would have the same transition temperatures, but this degeneracy could be lifted by
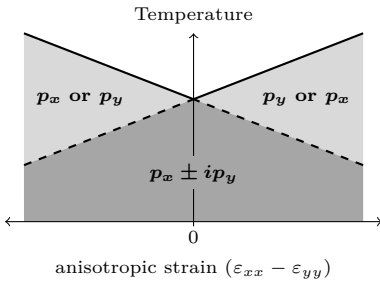

Fig. 2.10: **Hypothesis for $p_x \pm ip_y$ superconductivity.** General phase diagram expected for $p_x \pm ip_y$ superconductivity in a tetragonal crystal subject to a small, volume-preserving, but symmetry-breaking strain $\varepsilon_{xx} - \varepsilon_{yy}$. Reproduced from [33].
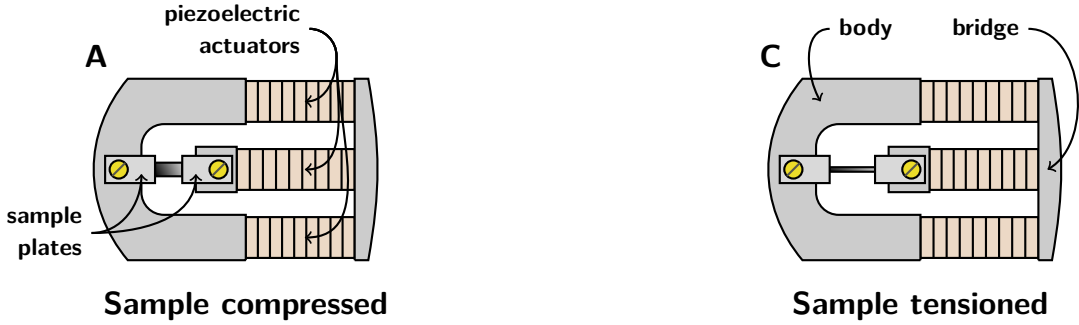
Fig. 2.11: **Principle of operation. A.** The sample is compressed by extending the middle piezoelectric actuator. **B.** Sample at zero strain. **C.** The sample is tensioned by extending both outer actuators and pushing the bridge piece out.

breaking the symmetry between the x and y directions. This can be achieved using in-plane uniaxial strain. Based purely on symmetry considerations the phase diagram in figure 2.10 was predicted for the T_c dependence on anisotropic strain [62, 63].

To test this hypothesis a device capable of applying both tension and compression is needed. High homogeneity and continuous *in situ* adjustability were also among the aims. The implementation devised by Clifford Hicks is described in detail in reference [34]. My personal contribution to that 'phase 1' development was a series of finite element calculations that enabled the calibration of the sample strain and helped optimise the strain homogeneity by changing the way samples were mounted (see section 2.5.1). Here I will only discuss the salient features and mention some improvements implemented to the original device for my main PhD research. A schematic of the device is shown in figure 2.11, and the principle of operation is also detailed.

For this technique the sample is first shaped into a long thin bar and then firmly fixed across the gap between the two sample plates using epoxy. One end is fixed stationary to the main body of the device while the other is movable. The position of the movable sample plate is controlled by the three piezoelectric actuators. A positive voltage to the central actuator causes it to extend, compressing the sample. Tensioning the sample is achieved by applying a positive voltage on the outer two stacks, pushing the bridge piece out, and pulling on the sample through the central stack. All three stacks have equal lengths so, in principle, since they are offset from the sample, their thermal expansion should not affect the sample while the temperature of the rig is varied. In practice differences between stacks mean that this is considerably reduced but not completely eliminated.

Since the piezo stacks are much longer than the sample a large

sample strain can be achieved. This was the first improvement made over the original device for the work I report. In the first iteration of the device 4 mm stacks were used, but now we have a cryostat with a much large bore and we upgraded to 18 mm stacks. In addition to the longer stacks I first used a fibre-based interferometer to compare the performance of an alternative manufacturer of piezoelectric actuators at cryogenic temperatures, where there is generally no technical data specified, and found significant improvement with actuators from PI Ceramic GmbH.

The sample strain is given by the stroke length of the stack divided by the strained length of the sample. The 'strained length' of the sample will be described in detail later but because the sample is held with a soft epoxy the length over which the strain is applied is not exactly the same as the gap between the sample plates. Typically the strained length is ∼1 mm, and at 1 K with 18 mm stacks[6] the stroke length is up to ∼50 μm (-400 to $+600$ V), so a strain range of 5 % is possible if the sample and epoxy mounting are able to withstand this. In practice I have achieved tensile strains of ∼0.25 % before the sample breaks, and compressive strains up to 1 % before the epoxy starts to give way.

A few other improvements were made to the device for the work in this thesis. The main body of the device is now made from one piece of titanium as opposed to many pieces held together with screws and epoxy as in the first iteration. Making the device in this way makes it overall much stiffer and easier to assemble; however, differential thermal expansion between the sample and the device is now an important consideration. Titanium has an atypically small thermal expansion for a metal. Between 4 K and 300 K it is only ∼0.15 % [64], much less than that of the typical samples we have measured. The consequence of this is that even though the sample is mounted at zero strain at room temperature, by the time the rig is cooled down to cryogenic temperatures the sample is put under severe tension. In the original device copper foils were incorporated to try and match the thermal expansion of the device to that of Sr_2RuO_4. With the device now made as one solid block, incorporating additional foils to compensate the differential thermal expansion is no longer possible. Instead, the piezo actuators must be used to actively compensate the differential thermal expansion and maintain the sample close to zero strain while cooling the device to cryogenic temperatures. With the larger range of the longer stacks the sample can still always be brought back to zero strain.

Since the piezo stacks are very hysteretic an independent measure of the strain is required. The resistive strain gauge used in the first generation device has now been replaced by a capacitive strain gauge. The capacitor is a parallel plate capacitor in line with and

[6] Part number P-885.51 from PI Ceramic GmbH.

To FPS3010

$$y = \frac{\varepsilon_0 \ 15.95 \ \mathrm{mm}^2}{x + 25.12 \ \mu\mathrm{m}}$$

$T = 1.2$ K

Capacitance (pF) — Displacement (μm)
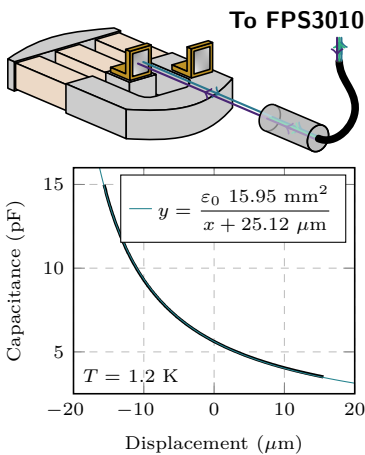
Fig. 2.12: **Capacitor calibration.** A hermetic feedthough at the top of the cryostat brings the fibre heads of the attocube FPS3010 interferometer down to low temperatures. The FPS3010 interferometer is a Fabry-Pérot type and takes the first reflection from the sensor head itself and the second from mirrors attached to the uniaxial stress device. By using multiple fibres and mirrors placed at different points on the device an accurate calibration of the capacitive displacement sensor was achieved.
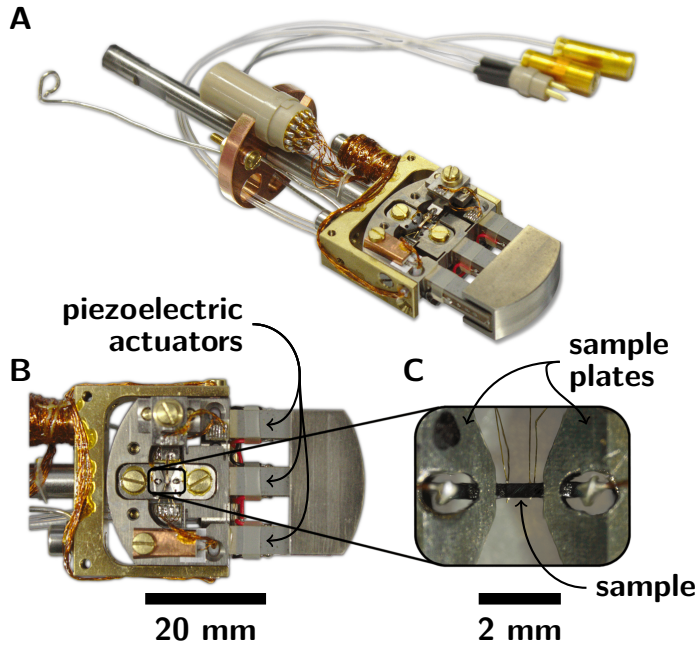
Fig. 2.13: **Uniaxial stress cell. A.** Overview of the whole device including frame and wiring. **B.** Detailed section of the main body of the device. **C.** A typical sample mounted for electrical resistivity measurements.

underneath the sample. To check the linearity and accuracy of the capacitive sensor a fibre-based interferometer was adapted for use in our cryostat to make an accurate calibration. The calibration of the capacitor against the interferometer is shown in figure 2.12. The characteristic inverse plate separation dependence can clearly be seen. By incorporating a capacitive strain gauge instead of a resistive one the applied strain is known to much higher precision. With the capacitive gauge the resolution is ∼0.1 nm compared to ∼2 nm with the resistive gauge. The capacitive strain gauge is also much less sensitive to temperature and magnetic field, which was important for this work. It is well known that piezoelectric actuators creep; after a step change in voltage the displacement changes with time even with an unchanging drive voltage. The amount of creep decreases logarithmically with time and is well characterised by the form $\Delta L(t) \approx \Delta L_{t=0.1 \text{ s}}(1 + \gamma \ln(t/0.1 \text{ s}))$ [54, 53]. γ is the creep factor and can range from tens of seconds to weeks [54]. The relaxation mechanisms responsible for creep slow down significantly at low temperatures but it is still necessary to use the capacitor in a feedback loop to keep the strain in the sample constant throughout a measurement.

An assembled device used for the work in this thesis is shown in figure 2.13. This whole part can be detached from the cryostat

and worked on separately while preparing the sample.

When a sample is uniaxially loaded it is characterised as being under uniaxial stress. With the contact only on two opposing end faces it will not deform completely uniaxially since, in its central section, the sample is free to expand in the transverse direction according to its own Poisson's ratio. To achieve strictly uniaxial strain the transverse expansion would have to be held at zero.

Our device, that has the sample supported only at the ends, therefore puts the sample under conditions of uniaxial stress. However, the device is not a controlled stress device. The whole device is much stiffer than the sample, including the piezos, and the force applied to the sample is typically less than 50 N. What is controlled is the displacement of one end of the sample. A voltage is dialled in, the piezos deform, and the sample must comply or give up the ghost. We therefore have a sample under conditions of uniaxial stress but, in general, we know the strain along the pressure axis more accurately than the stress.

This new technique gives many opportunities for measurements. The sample is exposed and visible once mounted in the device and can have an unobstructed upper surface. This makes the device compatible with a large number of experimental techniques. I have concentrated on resistivity and AC magnetic susceptibility but it would also be possible to measure many other properties such as Seebeck and Nernst effect, thermal conductivity, heat capacity using an AC technique or the 3ω technique, Raman spectroscopy, optical conductivity and nuclear magnetic resonance (NMR). The accessible upper surface should allow in principle surface sensitive techniques to be measured such as angle-resolved photoemission spectroscopy (ARPES), scanning tunnelling microscopy (STM) and scanning squid or hall probe measurements. Additionally in a cleverly designed rig with access from both sides, scattering techniques such as soft and hard X-ray scattering are possible.

2.5.1   Sample mounting

One of the key improvements of this device is the sample mounting. Relative to the other techniques discussed in section 2.4, it is the sample mounting which, in principle, allows significantly better strain homogeneity to be achieved. The sample is held in the device using epoxy such that it can be put under tension or compression. The epoxy is important as it conforms to the shape of the sample and sample plates, which alleviates the need for precise polishing. However the sample should still have a constant cross-section. The epoxy prevents the sample ends from pivoting, which increases the buckling limit of the sample, allowing higher strains to be achieved or higher length-to-width aspect ratios to be used. And as I will
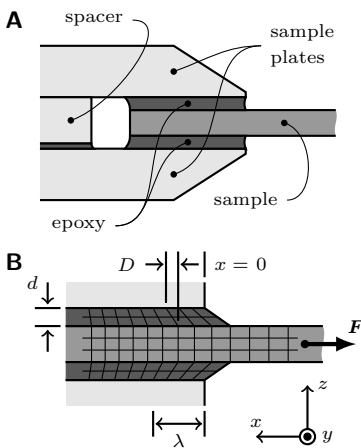
Fig. 2.14: **Model for the effective sample length. A.** Schematic of the symmetric sample mounting. **B.** When a force $\boldsymbol{F}$ is applied to the sample, the load is transferred through the epoxy to the sample plates over a characteristic length scale λ. See text for further details.

show later a softer epoxy is beneficial for strain transmission as it deforms over a certain length of the sample, reducing stress concentration at the mounting points and hence minimises the possibility of sample failure.

The sample should always be mounted as symmetrically as possible to eliminate bending. This is best achieved by using two sample plates sandwiching the sample. A spacer needs to be included at the back of the sample plates, behind the sample, to prevent the sample being crushed during assembly but also to set the correct epoxy thickness. See figure 2.14 for a schematic of the sample mounting.

Figure 2.15 shows the effect of suboptimal sample mounting. Superconducting transitions for two different samples of Sr_2RuO_4 are shown at zero strain and at 0.12 % tension. The first sample was mounted by embedding the ends of the sample in an epoxy droplet only and it can be seen that this led to significantly more broadening of the transition as the sample is strained compared to a sample mounted more symmetrically with a capping foil. Since the epoxy is quite soft, the load is mostly transmitted by the lower side of the epoxy droplet, as indicated by the red shading in the figure, and this causes the sample to bend inducing a strain gradient though the whole sample.

The epoxy is nearly always going to be softer than the typical samples and the sample plates. This means the displacement of the sample plates, as measured by the strain gauge, is not all applied to the sample since the epoxy is also deforming. An approximation for the load transfer length, the length over which the epoxy deforms and the force is transmitted to the sample, can be calculated analytically after a few assumptions. Starting from the geometry set out in figure 2.14B we make the following approximations. The sample's width, w, is much greater than its thickness, t, such that bonding on the side walls of the sample is insignificant. We also assume the epoxy has much lower elastic constants than both the sample and and sample plates. After this approximation we can take the sample plates to be perfectly rigid and also neglect any shear strains in the sample. This simplification sets ε_{xx} to be constant in both y and z. After these approximations the force at any point in the sample, given by Hooke's Law, is

$$F(x) = Ewt\varepsilon_{xx}, \qquad (2.22)$$

where E is the Young's modulus of the sample. Additionally, we know how the force varies along the length of the sample due to the shearing of the epoxy layers as

$$\frac{dF(x)}{dx} = 2w\sigma_{xz}(x) \approx 2wG\frac{D(x)}{d}, \qquad (2.23)$$
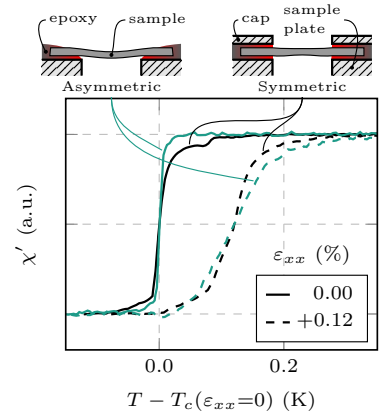
Fig. 2.15: **Effect of strain inhomogeneity.** A comparison of two mounting conditions on the superconducting transition of Sr_2RuO_4. At zero strain the sample mounted asymmetrically in a soft epoxy droplet (blue curves) has a much sharper transition than the sample mounted more symmetrically with a cap foil (black curves). However, despite the asymmetrically mounted sample being the cleaner of the two, under strain it broadens significantly more and has a larger transition width than the less broadened but dirty symmetrically mounted sample. Reproduced from [65].

where σ_{xz} is the shear stress of the epoxy layer, G the shear modulus of the epoxy, and d and $D(x)$ are the epoxy thickness and displacement of the sample at position x from its unloaded position, respectively, as defined in the figure. Equating these two, we can solve for the displacement, $D(x)$, of the sample

$$\frac{dF}{dx} = Ewt\frac{d\varepsilon_{xx}}{dx} = 2wG\frac{D(x)}{d}$$
$$\frac{d^2D(x)}{dx^2} = \frac{2G}{Etd}D(x) \tag{2.24}$$

$$D(x) = D(0)\exp(-x/\lambda), \quad \lambda = \sqrt{\frac{Etd}{2G}}. \tag{2.25}$$

The strain therefore decays exponentially into the epoxy mounts with a characteristic length scale λ. For an epoxy we work with Stycast® 2850FT[7] with catalyst 23LV. The elastic properties of Stycast 2850FT do not appear to have been measured at cryogenic temperatures. Ojeda *et al.* used dynamic mechanical analysis (DMA) to study the viscoelastic properties of Stycast 2850FT hardened with catalysts 24LV and 9 [66]. They carried out measurements down to $-130\,°$C looking for the glass transition temperature and to determine the complex modulus. For both hardeners the storage modulus, E', increases as the temperature is lowered but begins to saturate at lower temperatures after the glass transition temperature at $\sim-40\,°$C. By $-130\,°$C the storage modulus for the Stycast cured with catalyst 24LV reached ~ 11.7 GPa and for catalyst 9 $\sim$16.2 GPa.

The elastic properties of Stycast 1266, an unfilled version of 2850FT, have been measured at cryogenic temperatures [67]. It has similar behaviour; the Young's modulus increases with decreasing temperature before starting to saturate, this time at around 100 K. The low temperature value, approximately constant below 77 K, is $\sim$4.5 GPa.

If Stycast 2850FT cured with catalyst 23LV behaves similarly, we can expect a Young's modulus of approximately 15-20 GPa at low temperatures. The shear modulus, G, is related to the Young's modulus, E, and Poisson's ratio, ν, of an isotropic material by $G = E/2(1 + \nu)$. Taking the Young's modulus of Stycast to be 15 GPa and the Poisson's ratio as 0.3 the shear modulus would be $\sim$6 GPa.

Using a typical sample as an example, in this case Sr_2RuO_4 with $E = 176$ GPa [68], and dimensions $t = 100$ μm and $d = 25$ μm the characteristic length is $\lambda \sim 200$ μm. The strain falls to $\sim 1/e$ of the average value of the exposed portion of the sample in the first 200 μm of the epoxy. Therefore it is best to mount the sample with an overlap between the sample and sample plates of at least 2-3$\times\lambda$ to ensure enough epoxy length for proper strain transmission to

[7] Henkel Loctite, formally Emerson and Cuming.

the sample.

From equation 2.25 we can also calculate the shear stress in the epoxy layer. The largest shear will be at the end of the sample plates

$$\sigma_{xz}(0) = G\frac{D(0)}{d} \ . \tag{2.26}$$

In order to optimise the mounting we want to compare the maximum shear stress in the epoxy for a given amount of strain achieved in the sample. In this approximation scheme the strain achieved in the sample is the same as the strain at the edge of the mounts

$$\varepsilon_{xx}(x) = \frac{dD(x)}{dx} = -\frac{D(0)}{\lambda}\exp\left(-\frac{x}{\lambda}\right) \ , \tag{2.27}$$

$$\varepsilon_{\text{sample}} = \varepsilon_{xx}(0) = -\frac{D(0)}{\lambda} \ . \tag{2.28}$$

So the maximum stress in the epoxy is given by

$$\sigma_{xz,\text{max}} = G\frac{\varepsilon_{\text{sample}}\lambda}{d} = \varepsilon_{\text{sample}}\sqrt{\frac{EtG}{2d}} \ . \tag{2.29}$$

The shear strength of Stycast 2850FT has been measured, for instance by Camp *et al.* [69] and Ojeda *et al.* [66]. It is found to be in the range of 10-50 MPa increasing slightly towards lower temperatures. But the results show quite some deviation which is likely to do with the exact care in the preparation of the Stycast. These tests typically used much thicker layers, up to 3 mm, and so it is easier to include air bubbles leading to a failure point [69]. By carefully preparing the Stycast, i.e. making sure to use the exact mix ratio, mixing thoroughly, then degassing the epoxy before baking at elevated temperatures to achieve the strongest bond, we have reliably been able to achieve strains of -1 % for a sample cross section of 100 μm $\times$ 300 μm, corresponding to a pressure of $\sim$1.8 GPa and a shear stress in the epoxy of $\sim$500 MPa. This value was not actually the limit of the Stycast but was the limit of motion of the device before the capacitor plates shorted, meaning even higher strains should still be possible. This shear stress is significantly higher than previously measured values but the very thin layer and the very low temperatures may well increase the yield stress of the epoxy. The response of the Stycast was not completely elastic up to these highest strains, in fact we quite regularly saw the epoxy start to slip around a strain of ~-0.3 % (a shear stress of $\sim$150 MPa). This can be seen during a strain increase; the voltage is smoothly ramped up but there is a sudden jump in the capacitance when the epoxy slips, see figure 2.16. The slippage in the epoxy, however, is not fatal. Instead, it seems to find a stronger bonding point further back in the mount. We know
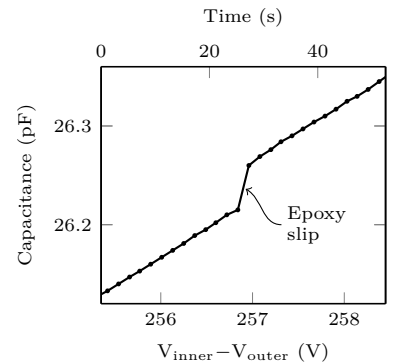

Fig. 2.16: **Epoxy slippage.** With the strain increasing steadily a jump in the capacitance is observed whenever the epoxy slips.

this by comparing the sample properties before and after the slip and each time we go to a new highest strain the sample length must be redetermined by comparing to the initial properties of the sample at low strains before the epoxy slipped for the first time.

As well as the sample failing due to the limit of the epoxy, the sample can also fail if you reach the intrinsic buckling limit. The critical load for buckling a beam is given by Euler's formula

$$F_{cr} = \frac{\pi^2 EI}{(KL)^2} \,, \tag{2.30}$$

where E is the Young's modulus of the material, I is the minium area moment of inertia of the cross section of the beam, L is the length of the beam and K is an effective length factor for the beam to take into account the constraints at the ends. For our sample mounting, both the rotational and translational motion of both ends of the sample are fixed. This makes the K factor equal to 0.5. The area moment of inertia of a beam with rectangular cross-section, width and thickness, w and t, is $I = t^3 w/12$. So the critical strain for buckling, ε_{cr}, is

$$\varepsilon_{cr} = \frac{\pi^2 t^2}{3L^2} \,. \tag{2.31}$$

This depends on the aspect ratio (t:L) squared and for the typical dimensions I used earlier, $L/t = 10.5$, the theoretical critical strain for bucking is 3 %.

So far I have shown only analytical estimations of the strain transmission, but for a complete analysis a finite element simulation was programmed to determine the strain transmission more precisely. This will be the subject of the next section.

2.5.2 Sample mounting models

In order to optimise the sample mounting scheme I used finite element analysis to investigate the possible mounting scenarios. For each I will quantify once more the load transfer length and assess each in terms of the strain homogeneity and the sample bending.

Here I will discuss four models for the sample mounts, all depicted in figure 2.17. They are: (1) "Rigid:" here the sample is fixed with hard, perfectly rigid epoxy on its top and bottom surfaces at both ends. (2) "Symmetric epoxy:" a softer epoxy bonded on both the top and bottom surfaces to perfectly rigid sample plates. (3) "Asymmetric epoxy:" the same soft layer of epoxy but only the bottom surface is bonded to a sample plate. (4) "Symmetric thick epoxy:" the same as model 2 but with thicker layers of epoxy on both sides. For all the models the sample and epoxy are taken to be isotropic. We set the Young's modulus of the sample to be 10× that
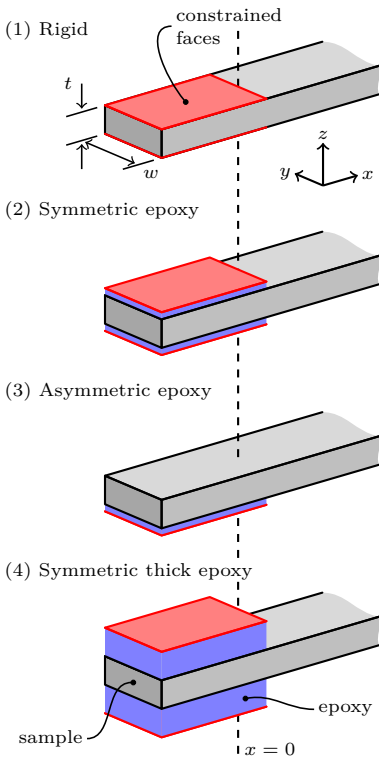
Fig. 2.17: **Mounting models.** Mounting models used in the finite element analysis. Red faces have applied displacement constraints, and blue volumes are epoxy. Reproduced from [34].

of the epoxy, and the sample and epoxy to both have a Poisson's ratio of 0.3. We use aspect ratios close to those of the typically mounted samples: the sample's width, w, is set to $3\times$ the sample's thickness, t, and the length (gap between the sample plates) to $3.5w$. The thin layers of epoxy are $0.25t$ and the thick layers in model 4 are equal to the sample's thickness. The sample plates are not directly modelled but the boundary conditions imposed on the models are such to sufficiently capture their effect. Only the faces of the epoxy that would make contact with the sample plates, or the end portions of the sample in the rigid epoxy model, have applied displacement constraints; the constrained faces are illustrated in figure 2.17. The bulk of the epoxy and sample is not constrained. Displacement rather than force constants are used
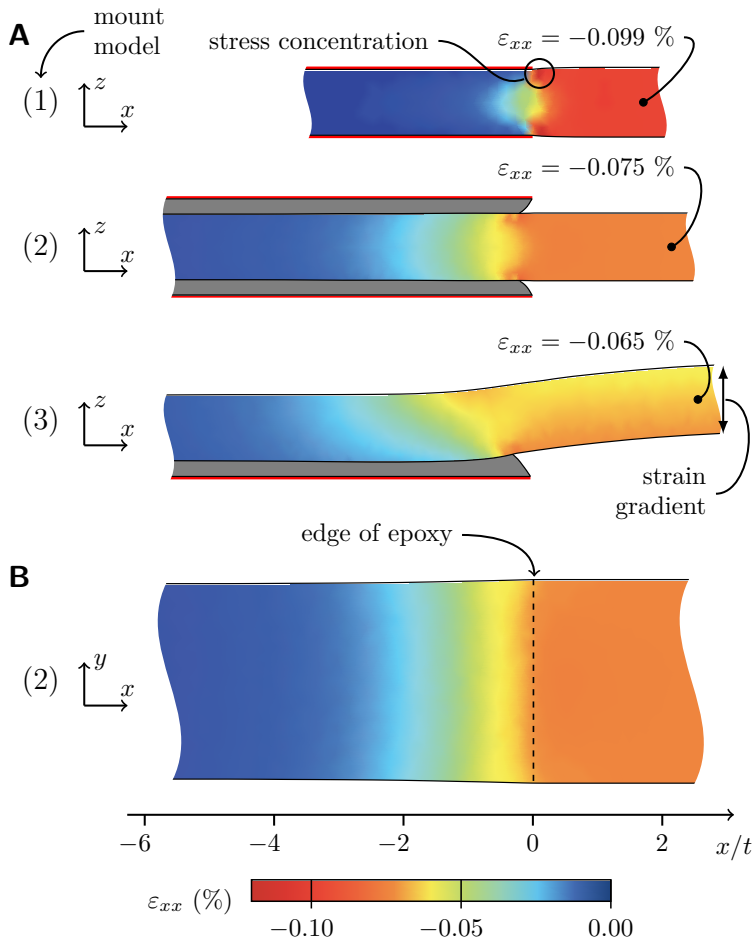
Fig. 2.18: **Fea simulations.** Strain ε_{xx} for samples mounted as in the models of figure 2.17. In all the models the sample plates, represented by the thick red lines, were moved towards each other by 0.1 % of L. The deformations have been exaggerated 200 times. **A.** Cuts through the centre xz-plane of the sample. **B.** Cut through the centre xy-plane of the sample for mounting model 2.

Fig. 2.19: **Strain along the centre-line of the sample.** Strain ε_{xx} along the centreline of the sample for the mounting models in figure 2.17. The legend includes the load transfer lengths, λ, from fits to the portion of the sample inside the mounts. Negative x/t corresponds to where there is epoxy, the scale is the same as in figure 2.18.
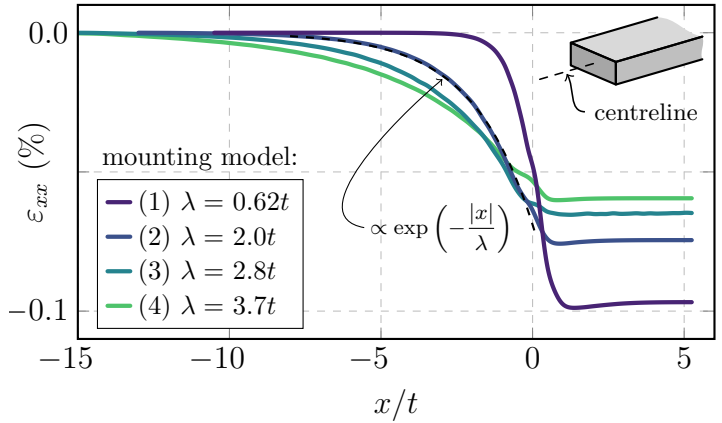
since it is the strain that is controlled by the device, not the stress. These faces have constrained x, y and z displacements. Their y and z displacements are held at zero, i.e. we assume the sample plates are not expanding or contracting transversely. The x displacement sets the applied strain, and for a model with an applied strain of -0.1 % the constrained faces are displaced towards each other by 0.05 % $\times L$.

For these calculations I programmed a custom FEA simulation incorporating the meshing capabilities of Gmsh [70] and matrix solvers in MATLAB® [37]. Each model had on the order of 10^6 elements, all linear tetrahedrons. The end portions of the sample were always made much longer than the load transfer length $\lambda$ to negate effects due to only partial transmission of the load. No effects of differential thermal expansion are included in the models presented in this thesis.

The simulation results of the models in figure 2.17 are shown in figures 2.18 and 2.19. Figure 2.18 shows the strain ε_{xx}. The thick red lines mark the constrained faces which were moved towards each other by 0.1 % of L and the deformations have been exaggerated 200 times. The three plots in part A of figure 2.18 show cuts in the centre xz-plane of the sample for mounting models 1, 2 and 3. The plot in panel B shows a cut the centre xy-plane for mount model 2.

Figure 2.19 shows the ε_{xx} strain along the centreline of the sample for all the mounting models. Here one can clearly see the exponential decay of the strain into the mount as well as the highly homogeneous region in the centre of the sample. The load transfer length, λ, is shown for each model and is taken from a fit to the strain along the centreline of the sample in region of the sample within the mount.

The load transfer length is shortest for the rigid epoxy model and correspondingly the highest strain is achieved in this sample, but the cross-section through the xz-plane in figure 2.18 clearly shows very high stress concentration right at the edge of the mounts. This
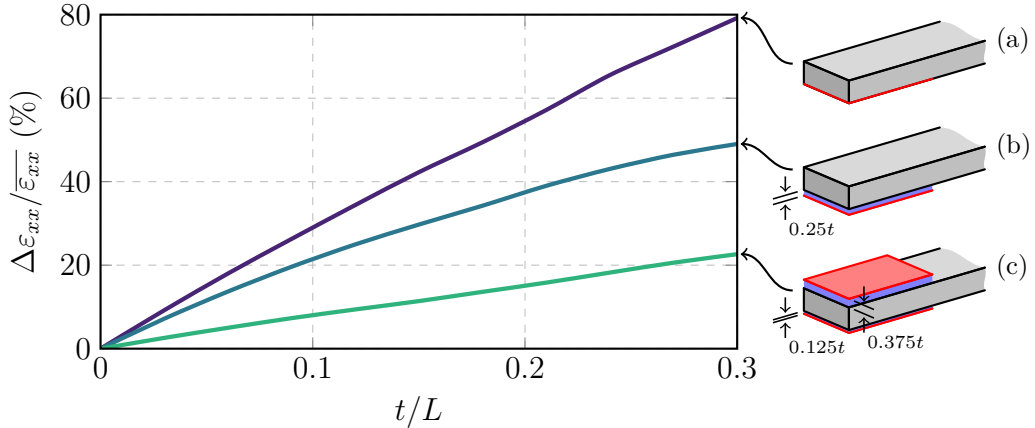
Fig. 2.20: **Bending induced strain inhomogeneity.** The difference in strain between the top and bottom of a bent sample at the centre divided by the average strain across the central plane of the sample plotted against the sample's aspect ratio. The three cases from top to bottom are: (a) rigid epoxy holding only the lower sample face; (b) soft epoxy on the under side of the sample with a thickness equal to $0.25t$; (c) a sample mounted asymmetrically between top and bottom sample plates. The sample is off centre by $0.125t$ and the total space between the two plates is $1.5t$.

would be the failure point for a sample mounted with this scheme. In the models with the layers of soft epoxy the stress concentration is reduced and, we expect, higher strains can ultimately be achieved. However, the exact thickness of the epoxy leads to some uncertainty in the exact amount of strain achieved in the sample; take note of the range of strains seen at the middle of the sample for the models with soft epoxy in figure 2.19.

For samples mounted in symmetrical mounts the strain homogeneity is very high, see both figures 2.18B and 2.19. The inhomogeneity dies away moving towards the sample centre so measurements should be designed to be sensitive only to the central region of the sample. A guide for the length of sample to exclude from both ends of the sample is given in table 2.1. This length says that after excluding this amount at the ends of the sample, the strain ε_{xx} across the rest of the volume of the sample does not differ from the average strain at the centre of the sample by more than the given percentage. So to achieve a strain inhomogeneity less than 5 % for a sample mounted using model 2, a length equal to $0.2w$ of the sample needs to be excluded from both ends of the sample. With suitable sample mounts it is therefore possible to achieve very high strain homogeneity over almost the entire exposed region of the sample.

Any asymmetry in mounting causes the sample to bend as shown in figure 2.18A(3) and this introduces further strain inhomogeneity; there is a clear strain gradient between the bottom and top of the sample. This inhomogeneity can be quantified by taking the

Table 2.1: **Guide for the end portions of the sample to exclude from measurements.** Length at the end of the sample to exclude in order to achieve a given level of strain homogeneity. Mounting models and dimensions as per figure 2.17.

| | % Inhomogeneity | |
Mounting model	5 %	1 %
1	$0.5w$	$0.9w$
2	$0.2w$	$0.5w$
4	$0.1w$	$0.4w$

difference in strain between the top and bottom divided by the average strain across the central plane of the sample. This quantity is plotted in figure 2.20 for a range of sample aspect ratios and three different asymmetric mounting models. The inhomogeneity is worst for a sample mounted with rigid epoxy from a single side. There is improvement with a softer epoxy but the inhomogeneity is still large. For example with an aspect ratio (L/t) of 20, not far below the buckling limit, the inhomogeneity is still above 10 %. It is clear then that symmetric sample mounting should always be aimed for. The final curve in figure 2.20 shows a problem that might occur when symmetrical mounting is aimed for but the sample ends up off centre in the mount. Here the total space between the mounting plates encasing the sample is $1.5t$ so a symmetrically mounted sample would have layers of epoxy $0.25t$ thick on each side but here the bending induced inhomogeneity is shown for the case when the sample moves half this distance off centre. The inhomogeneity is still better than the sample mounted only from a single side, but for small aspect ratio (L/t) samples the inhomogeneity can still be quite significant.

2.6   Recommended working parameters

Throughout the work for this thesis we were aiming to push the limit of achievable strain. With the longer stacks of the new devices, the range of motion of the device is no longer the limiting factor in terms of the achievable strain and we had to consider the other possible modes of failure carefully. As a summary, I will outline these considerations in a step by step recipe for preparing and mounting samples to reach high strains.

Three main modes of failure can limit the applied strain. First, if the stress within the sample reaches the yield strength, permanent deformation will occur. This is an intrinsic limit of the sample and cannot be controlled, thus setting an upper limit of strain. It is important however to ensure that the sample surfaces are prepared as well as possible, free from chips and cracks in the surface, as these lead to points of stress concentration and premature failure. The sample must also be of uniform cross section to achieve a homogeneous strain distribution. During measurement it is necessary periodically to release the strain and check to see if the elastic limit has been exceeded. If it has, the sample's properties will not return to the previous values once it has been brought back to a lower strain. During my measurements on Sr_2RuO_4 and $Sr_3Ru_2O_7$ presented in the following chapters I never observed such effects and thus always remained within the elastic limit, for these measurements the yield strength was not yet the limiting factor.

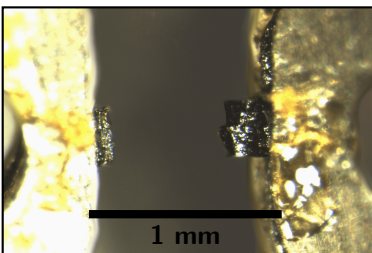The second mode of failure is through sample buckling. The

Fig. 2.21: **Buckled sample.** Photograph showing the stumps of the sample that remain after the sample buckles and the central portion breaks away.

sample is a long thin bar only supported at the ends so after a certain level of compressive strain the sample is susceptible to buckling as described in section 2.5.1. The critical load for buckling is given by Euler's formula. For a sample fixed without allowing rotation or translation of both ends and with a rectangular cross-section, width and thickness, w and t, the theoretical critical strain is $\varepsilon_{cr} = \pi^2 t^2/3L^2$, where L is the length of the strained part of the sample. The recommended useable range, however, is only 60 % of this [71]. A shorter sample therefore is better for reaching the absolute highest strains, but the strain homogeneity also needs to be kept in mind. The portions of the sample inside the epoxy mounts are not strained so between these and the middle of the sample there are regions of inhomogeneous strain. Through guidance from my simulations we know it is best to leave a length roughly equal to the width of the sample at each end and try to measure exclusively in the central portion of the sample. For my measurements I chose to use a width of 300 μm and make the sample length, the gap between the sample plates, 1 mm. This gives a large enough measurement region where the strain should be homogeneous and leaves enough space for all the wires to the sample and some space for susceptibility coils. For the measurements on Sr_2RuO_4 I was aiming for a maximum strain of -1.5 %, requiring that the sample's thickness be at least 90-100 μm.

The third failure point is the epoxy holding the sample to the sample plates. The thickness of the epoxy layer between the sample and sample plates can be varied to limit the shear stress in the epoxy, see section 2.5.1 and figure 2.22. The maximum shear stress in the epoxy, when there are sample plates above and below to transmit the applied force, is approximately $\tau_{max} = \varepsilon_{sample}\sqrt{EtG/2d}$, where E is the sample's Young's modulus, G is the shear modulus of the epoxy, d is the epoxy depth. It is therefore best to increase the depth of the epoxy to limit the maximum shear stress, but one must also bear in mind that the length of sample that needs to be embedded in the epoxy to ensure adequate strain transmission also increases as the epoxy depth is increased. This means the epoxy depth should only be increased while there is a long enough length of spare sample at each end held in the epoxy. Increasing the epoxy depth further reduces the amount of strain transmitted. The shear stress decays roughly exponentially with the distance from the end of the mount with a characteristic length scale of $\lambda = \sqrt{Etd/2G}$, so a distance of 2-3$\times\lambda$ is desirable to achieve adequate strain transmission.

As first mentioned in section 2.5.1, for my measurements I used Stycast 2850FT with catalyst 23LV as the epoxy as it is well suited to cryogenic temperatures and has a relatively high shear strength. Stycast is much softer than the sample with a shear

$$D(x) = -\lambda \varepsilon_{sample} \exp(-x/\lambda)$$

$$\lambda = \sqrt{\frac{Etd}{2G}}$$

$$\tau_{max} = G\frac{\lambda \varepsilon_{sample}}{d} = \varepsilon_{sample}\sqrt{\frac{EtG}{2d}}$$
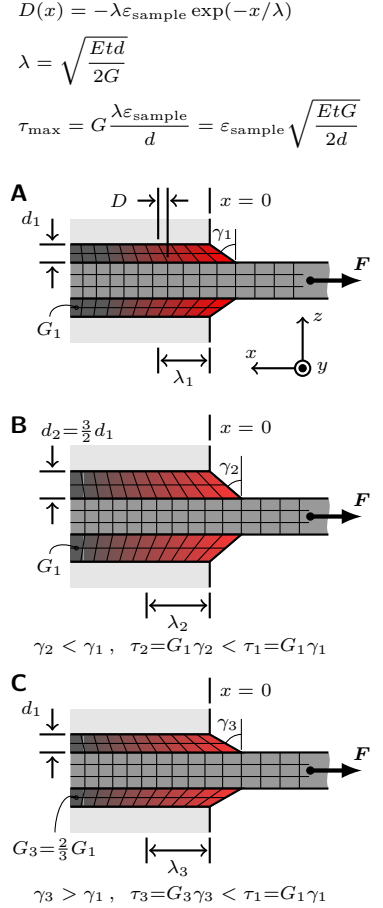
Fig. 2.22: **Effect of epoxy depth and shear modulus. A.** A thin layer of epoxy with a large shear modulus leads to stress concentration in the sample and epoxy near the edge of the sample plate. **B.** By increasing the depth of the epoxy layer the shear stress in the epoxy is reduced and the length over which the strain transmission occurs is increased. However the depth of the epoxy should not be increased so far that the transmission length exceeds the size of the sample plates else only partial transmission will occur. **C.** Reducing the shear modulus of the epoxy also reduces the shear stress in the epoxy and the stress concentration at the sample ends but the shear strain in the epoxy is increased so care must be taken to stay within the limits of the epoxy.

modulus estimated to be ∼6 GPa at low temperatures. The sample plates used in our strain device offer up to 400-500 μm of overlap with the ends of the sample so by fixing the epoxy depth to 25 μm this space is utilised to its full potential. To achieve this separation accurately a foil was fixed to one of the sample plates, further back on the plate than the sample, and polished to 150 μm thick so that when it was combined with the second sample plate sandwiching the sample the correct separation was achieved, see figure 2.14. There still is some uncertainty in making sure the sample sits in the centre between the sample plates above and below the sample but I found in practice that careful application of the epoxy with equal distribution above and below the sample without excess meant the sample naturally found the centre as the epoxy cured. Stycast 2850FT is also a filled epoxy with specified particle diameters up to 45 μm, but in practice, probably due to our preparation and application method, the larger particles tended to be absent but the smaller particles may have been helping to centre the sample. It was difficult to verify if the sample was centred directly after the mounting stage since there was no line of sight to the side of the sample in our device, but after samples were removed from the rig this was always checked.

The shear stress in the epoxy can also be reduced by using a softer epoxy but at the expense of also increasing the shear strain in the epoxy. A softer epoxy needs to have a proportionally larger yield strain in order to achieve the same sample strains. Stycast 2850FT appears to be ideally suited in this range with a low enough shear modulus to prevent serious stress concentration in the sample, but a large enough yield strength to reach high sample strains. For most epoxies the elastic properties are only known close to room temperature but even comparing these values Stycast is well suited, see table 2.2. Some caution should be taken though when comparing these results directly since the shear tests on which this data are based can be strongly affected by surface preparation, material choice, and epoxy thickness. However once coupled with fact that

Table 2.2: **Mechanical properties of select epoxies.** Shear modulus and lap shear strength of several epoxies tested at room temperature. Where the shear modulus was unknown, the measured Young's modulus with an assumed Poisson's ratio of 0.3 was used to calculate the shear modulus.

	Shear modulus	Lap shear strength
Stycast® 2850FT [69]	∼4 GPa	∼40 MPa (Blasted stainless steel)
EPO-TEK® H74 [72]	∼2 GPa	∼11 MPa (Unknown)
EPO-TEK® H20E [73]	∼2 GPa	∼10 MPa (Unknown)
Araldite® [74]	∼1 GPa	∼18 MPa (Blasted stainless steel)
MasterBond® EP29LPSP [75]	∼1 GPa	∼15 MPa (Aluminium)

Stycast's thermal expansion is matched to that of brass it seems an ideal epoxy for our purpose and perhaps had another epoxy been chosen instead during the initial tests of the first uniaxial stress device, a premature failure may have written off the whole idea.

2.7   Conclusions

Traditional uniaxial pressure measurements are technically challenging and extreme care must be taken to ensure high strain homogeneity. The technique described here, where a long narrow bar is strained across a vice, offers significant improvements and can achieve very high strain homogeneity in the central portion of the sample. When experiments are designed to be sensitive to this central portion of the sample this is then a very effective technique.

The strain range now achievable is no longer a weak perturbation but can be a very significant energy scale. To put it in perspective, one would expect that a strain of 1 % can change the Fermi level by approximately 1 % of the band width. For Sr_2RuO_4 and straining along the [100] direction the band width in this direction for the γ band is $\sim$3 eV [6]. The energy scale of the achievable strain range is therefore order $\sim$30 meV equivalent to a temperature of $\sim$300 K or a magnetic field of $\sim$600 T.

Figure 2.23 shows preliminary measurements on the high temperature superconductor $YBa_2Cu_3O_{7-\delta}$ made with this uniaxial stress technique. Small concentric coils with diameters 250 μm for the pick-up coil and 1.5 mm excitation coil were placed above the centre of the sample to measure AC magnetic susceptibility. Over a strain range of close to 1 %, an equivalent pressure range of $\sim$1.6 GPa [76], there is very little broadening of the superconducting transition, rather just a rigid shift of T_c to higher temperatures.

After carrying out some simple analytic approximations for the strain transmission and further detailed FEA simulations we can provide some guidelines, readily achievable in experiments, for the best procedure for mounting samples. High strain is best achieved by using soft and moderately thick layers of epoxy, bonding a thin sample to rigid sample plates, encasing the sample from above and below. The inhomogeneity from these sample mounts decays over a distance roughly equal to the width of the sample, so length to width aspect ratios greater than $\sim$3:1 should be used to provide a large enough homogeneous portion in the centre of the sample. Any asymmetry in the sample mounting causes the sample to bend when strained, creating a strain gradient across the sample's thickness. The strain inhomogeneity can be large if the correct care is not taken but the bending inhomogeneity can be minimised by using long, thin samples. Care must still be taken to stay below the bucking limit however. The soft epoxy leads to some uncertainty
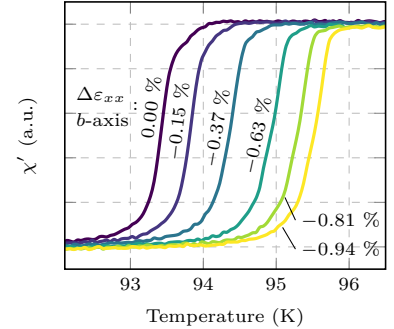

Fig. 2.23: **$YBa_2Cu_3O_{6.92}$ susceptibility against temperature.** Real part of the susceptibility χ against temperature for a sample of $YBa_2Cu_3O_{6.92}$ compressed along the b-axis.

in the exact sample strain achieved so a finite element simulation is required to determine the strain transmission more precisely.

The Physics of Sr_2RuO_4 Approaching a Van Hove Singularity

<div style="border:1px solid">

3

</div>

3.1 Introduction

Materials with strong electron-electron correlations are of particular importance in the study of condensed matter physics as it is here where conventional theories are often seen to be violated and exotic phases such as superconductivity and magnetism emerge. The transition metal oxide Sr_2RuO_4 shares the same layered perovskite crystal structure as the parent compound of the prototypical high-T_c superconductor $La_{2-x}Sr_xCuO_4$ and attracted considerable interest after superconductivity was also found here by Maeno *et al.* in 1994, albeit at much lower temperatures [77]. Since then the superconductivity has been established to be unconventional in nature, but many open questions remain regarding the microscopic origin of the superconductivity and the exact pairing symmetry. What is known is that the superconductivity condenses from a firmly established and well characterised Fermi liquid [6].

To better understand mysteries such as the order parameter symmetry of an unconventional superconductor it can be beneficial to venture into neighbouring phase space. Hydrostatic pressure is often used, but in Sr_2RuO_4 its effects are disappointing. It is known to suppress the superconducting transition temperature and at the same time reduce the quasiparticle mass enhancements [78]. What may prove to be of particular importance in Sr_2RuO_4 is the close proximity of one of its three conduction bands to a Van Hove singularity. This is a special point in the band structure where the group velocity of the quasiparticles goes to zero and the density of states diverges (in 2D systems). Tuning towards a Van Hove singularity is of interest not just in terms of superconductivity but also for the study of a more general problem. Strong quasiparticle renormalization and quasiparticle-quasiparticle scattering can occur near such singularities in the density of states and it has been postulated that for the cuprate superconductors some of the unusual behaviour observed may be the consequence of a Van Hove singularity close to the Fermi level. For Sr_2RuO_4 the Fermi level can be made to traverse the Van Hove singularity by electron doping, heterovalent substitution of La^{3+} for Sr^{2+} [79, 80], or by introducing biaxial strain though lattice mismatch of epitaxially grown thin films [81].

These experiments provided useful information about the metallic properties, but the extreme sensitivity of the superconductivity of Sr_2RuO_4 to disorder meant that no superconductivity could be observed in either study.

Applying uniaxial stress to bulk samples has also demonstrated the importance of the Van Hove singularity in Sr_2RuO_4 [33]. An applied strain of ~ -0.2 % was shown to cause an enhancement of the superconducting critical temperature by ~ 40 %, which was argued to be caused predominately by the increase in density of states as the Van Hove singularity is brought closer to the Fermi energy.

Uniaxial stress is particular well suited, at least in principle, for tuning towards Van Hove singularities compared to hydrostatic pressure or even biaxial stress. Under uniaxial stress a smaller volume change takes place so it is a lower-energy distortion, and crucially a circular Fermi surface becomes elliptical extending out towards the zone boundaries in two opposite directions. In comparison, any distortions to the Fermi surface on a square lattice under biaxial stress must be four-fold symmetric. Without a significant volume change of the Fermi surface, the only way for the Fermi surface to get closer to the zone boundary is for four lobes to grow out in a cross shape, overall a much higher energy configuration than the two fold distortion under uniaxial stress. In terms of hopping integrals, uniaxial pressure directly affects the ratios of nearest-neighbour hoppings, whereas biaxial stress or hydrostatic pressure can only alter the balance between nearest- and next-nearest-neighbour hopping, which has a generally weaker effect.

As stressed earlier in this thesis, uniaxial stress has the benefits that it is both a clean and continuous tuning parameter. We are now in the situation where we can achieve much larger uniaxial stresses motivating a continuation and extension of the previous study. We extended the strain range all the way to -1 %, higher than was thought possible for this rather brittle metal oxide.

At a strain of -0.55 %, I observe a maximum in T_c of ~ 3.5 K after which T_c decreases again rapidly with higher strains. I have also measured resistivity, magnetoresistance and Hall effect, all of which are consistent with the Fermi level traversing the Van Hove singularity, producing a Lifshitz transition. We observe signatures of quantum criticality as the transition is approached, thus providing the unique opportunity to study a topological Lifshitz transition in a system which is exquisitely clean and with a continuous tuning parameter that introduces minimal disorder. We see that the density of states changes in a very restricted part of the Brillouin zone due to the Van Hove singularity affect the temperature-dependent scattering of all the quasiparticles.

This chapter will continue with an introduction to the salient features of Sr_2RuO_4 relevant to the discussion of the results later on along with the necessary background physics. Section 3.3 will detail the experimental methods and measurements undertaken before the results are presented in section 3.4 along with complementary discussions.

3.2   Background physics for Sr_2RuO_4

3.2.1   Fermi liquid properties of Sr_2RuO_4

The majority of the work on Sr_2RuO_4 has focused on the unconventional nature of the superconducting state. However the normal state has also been extensively studied and firmly established as a quasi-two-dimensional strongly correlated Fermi liquid [6].

As was first introduced in section 1.1, the nominal valence of the ruthenium ion in Sr_2RuO_4 is Ru^{4+}, leaving four remaining electrons in the $4d$ shell. In the layered perovskite structure of Sr_2RuO_4, shown in figure 3.1, the ruthenium ions are at the centres of RuO_6 octahedra. The crystal field of the oxygen ions splits the five degenerate $4d$ states into a low-lying triplet, namely the t_{2g} levels d_{xy}, d_{xz}, and d_{yz}, and a higher doublet, the e_g states $d_{x^2-y^2}$ and d_{z^2}. The four valence electrons are distributed amongst the three bands formed from the t_{2g} levels [83].

The large interplane separation of this layered structure means there is very little overlap of the orbitals along the c-axis and therefore very little dispersion along the c-axis, so the band structure is approximately two dimensional. The d_{xz} atomic orbitals are mostly oriented in the xz-plane, giving a significant overlap between nearest neighbours along the x-axis but not along the y-axis. The band formed from these orbitals is therefore expected to be almost one dimensional; an open sheet roughly perpendicular to the x-axis. Similarly, the d_{yz} states produce a sheet perpendicular to the y-axis. The d_{xy} orbitals on neighbouring rutheniums have a strong overlap along both the x- and y-directions through their shared oxygens and also with the next-nearest neighbours since their lobes are at 45° to the crystal axes. They combine to produced an approximately cylindrical sheet.

Mixing between the d_{xy} derived band and the d_{xz} or d_{yz} bands will be weak because they have different parity under the reflection $z \to -z$ but the two one-dimensional surfaces can hybridise and these combine to form an electron like cylinder, β, around the centre of the zone and a hole like cylinder, α, centred around the zone corners, see figure 3.2 B and C. The d_{xy} derived band is also electron like and is centred in the zone [6]. It is given the name γ.

This simple tight-binding picture matches qualitatively and

Fig. 3.1: **Crystal structure of Sr_2RuO_4.** Perovskite structure with RuO_2 layers separated by SrO spacer layers. Each Ru ion is at the centre of a RuO_6 octahedron. The low temperature lattice constants are $a = 3.86$ Å and $c = 12.72$ Å, tetragonal space group $I4/mmm$ [82].

Fig. 3.2: **Fermi surfaces of Sr_2RuO_4.**
A. In-plane Fermi surface cross sections obtained from an ε_F intensity map in an ARPES study by Damascelli *et al.* [84]. The first Brillouin zone is shown and the naming of the three surfaces α, β and γ. **B and C.** The d_{xz} and d_{yz} bands hybridise to form the the α and β surfaces. Adapted from [6].
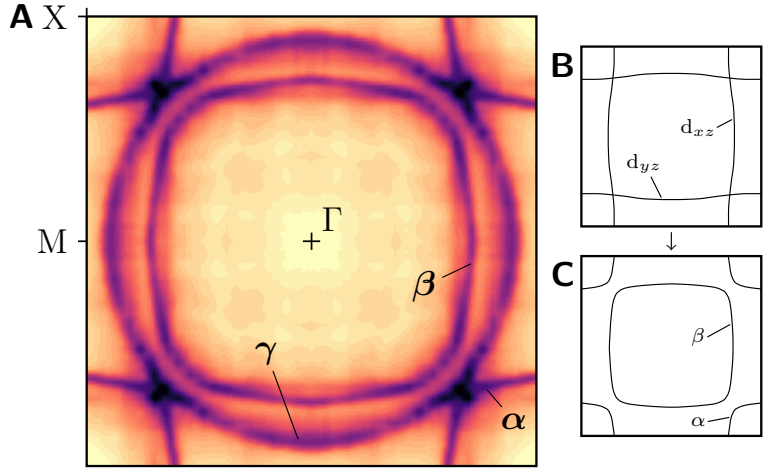
semi-quantitatively with the measured band structure [6]. Angle-resolved photoemission spectroscopy by Damascelli *et al.* [84] confirmed the *k*-space structure of the Fermi surfaces and extensive quantum oscillation [6, 83, 85–87] and angle-dependent magnetoresistance oscillations (AMRO) measurements [88, 86] have provided an extremely detailed experimental determination of the Fermi surface, including the interlayer dispersions [6]. While the simple picture described above and shown in figure 3.2 provides a good starting point for the electronic structure of Sr_2RuO_4, in order to quantitatively understand the behaviour and unconventional superconductivity of Sr_2RuO_4, more detailed knowledge was required. Further details can be found in the comprehensive compilation of results given by Bergemann *et al.* [6] where they also discuss the intricate peculiarities of the Fermi surface which are thought to be responsible for some of the competing instabilities.

The first indications of Fermi liquid behaviour in Sr_2RuO_4 came from measurements of the specific heat, Pauli spin susceptibility and resistivity [89]. The *T*-linear part of the specific heat γ is quite large at 38 mJ mol^{-1}K^{-2} [89] and so is the *T*-independent spin susceptibility χ_s at 1.7×10^{-4} [90]. The ratio of these two is the Wilson ratio $R_W = (\pi^2 k_B^2 N_A V/6\mu_0\mu_B^2) \times (\chi_s/\gamma) = m^*_{susc}/m^*$, and is equal to 1.5. For a free electron gas R_W is unity. In Sr_2RuO_4 R_W is larger but still suggests a common origin for the enhancements of the electronic specific heat and the spin susceptibility [89].

At low temperatures the resistivity follows the characteristic $\rho_0 + AT^2$ form, suggesting that the low temperature *T* dependence is dominated by the quasiparticle-quasiparticle umklapp processes of the Fermi liquid. T^2 behaviour is seen up to almost 25 K in both the in-plane resistivity ρ_{ab} and the out-of-plane resistivity ρ_c with *A*-coefficients of $A_{ab} \sim 6$ nΩ cm/K^2 and $A_c \sim 5.5$ $\mu\Omega$ cm/K^2 [6], see figure 3.3. The resistivity is highly anisotropic, as expected
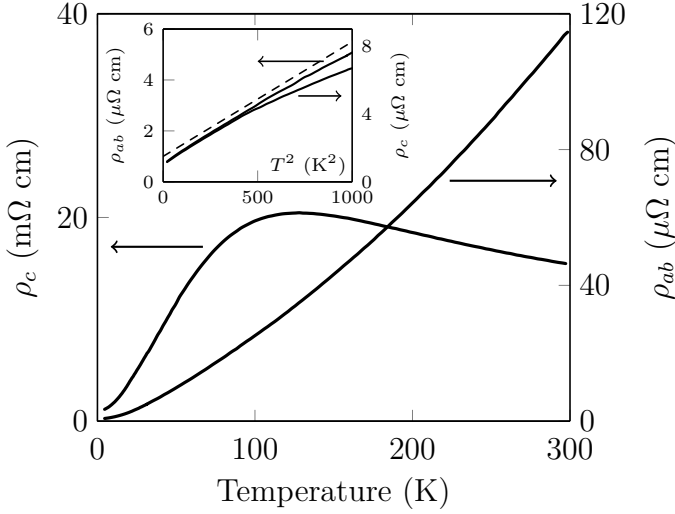
Fig. 3.3: **Resistivity against temperature.** In-plane ρ_{ab} and out-of-plane ρ_c resistivity for Sr_2RuO_4. The inset show the T^2 dependence at low temperatures, the dashed line is a linear guide for the eye. Reproduced from [92].

from the crystal structure, with a low temperature anisotropy as high as $\rho_{0,c}/\rho_{0,ab} \sim 4000$ [91].

The most definitive evidence for the Fermi liquid state comes from quantum oscillation measurements [83] which were also used to refine the experimentally determined Fermi surfaces. In a sufficiently large magnetic field quasiparticles can be driven around the Fermi surfaces by the Lorentz force. The cyclotron orbits of the quasiparticles are quantised due to the wave-like nature of the quasiparticle wavefunctions and the quasiparticles reside on a series of discrete cylinders in *k*-space called Landau levels. The radius of a Landau level is inversely proportional to the strength of the magnetic field and as the field is swept these Landau levels pass successively through the Fermi energy, causing oscillations in the material's properties. The Shubnikov-de Haas effect refers to quantum oscillations in the resistivity and the de Haas-van Alphen effect refers to oscillations in the magnetization but virtually all properties dependent on the density of states at the Fermi level should show some level of oscillation.

The oscillation frequencies yield the areas of extremal Fermi surface cross sections normal to the applied field direction. From the amplitudes of the oscillation more information can also be extracted including the quasiparticle masses [93]. Fermi liquid theory predicts a particular form for how the oscillation amplitude is attenuated with increasing temperature. The Fermi surface becomes more smeared out at higher temperatures due to thermal excitations and the amplitude of the oscillations is exponentially reduced. By fitting to the temperature dependence of the osculatory amplitude, the mass can be extracted for each band individually.

For Sr_2RuO_4 the cyclotron masses are determined as $m_\alpha^*/m_e = 3.3$, $m_\beta^*/m_e = 7.0$ and $m_\gamma^*/m_e = 16$ where m_e is the bare electron

mass [6]. From the quasiparticle masses the individual specific heat contributions of the three Fermi surfaces can be calculated and their sum provides another consistency check which matches well with bulk measurements [83]. The accumulation of all this evidence leads logically to the conclusion that the normal state of Sr_2RuO_4 is well described by Fermi liquid theory and strong correlations lead to moderately heavy Landau quasiparticles, with masses enhanced in all bands by a factor of 3-4 [83].

3.2.2 Superconductivity of Sr_2RuO_4

In Sr_2RuO_4 the Fermi liquid is unstable to the formation of a superconducting state below 1.5 K in the clean limit [61]. Here the low lying excitations are no longer the Landau quasiparticles but instead bound states of Cooper pairs are formed at the Fermi energy.

After superconductivity was first discovered in mercury by Onnes in 1911 [19] two defining characteristics became apparent: firstly the superconductor is a zero resistance state and secondly the superconductor expels magnetic field, not as consequence of the zero resistance but a defining property though an effect known as the Meissner-Ochsenfeld effect which showed that the superconducting state must be a new equilibrium thermodynamic phase, accessible only through a phase transition. A phenomenological model of superconductivity was first proposed by Ginzburg and Landau [94] in 1950. Then just a few years later Bardeen, Cooper, and Schrieffer jointly proposed the first microscopic theory for superconductivity; their BCS theory [95]. The essence of their ingenuity was to move away from the independent electron thinking of the day and consider a state where the electrons acted together as one inseparable entity. BCS theory is a beautiful example of emergence where something so simple can emerge from the complexities of the many particle soup.

Cooper first attacked the problem by showing that two electrons above a filled Fermi sea are unstable towards pairing up in the presence of any arbitrarily small attractive interaction. The two particle wave function for these extra electrons can be written in terms of Bloch waves as

$$\Psi(\mathbf{r}_1, \mathbf{r}_2) = \frac{1}{\sqrt{2}}(|\uparrow_1\downarrow_2\rangle - |\downarrow_1\uparrow_2\rangle) \sum_{|\mathbf{k}| \geq k_F} \varphi_\mathbf{k} e^{i\mathbf{k}\cdot(\mathbf{r}_1 - \mathbf{r}_2)} \qquad (3.1)$$

where a zero total momentum state has been chosen as it seems most likely to be lowest in energy. The spin part of the wavefunction is antisymmetric with respect to particle exchange and the spatial part is symmetric, maintaining an overall antisymmetric state for these two fermions. Subject to a weak attractive interaction $V(\mathbf{r}_1 - \mathbf{r}_2)$
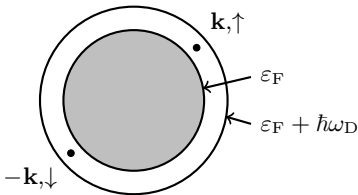

Fig. 3.4: **Cooper Pairs.** The Cooper problem with two electrons outside a filled Fermi sea and an interaction that is attractive while the electron energies are within $\hbar\omega_D$ of the Fermi energy. Reproduced from [96].

the eigenvalues of the Schrödinger equation become

$$\left[-\frac{\hbar^2}{2m^*}\nabla_1^2 - \frac{\hbar^2}{2m^*}\nabla_2^2 + V(\mathbf{r}_1 - \mathbf{r}_2) \right] \Psi(\mathbf{r}_1, \mathbf{r}_2) = E\Psi(\mathbf{r}_1, \mathbf{r}_2) \quad (3.2)$$

$$\sum_{|\mathbf{k}| \geq k_F} (2\varepsilon_\mathbf{k} + V(\mathbf{r}))\varphi_\mathbf{k} e^{i\mathbf{k}\cdot\mathbf{r}} = E \sum_{|\mathbf{k}| \geq k_F} \varphi_\mathbf{k} e^{i\mathbf{k}\cdot\mathbf{r}_1} \quad (3.3)$$

$$2\varepsilon_\mathbf{k}\varphi_\mathbf{k} + \sum_{\mathbf{k}'} V_{\mathbf{k}'-\mathbf{k}}\varphi_{\mathbf{k}'} = E\varphi_\mathbf{k}. \quad (3.4)$$

We assume a weak attractive interaction in only a thin shell around the Fermi surface such that

$$V_{\mathbf{k}'-\mathbf{k}} = \begin{cases} -|V_0| & \varepsilon_F < \varepsilon_\mathbf{k} < \varepsilon_F + \hbar\omega_D \\ 0 & \text{otherwise} \end{cases}. \quad (3.5)$$

Then solving 3.4 self-consistently

$$-|V_0| \sum_{\mathbf{k}'} \varphi_{\mathbf{k}'} = (E - 2\varepsilon_\mathbf{k})\varphi_\mathbf{k} \quad (3.6)$$

$$1 = -|V_0| \sum_{\mathbf{k}} \frac{1}{E - 2\varepsilon_\mathbf{k}} \quad (3.7)$$

$$1 = -|V_0| \int_{\varepsilon_F}^{\varepsilon_F + \hbar\omega_D} \frac{1}{E - 2\varepsilon_\mathbf{k}} g(\varepsilon_F) d\varepsilon \quad (3.8)$$

$$E = 2\varepsilon_\mathbf{k} - 2\hbar\omega_D e^{-2/|V_0|g(\varepsilon_F)}. \quad (3.9)$$

The energy as a pair is lowered compared to the two independent states; a bound state exists. We call these bound states of two electrons Cooper pairs.

The question still remains how there can be an attractive iteration to facilitate paring up when naively we think of the electrons repelling each other due to Coulomb repulsion? BCS found the answer in the coupling between the electrons and the lattice. In a metal the ions forming the lattice are not stationary, in reality they can vibrate and oscillate about their minimum energy positions. Collective excitations of the ions exist, waves that move though the lattice, called phonons and each phonon will produce a modulation in the charge density. An electron moving through the lattice is therefore subject to these periodic potential modulations and can undergo diffraction. When an electron scatters off a phonon the momentum of the Bloch wave changes as it exchanges momentum with the lattice but importantly the total crystal momentum is still conserved. In this way two electrons can indirectly interact. One electron can scatter producing a phonon which propagates
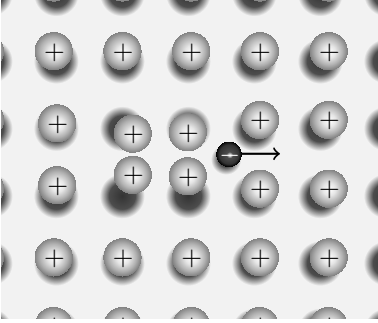
Fig. 3.5: **Electron phonon interaction.** An electron travelling though the lattice disturbs the ions' positions creating an excess positive charge behind the electron. Reproduced from [97].

for a while before it is absorbed by a second electron. The electrons exchange momentum though the creation and annihilation of phonons. The effective iteration that exists turns out to be attractive at small energies and is just what we were looking for to facilitate paring.

A simplified but more intuitive picture is sketched in figure 3.5. The electrons not only repel each other but they are also attracted to the positively charged ions making up the lattice. As an electron passes through the lattice the ions in the lattice are pulled towards the electron. The electrons are travelling relatively fast and the ions are much heavier so it takes longer for the disturbance of the ions to relax and a tube of excess positive charge follows behind the electron. A second electron can be attracted to the first by the retarded distortion of the lattice.

The importance of the electron-phonon interaction and confirmation of BCS's ideas came from the isotope effect. It is seen experimentally that for many superconductors the superconducting transition temperature depends on the mass of the crystal lattice, $T_c \propto M^{-1/2}$. The superconducting critical temperature depends on the binding energy of the Cooper pairs and for the electron-phonon interaction this depends on the Debye energy ω_{D} which not coincidentally has the same dependence on the isotope mass. It also helps explain why the inherently worse conductors are better superconductors. The strong electron-phonon interactions that increase the resistivity in the normal state also increase the superconducting binding energy and transition temperature.

So far all that was said above applied only to two electrons above a filled Fermi sea so these ideas still needed to be extended to real metals with many electrons. The last piece of the puzzle came from Schrieffer and his idea of a macroscopic wavefunction. Continuing from Cooper's findings the true ground state is expected to involve some coherent state of Cooper pairs. Looking for uniform translationally invariant solutions it is more convenient to work in **k** space and continue with second quantised notation. The pair creation operator $\hat{P}_{\mathbf{k}}^{\dagger} = c_{\mathbf{k}\uparrow}^{\dagger} c_{-\mathbf{k}\downarrow}^{\dagger}$ creates a pair of fermions with zero total crystal momentum and total spin zero. The operators $c^{\dagger}$ and c satisfy the commutation rules for fermions. The conjecture of Schrieffer was that the ground state should be a coherent state of Cooper pairs

$$|\Psi_{\mathrm{BCS}}\rangle \propto \exp\left(\sum_{\mathbf{k}} \alpha_{\mathbf{k}} \hat{P}_{\mathbf{k}}^{\dagger}\right)|0\rangle \qquad (3.10)$$

where $|0\rangle$ is the empty vacuum state. Using the fact that the operators commute and $c_{\mathbf{k}\uparrow}^{\dagger} c_{\mathbf{k}\uparrow}^{\dagger} = 0$ it is more straight forward to

write

$$|\Psi_{\text{BCS}}\rangle \propto \prod_{\mathbf{k}} \left(1 + \alpha_{\mathbf{k}} \hat{P}_{\mathbf{k}}^{\dagger}\right)|0\rangle \qquad (3.11)$$

and after normalising we end up with the BCS wavefunction

$$|\Psi_{\text{BCS}}\rangle = \prod_{\mathbf{k}} \left(u_{\mathbf{k}}^{*} + v_{\mathbf{k}}^{*} \hat{P}_{\mathbf{k}}^{\dagger}\right)|0\rangle\,, \quad |u_{\mathbf{k}}|^2 + |v_{\mathbf{k}}|^2 = 1\,. \qquad (3.12)$$

The BCS wavefunction is based on a variational method where the parameters $u_{\mathbf{k}}^{*}$ and $v_{\mathbf{k}}^{*}$ are found by minimising the total energy. The relevant Hamiltonian, for this, including the attractive interaction between the Cooper pairs is

$$\hat{H} = \sum_{\mathbf{k},\sigma} \varepsilon_{\mathbf{k}} c_{\mathbf{k}\sigma}^{\dagger} c_{\mathbf{k}\sigma} - |V| \sum_{\mathbf{k},\mathbf{k}'} c_{\mathbf{k}'\uparrow}^{\dagger} c_{-\mathbf{k}'\downarrow}^{\dagger} c_{-\mathbf{k}\downarrow} c_{\mathbf{k}\uparrow}\,. \qquad (3.13)$$

Instead of minimising $E = \langle\Psi_{\text{BCS}}|\hat{H}|\Psi_{\text{BCS}}\rangle$ we can apply an approximation and look for the mean-field ground state which, although not the exact solution, is almost exact in the limit of weak coupling. After the substitution

$$c_{\mathbf{k}\uparrow}^{\dagger} c_{-\mathbf{k}\downarrow}^{\dagger} c_{-\mathbf{k}\downarrow} c_{\mathbf{k}\uparrow} \approx \langle c_{\mathbf{k}\uparrow}^{\dagger} c_{-\mathbf{k}\downarrow}^{\dagger}\rangle c_{-\mathbf{k}\downarrow} c_{\mathbf{k}\uparrow} + c_{\mathbf{k}\uparrow}^{\dagger} c_{-\mathbf{k}\downarrow}^{\dagger} \langle c_{-\mathbf{k}\downarrow} c_{\mathbf{k}\uparrow}\rangle \qquad (3.14)$$

the Hamiltonian becomes

$$\hat{H} = \sum_{\mathbf{k},\sigma} (\varepsilon_{\mathbf{k}} - \mu) c_{\mathbf{k}\sigma}^{\dagger} c_{\mathbf{k}\sigma} - \sum_{\mathbf{k}} \left(\Delta c_{\mathbf{k}\uparrow}^{\dagger} c_{-\mathbf{k}\downarrow}^{\dagger} + \Delta^{*} c_{-\mathbf{k}\downarrow} c_{\mathbf{k}\uparrow}\right) \qquad (3.15)$$

and we see the gap function for the first time

$$\Delta = |V| \sum_{\mathbf{k}} \langle c_{-\mathbf{k}\downarrow} c_{\mathbf{k}\uparrow}\rangle\,. \qquad (3.16)$$

The Hamiltonian is quadratic and can thus be solved exactly by a suitable change of basis to diagonalise the Hamiltonian. In this case it is a Bogoliubov transformation $b_{\mathbf{k}\sigma} = u_{\mathbf{k}} a_{\mathbf{k}\sigma} + v_{\mathbf{k}} a_{-\mathbf{k}-\sigma}^{\dagger}$. The energy eigenvalues for the states created by these new operators are $\pm E_{\mathbf{k}}$ where

$$E_{\mathbf{k}} = \sqrt{(\varepsilon_{\mathbf{k}} - \mu)^2 + |\Delta|^2}\,. \qquad (3.17)$$

Making reference to figure 3.6 we now have the following situation. Above the the critical temperature, in the normal state, $\Delta = 0$. Here the quasiparticle excitations are the normal particle and hole excitations from the Fermi sea, the dashed lines in the figure. But below the superconducting transition temperature the excitation spectrum is modified to $\pm E_{\mathbf{k}}$ and there is now a minimum energy of 2Δ for excitations. This is the energy gap of the superconductor. The Bogoliubov quasiparticles are slightly strange; they are a
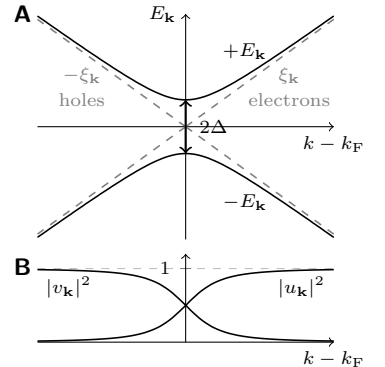

Fig. 3.6: **Energy Gap. A.** Energy eigenvalues $\pm E_{\mathbf{k}}$ of the BCS wavefunction near the Fermi energy. The dashed lines show the electron and hole energies in the normal metal. **B.** BCS quasiparticle weights, $|v_{\mathbf{k}}|^2$ for electrons and $|u_{\mathbf{k}}|^2$ for holes. Reproduced from [96].

mixture of the electron creation and annihilation operators. Each state can be thought of as a quantum superposition of both electrons and holes without a fixed number. The fermion weights for these states are plotted in panel B of figure 3.6.

At finite temperature the quasiparticle energy levels have occupations according to the Fermi-Dirac distribution $\langle b_{\mathbf{k}}^{\dagger} b_{\mathbf{k}} \rangle = f(E_{\mathbf{k}})$. The gap function, equation 3.16, can thus be rewritten in terms of these new quasiparticles to find the finite temperature value of the BCS gap. A plot of the temperature dependent gap is shown in figure 3.7. The gap grows continuously from zero at T_c to its maximum value of $\Delta(0) = 1.76 k_{\mathrm{B}} T_c$ at zero temperature. The gap is a representation of the condensed phase, and its growth is loosely analogous to that of the superconducting order parameter below a continuous phase transition at T_c.

Fig. 3.7: **BCS gap.** The BCS gap as a function of temperature. Reproduced from [98].

For most simple metallic superconductors the predictions of BCS theory such as the ratio of the zero temperature gap to T_c and the magnitude of of the jump in specific heat at T_c are strikingly accurate, but this is not yet the end of the story. As it was introduced above BCS theory applies and works extraordinarily well for phonon mediated weak coupling superconductors. However, for materials with strong electron-electron correlations the larger Coulomb repulsion precludes the pairing by exchange of phonons. Superconductivity is, however, still observed in some cases and extensions to BCS's original ideas are needed to describe these new superconductors.

When writing down the wavefunction of the Cooper pairs, equation 3.1, a spin singlet state was chosen but this was with some foresight and is not in general a requirement. A more general wavefunction can be written as the product of the pair's orbital and spin wavefunctions

$$\Psi(\mathbf{r}_1, \sigma_1, \mathbf{r}_2, \sigma_2) = f(\mathbf{r}_1 - \mathbf{r}_2)\chi(\sigma_1, \sigma_2)\,. \qquad (3.18)$$

We only need to be sure to maintain overall anticommutation of the two fermions. The spin part $\chi(\sigma_1, \sigma_2)$ can have total spin $S = 0$, a singlet, or $S = 1$, a triplet state. The orbital part can be expanded in Laplace's spherical harmonics Y_l^m and the orbital parity is then $(-1)^l$. The antisymmetric spin-singlet state must be accompanied by a symmetric orbital wavefunction, $L = 0$ (s wave), 2 (d wave), etc., where the names are in analogy to those of the atomic orbitals. The spin-triplet state must take $L = 1$ (p wave), 3 (f wave), etc.[8] Decomposing the wavefunction into spin and orbital parts, although instructive here, is in general not always possible due to the presence of spin-orbit coupling. Strictly speaking it is better, rather than talking about a spin-singlet or spin-triplet state, to describe the parity of the state as this still

[8] In the presence of a crystal lattice one cannot strictly expand in terms of these spherical harmonics anymore but this has become the convention for the naming scheme so I stick with it here.

remains after the addition of spin-orbit coupling. However despite this, the convention of describing an odd-parity superconductor as spin-triplet and an even-parity state as spin-singlet is still widely used.

Strongly interacting electron systems are characterised by large on-site Coulomb repulsion, so naively wavefunctions with a high probability of the electrons being close together are unfavourable and the wavefunctions with finite orbital angular momentum are expected.

By extending BCS theory like this it can be used to describe more general interaction terms with both **k**- and spin-dependence. The gap structure needs no longer to be isotropic, instead it can vary around the Fermi surface. There can be phase and amplitude changes as well as nodes in the gap structure. Nodes in the gap structure mean there are excitations at specific **k** states that do not possess a gap even at zero temperature. In the first 70 years after the discovery of superconductivity all new superconductors were spin-singlet *s*-wave superconductors, and so after the discovery of something different, these superconductors with higher orbital angular momentum were termed unconventional. Nowadays a more precise definition of unconventional superconductivity is one where the gap averages to zero over the Fermi surface

$$\sum_{\mathbf{k}} \Delta(\mathbf{k}) = 0 \,. \tag{3.19}$$

There is considerable evidence that the superconducting state in Sr_2RuO_4, a strongly interacting Fermi liquid, is indeed unconventional. Non-magnetic impurities lead to a strong suppression of T_c [99]. In a conventional *s*-wave superconductivity T_c is unaffected by elastic impurity scattering as shown by Anderson [100]. Elastic impurity scattering acts to mix all the different **k** states and so for a conventional superconductor with an uniform gap the superconductivity is not affected. However for an unconventional superconductor this averaging drives the gap to zero as per equation 3.19. Sr_2RuO_4 is perhaps the most disorder-sensitive of all known superconductors; a residual resistivity of less than 1 $\mu\Omega\,cm$ is required to observe superconductivity, a corresponding mean free path of $\sim$0.1 μm. The extreme sensitivity of the superconductivity to disorder prompted the growth of exquisitely clean samples which can now have mean free paths as long as several microns [61].

Since the establishment of the unconventional nature of the superconductivity there has been considerable speculation as to the exact pairing symmetry but after more than two decades of research this has still not been nailed down with certainty. At first, the similarity of the enhancements of specific heat and spin susceptibility in Sr_2RuO_4 to that of ^{3}He led to the exciting suggestion
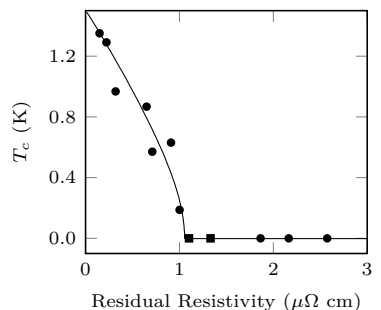
Fig. 3.8: **Impurity effect on superconductivity in Sr_2RuO_4.** The superconducting transition temperature as function of residual resistivity for a variety of samples with different purity levels. The solid line is a fit of the Abrikosov-Gor'kov pair-breaking function to the data. Superconductivity is destroyed when the mean free path becomes similar to the superconducting coherence length. The extreme sensitivity of the superconductivity to non-magnetic impurities is expected only for unconventional pairing. Reproduced from [99].

that superconductivity could be spin-triplet, an electron analogue of superfluid ^{3}He [101]. Much work has focused on this possibility, but the results thus far are still not definitive [61].

A study of the superconducting properties of Sr_2RuO_4 was not the primary aim of the work in this thesis. Therefore I do not wish to dwell too much longer on the current state of established superconducting properties but only give perhaps the most important results to date. For further background on the superconductivity in Sr_2RuO_4 readers are referred to one of the many extensive reviews on the topic [61, 102–104].

To test the prediction of spin-triplet superconductivity measurements can either look for an odd parity orbital part of the wave function and then infer the spin part must be triplet or measurements can directly tackle the spin part. It is now known, however, that spin-orbit coupling is important in Sr_2RuO_4. The fact that it is important means that the orbital and spin parts cannot strictly be separated like this, however, this language is still widely used for Sr_2RuO_4 as it is helpful with interpretation, so I will continue with it here but some level of caution should be kept in mind.

The Meissner effect normally precludes measurements of the spin susceptibility in the superconducting state but nuclear magnetic resonance (NMR) still has access to the spin susceptibility within the superconducting state. In an itinerant system spin susceptibility in a magnetic field is due to the Zeeman splitting of the Fermi surface. The Fermi surface splits into a spin-up surface lowered in energy by $\mu_B H$ and an spin-down surface raised in energy by $\mu_B H$ but overall the free energy is lowered by $\frac{1}{2}\chi_s H^2$. Shifting of the Fermi surfaces mean the states $\mathbf{k}\uparrow$ and $-\mathbf{k}\downarrow$ no longer exist together at the Fermi level. The singlet Cooper pair cannot form unless the gain in free energy from superconductivity condensation overcomes this spin splitting. In a weak field this is typically possible and the spin susceptibility is reduced to zero as temperature goes to zero. For spin-triplet Cooper pairs the components with equal spin paring are unaffected by the spin polarisation of the Fermi surface so the spin susceptibility is typically unaffected at T_c. The exact response depends on the type of p-wave order parameter but the change can be predicted. Ishida *et al.* [105] used the Knight shift measured by NMR to determine the spin susceptibility. As direct evidence against singlet superconductivity they observe no change in the Knight shift as the temperature is lowered through T_c, see figure 3.9. Complementary results from polarized neutron scattering by Duffy *et al.* [106] confirm the unchanging spin susceptibility as superconductivity sets in, suggesting a spin-triplet state and hence an odd parity state.

Evidence from parity sensitive measurements also seems to corroborate these results. Nelson *et al.* [107] joined Sr_2RuO_4 to a

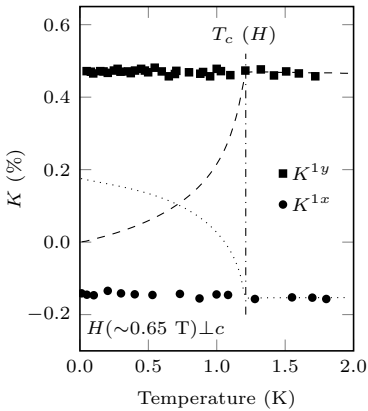

Fig. 3.9: **Knight Shift against temperature.** The temperature dependence of the Knight shift measured at the two different oxygen sites as the sample is cooled through T_c. The dashed lines are the expected form should the Cooper pairs be spin singlet paired as $d_{x^2-y^2}$. The independence of the Knight shift on temperature is strong evidence for triplet pairing. Reproduced from [105].

conventional superconductor $Au_{0.5}In_{0.5}$. The interface between two superconductors makes a Josephson junction, a device in which a supercurrent flows between the two superconductors because of any differences in the phase of the superconducting wave function from one superconductor to the next. Even though the parity of the Cooper pairs is expected to be different in Sr_2RuO_4 and conventional superconductors the tunnelling of Cooper pairs is still possible in the presence of spin-orbit coupling [108, 109]. Nelson *et al.* put one such junction on opposite *ac*-faces of a Sr_2RuO_4 single crystal. For a spin-triplet superconductor the orbital part of the Cooper pair wavefunction must be antisymmetric, i.e. it changes phase by π through a rotation of 180°. By placing two Josephson junctions on opposite faces and connecting them with an additional superconducting link there is a overall phase shift of π when traversing the ring. There must then be an accompanying supercurrent and this type of junction is known as a π-junction. By measuring the magnetic field dependence of the current that can be passed through such a device the parity of the superconductor can be identified. The results of Nelson *et al.* suggest an odd parity orbital wavefunction in agreement with the NMR and polarized neutron scattering, although the presence of domains in the junction could complicate the analysis.

If Sr_2RuO_4 is a spin-triplet superconductor the orbital part of the pair wavefunction needs to be specified for each of the three triplet states. The same is true for the gap function and this is typically done by introducing some additional notation

$$\Delta(\mathbf{k}) = \begin{pmatrix} \Delta_{\uparrow\uparrow}(\mathbf{k}) & \Delta_{\uparrow\downarrow}(\mathbf{k}) \\ \Delta_{\downarrow\uparrow}(\mathbf{k}) & \Delta_{\downarrow\downarrow}(\mathbf{k}) \end{pmatrix} = i(\Delta_{\mathbf{k}}\boldsymbol{I} + \mathbf{d}(\mathbf{k}) \cdot \boldsymbol{\sigma})\sigma_y \qquad (3.20)$$

where $\boldsymbol{\sigma} = (\sigma_x, \sigma_y, \sigma_z)$ is a vector of Pauli matrices, $\boldsymbol{I}$ is the 2×2 unit matrix, $\Delta_{\mathbf{k}}$ is a scalar and $\mathbf{d}(\mathbf{k})$ is a three component complex vector. A singlet superconductor is described by setting $\Delta_{\uparrow\uparrow} = \Delta_{\downarrow\downarrow} = 0$ and $\Delta_{\uparrow\downarrow} = -\Delta_{\downarrow\uparrow} = \Delta_{\mathbf{k}}$, equivalently setting $\mathbf{d}(\mathbf{k})$ to zero and leaving $\Delta_{\mathbf{k}}$ finite. In the triplet case $\Delta_{\uparrow\downarrow} = \Delta_{\downarrow\uparrow} = \Delta_0$ and $\Delta_{\mathbf{k}}$ is zero. In full

$$\begin{pmatrix} \Delta_{\uparrow\uparrow}(\mathbf{k}) & \Delta_{\uparrow\downarrow}(\mathbf{k}) \\ \Delta_{\downarrow\uparrow}(\mathbf{k}) & \Delta_{\downarrow\downarrow}(\mathbf{k}) \end{pmatrix} = \begin{pmatrix} -d_x(\mathbf{k}) + id_y(\mathbf{k}) & d_z(\mathbf{k}) \\ d_z(\mathbf{k}) & d_x(\mathbf{k}) + id_y(\mathbf{k}) \end{pmatrix}.$$
$$(3.21)$$

The *d*-vector notation introduced by Balian and Werthamer [110] as above is useful since it now transforms just like a vector under spin rotations. The *d*-vector fully describes the triplet superconducting state including all symmetries, spin and orbital angular momentum and the nodes in the gap structure. In a crystalline environment the *d*-vector must match the point group symmetry of the crystal but for Sr_2RuO_4 there are still numerous choices remaining, a list
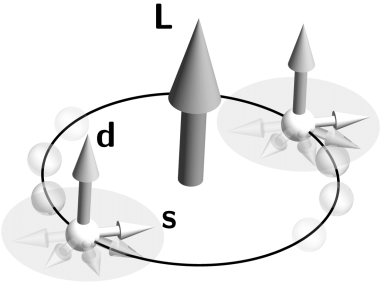
Fig. 3.10: **d Vector.** A sketch of the Cooper pair d-vector $\mathbf{d} = \Delta_0\hat{\mathbf{z}}(k_x \pm ik_y)$ showing the pairs angular momentum **L** and the spins of the electrons in the pair **s**.
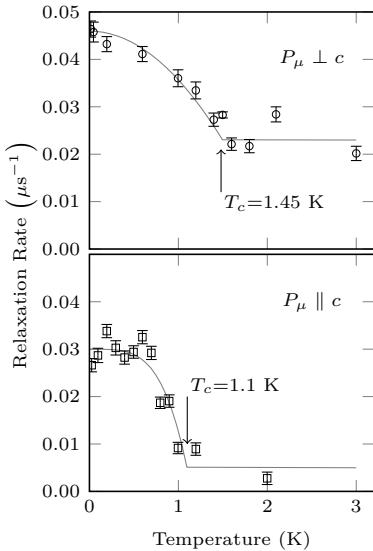
Fig. 3.11: **Muon spin-relaxation rate.** The muon-spin relaxation rate shows an abrupt change on cooling at T_c in zero applied magnetic field. Two different samples with different T_c's show it is a feature of the superconductivity suggesting the development of spontaneous magnetic fields breaking time-reversal symmetry. Reproduced from [111].

of which can be found in [61], and it is left up to experimental determination to identity the exact order parameter.

One of the most promising candidates is the *d*-vector

$$\mathbf{d} = \Delta_0\hat{\mathbf{z}}(k_x \pm ik_y). \tag{3.22}$$

$\hat{\mathbf{z}}$ points along the normal to the *ab*-plane. The spin is zero along the direction of **d** so the spins of the Cooper pair are confined to the *ab*-plane and are both in a spin aligned state. The orbital part has angular moment $l = 1$ with both orientations $L_z = \pm 1$ possible. This implies the relative orbital motion of the electrons forming the Cooper pair can be either clockwise or anticlockwise. The two orientations are degenerate but within a given domain all the Cooper pairs have the same rotation direction. This state is termed chiral because picking out a specific direction breaks another symmetry, namely time-reversal symmetry.

Some experimental probes are sensitive to the effects of broken time-reversal symmetry and the results suggest that Sr_2RuO_4 may indeed be a chiral superconductor. The chiral Cooper pair wave-function has an overall magnetic moment but no bulk magnetic moment is expected since there must still be a Meissner effect and a screening current should be set up. However in the vicinity of impurities and domain edges the Meissner screening may not always be perfect and small local fields are expected. In the technique of muon spin rotation a muon is incident on the sample, it comes to rest, interacts with the local magnetic field, and then decays emitting a positron in a direction correlated with the spin's direction, and so is sensitive to local magnetic field distribution. The first studies of μSR on Sr_2RuO_4 by Luke *et al.* [112] in 1998 found the appearance of spontaneous magnetic fields coinciding with the onset of T_c. This was verified by looking at samples with varying T_c's [111].

Evidence for broken time-reversal symmetry has also been seen in measurements of the polar Kerr effect. The polar Kerr angle measures the polarisation rotation between incoming and reflected linearly polarised light. A non zero angle occurs when right and left circularly polarized light are reflected with a different phase shift. The magnitude and direction of rotation depend on the magnetisation of the surface. Polar Kerr effect measurements on Sr_2RuO_4 see an increase of rotation coinciding with T_c increasing to approximately 100 nrad at zero temperature [113].

Although these measurements give strong evidence for broken time-reversal symmetry, the story is not so clear. The currents thought responsible for the additional muon relaxation rate should be detectable with other local magnetisation measurements. Scanning SQUID and Hall probe microscopy have not be able to identify

these fields at the level of even 1 % of the predicted values by theory, and by μSR [114–117].

Other physical properties also add to the puzzle. The electronic specific heat of Sr_2RuO_4 gives a clear signature of unconventional superconductivity [119]. The specific heat of a conventional superconductor, which depends on the quasiparticle density at low temperatures, grows exponentially from zero at low temperatures. The specific heat of Sr_2RuO_4 on the other hand clearly shows linear behaviour down to below 100 mK, see figure 3.13. This, in combination with several other results, including thermal conductivity [120–122], NQR [123], London penetration depth [124, 125] and ultrasound attenuation [126], all point towards a quasiparticle density that varies linearly in temperature from $T_c/2$ to at least 100 mK. This suggests that there may well be nodes in the gap structure or at the very least zeros or very deep minima, but no consensus has been reached about where and in what direction these nodes might be.

The superconducting phase diagram for Sr_2RuO_4 in applied magnetic fields also adds to the mystery. Increasing magnetic field, at some point, will destroy the superconducting state. For a spin singlet superconductor this can happen when the Zeeman energy from spin polarizing the Fermi surface, as discussed earlier in relation to the spin susceptibility, outweighs the condensation energy gain. For spin triplet superconductors certain Cooper pairs with equal spin pairing should be exempt from this breakdown, known as the Pauli limit. The *d*-vector most commonly used for Sr_2RuO_4 is one such example. The alternative mechanism for the eventual destruction of the superconducting state involves the creation of vortices in the superconducting state. In a type of superconductor, known as a type-II superconductor, above a certain critical field strength it becomes energetically unfavourable to keep screening the entirety of the magnetic field and some magnetic field enters the superconductor in concentrated lines called vortices. The core of a vortex returns to the normal metallic state and superconducting screening currents flow around the vortex. Each vortex concentrates one flux quantum of magnetic field and as the applied field is increased further, more and more vortices enter the material until the entire material returns to the normal state at the upper critical field, also known as the orbital limiting field.

Sr_2RuO_4 is a type-II superconductor but the anisotropy of the upper critical field is highly unusual. The critical field for field applied along the c-axis is 0.07 T and increases as the field is rotated towards the *ab*-plane. From Ginzburg-Landau theory the upper critical field is given by $H_{c2} = \Phi_0/2\pi\xi^2$, where the coherence length ξ depends on the effective mass as $\xi \propto 1/\sqrt{m^*}$. The two dimensional band structure of Sr_2RuO_4 has a much larger effective
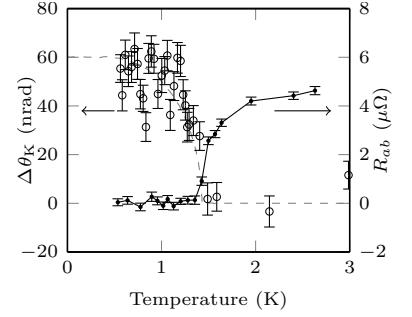
Fig. 3.12: **Polar Kerr effect.** The polar Kerr angle vs. temperature in zero applied magnetic field along with the samples electrical resistance showing that the increase in rotation coincides with T_c. The non zero rotation angle below T_c is further evidence for time-reversal symmetry breaking. Reproduced from [118].
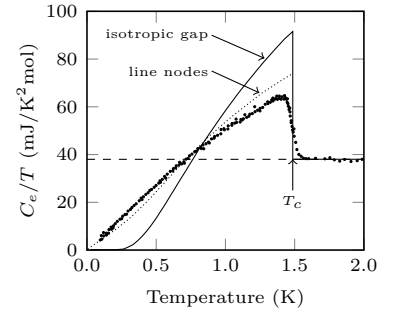
Fig. 3.13: **Electronic specific heat of Sr_2RuO_4.** The electronic specific heat divided by temperature. The specific heat varies linearly with temperature over a large range, inconsistent with a fully gapped superconductor. Reproduced from [119].
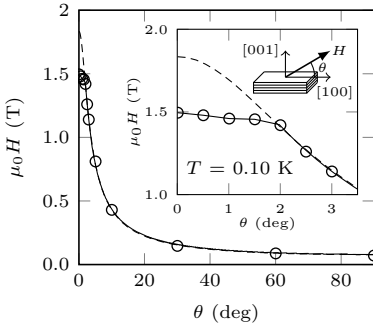
Fig. 3.14: **Field angle dependence of the upper critical field.** The upper critical field H_{c2} is limited for fields close to the *ab*-plane compared to the predictions from Ginzburg-Landau theory with an anisotropic effective mass. Reproduced from [128].
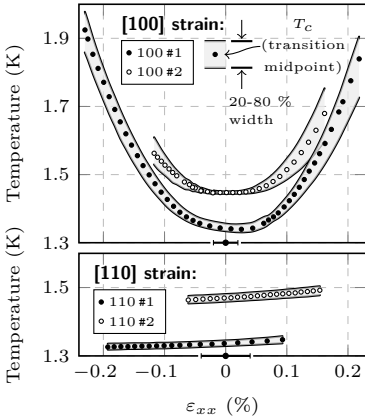
Fig. 3.15: **The superconductivity of Sr_2RuO_4 under strain.** T_c versus strain for strain applied along the [100] direction and [110] direction. The strong increase in T_c for both [100] oriented compression and tension is thought to be due to increased density of states at the Fermi level as the γ band approaches a Van Hove singularity in the band structure. Reproduced from [33].

mass along the out of plane direction so there should also be an anisotropy of the upper critical field [127]. For angles larger than 2° from the *ab*-plane this Ginzburg-Landau theory with an anisotropic effective mass fits the data well [128], see figure 3.14, although the fitted anisotropy is smaller than that obtained in the dHvA band structure measurements [6]. Within 2° of the *ab*-plane the increase of the critical field is cut-off and the transition turns first order below ∼0.8 K suggesting something else is at play rather than normal orbital limiting.

One last experiment which is of direct importance to the work being presented in this thesis is the first uniaxial strain study by Hicks *et al.* [33]. In the tetragonal crystal symmetry of Sr_2RuO_4 the *d*-vector $\mathbf{d} = \Delta_0\hat{\mathbf{z}}(k_x \pm ik_y)$ is degenerate but upon breaking the symmetry by applying an orthorhombic distortion, the degeneracy is lifted and either the $\mathbf{d} = \Delta_0\hat{\mathbf{z}}k_x$ or $\Delta_0\hat{\mathbf{z}}k_y$ state is favoured [62,63]. Hicks *et al.* set out with the aim to apply an orthorhombic distortion and search for the predicted discontinuity in $dT_c/d\varepsilon$ of the superconducting T_c at zero strain (see figure 2.10), a v-shaped kink between the p_x and p_y states. No such kink was observed as can be seen in figure 3.15, but the strong increase in T_c for [100] oriented strain was part of the motivation for this work. Almost no change in T_c is observed for [110] oriented strain. After comparison to band structure calculations it appeared that the dominant effect increasing T_c is the change in density of states as the γ band approaches a Van Hove singularity when the strain is applied along a [100] direction. The importance of Van Hove singularities in Sr_2RuO_4 will be further discussed in the following section.

In conclusion, after extensive experimental efforts there is still no consensus on a pairing symmetry compatible with all the experimental results. Some key experiments point towards a spin-triplet paired state but even these can be put under scrutiny. Knight shift measurements of spin susceptibility see no change though T_c when the field is in the *ab*-plane but no change is also seen when the field is along the sample's *c*-axis and this is not expected for the $\mathbf{d} = \Delta_0\hat{\mathbf{z}}(k_x \pm ik_y)$ state where the spins lie in the *ab*-plane. It was proposed that the probing field may have been strong enough to rotate the *d*-vector but several arguments against this have been laid out by Zutić and Mazin and once the NMR measurements have been put under question they point out that a spin-triplet state is not the only compatible choice but also the chiral spin-singlet $\Delta_0(\mathbf{k}) \propto (k_x + ik_y)k_z$ is equally consistent with many experimental results [129].

Much work has focused on the superconducting properties of Sr_2RuO_4 as they appear very unusual and confirmation of the usual triplet pairing state would be a worthy accomplishment in its own right but if the preferred chiral *p*-wave state is confirmed there

could also be important practical applications. A chiral *p*-wave superconductor should host quasiparticle excitations which are Majorana fermions, a quasiparticle which is also its own hole, in analogy to Majorana fermions in particle physics which are their own antiparticles. The unusual particle statistics associated with Majorana fermions offers a route to quantum computing if there are no nodes in the gap function and they are suspected to be especially well suited for low-decoherence quantum information processing [130, 131].

3.2.3 Van Hove singularities and Lifshitz transitions and their connection to Sr_2RuO_4

The density of states as a function of energy of a material is a key quantity for determining its electronic properties. The number of available states constrains the possible excitations, but when large enough, it can be a facilitator for a number of instabilities of the Fermi liquid. We saw the example of superconductivity in section 3.2.2 and later, in section 4.2.1, we will come across the Stoner criterion in relation to the instability to magnetic ordering as well as forming charge and spin density waves. With a high density of states at the Fermi level a small perturbation lowering the energy of the occupied states can contribute a significant energy saving, overcoming the competing penalties of ordering.

The density of states is the number of allowed wave vectors per unit energy at each energy of the system. Mathematically this is

$$g(\varepsilon) = \int\limits_{S(\varepsilon)} \frac{1}{4\pi^3} \frac{1}{|\nabla \varepsilon(\mathbf{k})|} dS \,, \tag{3.23}$$

where $S(\varepsilon)$ is the contour of constant energy ε, the integral is over this surface and a continuum approximation is justified. The density of states in energy depends inversely on the gradient of the band's dispersion, $|\nabla \varepsilon(\mathbf{k})|$. For a simple free electron like band this point is also easy to see using the notion of the Fermi velocity as introduced in section 1.1

$$g(\varepsilon_{\mathrm{F}})_{3D} = \frac{k_{\mathrm{F}}^2}{\pi^2 \hbar v_{\mathrm{F}}}, \qquad g(\varepsilon_{\mathrm{F}})_{2D} = \frac{k_{\mathrm{F}}}{\pi \hbar v_{\mathrm{F}}} \,. \tag{3.24}$$

In non-free electron like bands the density of states is largest at points were the dispersion is flat. These critical points can be maxima, minima or saddle points in the band structure and are called Van Hove singularities (VHs) after their first identification by Van Hove in 1953 for the case of the phonon density of states [132]. In three dimensions the singularity in the integrand is integrable, yielding a finite density of states but with a kink where the density

Fig. 3.16: **Van Hove singularities in Sr₂RuO₄.** The γ band in Sr_2RuO_4 lies very close to a saddle point Van Hove singularity. **A.** Tight binding model of the band structure at energies close to the Fermi level. The tight-binding parametrisation is from a fit to the experimentally determined band structure by Bergemann *et al.* [6] with the correct many-body renormalization from Shen *et al.* [80]. **B.** With this tight-binding description the density of states peaks at ~14 meV above the Fermi energy where the γ band changes character from electron like to hole like.
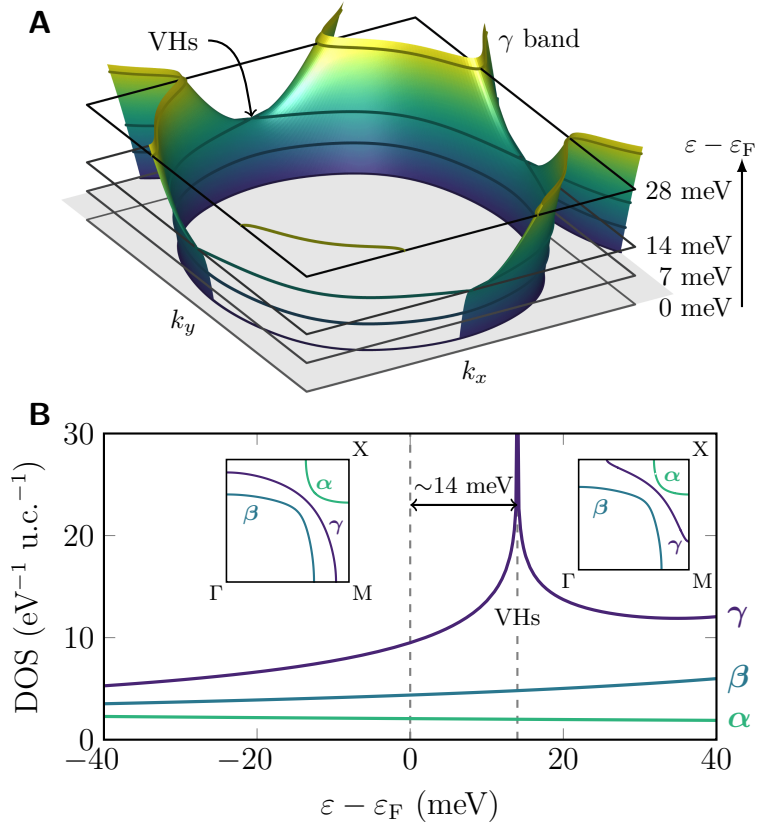
[9] When counting the number of VHs's language complications can lead to some confusion. The M points at the edge of the zone are shared with the adjacent zones so strictly speaking this means there are a total of two equivalent Van Hove points per tetragonal zone which would become two non-equivalent points if the lattice was distorted orthorhombically.

of states is not differentiable [3]. In two dimensions the density of states diverges logarithmically at a saddle point VHs.

A two dimensional tight-binding model on a square lattice, side a, with nearest and next-nearest neighbour hoppings, t and t', has saddle points at the M points of the Brillouin zone $(\pm\pi/a, 0)$ and $(0, \pm\pi/a)$ [9].

$$E(\mathbf{k}) = E_0 - 2t(cos(k_x a) + cos(k_y a)) - 4t'cos(k_x a)cos(k_y a). \quad (3.25)$$

This is the scenario for the γ band in Sr_2RuO_4, and a plot of the energy landscape for the two dimensional approximation of the γ band is shown in figure 3.16. The natural filling level of the band lies very near to the VHs and the properties of Sr_2RuO_4 are expected to be influenced by this proximity to a diverging density of states.

If the filling of the band can be raised, bringing the Fermi level to higher energy, the density of states will diverge as the Van Hove singularity is approached and the band will change character from electron like to hole like as the Van Hove singularity is passed. The Fermi surfaces before and after passing the Van Hove singularity are topologically distinct. They cannot be transformed into one

another by only continuous deformations alone, such as stretching and bending. Instead, a hole/neck must be be opened in the surface. This type of topological transition of the Fermi surface is known as a Lifshitz transition and it occurs concomitant with the Fermi level traversing a VHs [133]. Lifshitz classified two such types of transition; in a three dimensional system the collapse/join of a neck in the Fermi surface or the appearance/disappearance of a detached region of the Fermi surface, see figure 3.17.

A cornerstone for understanding classical phase transitions was the concept of symmetry. The ordering in a particular phase can be described by the symmetry properties it possesses and to change into another distinct phase at least one of the symmetries must change. Landau developed a general theory for continuous transitions between phases with different symmetries and showed that one must encounter a singularity in the free energy density at the phase transition [134]. The symmetry that is broken between the two phases describes an order parameter for the phase transition; zero in one phase and growing continuously in the other, starting from zero at the phase transition. The low energy properties of a system can also be described as the consequence of broken symmetries; well-known examples are phonons and spin waves [135].

Landau's symmetry breaking theory proved very successful and has had a profound impact on the understanding of phase transitions, but it cannot describe the type of transition identified by Lifshitz. A Lifshitz transition is not connected with any broken symmetry or associated long-range order. The distinction between the phases is rather described by their topology. The idea is that a phase transition can exist not only between states with different symmetry but also between states that have different topological order but still maintain the same symmetries. For a system of free fermions, like the free electron gas, the topological order is the topology of the Fermi surface.

A Lifshitz transition, strictly speaking, can only take place at zero temperature. Only here can the Fermi surface itself can be defined precisely. As such a Lifshitz transition cannot be connected to any finite temperature transition, however, since usually $T \ll \varepsilon_F/k_B$ the effects of such a transition can still be apparent at finite temperatures but with the singularity slightly smoothed out.

A continuous phase transition at zero temperature is a quantum phase transition. At zero temperature the energy density of the ground state plays the role of the free energy density in Landau's theory. And just as a singularity in the free energy marks a symmetry breaking phase transition, a singularity in the ground state energy density as a function of the tuning parameters of the Hamiltonian of the system, such as the chemical potential, signifies a quantum phase transition.
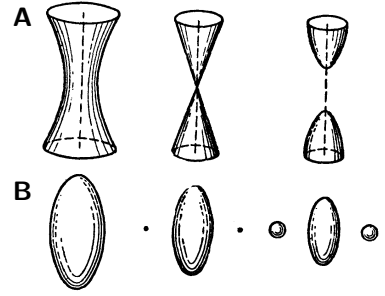
Fig. 3.17: **Lifshitz transitions. A.** The collapse of a neck in a Fermi surface. **B.** Appearance/disappearance of a new detached region of Fermi surface. Reproduced from [133].

Lifshitz transitions provide an exciting benchmark for modern physics highlighting the need for an understanding of physics beyond the paradigm of Landau's theories, both of non-symmetry breaking continuous phase transitions and the breakdown of Fermi liquid theory. They have been used to explain anomalous pressure dependencies of superconductivity in a variety of materials including, for example, thallium [136–138], rhenium [139] and niobium [140]. In each of these materials the non-linear dependence of T_c on pressure was explained due to a varying density of states due to the Fermi level crossing critical points in the band structure associated with the appearance or disappearance of new parts of the Fermi surface. Some features of the high-T$_c$ cuprate phase diagram can also be attributed to Lifshitz transitions. Benhabib *et al.* [141] could follow the closing of the unusual normal-state pseudogap state with doping on the highly overdoped side of the superconducting dome. A Lifshitz transition was argued to coincide with the closing of the pseudogap where the active hole-like Fermi surface becomes electron-like at a Van Hove singularity. In high magnetic field a change in sign of the Hall coefficient with doping was observed by LeBoeuf *et al.* [142] and is attributed to another Lifshitz transition, this time on the far underdoped side of the phase diagram. The metal-insulator crossover was argued to coincide with this transition and to be due to the emergence of an electron pocket in the Fermi surface at low temperature. The complexity of the cuprate phase diagram, however, especially once including doping, temperature, field and different material specific peculiarities, means there is not yet an accepted consensus across the whole phase diagram for the variety of competing phases present.

The Lifshitz transition in Sr$_2$RuO$_4$ can be induced by heterovalent substitution of La^{3+} for Sr^{2+} in Sr$_{2-y}$La$_y$RuO$_4$. Each lanthanum adds one extra electron, raising the filling of the Fermi level. Quantum oscillation measurements showed that the effect is a rigid band shift up to at least y=0.06, which was the limit for observing the oscillations due to the increased disorder with further substitution [143, 80]. Angle resolved photoemission spectroscopy (APRES) measurements on the substitution series show that the Lifshitz transition, where the γ band changes from electron-like to hole-like, occurs between y=0.18 and 0.27 [80].

Biaxial strain can also be used to reach the Van Hove singularity. By tuning the balance between the nearest and next-nearest neighbour hopping terms the shape of the Fermi surface can be adjusted. Reducing the relative strength of the next-nearest neighbour hopping term decreases the circularity of the γ Fermi surface and the band approaches closer to the M points of the Brillouin zone. The multiband nature of Sr$_2$RuO$_4$ also allows interorbital

Fig. 3.18: **Resistivity of Sr$_{2-y}$La$_y$RuO$_4$.** **A.** In-plane resistivity against T^2 for y=0 to 0.27. The inset shows ρ vs. $T^{1.4}$ for y=0.20, the doping closest to the Van Hove singularity. **B.** Resistivity temperature exponent, α, for a nominal temperature dependence $\rho = \rho_0 + AT^\alpha$ calculated from the logarithmic derivative of the resistivity. Reproduced from [79].

electron transfer from the d_{xz} and d_{yz} orbitals into the d_{xy} orbital changing the relative filling of the three bands. Biaxial strain is possible by growing thin films of Sr_2RuO_4 using molecular beam epitaxy (MBE) on a substrate with a mismatched lattice constant. Burganov *et al.* [81] used APRE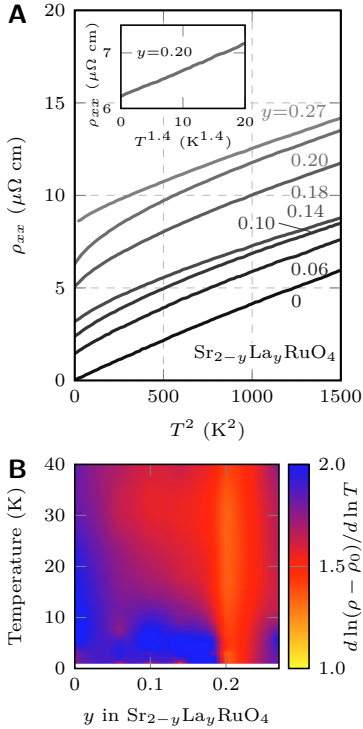S to study such films and track the approach to the Van Hove singularity. They found it was only possible to grow Sr_2RuO_4 on a substrate with a mismatched lattice constant of up to 1.0 % before the films relaxed but by exchanging Sr for Ba, a larger ion, the strain range could be increased. The Ba_2RuO_4 films were found to be isostructural and isoelectronic to Sr_2RuO_4 and the Van Hove point was reached almost exactly for Ba_2RuO_4 on $SrTiO_3$.

The tuning method at the heart of this thesis, uniaxial stress, should also be capable of inducing the Lifshitz transition. It directly affects the nearest neighbour hoppings, enhancing the hopping along the pressurised direction and suppressing it along the perpendicular direction. This decreases the bandwidth along the direction perpendicular to the pressure axis and increases it parallel to the pressure axis, thus extending the Fermi surface out towards the M points perpendicular to the direction of the applied pressure. The Lifshitz transition induced by uniaxial stress changes the Fermi surface from a closed electron-like surface to an open one as the band passes through only one of the two, now non-equivalent, pairs of Van Hove singularities at the M points of the zone. Even though these methods for reaching the Van Hove singularities are different, it is still beneficial to make comparisons between the three techniques.

Even in the presence of disorder for both the substitution series and the thin films, resistivity measurements suggest a breakdown of Fermi liquid behaviour as the Van Hove singularity is approached. Away from the Van Hove singularity, on both the high and low side, a T^2 dependence of the resistivity is observed but close to the Van Hove singularity $T^{1.4}$ behaviour is observed for both techniques (see figures 3.18 and 3.19). However, the level of disorder in both these samples is rather high, such that the impurity scattering accounts for a large proportion of the resistivity. At its most in the lanthanum series it is almost two times as large as the temperature dependent contribution even over this already quite large temperature range, and therefore any detailed analysis based on the exact temperature dependent resistivity exponent should be sceptical.

For the lanthanum substituted samples an enhancement of the linear term in the specific heat is also observed, and it peaks at the same doping as the largest deviation from Fermi liquid behaviour in the resistivity [79]. ARPES measurements on the lanthanum substituted samples show that the large mass renormalisation in Sr_2RuO_4 is mostly unaffected by the doping but biaxially strained films show a monotonically increasing mass enhancement with
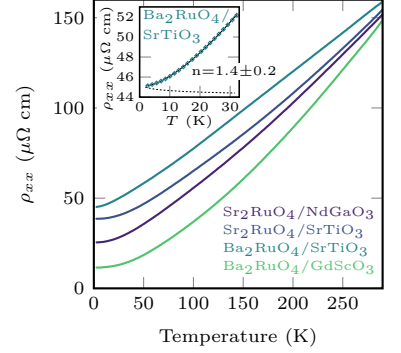
Fig. 3.19: **Resistivity of biaxial strained thin films.** Temperature dependence of resistivity for a set of Sr_2RuO_4 and Ba_2RuO_4 films. The inset shows the film closest to the Van Hove singularity with a low temperature fit to the Fermi liquid model with weak localisation scattering in 2D. Reproduced from [81].

increasing Ru-O bond distance. The difference here is chiefly due to the way the γ band is brought towards the Van Hove singularity but the key point from both measurements is that the system can be tuned to a quantum critical regime where deviations from Fermi liquid theory are observable at the topological Lifshitz transition of the γ band.

Uniaxial stress is ideally suited for continuing this study of Sr_2RuO_4 tuned to the Van Hove singularity. As stressed earlier, uniaxial stress is both a continuous tuning parameter and one that does not add additional disorder, so should add valuable insight to this intriguing problem not only of the normal state physics but also for the first time the superconducting properties.

3.3   Experimental methods

We use uniaxial stress as our method of choice for tuning electronic properties. The apparatus, and the modifications made for this work, were thoroughly described in chapter 2 of this thesis. The method for mounting a sample is also described in detail in chapter 2 so here I just refer the reader to figure 3.21 where a schematic diagram highlights the key features.

Guided by the first uniaxial strain study and band structure calculations, the Van Hove singularity is expected to be reached with a strain of 0.5–1 % applied along a [100] direction [33]. This is a very large strain, especially for something as brittle as the oxide Sr_2RuO_4. There seemed to be no chance of reaching the Van Hove singularity through tensioning the sample, as it was seen that samples break at significantly lower strains than this in tension, but we believed that with careful preparation compressive strains of this magnitude may be viable.

As was highlighted in chapter 2 precise sample preparation is key for reaching high strain. The samples used in this study, grown by Alexandra Gibbs in St. Andrews and Yoshi Maeno's group in Kyoto, were first aligned using the back-reflection Laue method, see figure 3.20, before being moved to a lapping saw to be cut to size. The samples were then finished using fine mechanical polishing to bring them to their final dimensions and produce the highest quality surfaces. This accuracy in cutting and polishing is essential in order to reach high strain. See figure 3.22 for an example of a finished sample. It was suggested that the cutting and polishing steps can introduce unwanted dislocations at the edges and that post cutting and polishing the samples should be annealed to relieve these stresses. This was carried out for one sample, annealing at 500 °C for 2 days in air, however no noticeable differences were observed.

When aiming for very high strains the sample dimensions and
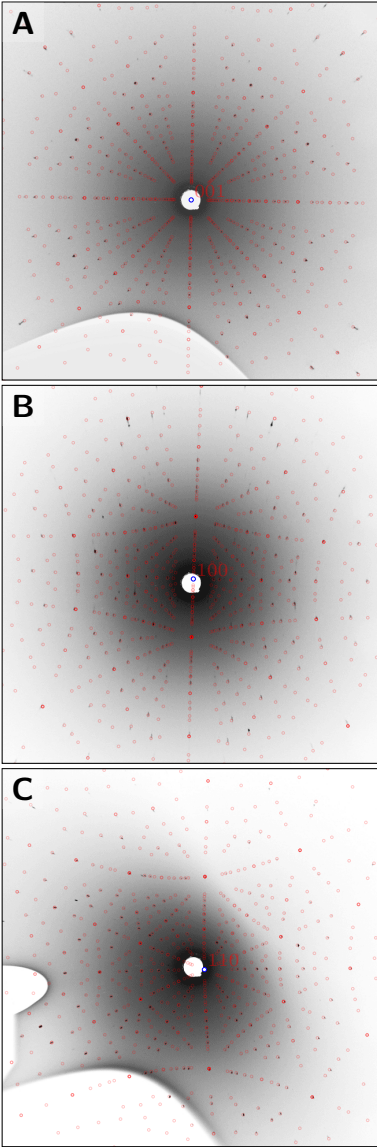
Fig. 3.20: **Sample alignment.** Pictures of X-ray back-reflection Laue diffraction patterns with simulated fits from OrientExpress [144] overlaid in red. **A** c-axis aligned with the X-ray beam, **B** a-axis and **C** the [110] direction.
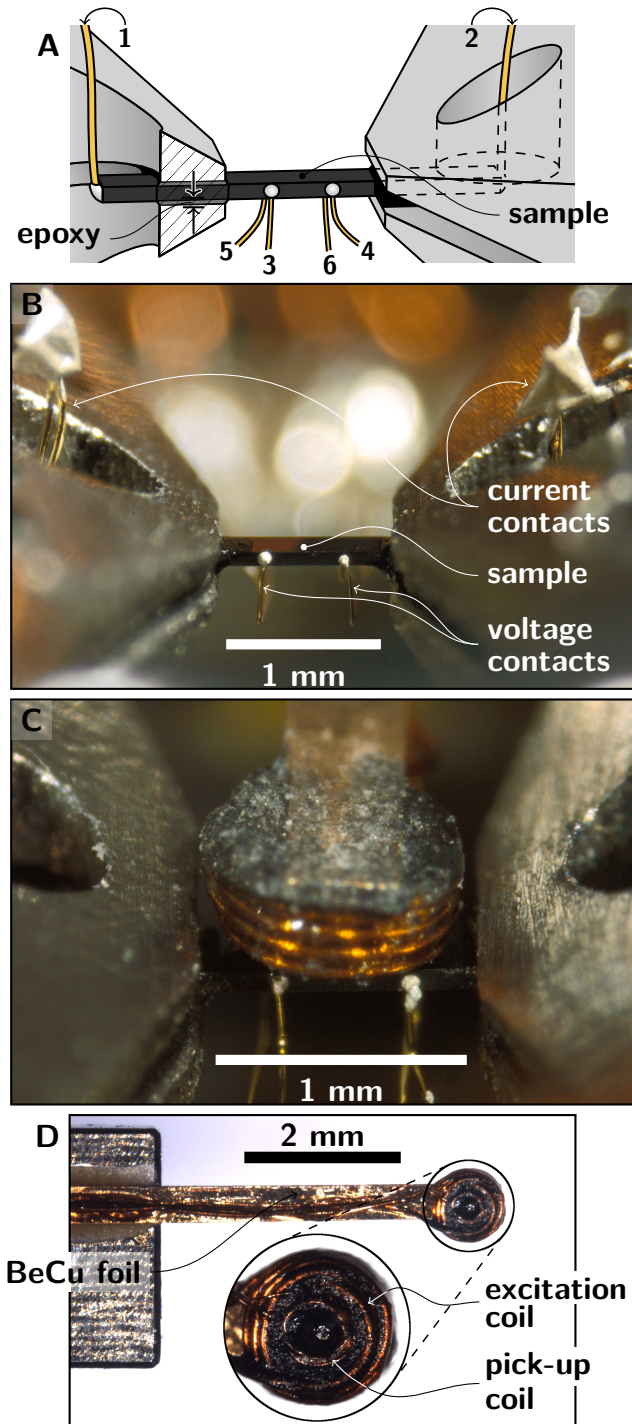
Fig. 3.21: **Mounted Sample. A.** Mounting schematic showing the epoxy holding the sample between the sample plates and the numbering of electrical contacts. **B.** Electrical resistivity setup for sample 3. **C and D.** AC magnetic susceptibility setup. Concentric coils of diameter $\sim$300 μm and $\sim$600 μm are mounted on a flexible cantilever and positioned above the sample.
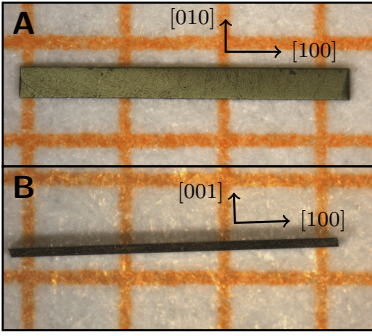
Fig. 3.22: **Cut and polished sample.** Sample 3 before attaching electrical contacts and mounting in the rig. Square millimetre paper for scale.

mounting procedure need to be carefully considered. The procedure to follow when deciding on these dimensions is laid out in section 2.6. With the aim of reaching compressive strains up to -1.5 %, the sample needed to be at least 90-100 μm thick to prevent buckling when the sample is 1 mm long, a length chosen to leave enough space for all the measurement wires and AC susceptibility coils. Stycast 2850FT was used to secure the sample to the sample plates. An epoxy thickness of 25 μm was used such that the full length of the sample plates was utilised for transmitting the strain and therefore reducing the stress concentration at the edges of the sample plates as much as possible.

The main aim of this investigation was to observe what effect passing though the Van Hove singularity has on the resistivity, but since the resistive signature of superconductivity can be unreliable in Sr_2RuO_4, due to percolating paths that appear to be especially present in strained samples shorting out the contacts, I also measured the magnetic response of superconductivity. With careful planning both measurements can be incorporated into the strain rig simultaneously.

AC magnetic susceptibility was used to detect the superconducting T_c. Two concentric coils were wound and mounted on a flexible cantilever so they could be positioned exactly above the centre of the sample, see figure 3.21 panels C and D. The larger of the two coils, used for the driving field, was made from superconducting NbTi wire to introduce minimal heating and had a diameter of $\sim$600 μm. Fixed within this coil was the pick-up coil, made from 15 μm diameter copper wire, with a diameter of $\sim$300 μm. By measuring the mutual inductance between these two coils the sample's magnetic susceptibility can be determined. There is no counter-wound compensation coil here and the uncertainty in the exact geometry means that this technique is only sensitive to relative changes in susceptibility and cannot easily be calibrated. The large offset voltage present is not a problem for measurement when a lock-in amplifier with a high enough resolution is used. Depending on the dynamic reserve in use, something with a 16 bit or higher analog-to-digital converter is desirable. The superconducting transitions are then resolvable without noticeable quantization noise. The standard method for low noise AC susceptibility measurements is to use an impedance matching transformer mounted at low temperatures. Unfortunately the cryostat used for this study cannot incorporate such low temperature transformers so all amplification had to be carried out at room temperature. When using an AC driving current, amplitude I, the measured voltage across the pick-up coil is $V = 2\pi M f I$ with a 90 degree phase lag. M is the mutual inductance between the two coils and f is the AC driving frequency. When the frequency dependence of the measurements

is not significant, running at higher frequencies can increase the signal-to-noise ratio back to what is possible with the best low temperature transformers which are themselves frequency limited. The typical excitation field was $\sim$0.2 Oe RMS, mostly parallel to the sample's c-axis, at a frequency between 1 kHz-10 kHz.

To measure the resistivity six electrical contacts where made to the sample. The standard procedure for Sr_2RuO_4 is to use high temperature curing silver loaded epoxy 6838 from DuPont which produces reliably low resistance contacts. Six 25 μm diameter gold wires were joined to the sample with the silver epoxy before curing at 450 °C for 5 minutes. All contacts were verified <0.3 Ω. All the wires are added to the sample before it is mounted in the rig because the device cannot be heated above 150 °C. Once the sample was loaded into the rig the other end of the gold wires were soldered to bonding pads on the device.

The restrictions put on the sample's geometry from the buckling limit and the strain homogeneity are particularly unfavourable for resistivity measurements. The sample has to be quite thick and the contacts must be placed close together in the homogeneously strained region. This is the exact opposite of the normal procedure for high-sensitivity resistivity measurements. The resistivity of Sr_2RuO_4 is also very highly anisotropic, $\rho_{0,c}/\rho_{0,ab} \sim 4000$, so meticulous care must be taken when placing the contacts. Any asymmetry in the current contacts leads to inhomogeneous current flow with a component along the sample's c-axis, and this becomes much easier to inadvertently include as the samples get thicker. The scale of this problem is best pictured in a simple geometrical representation. For an equivalent sample with isotropic resistivity to possess the same value of c-axis resistance, its thickness along the c-axis needs to be bigger by the square root of the resistive anisotropy, $\sim\sqrt{4000}$. A homogeneous current is only achieved if the contacts inject current uniformly over the entire end faces of the sample and the challenge in achieving this is clearly apparent in the geometrical representation where the sample is now notably thicker than its own length. For isotropic samples typically one just places the voltage contacts a distance greater than one width from the end of the sample and any inhomogeneity in the current distribution is ignored. The inclusion of a c-axis component to the measurement is easy to identify in Sr_2RuO_4. The overall magnitude of the measured voltage will be too large and in addition the temperature profiles for the in-plane and c-axis resistivity are quite different, noticeably there is a turn over in the c-axis resistivity around 100 K. For the first sample measured in this study this feature was observed so only the susceptibility data is analysed for sample 1.

The resistivity measurements are further complicated by the extremely high quality of the samples. The samples used in this

study had residual-resistivity ratios up to 1200, a low temperature resistivity of ∼0.1 $\mu\Omega$cm. Once a thicker sample is used and the contacts are placed close together in the middle, the voltage signal is significantly reduced. In fact the effect is so drastic that it puts the measurement outside the capabilities of most standard measurement systems. A typical single-ended current source combined with a modern high performance preamplifier and lock-in amplifier can only provide 100 dB of common mode rejection. If the end of the sample could be held only 1 Ω from ground a CMRR of at least 120 dB is still required to bring the common mode signal down to 10 % of the real signal and in a real cryostat with long wires coming out to room temperature the resistance to ground is typically in the range 20-50 Ω. Here the signal from the common mode that is added by the preamplifiers alone is ∼20-50 times larger than the signal from the sample.

To overcome these limitations I designed and built a custom dual end current source with active common mode rejection. This is capable of keeping the common mode signal to less than ∼0.5 % compared to the signal from the residual resistivity alone. Details of the design can be found in appendix A.

Noise was always going to be an important consideration for these measurements of a highly conducting sample with an unfavourable geometry. As for the susceptibility measurements the use of low temperature transformers was excluded because none could be mounted in the cryostat used for the measurements. Normally the next best choice for amplification is a room temperature transformer, but the cryostat presents a relatively large source impedance due to beryllium-copper wiring and this influences the gain of the transformer as well as the noise. Instead, active preamplifiers were used and once combined with a lock-in amplifier noise levels slightly better than 2 nV/$\sqrt{\text{Hz}}$ at the input to the preamp could be achieved, a corresponding RMS noise of ∼0.7 nV with a 1 s 12 dB/octave phase sensitive detector. At its worst the corresponding signal-to-noise ratio was slightly better than 20, and therefore still adequate for these measurements.

In total three samples were measured during this study, each from a different crystal growth. The first sample suffered from inhomogeneous current flow, as mentioned above, so only the susceptibility data are presented.

For the second sample, in addition to the regular longitudinal resistivity measurement, I measured the transverse resistivity. Making reference to figure 3.21, if instead of passing the current along the bar between contacts 1 and 2 and current is passed between contacts 3 and 5, a qualitative measure of the transverse resistivity can be obtained from the voltage across contacts 4 and 6. This is only a qualitative measure of the transverse resistivity since it is

Table 3.1: **Sample dimensions.** Relevant parameters for calculating the strain transmission to the sample through the epoxy. The strain of the peak in T_c for each sample is also listed.

number	growth	w (μm)	t (μm)	L_{gap} (μm)	d_{epoxy} (μm)	transmission (%)	$\varepsilon_{xx,peak}$ (%)
1	WDO3	295	100	1000	≈25	70	-0.50
2	A1	310	100	1000	≈25	70	-0.59
3	C362	320	90	1100	≈25	73	-0.56

not independent of the longitudinal resistivity which determines the spreading out of the current stream lines across the sample. The voltage measured between contacts 4 and 6 decreases exponentially as the contact separation, 3 to 4, increases. Placing the contacts closer together is therefore better for the transverse measurement, but the longitudinal measurement signal decreases linearly if this is done so a balance between the two must be picked. I chose to use a separation of 300 μm, biasing the measurement towards the longitudinal response since optimising the signal-to-noise ratio for the longitudinal resistivity measurement was my main priority. Double wiring was used for all contacts, providing twisted pairs for both the longitudinal and transverse geometries. This also facilitates the simultaneous measurement of magnetresistance and Hall effect in magnetic field. A computer controlled switch was installed and programmed to automatically change between all three measurement geometries during operation allowing for almost simultaneous measurements of longitudinal and transverse resistance as well as Hall effect in the presence of an external magnetic field.

For the third sample the contacts were placed further apart at 500 μm and the sample was made 100 μm longer to keep the contacts one width from the ends. This was to achieve still cleaner measurements of the longitudinal resistivity and the transverse measurements were not attempted. The same wiring was however still used so that the Hall effect could also be measured.

The strain device used for this study uses a parallel plate capacitor to monitor the applied strain. From the capacitance we can determine the applied displacement to the sample plates but two further pieces of information are required to convert this to a strain. The first is the zero position of the scale. Even if in principle the sample is mounted at zero strain at room temperature the corresponding capacitance value will not be that of zero strain at cryogenic temperatures because there will nearly always be a differential thermal contraction between the sample and the titanium device (see section 2.5). A separate determination of the zero strain position is required. This can typically be identified from a feature that is symmetric with applied strain or a quantity that is isotropic at zero strain but not at finite strain. For Sr_2RuO_4 we

can use the fact that T_c is highly symmetric with applied strain to identify a zero position of the sensor.

The second piece of information is the strained length of the sample. Dividing the measured displacement by this length gives the sample strain. As described in chapter 2 the strained length of the sample is not the same as the gap between the sample plates, as the soft epoxy holding the sample to the plates also deforms. I used finite element simulations to estimate the magnitude of the displacement lost in the epoxy. However due to uncertainties in the elastic properties of the epoxy all quoted strains have an uncertainty of $\sim$20 % (a systematic error affecting all measured strains equally). Table 3.1 lists all the sample dimensions necessary for implementing these finite element simulations and the calculated strain transmission values. The elastic properties of Sr_2RuO_4 were taken from Paglione *et al.* [68] and the epoxy was assumed to have a Young's modulus of 15 GPa and Poisson's ratio of 0.3.

All measurements were carried out with the sample in vacuum, thermally anchored to a 1 K pot. By pumping on a small pot of liquid helium evaporative cooling reduces the temperature of the liquid helium below its atmospheric pressure boiling point of 4.2 K. A small flow is allowed between the main helium reservoir and the 1 K pot to continuously replenish the helium pumped away and a stable base temperature of 1.2 K can be reached. By using resistive heaters to work against the cooling power of the 1 K pot the temperature of the cryostat can then be varied. With this system it is possible to operate up to almost 100 K. At the higher temperatures there is obviously no longer liquid helium in the 1 K pot but it just acts as a heat exchanger with the helium gas flowing though. One notable design feature of the cryostat is the large internal space, a diameter of 75 mm. This was useful for incorporating large strain rigs. The cryostat sits within a large bore superconducting magnet producing fields up to $\pm$6 T. Figure 3.23 shows the inside of the vacuum can. This cryostat was used for the majority of the measurements but in addition to installing this cryostat and the accompanying measurement rack I also set up a second cryostat with an adiabatic demagnetisation cooling stage and this was used for the initial characterisation of the samples before cutting using AC susceptibility.

In our laboratory the type of measurements and the measurement protocols change quite frequently so I programmed a computer control system that could straightforwardly accommodate these changes with no hindrance to flexibility. This flexibility also allows the software to be employed for different cryostats straightforwardly and is currently running on at least four cryostats. The software suite uses a modular structure to accomplish this goal. There are three main parts. First each instrument requires its own class file

**4 K
IVC
flange**

**1 K
Pot**
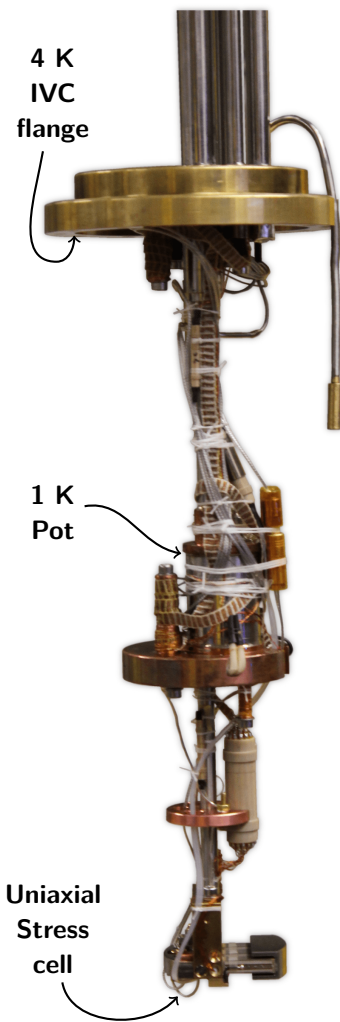
**Uniaxial
Stress
cell**

Fig. 3.23: **Low temperature cryostat.** Business end of a 1 K pot sample in vacuum cryostat. This cryostat has a large 75 mm internal diameter to accommodate large uniaxial stress cells.

which acts as an interpreter between the instrument and the core codebase. Mnemonics can also be used here to help recall common message strings for each instrument. Secondly a set of functions implementing common routines such as PID control, data recording and live plotting are implemented and these make for easy control of the temperature, magnetic field, sample strain, etc. Lastly all the parts of the suite are linked together through a graphical user interface (GUI). The GUI allows a user to take immediate control of the cryostat or program measurement scripts which can be scheduled as the user requires, enabling easy continuous operation. The flexibility remains in the scripting language as well, because the full programming syntax of Matlab is at the users disposal; for and while loops, if and else statements, local variable creation, etc. This allows for both quick and simple measurement scripts but also scripts as complex as can be imagined. New features can easily be added without having to modify any existing parts of the program. For instance a new instrument only needs its own class file and none of the existing code needs to be modified to begin using the instrument and recording data.

The software allows for automatic control of the experiment for several days at a time, with measurement only needing to be interrupted to keep the level of liquid helium in the main bath topped up. Data analysis scripts can also be run from within the GUI on the measured data and given a set of rules, there is nothing in principle preventing the computer from making a measurement, running the data analysis script, and then determining the next step of the measurement from the result. This type of procedure could be used, for instance, to locate the peak in T_c with strain without requiring any human interaction.

3.4   Results and discussions

The results for Sr_2RuO_4 under uniaxial stress will be presented in two parts. First I will describe the effect of uniaxial stress on the superconductivity, presenting measurements of magnetic susceptibility and showing the dependence of T_c on strain and the upper critical field at strain. Then a second part will be dedicated to the normal state properties under strain, focusing on the resistivity, magnetoresistance and Hall effect measurements.

3.4.1   Superconducting properties under strain

3.4.1.1   Change in T_c with strain

Figure 3.24 shows AC susceptibility measurements against temperature at a series of compressive strains. When the sample is subject to either uniaxial compression or tension the superconduct-
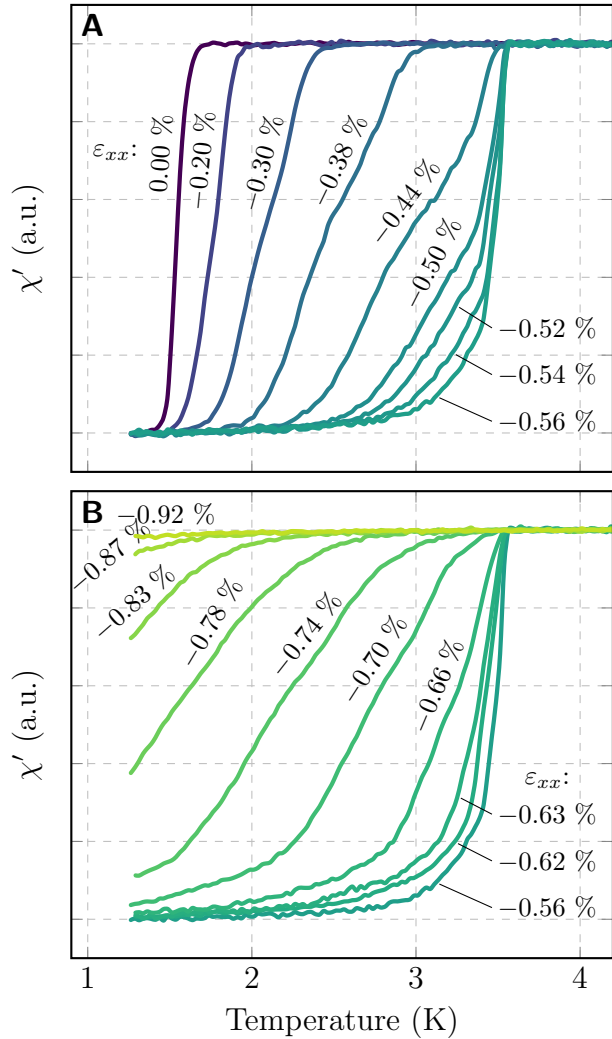
Fig. 3.24: **Susceptibility against temperature.** Real part of the susceptibility χ for sample 3 against temperature. **A** Strains below the peak T_c, **B** above the peak. No normalisation or offsets are applied to the curves.

ing transition temperature is enhanced, corroborating the results of Hicks *et al.* [33]. As can be seen from the figure the transitions become somewhat broader as the transition temperature moves to higher temperature with increasing strain. The amount and shape of this broadening varies from sample to sample, see figures B.1 and B.2 in appendix B for comparison, so it is likely this effect is extrinsic and is most probably due to differing strain homogeneity. As described in detail in section 2.5, imperfections in mounting can cause the sample to bend, imposing a strain gradient across the thickness of the sample when it is strained. The presence of dislocations or ruthenium inclusions in Sr_2RuO_4 could also present some local strain disorder producing variations between samples. However it is clearly apparent that the transition temperature reaches a maximum with applied strain and that as the maximum T_c is approached the transitions become very sharp. The maxi-
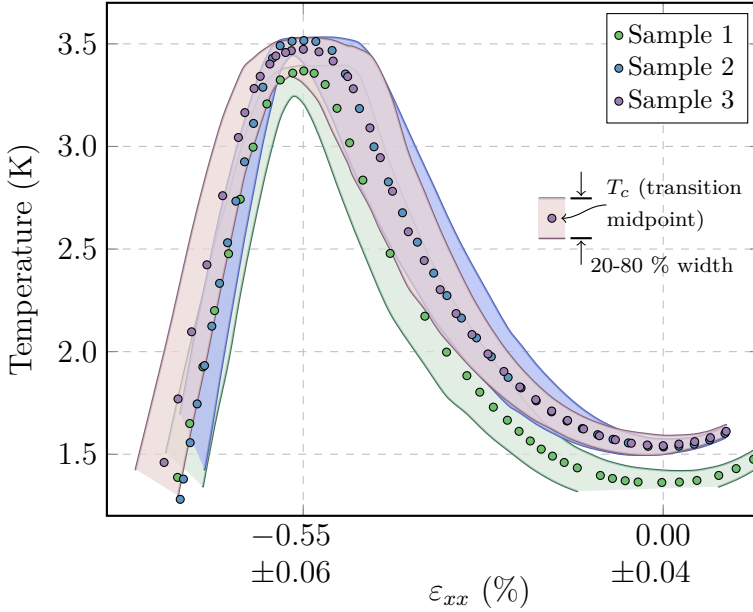
Fig. 3.25: T_c **against strain for all three samples.** The points are the mid points (50% levels) of the transitions shown in figures B.1, B.2 and 3.24. The 20 and 80% levels of the transitions are shown as lines to give a measure of the transition width. Here the strain scales have been normalised so the peaks in T_c coincide at their average value of (-0.55 ± 0.06) %.

mum T_c is enhanced by a factor of $\sim$2.3 over the unstrained value. Compressing beyond this maximum causes a rapid suppression of T_c, causing it to fall below even its zero strain value, and the transitions broaden substantially once more. For broadening as the result of strain inhomogeneity the width of a particular transition at strain should be related to the slope of the T_c vs. strain curve at that strain. Qualitatively this is in agreement with the observed broadening, suggesting the dominant cause of the broadening is indeed strain inhomogeneity.

The response to applied strain was fully elastic. In fact the curves in figure 3.24 are not from one single sequence with increasing strain but rather are only a small subset of the total number of measurements where the strain was cycled four times over the maximum and back to zero, measuring both while increasing and releasing the strain, and each time reproducing the same results. This is in contrast to measurements by Taniguchi *et al.* [145] where there is strong evidence for plastic deformation in samples pressurised at room temperature in traditional uniaxial pressure cells. Dislocations are known to induce local higher-T_c superconductivity [146] so by applying strain at low temperatures we reduced the risk of plastic deformation. The stringent requirements on sample preparation for traditional uniaxial pressure cells, as de-
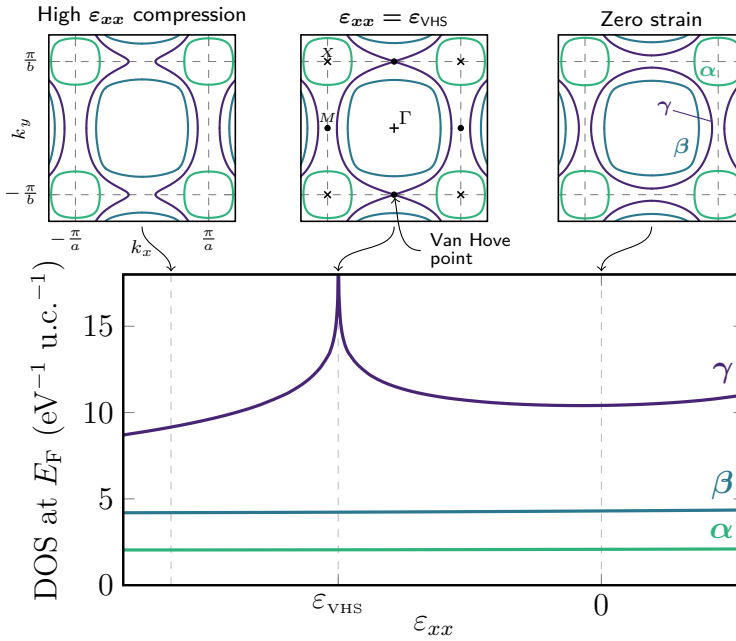
Fig. 3.26: **Density of states and Fermi surface calculations.** The density of states at the Fermi energy as a function of applied anisotropic strain as calculated from a tight-binding model including strain dependent hopping terms, see main text for details. Three representative Fermi surfaces show the effects of applied strain on the band structure and highlight the Lifshitz transition as the γ-band reaches the Van Hove point.

scribed in section 2.4, may also be playing a role in the Taniguchi measurements.

The nominal strain at which the peak in T_c was observed varied slightly between the three samples, see table 3.1, but within our uncertainty in determining the strain scale. The profile of T_c against strain for all three samples is plotted in figure 3.25. Here the strain scales have been normalised so that the peaks in T_c all coincide at their average value of $\varepsilon_{xx}=(-0.55\pm0.06)$ %.

The combined strain data from these three new strained samples of Sr_2RuO_4, and from measurements on $Sr_3Ru_2O_7$ presented in the next chapter, suggest that the strains determined by Hicks *et al.* in Ref. [33] are ∼30 % too low. This is most probably due to the technique used to measure the strain. In Ref. [33] a resistive strain gauge was used to monitor the displacement of the device but it now seems likely that this may have imposed some mechanical resistance on the motion of the device. Additionally, a temperature dependence of the gauge coefficient could have skewed results. The capacitive sensor used in this new strain rig is less affected by temperature and imposes no mechanical resistance so more confidence can be placed in the results presented here.

Band structure calculations show that anisotropic strain will

drive the γ-band towards the Van Hove singularity and increase the density of states at the Fermi level. This can also be seen in a simple tight-binding model which incorporates the effects of anisotropic strain through strain dependent hopping parameters. To first approximation at low strains the hopping parameters can be taken to change linearly with applied strain. Using the tight-binding parametrisation by Bergemann *et al.* [6] from fits to the experimentally determined band structure and the correct band renormalization from Shen *et al.* [80] as a starting point, the effects of anisotropic strain can be included by scaling all hoppings along the pressurised direction by $(1 - \alpha \varepsilon_{xx})$ and along the transverse direction by $(1 + \alpha \nu_{xy} \varepsilon_{xx})$. ν_{xy} is the in-plane Poisson's ratio which has been experimentally determined by Paglione *et al.* [68] and α is an adjustable parameter to scale the effect of applied strain. In this model the chemical potential must also be adjusted slightly with strain to keep the total electron count constant. A plot of the density of states at the Fermi level against strain in this model is shown in figure 3.26 along with the Fermi surfaces predicted as the γ-band reaches the Van Hove point and at a much higher strain beyond the Van Hove point. The density of states diverges for the γ-band as the Van Hove singularity is approached and the band changes character from a closed electron pocket to an open orbit running along k_y in the Brillouin zone at the Lifshitz transition.

In BCS theory the BCS gap, $|\Delta|$, grows with increasing density of states at the Fermi level. T_c is related to the size of the BCS gap and in a material with a k-dependent gap it is proportional to the k-space average of $|\Delta(\mathbf{k})|$. The experimental observation of an enhanced T_c is therefore qualitatively expected as the density of states grows with applied strain. However, for the widely favoured p-wave pairing symmetry the gap must change phase by π under inversion. This leads to frustration as the γ-band approaches the Van Hove point which is inversion invariant, and therefore the gap must locally be zero at the Van Hove point. In contrast, an even-parity pairing symmetry is not subject to the same frustration constraints and one might expect a stronger enhancement of T_c for an even-parity state as the density of states is increased by the Van Hove point.[10]

Bearing this in mind, the peak in T_c may be a result of the peaking density of states and coincide with the Lifshitz transition or frustration may take over before the Van Hove singularity is reached and the enhancement could be cut off at a lower strain. Weak-coupling calculations by T. Scaffidi [147] on a similar tight-binding parametrisation of the strained Fermi surface suggest that, even in the presence of this frustration, odd-parity order is still enhanced and T_c peaks as the Van Hove singularity is surpassed. The slow fluctuations associated with the proximity of the γ-band to the Van

[10] BCS estimates are expected to be accurate for a single band metal with a small gap but in a multiband system like Sr_2RuO_4 these estimates refer only to the average gap which can already be a big approximation when, like in Sr_2RuO_4, there are large changes around the Fermi surface. This analysis also completely overlooks the potential for interband coupling, so it should only be taken as a guide.

Hove singularity are seen to contribute to superconductivity on the α and β bands through inter-orbital interaction terms. Further evidence supporting the coincidence of the peak in T_c and the Van Hove singularity comes from normal state resistivity measurements which will be presented in the next part of this section. One other alternative proposed by Liu *et al.* [148] is competition with a spin density wave state that is predicted to be stabilized with compressive strain, and whose formation cuts off the increase in T_c. However, the transport data in the next section seems to be inconsistent with this and together with the resistivity results about to be presented it seems most likely that the peak in T_c does coincide with the Van Hove singularity.

3.4.1.2 Upper critical field at the peak in T_c

Valuable information on the density of states related effects on the superconductivity can also be extracted from the upper critical field. For all my measurements the sample was aligned with its *c*-axis parallel to the applied field direction, mainly to facilitate transverse magnetoresistance and Hall effect measurements, but I also measured $H_{c2\|c}(T)$. Following the suppression of T_c with applied magnetic field is quite easy for optimally strained Sr_2RuO_4. Since the transitions are so sharp, the clear kink can be identified as the onset temperature, see figures 3.27 and B.3. Figure 3.28 shows the curve $H_{c2\|c}(T)$ for Sr_2RuO_4 strained to its peak T_c. There is a clear upward curvature of $H_{c2\|c}(T)$, with a slope $|dH_{c2\|c}/dT|$ increasing down to the lowest temperatures measured. This is in contrast to a typical BCS type superconductor where a downward curvature is expected but similar behaviour has been observed in other materials which have multicomponent order parameters with significantly different gap magnitudes on different parts of

Fig. 3.27: **Susceptibility measured at the peak in T_c at various applied fields $H \parallel c$.** Real part of the susceptibility χ measured as the temperature is swept up and down for sample 1. The y axis is the mutual inductance between the two coils of the susceptibility sensor. The field was incremented at the bottom of each temperature ramp, in the superconducting phase. This disrupts the vortex lattice and is responsible for the apparent hysteresis.
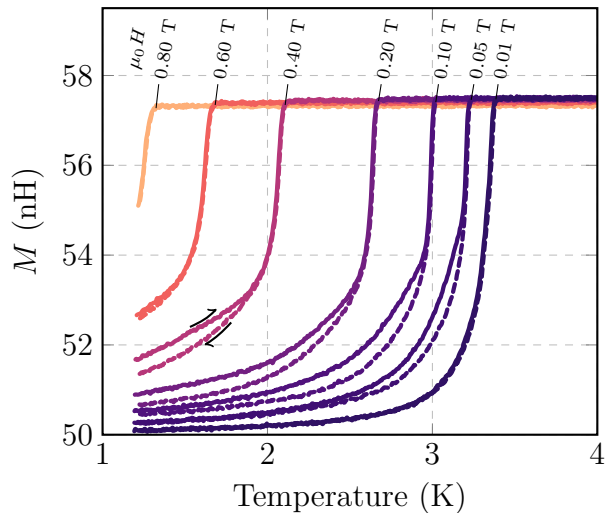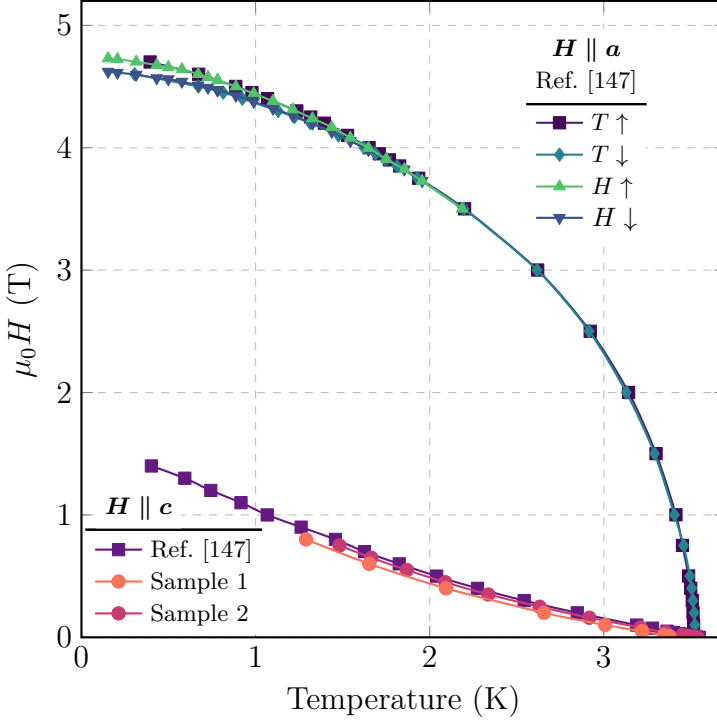
Fig. 3.28: H_{c2} **against temperature at the peak in T_c.** $H_{c2\parallel c}$ against temperature for samples 1 and 2 compressed to the peak in T_c together with $H_{c2\parallel a}$ at the peak in T_c with compressive strain applied along a measured by A. Steppke [147].

the Fermi surfaces [149, 150]. For reference the critical field of unstrained Sr_2RuO_4 is shown in figure 3.29 and there is very little to no upward curvature.

For an orbitally limited type-II superconductor, the field that completely fills the sample with vortices and destroys superconductivity depends on the coherence length, $H_{c2} = \Phi_0/2\pi\xi^2$. From BCS theory we know that the coherence length is proportional to the ratio of the Fermi velocity and the magnitude of the superconducting gap; $\xi = \hbar v_F/\pi\Delta$. Relating v_F to the density of states using equation 3.24 it can be seen that the upper critical field depends on the product of the density of states and the gap magnitude squared $(|\Delta|g(E_F))^2$, averaged around the Fermi surface. T_c, on the other hand, is proportional to the average of the gap. Therefore if H_{c2} increases more than linearly with T_c^2 this amounts to further evidence for the importance of the diverging density of states for the superconductivity and that the regions of Fermi surface where the density of states is large must coincide more with the regions where the gap also has a large magnitude.

From figure 3.28, extrapolating $H_{c2\parallel c}(T)$ to zero temperature shows that $H_{c2\parallel c}$ is enhanced by more than a factor of twenty relative to its unstrained value of $\sim$0.07 T. T_c itself is only enhanced by a factor of $\sim$2.3 so $H_{c2\parallel c}$ increases significantly more than linearly with T_c^2. In fact $H_{c2\parallel c}/T_c^2$ is enhanced by a almost a factor four. The shape of the critical field line $H_{c2\parallel c}(T)$ is quite different between
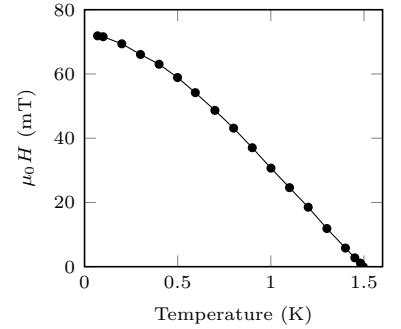
Fig. 3.29: **c-axis critical field of unstrained Sr_2RuO_4.** Reproduced from [151].

unstrained and strained Sr_2RuO_4 so in case different field limiting mechanisms are playing a role another check is to compare the initial slopes $dH_{c2\|c}/dT$ right at T_c. Extrapolating this slope to zero temperature for unstrained Sr_2RuO_4 yields a field of $\sim$0.09 T and for optimally strained Sr_2RuO_4 a field of $\sim$1.0 T. Even using this criterion the critical field is enhanced over T_c^2 by a factor of 2.

It seems then, by either method of comparison, that the locally diverging density of states, which is restricted to the M point of the Brillouin zone, is helping to boost the upper critical field. But for a odd-parity superconducting state, where the gap must go to zero at the M point of the zone, this statement seems contradictory and opens the question of whether optimally strained Sr_2RuO_4 could be even-parity.

For an orbitally limited superconductor, an increase in the zero temperature critical field by a factor of twenty implies a decrease in the coherence length by a factor of $\sqrt{20}$. Sr_2RuO_4 is such a disorder sensitive superconductor that this should have implications on the Abrikosov-Gor'kov disorder-induced pair breaking at optimal strain. We observe that quantitatively these predictions do agree within experimental error. The T_c of the slightly disordered sample 1 is 0.18 K lower than that of sample 3 at zero strain. At the optimal strain, where the coherence length is shorter and the sensitivity to disorder is accordingly reduced, the two T_c's should come closer together, which indeed they do; sample 1 has a T_c lower than sample 3 by only 0.11 K.

Concurrently with my critical field measurements, another group member, A. Steppke, was working on additionally measuring the in-plane critical field at strain. By using a dilution fridge mounted in a three axis vector magnet the in-plane direction could be accurately found and the critical field followed to the lowest temperatures. Steppke's data for the in-plane field direction additionally support the possibility of an even-parity state in strained Sr_2RuO_4 so I will discuss them briefly here.

Figure 3.28 also includes the data of $H_{c2\|a}(T)$. The in-plane critical field is also larger in optimally strained Sr_2RuO_4, but rather unusually, the enhancement is not as substantial as for the out of plane direction. The $H_{c2\|a}$ critical field is only enhanced by a factor of $\sim$3, from 1.5 T to 4.7 T. The critical field in optimally strained Sr_2RuO_4 is therefore significantly less anisotropic than in unstrained Sr_2RuO_4. $\Gamma = H_{c2\|c}/H_{c2\|a} \approx 20$ in unstrained Sr_2RuO_4 is reduced to $\sim$3 in optimally strained Sr_2RuO_4. This reduction in anisotropy is difficult to reconcile with only orbital limiting effects due to a reduction of the mass anisotropy. DFT calculations show there is still a strong 2D character to the band structure under strain [147] and the initial slope of H_{c2} at T_c, dH_{c2}/dT, does still show a much stronger deviation between the

in-plane and out-of-place field directions compared to the zero temperature values.

The first order nature of the transition, present in unstrained samples at low temperatures, is also seen in optimally strained Sr_2RuO_4, and persists to higher temperatures. The mechanism responsible for this change to a first order transition must therefore be promoted in optimally strained Sr_2RuO_4, allowing it to take over at higher energy scales. The observed change to first order suggests Pauli limiting effects. Quantitatively the measured in-plane critical field enhancements also agree with Pauli limiting. Both the Pauli limited critical field and T_c should scale linearly with the gap magnitude. So in unstrained Sr_2RuO_4 where $H_{c2\|a}/T_c \approx 1$ T/K, a value of $H_{c2\|a}/T_c \approx 1.3$ T/K in optimally strained Sr_2RuO_4 is consistent with a Pauli limited critical field.

In a perfectly 2D odd-parity superconductor with a *d*-vector along the *c*-axis the in-plane critical field should be infinite. So after taking all these observations together there is a strong case for the possibility that optimally strained Sr_2RuO_4 could be even-parity. This possibility is further discussed in Steppke *et al.* [147] where the authors use weak-coupling calculations to compare different gap symmetries and determine the expected T_c and $H_{c2\|c}$ variations with strain. The calculations indicated that a strong enhancement of H_{c2}/T_c^2 is indeed expected for an even-parity state strained to the Van Hove singularity but the same enhancement is not observed for an odd-parity state where the density of states increases most strongly at points where the gap is held at zero by symmetry.

Additional limiting mechanisms could also be responsible for the unusual critical fields. Ramires *et al.* [152, 153] have proposed that interorbital effects in the presence of strong spin orbit coupling can in principle lead to limiting of the in-plane critical field, which might reconcile the observed critical fields with an odd-parity state. However, the magnitude of the proposed effect still needs to be investigated by microscopic calculations, and it still does not help to explain the contradiction of the density of states diverging where the gap must be zero by symmetry but somehow still producing a substantial enhancement of the *c*-axis critical field.

This new strain study may also shed some light on the peculiar '3 K phase' found in eutectic crystals containing embedded ruthenium microdomains [154]. The 3 K phase is spatially non-uniform superconductivity that onsets at around 3 K near the interface between bulk Sr_2RuO_4 and ruthenium inclusions [155–157]. The similarities of the observed T_c's (a maximum of 3.5 K is also seen in the eutectic crystals [156]), the fact that that transitions are always very broad, and that the critical fields of the 3-K phase are similar to those shown in figure 3.28 [155] suggest it may well be the result of local internal strain around the inclusions. However,

direct observation of the strain field around the inclusions would be needed to fully confirm this hypothesis.

To summarise, a strong enhancement of the T_c of Sr_2RuO_4 is observed with compressive strain and T_c peaks at close to half a percent strain before falling off again rapidly. The maximum T_c is enhanced by factor of $\sim$2.3 and the c-axis critical field by more than a factor of twenty. The substantially larger enhancement of $H_{c2\|c}$ than of T_c^2 signifies the importance of the density of states change at the Van Hove singularity for the superconductivity. An odd-parity superconductor must have a parametrically small gap in the vicinity of the Van Hove point so this raises the possibility that optimally strained Sr_2RuO_4 might be even-parity. In the optimally strained sample a reduced critical field anisotropy further evidences this possibility, because Pauli limiting is a natural mechanism to explain the lower than expected in-plane critical field. However, multiband effects may mean that this analysis is too naive, and still allow the observations to be reconciled with an odd parity state.

If a even-parity state is indeed realised in optimally strained Sr_2RuO_4 two possibilities for the connection to the superconductivity of unstrained Sr_2RuO_4 exist. Either the evolution is continuous with strain and unstrained Sr_2RuO_4 is also even-parity, in which case a significant accumulation of results acquired in over twenty years of experimental study will require an alternative explanation, or there may be a transition at intermediate strain between the odd- and even-parity states. If this is the case a kink should exist in T_c vs. strain at the transition, however this may possibly be weak, and a similar kink or even a jump in $H_{c2\|c}$ should also be present. Investigating this should be a priority for future work, although strain inhomogeneity remains as an important complication for analysing data at intermediate values of T_c.

3.4.2   Normal state properties under strain

3.4.2.1   Resistivity temperature dependence

In figure 3.30 I show the principal normal state measurement results; a set of resistivity measurements over long temperature ramps from $\sim$1.3 K to 40 K at a series of applied strains. These measurements were repeated in two samples and are consistent with each other, see figure B.4 for the results from the second sample. Figures 3.31 and 3.32 represent the same data in alternative forms to help visualise the changes. In figure 3.31 a 3D surface map of the resistivity against strain and temperature is made by interpolating between all the measured temperature ramps. Figure 3.32 is a surface map of the elastoresistance, $(\rho_{xx}(\varepsilon_{xx}, T) - \rho_{xx}(0, T))/\rho_{xx}(0, T)$, made by subtracting the measurement at zero strain from all the others and then interpolating between each of the curves.
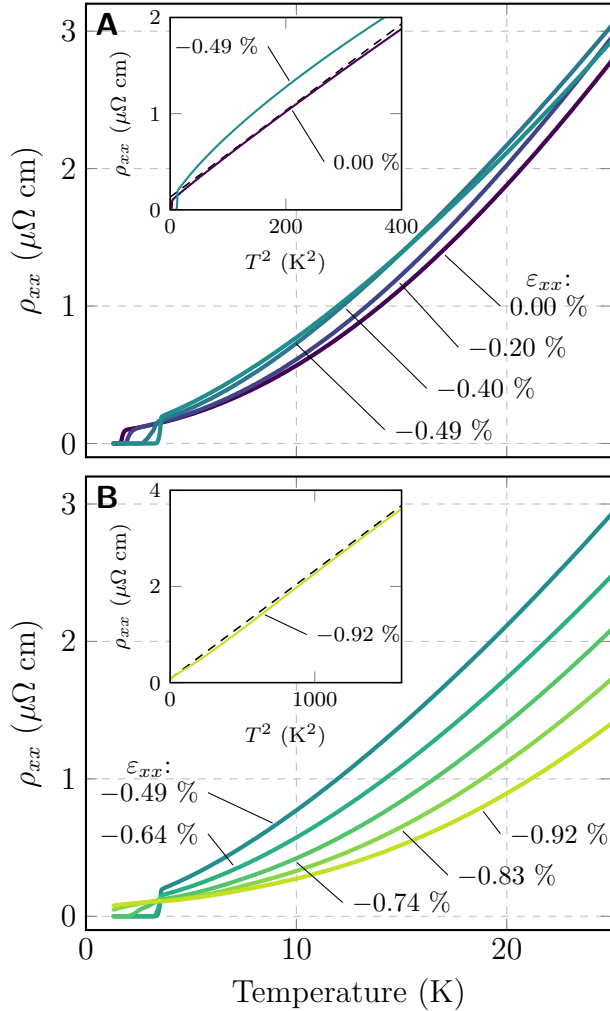
Fig. 3.30: **Resistivity against temperature. A** Longitudinal resistivity against temperature at strains below the peak in resistivity for sample 3. The inset shows the resistivity plotted against T^2 at zero strain, highlighting the Fermi liquid behaviour with a straight line as a guide to the eye, and for the strain where the lowest temperature exponent is observed. **B** At strains above the maximum in the resistivity, T^2 behaviour is recovered at high compression. The inset shows the larger extent of the T^2 region for the highest strain measured.

The inset to panel A of figure 3.30 highlights the zero strain T^2 Fermi liquid behaviour which is resolved up to almost ∼20 K, in agreement with the literature. Under compression the extent of the quadratic temperature dependence is reduced and a lower temperature exponent is observed in the vicinity of the peak in T_c. T^2 behaviour is recovered on the high compression side and is observed over a larger temperature range than previously at zero strain.
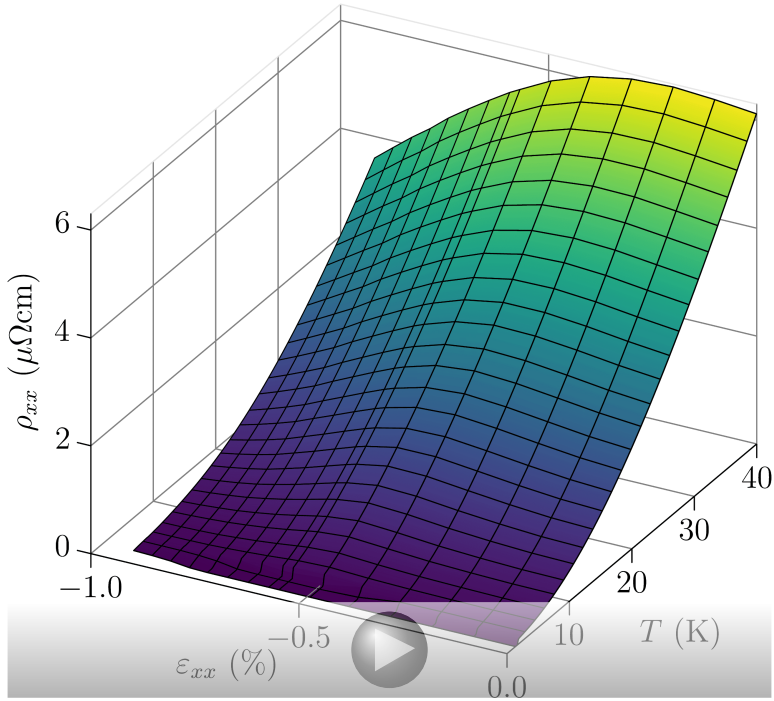
Fig. 3.31: **Resistivity against temperature and strain.** Longitudinal resistivity for sample 3 plotted against temperature and strain.
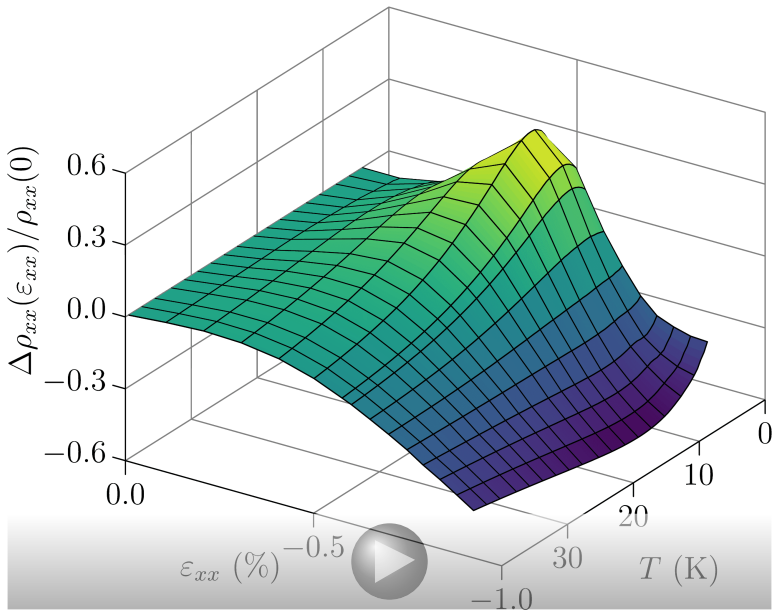
Fig. 3.32: **Elastoresistance against temperature and strain.** Elastoresistance $(\rho_{xx}(\varepsilon_{xx}, T) - \rho_{xx}(0, T))/\rho_{xx}(0, T)$ of sample 3 plotted against temperature and strain.

3.4.2.2 Resistivity strain dependence

The change in resistivity with strain at a fixed temperature is shown in figures 3.33 and 3.34. The curves in figure 3.33 are cuts through the surface plot in figure 3.32 at select temperatures whereas the measurements in figure 3.34 are from continuous strain ramps at fixed temperatures. Figure 3.34 shows both the longitudinal and transverse measurements as depicted in the top corners of the figure panels.

The resistivity at a given temperature peaks in the vicinity of the peak in T_c before falling again rapidly at higher strains even below its zero strain value, similar to the observed behaviour of T_c. This is seen in both the longitudinal and transverse resistivity measurements. Metallic behaviour is observed over the full range of strain tested. There are no signatures associated with competition from a spin density wave phase, as suggested by Liu *et al.* [148], where the opening of a gap is generally expected to increase the resistivity sharply.

The increase in ρ_{xx} with strain closely resembles the increase
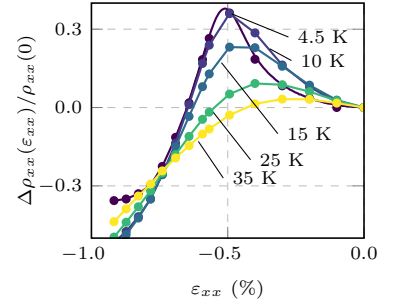
Fig. 3.33: **Elastoresistance against strain.** Change in longitudinal resistivity with strain at various temperatures for sample 3. Values are calculated by interpolating between separate temperature ramps at a series of constant strains except for 4.5 K where the strain was swept continuously.
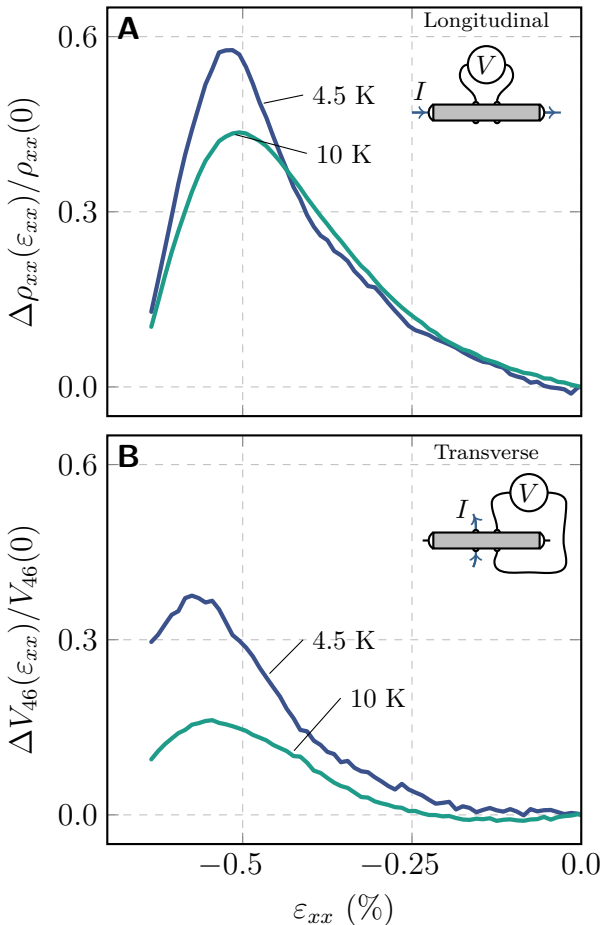
Fig. 3.34: **Longitudinal and transverse resistivity against strain.** Strain sweeps at constant temperatures for sample 2. **A.** Longitudinal resistivity measured in the traditional geometry. **B.** A qualitative measure of the transverse resistivity, see text for further details. This measurement geometry over exaggerates the intrinsic anisotropy.
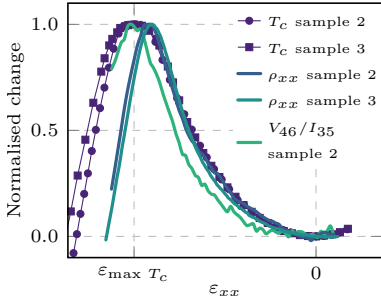
Fig. 3.35: **Comparison between T_c and resistivity enhancements.** Normalised change with strain of T_c, ρ_{xx} at 4.5 K and transverse resistivity at 4.5 K, e.g. $(T_c(\varepsilon_{xx}) - T_c(0))/(T_c(\text{max}) - T_c(0))$. The strain scales of the two samples have been adjusted so that their peaks in T_c coincide at the same strain, the resistivity data is also adjusted accordingly.

in T_c, see figure 3.35. Much as T_c is enhanced by the increasing density of states at the Fermi level, inelastic scattering in the normal state is also expected to scale with the density of states at the Fermi level, thus resulting in a peak in resistivity at the Lifshitz transition. ρ_{xx} is increased by ∼40-50 % at the peak, with a slight variation between the two samples. The two samples have slightly different residual resistivities, sample 2 being the cleaner with a resistivity at 4.5 K of ∼0.12 $\mu\Omega$ cm and sample 3 ∼0.19 $\mu\Omega$ cm, but both resistivities increase by approximately the same amount ∼0.07 $\mu\Omega$ cm at the peak.

The resistivity measured in a direction transverse to the direction of applied strain is expected to increase as a result of the geometric change but a clear peak is also apparent with applied strain. The quasiparticle scattering is therefore affected in all directions by the approach to the Van Hove singularity of only the γ band at just the $(0, \pm\pi/a)$ point of the Brillouin zone. Intriguingly the maximum in the transverse resistivity does not seem to coincide exactly with the peak in ρ_{xx}, instead occurring at a slightly higher strain. However, it is important to bear in mind what is being measured in the transverse geometry. The current is passed between two of the voltage contacts on opposite sides of the sample and the remaining two contacts, also opposite each other, are used to measure the voltage drop. This means there is always some component of ρ_{xx} in the measurement since this sets how far the current spreads out along the sample. The meaning of transverse is to describe a current direction predominately perpendicular to the direction of applied strain but here it does not necessarily imply the current is flowing purely in the *ab*-plane. The extreme resistive anisotropy in Sr_2RuO_4, $\rho_{0,c}/\rho_{0,ab}$ ∼4000, means that any slight vertical misalignment of the contacts on each side of the sample will lead to a small *c*-axis component of the current but a significant voltage because of the much higher out of plane resistivity. Finite element simulations show that the voltage actually measured for the transverse geometry of sample 2 at low temperature is approximately ten times larger than expected for when the current is fully within the *ab*-plane, and the measured RRR also shows this discrepancy. A contact misalignment of only ∼5 μm in opposite directions on each side of the sample is enough to provide a ten fold increase of the simulated voltage so over a 100 μm thick sample this is entirely feasible, especially as the silver paint may be physically contacting the full height of the sample but the electrical contact resistance might be varying slightly across each contact. At room temperature where the resistive anisotropy is only ∼120 the finite element simulation and measured voltage match well, but at low temperatures a significant contribution of the *c*-axis resistivity is expected to be contributing to the measured transverse resistivity.

To compare the longitudinal and transverse resistivities quantitatively, the Fermi surfaces must in principle be considered in three dimensions. The slight warpings of the Fermi surfaces in the k_z direction mean the Van Hove singularity is actually reached over a range of strain as different parts of the Fermi surface reach the Brillouin zone boundary at slightly different strain, however, DFT calculations suggest this width is less than the discrepancy observed here [147].

At elevated temperatures the peak in the longitudinal resistivity is flattened out as one would expect when thermal population of higher energy states above the Fermi surface smooths out the discontinuity in the density of states but a strong decrease in resistivity is still observed at strains above the suspected Lifshitz transition. The position of the peak also moves slightly with temperature, but extrapolating to find the zero temperature position still leaves a discrepancy with the strain of the T_c peak.

The peak in ρ_{xx} is also much narrower than that of T_c. This is not so surprising, because T_c can be affected by more than just the change in density of states. If for instance the pairing strength is also modified as the Fermi surface is distorted, this could result in a variation between the $\rho_{xx}(\varepsilon_{xx})$ and $T_c(\varepsilon_{xx})$ curves. It is then perhaps more likely that the peak in ρ_{xx} would coincide with the Lifshitz transition and T_c may peak close to but be extended around the Lifshitz transition.

3.4.2.3 Resistivity temperature exponent

So far we have good evidence we are seeing a clean Lifshitz transition in a multiband system that we can study with resistivity, arguably for the first time, but certainly for the first time at this level of purity. Because we have such a clean system, it is important to
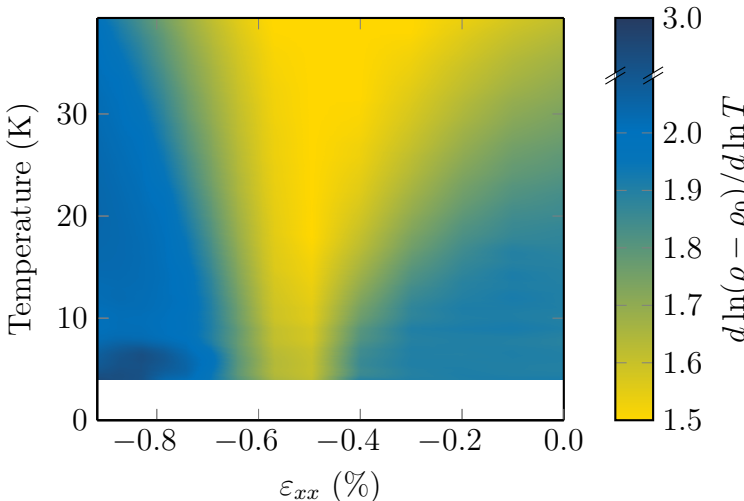
Fig. 3.36: **Resistivity temperature exponent.** The resistivity exponent, α, for sample 3 plotted against temperature and strain. ρ_0 was first extracted from fits of the type $\rho = \rho_0 + AT^\alpha$ and then α is calculated as a function of temperature by $d\ln(\rho - \rho_0)/d\ln T$. The figure is cut off below 4 K, due to percolating superconducting paths that can affect the resistivity strongly.

try and see how much physical significance we can give to the changes in resistivity. When the resistivity starts to deviate from the expected Fermi liquid T^2 temperature dependence it is usual to inspect the new temperature exponent to try and help interpret the results. A fit of the form $\rho = a + bT^c$ can be made to data where a, b and c are fitting parameters and a log derivative plot of the resistivity minus the residual resistivity can be made to inspect the change in temperature exponent. This plot can be seen in figure 3.36. Here the change in temperature exponent is presented more straightforwardly; Fermi liquid like T^2 behaviour is observed at both strains below and above the peak in ρ_{xx} but a lower power is observed in the vicinity of the resistivity peak, reducing to $\sim$1.5 at the lowest point.

Qualitatively similar behaviour is observed when the Lifshitz transition is induced by either La doping or epitaxial biaxial strain in thin films. However the power observed in both these experiments decreases to $\sim$1.4, lower than that observed at first sight here. This difference might be intrinsic. The Van Hove singularity is reached simultaneously in both the x and y directions of the Brillouin zone for the other two techniques whereas uniaxial pressure only approaches the Van Hove singularity along one direction. Significantly higher levels of disorder are also present in both the La doped system and the MBE films. To be vigilant however, it is worthwhile examining the quality of the fit used for extracting the exponent presented in figure 3.36 before addressing alternative interpretations. For reasons given in appendix B.1 regarding the possible effects of strain inhomogeneity and comparing with alternative trial fitting functions, at present we can only put an error of 0.1 on the exponent of 1.5 close to the suspected Lifshitz transition.

It is remarkable that for this multiband system in which only one out of its three Fermi surfaces passes through the Van Hove singularity, which itself is only one critical point on the surface at $(0, \pm\pi/a)$, such large changes in the temperature dependent resistivity occur. This shows that the 'hot' regions of the Fermi surface are not just shorted out by the unaffected sections and large regions of the Fermi surface must be affected by the approach to the Van Hove singularity.

Qualitatively a $T^{1.5}$ power law resistivity is also observed in polycrystalline spin-glass systems once the disorder has been frozen in [158]. The single crystals of Sr_2RuO_4 used here are not expected to exhibit this sort of behaviour, we note the particular low residual resistivity, $\rho_0 \sim$0.1 $\mu\Omega$cm, and that at zero pressure in comparably clean samples large quantum oscillation signals have been seen. A temperature dependence of the resistivity $\rho(T) - \rho_0 \propto T^\alpha$ with $\alpha <$ 2 is evidence for anomalous quasiparticle scattering not captured by the conventional quasiparticle interactions of Fermi liquid theory.

One such example is when a long range interactions increase the cross section for quasiparticle scattering. When I introduced Fermi liquid theory back in section 1.2 I used Fermi's golden rule to show that the lifetime of the quasiparticles goes like their energy squared so they are stable and well defined. In deriving this I made the assumption that the scattering matrix element is constant. This, however, is not always the case. For example near to a second-order phase transition fluctuations slow down as well as becoming increasingly long range, enhancing the scattering cross section. At a quantum critical point these fluctuations can grow without limit and the form of the scattering matrix element becomes important for determining the exact quasiparticle decay processes.

Quasiparticle-quasiparticle interactions by themselves are unable to relax the total momentum of the system which is required for a finite resistivity, and in normal Fermi liquid theory it is the umklapp processes that provide this. In the presence of critical fluctuations the scattering rate of fermions near the Fermi surface can still be calculated but the temperature dependence of the scattering rate does not necessarily straightforwardly translate to a temperature dependence of the resistivity [159]. In some studies that specifically concentrated on the possible mechanisms for relaxing the momentum, they found that the temperature exponents can be quite different for the momentum relaxing processes [160, 161]. Theory still remains unsettled on how best to account for the quantum-critical fluctuations on the temperature dependent resistivity, so instead this leaves us only to make empirical comparisons here.

Many intermetallic heavy fermion compounds host magnetic states at low temperatures and are also susceptible to pressure tuning. The Curie temperature of itinerant-electron ferromagnets MnSi, $ZrZn_2$ and Ni_3Al can be suppressed to absolute zero using hydrostatic pressure and near to the critical pressure power laws in the resistivity lower than 2 are observed, ranging from 1.5 to 1.7 depending on the purity and the material [162–166]. Some heavy fermion antiferromagnets also show similar behaviour. The Néel temperature of both $CePd_2Si_2$ and $CeIn_3$ can be driven to absolute zero using hydrostatic pressure whereupon non-Fermi liquid behaviour is observed in the vicinity of the QCP [167, 163, 168]. $CePd_2Si_2$ shows an anomalously low power amongst of these materials with a temperature exponent of 1.2 ± 0.1 for over nearly two decades in temperature.

In $NbFe_2$, a material reported to host a low temperature spin density wave near stoichiometry, a QCP can be reached this time not by using hydrostatic pressure but rather through varying its composition away from stoichiometry, suppressing the SDW order before giving rise to a ferromagnetic phase [169]. At the slightly Nb-

rich FM-AFM QCP, a $T^{1.5}$ power law dependence of the resistivity on temperature was also observed [170].

In Sr_2RuO_4 the quantum criticality evidenced by the lowered resistivity exponent is suspected to coincide with the strain induced Lifshitz transition and hence the additional scattering processes resulting in the breakdown of Fermi liquid theory may well have their origin in the proximity of the Van Hove singularity to the Fermi level. Band structure calculations of $NbFe_2$ have also highlighted this possibility as an explanation for the critical behaviour seen at the magnetic QCP in $NbFe_2$. Neal *et al.* [171] identified a critical point in the band structure and suggested that the underlying origin of criticality at the magnetic QCP may also be a result of the critical fluctuations associated with a vanishing quasiparticle velocity.
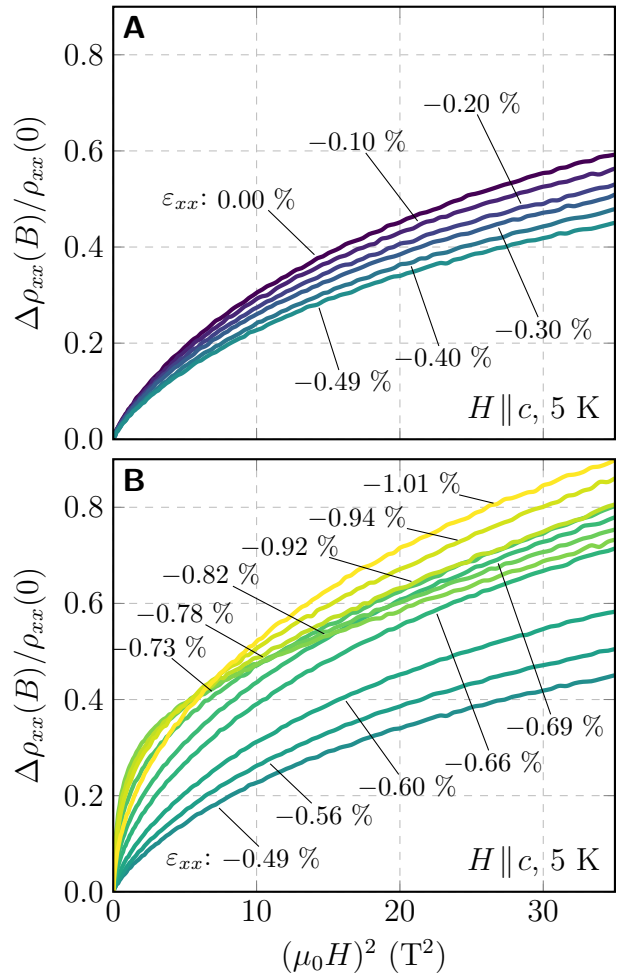
Fig. 3.37: **Magnetoresistance. A** Transverse magnetoresistance field sweeps at strains below the peak in resistivity for sample 3. **B** The same measurements at strains above the peak in resistivity.

3.4.2.4   Magnetoresistance

The transverse magnetoresistance ($H \parallel c$, $I \parallel a$) measured at 5 K for a series of applied strains is shown in figure 3.37. The magnetoresistance grows the fastest at low fields, almost proportional to the field squared, and crosses over to an approximately linear dependence at higher fields but no saturation is reached within the 6 T limit of the magnet system used for this strain study. The magnetotransport properties also show a marked change at the same strain as the resistivity peak. Compressive strain initially decreases the observed magnetoresistance reaching a minimum at the same strain as the peak in ρ_{xx}. Then at strains above the peak in ρ_{xx} the magnetoresistance increases again, but not monotonically, and around -0.8 % the shape of the magnetoresistance curves changes slightly.

Magnetoresistance measurements can be used for Fermi surface determination, not only from the Shubnikov-de Haas effect but also from saturation/non-saturation behaviour revealing open orbits in the Fermi surface. A classic example is that of copper where the positions at which the approximately spherical Fermi surface touches the Brillouin zone boundary can be identified by the field orientations that lead to a non-saturating magnetoresistance [172]. A closed orbit in general leads to a saturated magnetoresistance at sufficiently high fields whereas extended orbits drastically increase the saturation field and for field directions with open orbits saturation is not necessarily ever achieved [173].

In Sr_2RuO_4 the γ band is suspected to change from a closed electron orbit to an open orbit with applied strain. With the field along the c-axis of the sample an open orbit exists in the band structure only after the Lifshitz transition. However to observe the possibility of a non-saturating magnetoresistance the current direction is also important and when the open orbit lies along the y-axis in k-space, ρ_{yy} is expect to increase quadratically without limit but ρ_{xx} still saturates. Compressive strain leads to the γ band running along the k_y direction and therefore saturation of ρ_{xx} magnetoresistance resistance is still expected. A sensible extension would be to try and measure the transverse resistivity in field to see if the non-saturation behaviour can be observed. However, complications with the uncertain current direction may result in an inadvertent measurement of the longitudinal c-axis magnetoresistance and additional Hall voltage contributions that can appear if the geometry of the four contacts is not exactly square must be carefully subtracted.

3.4.2.5   Hall effect

The measured Hall effect is shown in figure 3.38. The low field Hall coefficient is mostly unchanged at low strain and the higher field

Fig. 3.38: **Hall Effect. A** Hall effect measurements at strains below the peak in resistivity for sample 3. **B** The same measurements at strains above the peak in resistivity.
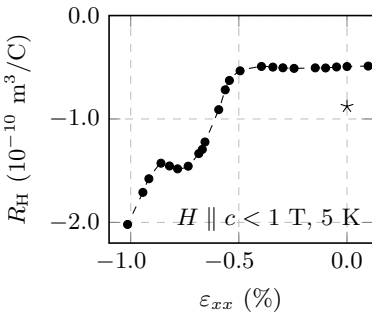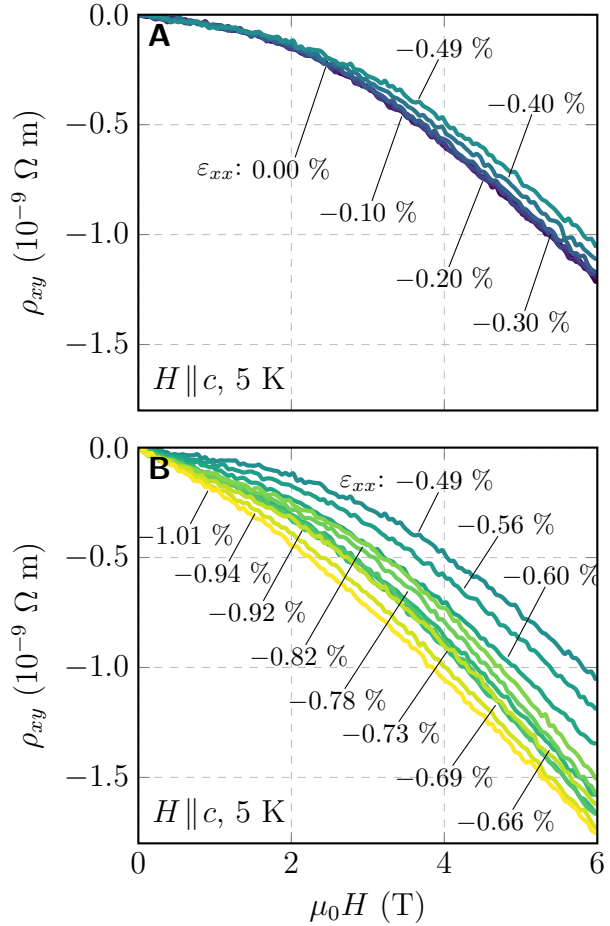
Fig. 3.39: **Weak-field Hall coefficient against strain.** The Hall effect coefficient below 1 T for sample 3 at 5 K plotted against strain. The star marks the Hall coefficient determined by Mackenzie *et al.* [174] in a dirtier sample.

Hall effect is only slightly reduced, reaching a minimum once again at the same strain as the peak in ρ_{xx}. At higher strain the Hall effect becomes larger and more negative, and is also non-monotonic, showing a deviation around -0.8 % strain.

Analysis of the weak-field Hall effect can conveniently be performed using the geometrical interpretation realised by Ong [175]. However, in such a clean sample the weak-field limit is small. Depending on what approximation one uses to calculate the scattering time and how one averages the three bands, the point where $\omega_c\tau$ is unity covers quite a range. However, making the simplest estimate using only the residual resistivity and the electron density $\omega_c\tau = B/ne\rho_0$, $\omega_c\tau$ reaches unity at a field of ~6 T. The weak-field limit is then when $\omega_c\tau \ll 1$, i.e. $B \ll 6$T. The field needed to suppress superconductivity at optimal strain, ~1.5 T, is quite a large fraction of this so to have a hope of measuring the weak-field limit at all strains the measurements were carried out at 5 K to avoid any effects of superconductivity. As best we can tell the Hall effect is linear below ~1 T so the data below this field were used

to calculate the weak-field Hall coefficient shown in figure 3.39. It is approximately flat until ~-0.5 % strain then it decreases, becoming more electron like.

Naively one would expect a discontinuity in the Hall effect at the Lifshitz transition as one species of Fermi surface changes character. One approximation for carrying out the Ong analysis is to use an isotropic scattering length ℓ for all parts of the Fermi surface. This approximation makes most sense for very low temperatures where the resistivity is dominated by impurity scattering. As an illustration of the Ong construction I will outline how this is realised.

Making reference to figure 3.40, we consider moving a point $\mathbf{k}$ around the Fermi surface and track $\boldsymbol{\ell}(\mathbf{k})$ the scattering length at each point. The vector $\boldsymbol{\ell}(\mathbf{k})$ maps out a closed area in the ℓ_x-ℓ_y plane and this area is directly proportional to the weak-field Hall conductivity

$$\sigma_{xy} = \frac{e^3}{2\pi^2\hbar^2}\boldsymbol{B}\cdot\int\limits_{\mathrm{FS}}\frac{d\boldsymbol{\ell}(\mathbf{k})\times\boldsymbol{\ell}(\mathbf{k})}{2}\ . \tag{3.26}$$

For $\mathrm{Sr_2RuO_4}$ we must do this mapping for each Fermi surface separately and then it is assumed that the conductivities of the three bands can be added in parallel. With a k-independent scattering length the area mapped out by $\boldsymbol{\ell}(\mathbf{k})$ as the point $\mathbf{k}$ is moved around the Fermi surface is simply a circle with area $\pi\ell^2$. But the circulation of the hole pocket is in the opposite sense to the
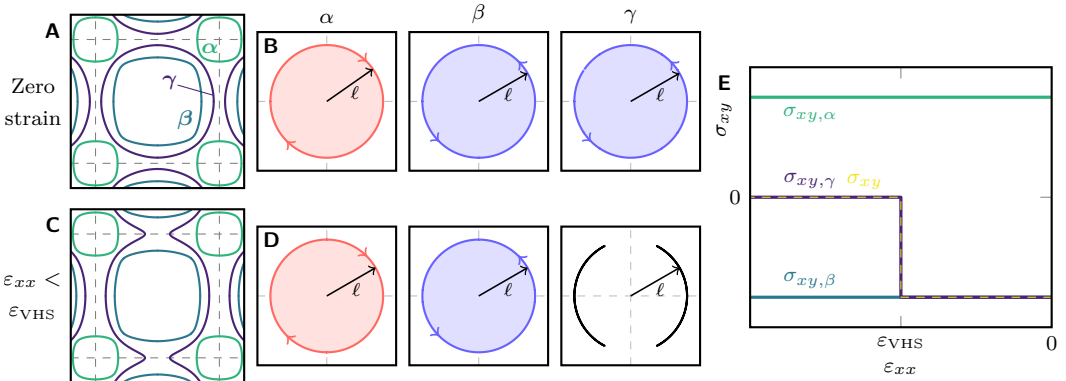
Fig. 3.40: **Isotropic-ℓ analysis of the Hall effect.** Using the geometric interpretation of the Hall conductivity by Ong the area swept out by the scattering length $\boldsymbol{\ell}(\mathbf{k})$ as $\mathbf{k}$ is moved around the Fermi surface defines the Hall conductivity. Pannel B shows this area for each of the three Fermi surfaces of $\mathrm{Sr_2RuO_4}$ at zero strain in the isotropic-ℓ approximation. The circulation of the α band is in the opposite direction to the other two bands and adds to the overall conductivity with the opposite sign. Above the Lifshitz transition the γ band no longer contributes to the Hall conductivity and the Hall coefficient is expected to fall to zero.

electron pockets, see figure 3.40. In the isotropic-ℓ approximation once the neck in the γ band is opened the area mapped out by $\boldsymbol{\ell}(\mathbf{k})$ on the γ band falls to zero. One would therefore expect the Hall coefficient, $BR_\mathrm{H} \approx \sigma_{xy}/(\sigma_{xx}\sigma_{yy})$, to jump to zero at the Lifshitz transition in the approximation of isotropic-ℓ scattering.

The measurements reported here are at higher temperatures than those at which the isotropic-ℓ approximation should really be applicable. Another possible simplification is to assume an isotropic scattering time, τ, rather than length, $\ell(\mathbf{k}) = v_\mathbf{k}\tau_\mathbf{k}$. At sufficiently high temperatures this is expected to be realised.

Mackenzie *et al.* [174] achieved good consistency in applying the isotropic-ℓ approximation to mK data in the unstrained material but the partial compensation of the three bands means that the interpretation of the Hall effect can be extremely difficult. This can be seen from the multiple sign reversals between low temperature and room temperature. The good agreement of the measured Hall coefficient and the calculated value in the isotropic-ℓ approximation by Mackenzie *et al.* does not still hold in these much cleaner samples. It is clear then that detailed interpretation of the Hall effect in Sr_2RuO_4 should be treated with scepticism. This is further evidenced from the magnetotransport measurements on the La substitution series [176]. In a similar vein to the uniaxial pressure effect, as the Lifshitz transition is reached with heterovalent substitution the circulation of the $\boldsymbol{\ell}(\mathbf{k})$ area should change from positive to negative for the γ band as it becomes a hole like orbit. This change of the Hall effect was however not observed and the Hall coefficient was positive for all the La doping levels measured.

To show that the effect of uniaxial pressure on the Hall coefficient at higher temperatures could be still more subtle I also show the results of a calculation of the weak-field Hall effect in the isotropic-τ approximation. Using the measured ρ_{xx} values to infer how τ could change with strain, the Ong construction can then be used to calculate σ_{xy}, this time taking into account the $\mathbf{k}$ variation of v_F in $\boldsymbol{\ell}(\mathbf{k}) = v_\mathrm{F}(\mathbf{k})\tau$ based on the tight-binding model introduced in section 3.4.1.1. The area swept out by $\boldsymbol{\ell}(\mathbf{k})$ on the γ band at various strains is show in figure 3.41 B and C. At zero strain the four fold symmetry of the Fermi surface can be seen where the Fermi velocity is lowest along the <100> directions. As the strain is increased the Fermi velocity close to the M point in the y-direction is reduced and the area swept out by the $\boldsymbol{\ell}(\mathbf{k})$ curve is pinched off at the Lifshitz transition. Above the Lifshitz transition two separate lobes of the $\boldsymbol{\ell}(\mathbf{k})$ curve exist, one from each part of the open orbit. In panel B of figure 3.41 the $\boldsymbol{\ell}(\mathbf{k})$ curves are scaled by τ at each strain so the pinching off can be seen more clearly. However by including a strain dependent τ this also changes the area of the $\boldsymbol{\ell}(\mathbf{k})$ curves and panel C shows the unscaled result. The
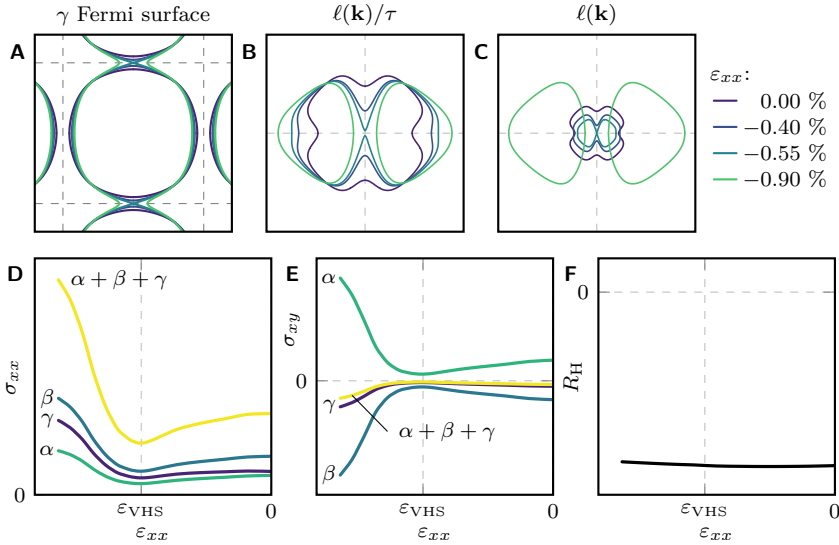
Fig. 3.41: **Isotropic-τ analysis of the Hall effect.** Using the measured ρ_{xx} resistivity from figure 3.34 an isotropic τ can be calculated and then used with the geometric interpretation by Ong to calculate the Hall effect. Panel A shows the γ Fermi surface at a series of strains and the area swept out by the scattering length $\boldsymbol{\ell}(\mathbf{k})$ around the Fermi surface at each strain is shown in panels B and C, where in B the data has been scaled by τ at each strain. The α and β Fermi surfaces are much less affected by uniaxial pressure and there is little change to the shape of the $\boldsymbol{\ell}(\mathbf{k})$ curves. The contributions of all three bands to the conductivities σ_{xx} and σ_{xy}, within the isotopic-τ approximation, are shown in panels D and E. The calculated weak-field Hall coefficient is shown in panel F and shows very little change with strain within the isotopic-τ approximation.

calculated σ_{xy} for each band is shown in panel E along with their sum, the overall conductance of the three bands. σ_{xy} decreases above the Lifshitz transition but since the Hall coefficient is the ratio of σ_{xy} with $\sigma_{xx}\sigma_{yy}$ which changes in the opposite direction, the resultant Hall coefficient shows very little change.

The isotropic-τ approximation should become valid at sufficiently high temperatures. This may be reached when the resistivity is at least an order of magnitude larger than its residual value. For the measurements presented here at 5 K, this ratio varies from 2 to 6 depending on the strain. Our data can therefore be expected to lie somewhere between the predictions of the two regimes that I have discussed, but be extremely sensitive to details of the scattering not included in either model.

The two calculations highlight the complications in interpreting Hall effect measurements in a multiband system, and show qualitatively that the picture can be quite varied and detail sensitive. However the overall picture of the Hall measurements is consistent with the other results. The most drastic change occurs at the same strain as the maximum in resistivity which is also the strain where the lowest temperature exponent is observed. This is also in
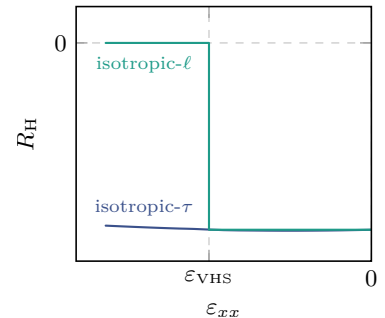
Fig. 3.42: **Comparison of isotropic-$\boldsymbol{\ell}$ and $\boldsymbol{\tau}$ Hall effect calculations.** A summary of isotropic-$\boldsymbol{\ell}$ and isotropic-$\boldsymbol{\tau}$ calculations showing the weak-field Hall coefficient variation with strain.

close vicinity to the maximum in T_c and is highly suggestive that a common origin for all these effects exists.

3.5   Conclusions

In this chapter I have demonstrated the usefulness and the unique capabilities of the uniaxial stress technique. I reported achieving the highest yet attained strains in Sr_2RuO_4, measuring magnetic susceptibility simultaneously with resistivity, both longitudinal and transverse to the applied strain direction. These measurements firstly confirm the enhancement of T_c under both in-plane compression and tension. By extending the strain range I have also identified that a maximum T_c is reached after which T_c drops steeply at higher strain. The highest T_c of ∼3.5 K is reached at a strain of $\varepsilon_{xx} = (-0.55 \pm 0.06)$ %. Measurements of the upper critical field $H_{c2\|c}$ highlight the significance of the density of states increase at the Van Hove singularity for the superconductivity as it is even more strongly enhanced than T_c^2, raising the possibility that optimally strained Sr_2RuO_4 is an even-parity, rather than an odd-parity, superconductor. Detailed measurements at intermediate strains will be useful for determining if such a change in order parameter occurs.

Measurements of the normal state properties show an apparent breakdown of Fermi liquid behaviour as the sample is strained close to the peak in T_c and the overall resistivity enhancement strongly suggests that we have indeed been able to reach the Van Hove singularity with uniaxial stress. The approach to the VHs appears to affect all the quasiparticles, increasing the scattering for all current directions, and affecting all the bands despite the density of states increase being localised to the M points of the zone along only one direction and only for the γ band. In the future, measurements of electronic heat capacity being pioneered by my colleagues You-Sheng Li and Michael Nicklas may also provide important information on the density of states increase as the sample is strained. Heat capacity measurements are still possible despite the strong thermal connection through the sample mounts by using AC methods at kilohertz frequencies.

Ultimate confirmation of the Lifshitz transition by experimental techniques directly sensitive to the Fermi surface topology may also be possible in the future but significant technical development will be necessary first. A miniaturised dHvA set up with suitable amplification may enable quantum oscillation measurements under strain or a significant increase in signal-to-noise ratio may allow Shubnikov-de Haas oscillations to be observed. Additionally, since the upper surface of the sample can remain exposed, ARPES measurements may also be possible, but the sensitivity of this

technique to electric fields would require a purely mechanical version of the device (i.e. one in which piezoelectric actuators are not used) to be developed first.

In a wider perspective these measurements highlight the significance of uniaxial stress as a new technique for tuning band structures, especially towards Van Hove singularities. Our work demonstrates that uniaxial pressure offers a much cleaner solution, for instance compared to chemical doping, and often a much more effective one, for instance compared to hydrostatic pressure. Hopefully then, this technique can be put into good use when applied to a whole host of other interesting materials.

Quantum Criticality and Metamagnetism of Strained $Sr_3Ru_2O_7$

<div style="text-align:right">

4

</div>

4.1 Introduction

As outlined in chapter 1, the field of strongly correlated electrons is dominated by emergent phenomena exhibiting exotic and intriguing properties. Identifying and characterising these phases has been the challenge for condensed matter physicists for the last few decades. One particularly fruitful avenue for discovering them has been to search in the vicinity of quantum critical points. By suppressing a second-order phase transition to absolute zero using a non-thermal tuning parameter, such as pressure or chemical doping, a quantum phase transition at zero temperature is produced. Here the effective electron-electron interactions become increasingly strong as the strength of quantum critical fluctuations diverges and as such, quantum critical points have become a breeding ground for new stable phases of matter.

The bilayer ruthenate, $Sr_3Ru_2O_7$, possesses much of this interesting behaviour. At low temperatures the properties are well described by Landau's Fermi liquid theory, a cornerstone of condensed matter physics, but strong interactions are clearly evident by the enhanced quasi-particle masses, giving a large heat capacity of 110 mJ/(Ru-mol K^2), and an even more strongly enhanced magnetic susceptibility with a Wilson ratio of $\sim$10 [177]. Magnetic fields reveal metamagnetic behaviour between 5–8 T depending on the orientation of the field [178]. At low temperatures quantum criticality is observed with field applied along the crystallographic c direction [179]. In the purest samples novel phase formation occurs, masking the quantum critical end point [180]. Two different spin density waves have been identified [181] and both are strongly susceptible to in-plane symmetry breaking magnetic fields, producing a large apparent electron nematic susceptibility in transport measurements [182].

Maintaining extremely low levels of disorder is crucially important for $Sr_3Ru_2O_7$ so any experiment designed to tune its properties must introduce no extra inhomogeneity at new scattering centres. For the first time we are able to use our new experimental capabilities to apply precisely controlled homogeneous uniaxial in-plane stress. It has previously been found that hydrostatic pressure

increases the metamagnetic transition fields for in-plane fields, ultimately reaching a QCEP at ~9.3 T for ~14 kbar [183,184]. Uniaxial pressure applied normal to the RuO_2 layers acts in the opposite direction, driving the metamagnetism to lower fields and ultimately inducing ferromagnetism at a moderate pressure of 0.1 GPa [185]. With the new uniaxial stress technique described in chapter 2 of this thesis, samples are shaped into long narrow bars and fixed across the jaws of a vice suitable for applying in-plane pressure.

We investigate the effect of in-plane pressure on the metamagnetism and associated quantum criticality but also use the precisely applied anisotropic strain to make detailed tests of the symmetry of the novel phases which are known to host orthogonally oriented density waves. Using these results we address the question of whether a spontaneous lowering of symmetry occurs at the formation of the novel phase or microscopic coexistence of the orthogonally oriented density waves maintains a weak C_4 symmetry that is highly susceptible to C_2 symmetry breaking fields.

The remainder of this chapter will be split into several sections, starting with an introduction to the relevant properties of $Sr_3Ru_2O_7$ and a discussion of the necessary background physics. Following this, in section 4.3, I will describe the experimental technique and the measurements undertaken before presenting the results in section 4.4 with accompanying discussions.

4.2   Background physics for $Sr_3Ru_2O_7$

The oxide strontium ruthenate has a layered perovskite structure built out of RuO_4 octahedra layers interspersed with Sr spacer layers. The variety of stacking options makes up a family following the Ruddlesden-Popper series [186, 187]. $Sr_3Ru_2O_7$ is the bilayer member of this series; $n=2$ in the general formula $Sr_{n+1}Ru_nO_{3n+1}$. Here n identifies the number of RuO_4 octahedra in the unit cell and a higher n corresponds to a more three-dimensional structure. The electrical properties are dominated by the planes of RuO_2 so as the crystal structure becomes more three-dimensional so does the resistivity. The $n=1$ member, Sr_2RuO_4, has a resistive anisotropy $\rho_c/\rho_a \approx 4000$ at low temperatures [91], in $Sr_3Ru_2O_7$ it is >500 [188], whilst in the $n=\infty$ material, $SrRuO_3$, the resistivity is isotropic [189]. The $n=1$ member, the subject of the third chapter of this thesis, is an unconventional superconductor but as the crystal structure becomes more three dimensional there is a tendency towards magnetic ordering. $SrRuO_3$ is ferromagnetic with a Curie temperature of ~160 K [190] and so is the $n=3$ member $Sr_4Ru_3O_{10}$ which has a lower Curie temperature of ~105 K [191–193]. $Sr_3Ru_2O_7$ is not ferromagnetic but is a strongly enhanced paramagnet thought to be in close proximity to a ferromagnetic

instability [177]. This is evidenced by the large Wilson ratio $\sim$10
[177] and also when only moderate uniaxial pressure is applied along
the c-axis the ferromagnetic ordering that occurs below 80 K [185].

     The crystal structure of $Sr_3Ru_2O_7$ is shown in figure 4.1,
in which the bilayers of RuO_4 octahedra can be seen. This is
a tetragonal representation of the unit cell but in reality each
RuO_4 octahedron is slightly rotated about the c-axis [195, 194, 196].
The rotations are correlated within and between each layer of the
bilayers. This means that, although an individual bilayer would
retain four fold rotation symmetry, as a whole the cooperative
rotations mean the unit cell is no longer C_4 symmetric. The new
crystal structure has an orthorhombic unit cell with space group
Bbcb and the principle axes are rotated 45° from the tetragonal cell,
see figure 4.2. The single layer Sr_2RuO_4 does not possess the same
rotation except at pristine cleaved surfaces [197, 198]. The rotation
has important consequences for the electronic band structure but
the orthorhombicity induces almost no anisotropy between the two
Ru-O-Ru bond directions. In practice no discernible difference is
observed in the electronic transport along the in-plane principle
axes of the unit cell and to fairly high experimental resolution the
transport is isotropic within the ab-plane [199].

    The band structure can be intuitively derived following the ideas
from Sr_2RuO_4. At the normal valencies for strontium and oxygen
the ruthenium ion is left in a $4d^4$ electronic configuration but once
in the octahedral crystal field the lower lying states come from
the t_{2g} manifold. The d_{xz} and d_{yz} orbitals form quasi-1D sheets
running along k_x and k_y in the Brillouin zone respectively and the
d_{xy} orbital leads to a circular sheet. For $Sr_3Ru_2O_7$ the number
of bands is doubled and interlayer coupling leads to substantial
bilayer splitting for some parts of the Fermi surface. After including
the RuO_4 octahedra rotations the size of the unit cell is doubled
and the bands are backfolded into the now smaller first Brillouin
zone. Hybridizing the remaining bands leads to a qualitative
similarity with the measured band structure [200] although the
lowered symmetry also introduces a small $d_{x^2-y^2}$-derived pocket
near the zone centre. Neighbouring bilayers are only weakly coupled
and the Fermi surfaces are quasi-two-dimensional. The observed
Fermi surfaces are shown in figure 4.2. In total there are six
distinct Fermi surfaces and the labels for each can be seen in
the figure. There is good agreement between the Fermi surface
measured by ARPES and with quantum oscillations [201, 200].
Combining traditional dHvA quantum oscillations and bespoke
magnetocaloric effect measurements, all the bands and their masses
can be measured. Once the multiplicity of some of the bands due
to the bilayer splitting is included, the Fermi surface areas satisfy
the Luttinger count consistent with observing all the bands, and

Fig. 4.1: **Crystal structure of $Sr_3Ru_2O_7$.**
A tetragonal representation of the layered perovskite structure without including any rotation of the RuO_4 octahedra. The undistorted unit cell belongs to the space group $I4/mmm$ with lattice constants $a \sim 3.9$ Å and $c \sim 20$ Å [194].

A

6.8°

a_o

a_t

● Ru   ○ O

B

M

Γ

X

C

γ_2

γ_1

M

β

Γ

δ α_1 α_2

X
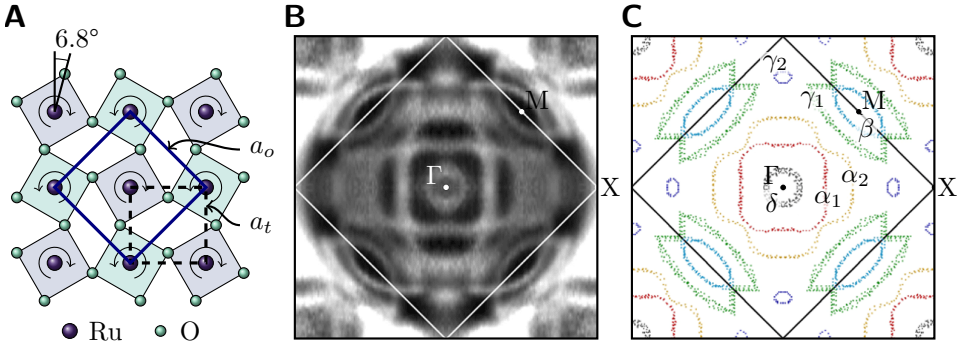
Fig. 4.2: **Fermi surfaces of $Sr_3Ru_2O_7$. A.** Cooperative rotation of the RuO_4 octahedra within the plane about the *c*-axis leads to a doubling of the unit cell and a $\sqrt{2}\times\sqrt{2}$ reconstruction of the Fermi surfaces. **B.** In-plane Fermi surface cross sections obtained in an ARPES study by Tamai *et al.* [201]. Data was taken in the first quadrant of the larger tetragonal Brillouin zone and the Fermi surface reconstruction can be clearly seen. **C.** Fermi surface contours extracted from the ARPES data and the naming scheme used throughout this thesis.

Fig. 4.3: **Metamagnetism in $Sr_3Ru_2O_7$.** Magnetisation against applied magnetic field in the *ab*-plane. At low temperatures there is a sudden rise in the magnetisation at approximately 5 T; a metamagnetic transition. Reproduced from [188].

more conclusively adding up the masses of each band to find their contribution to the electronic specific heat gives good agreement with the measured value [177]. I note here that although the γ_2 band is the smallest in area, it contributes almost half of the total electronic specific heat chiefly due to its high multiplicity and quasiparticle mass.

The history of $Sr_3Ru_2O_7$ is a classic example of how increasing material purity can be important to reveal new behaviour. A systematic crystal growth study by Perry *et al.* [202] produced single crystals with mean-free paths up to approximately 3000 Å as revealed by dHvA measurements [200]. The result is a fairly complex phase diagram with intertwined features resulting from strong electron-electron interactions, metamagnetism, quantum criticality, possible electronic nematicity and density waves. It is therefore quite instructive to follow the discoveries chronologically as an introduction to the material, as I will outline in the following sections.

4.2.1   Itinerant Metamagnetism

Initial characterisation measurements of the first single crystals of $Sr_3Ru_2O_7$ revealed a strongly correlated, quasi-two-dimensional Fermi liquid ground state with strongly enhanced paramagnetism [177]. The electrical transport is metallic and below ~10 K a coherent Fermi liquid like T^2 dependence is observed for both the in-plane and out-of-plane resistivity. Strong electron-electron correlations are suggested by the rather large low temperature electronic specific heat γ=110 mJ/(Ru-mol K^2) and the large Wilson

ratio of ~10. In high applied magnetic fields, itinerant electron metamagnetism was observed by Perry *et al.* [203].

Metamagnetism is empirically defined as a super-linear rise in the magnetisation occurring over only a short field range. Its origin can have quite different mechanisms for different metamagnets. Quite often, staggered local-moment materials exhibit metamagnetism when certain applied fields drive spin-flip or spin-flop transitions causing the sudden change in magnetisation [204]. However, the effect can also be observed in itinerant electron materials, such as $Sr_3Ru_2O_7$, in which its origin is the detailed structure of the density of states. Usually it is connected with a peak in the density of states in close proximity to the Fermi level.

In an itinerant electron system each of the allowed Bloch states is doubly degenerate because of the electron's spin, but in the presence of a magnetic field the states are split, lowering the energy of those with spin aligned with the field and raising that of the states that are anti-aligned to it. The chemical potential must remain constant across the spin split bands, so a small surplus of electrons develops in one band, as shown in figure 4.4. The number of electrons per unit volume of each spin band is given by

$$n_\uparrow = \frac{1}{2} \int_{-\infty}^{\infty} g(E + \mu_B B) f(E) dE \qquad (4.1)$$

$$n_\downarrow = \frac{1}{2} \int_{-\infty}^{\infty} g(E - \mu_B B) f(E) dE \qquad (4.2)$$

where $g(E)$ is the density of states at energy E and f the Fermi-Dirac distribution. This splitting is responsible for Pauli paramagnetism and can be used to calculate the magnetic susceptibility of the free electron gas when the orbital motion of the electrons is ignored. Working at $T=0$ K to neglect the smearing of the Fermi surface with temperature, and with small fields such that the splitting of the bands is also small (not a serious restriction given the scale of the Fermi energy in most metals), the number of electrons shifted from the minority- to majority-band is approximately $\frac{1}{2} g(E_F) \mu_B B$. The net magnetisation is given by $M = \mu_B (n_\uparrow - n_\downarrow) \approx g(E_F) \mu_B^2 B$ and the Pauli magnetic susceptibility is $\chi_P = M/H = \mu_0 \mu_B^2 g(E_F)$ [205].

In a material where the electronic density of states peaks in close proximity to the Fermi level, the application of a magnetic field spin splitting the bands can have a pronounced effect on the magnetisation if the peak is reached by the Zeeman splitting. The differential susceptibility $\chi = \partial M / \partial H$, or equivalently the rate at which the surplus electrons switch from the minority-band to the majority-band with applied field, depends on the density of states. Thus if the peak in the density of states approaches the chemical potential, the magnetisation will increase more steeply with field.
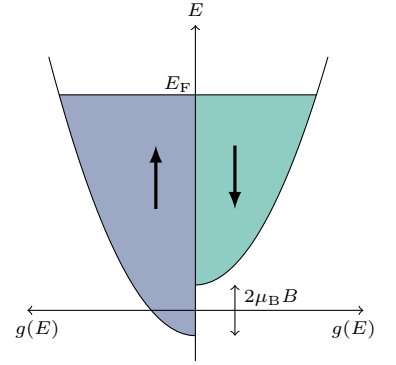
Fig. 4.4: **Pauli Paramagnetism.** The density of states of a band spin-split by the presence of a magnetic field B. Reproduced from [205].
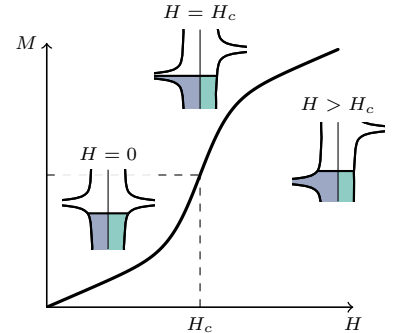
Fig. 4.5: **Metamagnetism caused by a peak in the density of states.** Magnetisation against field of an illustrative one band model with a peak in the density just above the Fermi level. The insets show the density of states splitting between the majority and minority spin band for various fields.

An illustrative one band model with a peak in the density is shown in figure 4.5. The magnetisation rises steeply in only a short field range as the peak in the density of states is sampled. Here the transition between the low- and high-polarised state is a continuous crossover and not a thermodynamic transition but in a suitably exchange-enhanced paramagnet this can turn into a first-order discontinuous jump.

Stoner postulated that the effect of the exchange interaction between electron spins can be taken into account by an additional average molecular field λM produced by all the neighbouring spins [206]. The potential energy can therefore be lowered by aligning spins

$$\Delta E_{\text{ex}} = -\int_0^M \mu_0(\lambda M')dM' = -\frac{1}{2}\mu_0\lambda M^2 \,. \tag{4.3}$$

The magnetic susceptibility is enhanced by the exchange interaction and, if it is large enough, spontaneous ferromagnetism can occur. At zero field there is a kinetic energy penalty for developing a spontaneous magnetisation. In order to flip a small number of spins within δE of Fermi surface they must be raised in energy by δE to occupy the lowest available states above the Fermi level in the other spin band. There are $\frac{1}{2}g(E_{\text{F}})\delta E$ down-spin electrons within δE of Fermi surface so the total kinetic energy penalty would be $\Delta E_{\text{K.E.}} = \frac{1}{2}g(E_{\text{F}})(\delta E)^2$. However this can be balanced by the interaction of the spontaneous magnetisation with the molecular field as described above

$$\Delta E_{\text{ex}} = -\frac{1}{2}\mu_0\lambda M^2 \tag{4.4}$$

$$= -\frac{1}{2}\mu_0\lambda\mu_{\text{B}}^2(n_\uparrow - n_\downarrow)^2 = -\frac{1}{2}\mu_0\mu_{\text{B}}^2\lambda g(E_{\text{F}})^2(\delta E)^2 \tag{4.5}$$

and hence the total energy change is

$$\Delta E = \frac{1}{2}g(E_{\text{F}})(1 - \mu_0\mu_{\text{B}}^2\lambda g(E_{\text{F}}))(\delta E)^2 \tag{4.6}$$

$$= \frac{1}{2}g(E_{\text{F}})(1 - \lambda\chi_{\text{P}})(\delta E)^2 \,. \tag{4.7}$$

Spontaneous ferromagnetism will occur when $\Delta E < 0$ which gives us the Stoner criterion for a ferromagnetic instability $\lambda\chi_{\text{P}} > 1$.

In a band that is not parabolic but does have a peak in the density of states close to the Fermi level it is still possible to achieve a field polarised exchange-split state when $\lambda < 1/\chi_{\text{P}}$ and this occurs as a first order metamagnetic transition [207]. Including the magnetic exchange interaction the magnetisation at a given field can be found by minimising the free energy
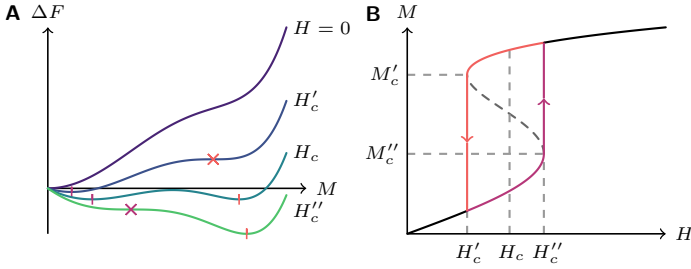
$$F(M) = \frac{1}{2}\int_0^{\mu_\uparrow} Eg(E)dE + \frac{1}{2}\int_0^{\mu_\downarrow} Eg(E)dE - \frac{1}{2}\mu_0\lambda M^2 - HM \tag{4.8}$$

given the constraints

$$n_\uparrow = \frac{1}{2}\int_0^{\mu_\uparrow} g(E)dE\,, \quad n_\downarrow = \frac{1}{2}\int_0^{\mu_\downarrow} g(E)dE\,, \quad n = n_\uparrow + n_\downarrow\,. \tag{4.9}$$

Figure 4.6 shows the free energy density for a similar illustrative band to that used in figure 4.5 with a peak in the density of states close to the Fermi level but now including the exchange interaction. At a sufficiently large field, H_c'' in the figure, the local maximum in the free energy density at finite magnetisation becomes an inflection point upon which the magnetisation discontinuously jumps to the now accessible global minimum. The transition is first order and is hysteretic as is evident in panel B. Shimizu [207, 208] analysed this sort of behaviour in a Landau-type expansion of the free energy in even powers of M

$$\Delta F(M) = \frac{1}{2}aM^2 + \frac{1}{4}bM^4 + \frac{1}{6}cM^6 - HM\,. \tag{4.10}$$

He showed that the necessary conditions for which the first-order metamagnetic transition can take place are $a > 0$, $b < 0$ and $c > 0$ with $3/16 < ac/b^2 < 9/20$. Wohlfarth and Rhodes [209] had previously shown that a sufficient curvature of the density of states is necessary to observe the first-order transition and their condition $gg'' > 3(g')^2$ makes sure $b < 0$ [210]. The first-order jump occurs because there is a sufficient number of states just above the chemical potential which do not present a large kinetic energy penalty but can result a large reduction of the Coulomb energy by aligning spins. This is the same idea as for the Stoner criterion but here the magnetisation only continues to increase while the density of states curvature is high enough.

Band structure investigations of $Sr_3Ru_2O_7$ by both ARPES and density-functional calculations identified heavy bands confined to a small energy window just below the Fermi surface for large
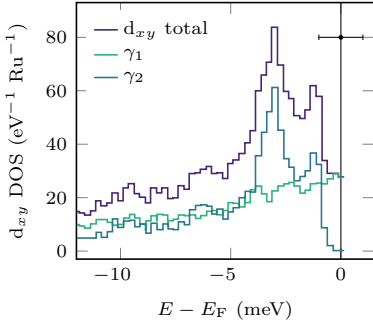
Fig. 4.7: **$Sr_3Ru_2O_7$ density of states.** Density of states for the d_{xy} derived bands in $Sr_3Ru_2O_7$ close to E_F. The γ_2 band has a saddle-type Van Hove singularities just below the Fermi energy. Reproduced from [201].
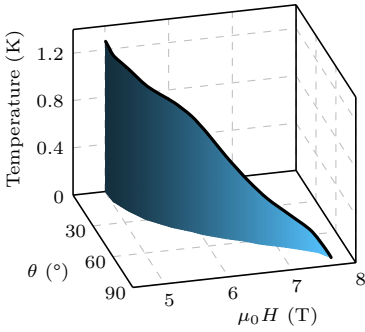
Fig. 4.8: **Metamagnetic phase diagram.** Empirical phase diagram for $Sr_3Ru_2O_7$ with fields applied at an angle θ to the *ab*-plane. The shaded surface marks the first order transition separating the low and high spin polarised regions and the black line is the line of critical end points. Reproduced from [178].

parts of the Brillouin zone [201, 211]. In particular, the top of the small hole pocket γ_2 is so close to the Fermi level that when first identified with ARPES it could not be determined unambiguously whether it contributed to the Fermi surface as it was below the energy resolution of the instrument. Later determination by dHvA and comparison to the specific heat [200] showed the γ_2 pockets do make up part of the Fermi surface and they play an important role since there are sharp peaks in the density of states just below the Fermi surface within the scale of Zeeman splitting achievable in the laboratory [201]. These peaks, the result of a saddle-type Van Hove singularity, can be attributed as the underlying cause of the observed metamagnetism, as proposed by Binz and Sigrist [212], before even their experimental identification. Since then Van Hove singularities have also been invoked to describe the metamagnetic behaviour in many other theoretical investigations of $Sr_3Ru_2O_7$ [213–218].

In samples with a residual resistivity of 2.4 $\mu\Omega$cm Grigera *et al.* found one first-order metamagnetic transition at ∼5 T with the field directed in the *ab*-plane [178]. By analysing both the real and imaginary parts of the AC susceptibility they could identify the critical endpoint terminating the line of first-order metamagnetic phase transitions at ≈1.25 K. What sparked particular interest was that rotating the field away from the *ab*-plane acts as a continuous tuning parameter for the critical endpoint. The critical endpoint moves to slightly higher fields as the field is rotated towards the *c*-axis but when the field is aligned within 10° of the *c*-axis the endpoint is depressed to below 50 mK, the base temperature of the measurements. With the field oriented along the c-axis there is clear evidence for quantum criticality, and this will be the subject of the next section.

4.2.2   Quantum criticality

Phase transitions are abundant in nature and associated with them are certain critical phenomena which, even though the microscopic orders may be completely different, give rise to many fundamental characteristics [219]. Phase transitions appear due to the necessity to balance ordering energy against the entropy of thermal fluctuations. For example, in a ferromagnet the exchange interaction favours the alignment of spins reducing the internal energy but at higher temperatures thermal fluctuations can maximise the entropy and the system prefers the disordered paramagnetic state. At such a second-order phase transition the order parameter, in this case the magnetisation M, is on average zero in the disordered phase and grows continuously from zero once the ordered phase is entered at the transition temperature. Even though the spatial average of the order parameter is zero in the disordered state, upon approaching

the phase transition droplets of order start to grow and fluctuate in and out of existence, i.e. some short range order develops. In the case of a ferromagnet one can say the spins are correlated over a short range called the correlation length. As the critical point is approached the correlation length diverges, $\xi \sim |(T - T_c)/T_c|^{-\nu}$ [11], and at the critical point the system becomes scale invariant. The critical nature of a thermal phase transition is only observed very close to the transition. The microscopic details become unimportant once there is no length scale other than the correlation length and the system is averaged over large distances. Here the behaviour falls into a universality class which only depends on the dimensionality and the symmetry of the order parameter, and the relevant statistical physics can be treated classically.

All this changes though if there exists a non-thermal tuning parameter, such as pressure, doping or magnetic field, that can suppress the transition temperature to absolute zero (see figure 4.9). A quantum phase transition is accessed at absolute zero and here it is no longer the thermal fluctuations that melt the order but rather the abrupt change of ground state is due to quantum fluctuations arising from Heisenberg's uncertainty principle. Since the critical nature of a thermal phase transition is only observed very close to the transition, one might ask why a quantum phase transition should be any more than just an academic curiosity since absolute zero temperature is never a practically achievable temperature. The answer is because unlike a thermal phase transition the effects of quantum criticality can be felt over a surprisingly much larger range.

The time scale of quantum critical fluctuations also depend on the distance from the critical point, but here the distance is along the tuning axis, $\tau \sim |p - p_c|^{-\nu z}$ [12]. The energy of these fluctuations goes to zero at the critical tuning, but even away from this tuning sufficiently high temperatures allow thermal population of finite-time modes associated with the quantum mechanically driven phase change, so the system can still look critical. In this scenario the dominant fluctuations are thermally driven but the fluctuations are those of a scale invariant quantum-critical ground state. This region defines the cone of quantum criticality shown in figure 4.9.

Pronounced effects due to quantum critical fluctuations have been observed experimentally and extensively studied, especially in heavy fermion materials [220, 221]. Here, relatively low temperature magnetic states are often found and these can be successfully suppressed to absolute zero by the application of magnetic field, doping, or pressure, leading to a quantum critical point (QCP). Some common behavioural traits are observed. The residual specific heat coefficient γ diverges upon approaching the quantum

[11] ν is a critical exponent. It characterises the nature of the phase transition and is an experimental observable.
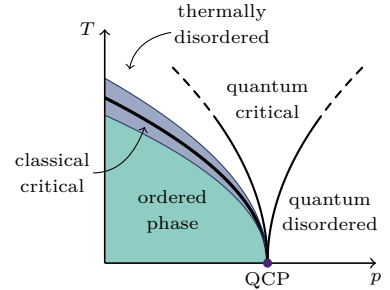
Fig. 4.9: **Quantum critical point.** Schematic phase diagram of a second-order phase transition giving rise to a quantum critical point. p is a non-thermal tuning parameter that suppress a second-order phase transition, thick black line, to absolute zero at the quantum critical point. At finite temperature and sufficiently close to the transition a classical critical region exists where the critical fluctuations are much lower in energy than the temperature and the thermal phase transition is universal. The effect of the quantum critical fluctuations, however, can be observed over a much larger region of phase space, see text for further details.

[12] z is the dynamical critical exponent.
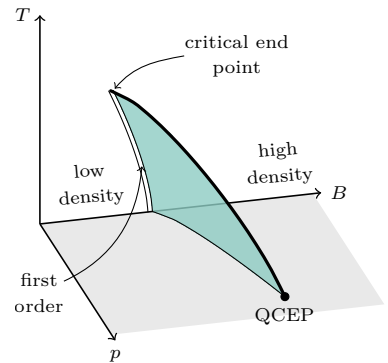
Fig. 4.10: **Quantum critical end point.** Schematic of a first-order transition giving rise to a quantum critical end point. A first-order transition with tuning parameter B has a critical end point when there is no symmetry breaking. If a second non-thermal tuning parameter, p, can suppress the critical end point to absolute zero a quantum critical end point is produced. In the case of $Sr_3Ru_2O_7$ p can be related to the angle of the applied field.
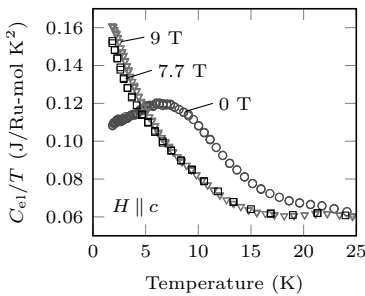
critical point, and this along with the observation of the resistivity exhibiting a linear temperature dependence seems to imply that the mass of the quasiparticles is diverging, and their characteristic energy scale vanishing, leaving only temperature as the remaining energy scale [219].

The fermionic criticality that creates this strange metallic state is still not fully understood, but QCPs provide more than just an exciting opportunity for modern theory because they are also a breeding ground for new stable phases of matter. Rather than face the mass divergence close to the QCP, more often than not it is observed that the electrons reorganise themselves into novel forms of order.

$Sr_3Ru_2O_7$ also shows quantum critical behaviour, but through a slightly different route. The quantum critical point as introduced above was achieved by suppressing a classically critical second-order phase transition to absolute zero using a non-thermal tuning parameter. The situation in $Sr_3Ru_2O_7$ is slightly different. As we saw in section 4.2.1, $Sr_3Ru_2O_7$ shows a first-order metamagnetic transition. Normally there are no critical fluctuations at the discontinuous jump of a first-order transition but since there is no symmetry breaking there is generally a critical endpoint terminating the line of first-order transitions and here critical fluctuations responsible for critical opalescence are observed. By suppressing the critical endpoint to absolute zero a quantum critical endpoint (QCEP) is obtained, exhibiting all the hallmarks of a quantum critical point.

With the field directed along the sample's *c*-axis, the QCEP is reached with a field of ∼8 T, and the magnitude of the field acts as a tuning parameter for the quantum critical fluctuations [222]. Measurements of the temperature-dependent resistivity at a series of applied fields spanning the quantum critical region show the classic behaviour of a QCP, see figure 4.11. At both low and high fields Fermi liquid T^2 temperature dependence is observed but over a smaller and smaller temperature window as the QCEP is approached and at the critical field T-linear resistivity is observed. Thermodynamic measurements are also consistent with the quantum critical scenario. Measurements of the temperature-dependent electronic specific heat show that in the vicinity of the critical field the low temperature specific heat diverges logarithmically [203], see figure 4.12.

As pointed out earlier, bare QCPs are not often observed in clean systems. Instead, a phase transition usually preempts the QCP. When the sample quality is high enough in $Sr_3Ru_2O_7$ this is also observed. There is often a tendency for superconductivity to form around a QCP [223] but the large magnetic fields used to reach the QCEP in $Sr_3Ru_2O_7$ prohibit superconductivity and an

Fig. 4.11: **Resistivity power law.** Temperature dependence of resistivity measurements of $Sr_3Ru_2O_7$ near the metamagnetic transition for fields applied along the *c* axis. The exponent of the temperature dependent part of the resistivity is plotted under the assumption that the resistivity varies as $\rho = \rho_0 + AT^\alpha$. Reproduced from [222].

Fig. 4.12: **Electronic specific heat.** The low temperature electronic specific heat of $Sr_3Ru_2O_7$ with magnetic field aligned along the sample's *c* axis. Close to the metamagnetic transition field 7.9 T the specific heat diverges logarithmically. Reproduced from [203].

alternative form of order develops. The next section will discuss the unusual properties of this novel phase.

4.2.3 Novel ordered phase

The appearance of the new phase in ultraclean samples was first identified by its striking resistive response and its magnetic susceptibility signature shown in figure 4.13 [224]. This novel phase is only observed in samples with residual resistivities less than $\sim$1 $\mu\Omega$cm so is highly disorder sensitive [224, 202]. Instead of the single metamagnetic jump at around 8T when the field is along the *c*-axis it is seen to bifurcate into two, one at approximately 7.85 T and 8.1 T. Between these fields the in-plane resistivity is enhanced by almost a factor of 2 with a sharp jump upon entering and leaving the phase. Later, a thorough series of thermodynamic measurements, including magnetisation, susceptibility, magnetostriction and thermal expansion, firmly established the thermodynamic phase change [180]. The phase is bounded by first-order transitions on both the low and high field sides which terminate at critical endpoints and are connected by a second-order line defining the roof of the phase. The appearance of this stable phase, in a region of phase space where electron-electron correlations are know to be particularly strong, received much attention, and it has been extensively studied. However there are still many puzzling questions which mean the order parameter has not yet been firmly established. I will now discuss the main experimental results, outlining the established properties of the novel phase and outline some of the remaining questions.

4.2.3.1 Electron nematicity

After an in-depth study of the magnetoresistivity not only as a function of field and angle to the *c*-axis but also the angle between the current and field by Borzi *et al.* [182] a large magnetoresistive anisotropy was identified in the region of novel phase formation. The observed transport properties demonstrate the key features of an electronic nematic state. This name comes from analogy with the nematic phase found in classical liquid crystals where elongated cigar-shaped molecules self-organise, breaking rotation symmetry but remaining spatially homogeneous, preserving translational symmetry. The equivalent state in an electronic system is developed when, due to the effects of electron correlations alone, the electronic degrees of freedom spontaneously develop a lower rotational symmetry than the lattice, breaking its point group symmetry. In a tetragonal crystal for example, this could be when the resistivity shows C_2 rotational symmetry while the lattice remains C_4 symmetric [13]. This behaviour appears to be exhibited by the novel phase
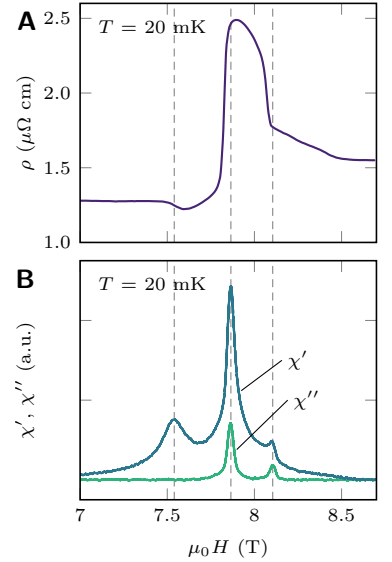
Fig. 4.13: **Resistivity and susceptibility signatures of the novel phase masking the QCEP. A.** The resistivity jumps by almost a factor of 2 upon entering the phase at $\sim$7.9 T and drops again steeply as the phase is exited at $\sim$8.1 T. **B.** AC susceptibility shows two first order transitions, one entering and exiting the phase, and an additional crossover at a lower field $\sim$7.5 T. Reproduced from [224].

[13] In the presence of any finite coupling between the outer electrons and the lattice, this electronic symmetry breaking will cause a lattice symmetry breaking, so in practice it comes down to a question of degree. If there is a small electronic change and a large structural one, the transition should be thought of as structural; if the reverse, it is described as an electronic state.
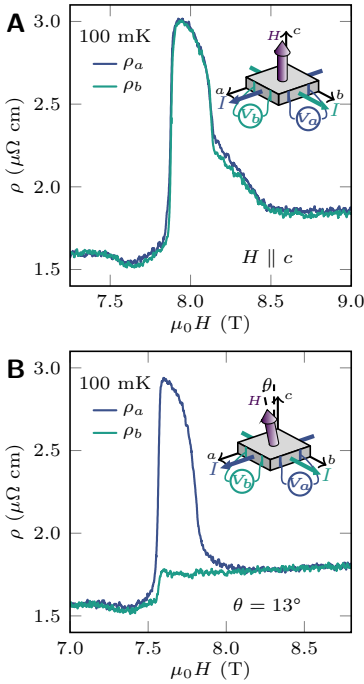
Fig. 4.14: **Electron nematic transport.** The two in-plane principle resistivity components, ρ_a and ρ_b, measured with different angles between the applied field and crystal axis. **A.** For field applied along the c-axis there is almost no anisotropy. **B.** With the field 13° from the c-axis tilted towards a a pronounced anisotropy is seen. The easy direction for current is along b, and the hard direction along a. Tilting the field towards b rather than a reverses the hard and easy directions. Reproduced from [182].
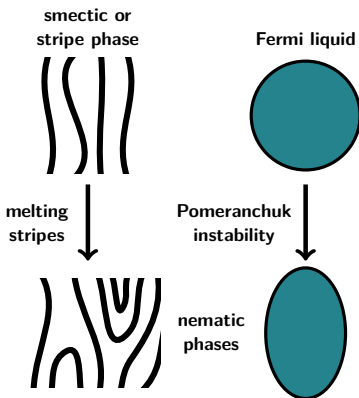
Fig. 4.15: **Electron nematics.** Two different mechanisms for producing electron nematic phases, see text for details. Reproduced from [226].

of $Sr_3Ru_2O_7$. Figure 4.14 shows the magnetoresistance measured along both the a and b crystallographic directions. In panel A, when the field is aligned with the c-axis, no in-plane anisotropy is observed but with a small tilt of the applied field, panel B, a significant anisotropy develops in the region of phase formation while the resistivity remains isotropic outside. Accompanying neutron diffraction measurements could not resolve any deviation from the square lattice, strongly suggesting that the anisotropy is electronically and not structurally driven. However, a small in-plane component of field is still required for the two-fold symmetric state to reveal itself. This last point though was attributed to possible domain formation that might occur when the field is first applied along the c-axis. In such a picture the effect of the in-plane field is merely to align the domains of orthogonally oriented order.

Electron nematic behaviour is usually considered from two different viewpoints, depending on whether the electrons are strongly or weakly coupled [225–227]. In the strongly coupled picture large Coulomb repulsion and exchange interaction terms tend to favour the localisation of the charge carriers but the addition of a small number of holes to the mix, which due to zero-point kinetic energy prefer to be delocalised, can lead to phase separation and the appearance of stripe phases [228]. Under the right circumstances one can imagine the melting of these stripe phases where the global translational symmetry breaking is lost but some resemblance to the striped phase is retained and a special orientation is picked out breaking rotational symmetry [229]. This state would be an electron nematic and can be thought of as a melted smectic phase [230, 231], see figure 4.15.

The physics of more weakly coupled electrons is well described by Fermi liquid theory, but there are many known instabilities of the Fermi liquid, a general phenomenological description of which was given by Pomeranchuk [232]. Fermi liquid theory quantifies the strength of the various possible interactions by the Landau parameters, also know as the f functions (see section 1.2). It is well known that the stability of the Fermi liquid requires that none of these interaction terms become too negative, i.e. attractive, because if they do, a distortion of the Fermi surface can occur, known as a Pomeranchuk instability. For an isotopic interaction term the Pomeranchuk instability is that of ferromagnetism spin splitting the Fermi surfaces. In the case of higher order interactions, such as a quadrupolar interaction, nematic instabilities can develop and anisotropic deformations of the Fermi surface can occur. In $Sr_3Ru_2O_7$ possible spherical to elliptical deformations of the Fermi surface have been proposed to be stabilised by the close proximity of Van Hove singularities and through spin-orbit coupling related effects [213–218].

It is difficult to reconcile the magnitude of the observed resistive
anisotropy with the intrinsic anisotropy from a distorted Fermi
surface due to a Pomeranchuk instabilities, especially considering
this is a multiband material. However, considering there ought to
be domains with orthogonally oriented nematic order, domain wall
scattering could account for a substantial fraction of the enhanced
resistivity. As I will show later on, this may not be the whole
picture, and an alternative explanation may still be needed.

4.2.3.2 Spin density waves

It is now known from a recent breakthrough magnetic neutron scat-
tering experiment that, in addition to the uniform metamagnetism
associated with the novel phase, there exists spatially modulated
magnetic order within the region of phase formation [181]. In the
discussion of the Stoner criterion and metamagnetism in section
4.2.1 an isotropic magnetisation was always assumed. In general,
however, periodic spatially varying magnetic states can also be
stabilised in certain situations and are called spin density waves
(SDW). The susceptibility at a certain modulation wavevector de-
pends on the properties of the Fermi surface. When large sections
of Fermi surface are parallel such that they can be connected by the
same vector in reciprocal space the susceptibility will be strongly
peaked at this wavelength which can easily mix these states, open-
ing a gap and lowering their energy [205]. These special vectors are
called nesting vectors and are generally found in quasi-1D systems.
Sufficiently strong nesting can also lead to charge density waves
(CDW). The mechanism is similar, though this time driven by a
spatial modulation of the charge density, i.e. a Peierls distortion
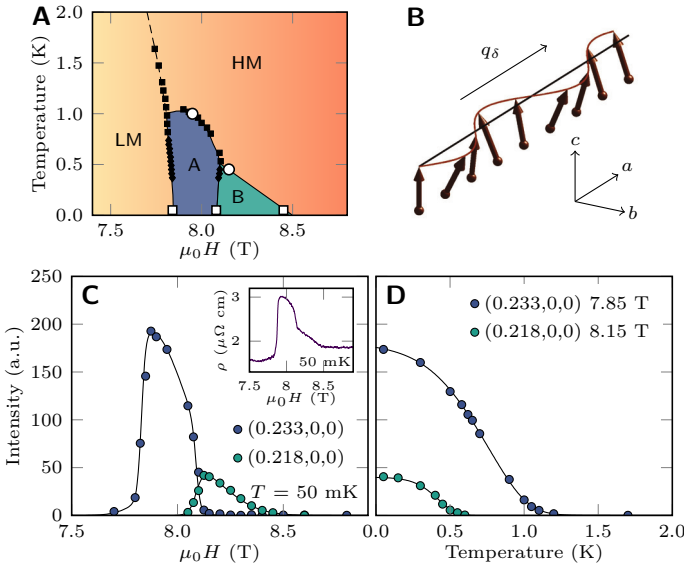
Fig. 4.16: **Spin density wave or-
dering in $Sr_3Ru_2O_7$. A.** Phase dia-
gram determined from neutron scat-
tering measurements. Open sym-
bols are the boundaries determined
from the scattering measurements
whereas the solid symbols are from
resistivity and susceptibility mea-
surements. The two blue shaded re-
gions mark the regions with SDWs of
different wavevectors. **B.** Proposed
structure of the spin density wave
within a single domain. **C and D.**
Magnetic field and temperature de-
pendence of the SDW Bragg peak
intensities. Reproduced from [181].

of the lattice. SDWs and CDWs can occur simultaneously but in suitably exchange-enhanced materials such that the susceptibility is sufficiently large that the *q*-dependent Stoner criterion is satisfied, spin ordering can occur alone. CDWs are primarily driven by electron-phonon coupling whereas SDWs arise from the electron-electron exchange interaction.

Lester *et al.* observed magnetic scattering peaks associated with an incommensurate spin density wave (SDW), i.e. its wavelength is not a rational fraction or integer multiple of the lattice constant, and stable at least on time scales shorter the instrument resolution of ∼1 GHz with a coherence length of at least 350 Å. Within the main novel phase described above the scattering peaks were observed at $(\pm\delta, 0, 0)$ and $(0, \pm\delta, 0)$ with δ=0.233. Above the second metamagnetic transition a spin modulation was still observed but with a slightly smaller wavevector, δ=0.218, persisting up to approximately 8.5 T. Comparing with the resistivity, figure 4.13A, this new phase corresponds to the tail observed on the high field side of the phase. Bruin *et al.* [233] had also previously reported resistive anisotropy extending outside of the main phase up to these fields. The formation of the SDW and the enhanced resistivity appear intimately linked. Panel C of figure 4.16 shows the intensities of the two scattering peaks, and once summed together they look remarkably like the observed resistivity enhancement. Further evidence corroborating this comes from the influence of a tilted field on the SDWs. When the field is along the *c*-axis the scattering peaks are C_4 symmetric, showing equal intensity at $(\pm\delta, 0, 0)$ and $(0, \pm\delta, 0)$, but once the field is tilted 10° towards the *a* axis only the peaks at $(\pm\delta, 0, 0)$ remain, mirroring the hard and easy directions observed in in-plane resistivity. A spin density wave gapping part of the Fermi surface provides a natural mechanism for enhancing the resistivity in the novel phase. The wavevector approximately matches the nesting vector of the α_1 and the γ_2 sheets. However, in this multiband material the number of states that can be gapped out in this simple weak-coupling picture still seems to be at odds with the 100 % resistivity increase.

The addition translational symmetry breaking of a spin density wave means the phase should no longer be described as a truly nematic state. However, a question of time scales means this cannot be irrefutably proven, especially since nuclear magnetic resonance measurements that are sensitive to much slower characteristic frequencies than the resolution limited neutron scattering measurements did not detect any divergence of the inverse relaxation rate associated with critical slowing down at the boundary of the A phase [234]. This means that a more slowly fluctuating smetic or melted smetic can not be indisputably ruled out.

4.2.4 Latest developments and motivation

Further investigation of the wider phase diagram has recently highlighted the possibility of a much richer phase diagram still to be discovered. Sun *et al.* [235] managed to measure heat capacity and magnetocaloric effect to much lower temperatures than had previously been attainted in $Sr_3Ru_2O_7$ and by following the signatures associated with each metamagnetic transition to lower temperatures could identify the first metamagnetic peak at ∼7.5 T, initially believed to be a crossover, with a second QCEP. There is evidence for a second lower energy scale suppressed to zero temperature at 7.5 T in addition to the QCEP already identified at 7.9 T which in the highest purity samples is masked by the novel phase formation. Measurements of the magnetic Grüneisen parameter by Tokiwa *et al.* [179] also demonstrated the same behaviour. Weak thermodynamic signatures for the second SDW-B phase can also be identified in the specific heat and magnetocaloric effect, however, the confidence with which the phase boundary can be identified is much lower than in the case of the A phase. Perhaps, then, even though these samples are considered to be of very high purity, there may still be an opportunity to uncover more phase formation in the remaining parts of the phase diagram which may be even more disorder sensitive. This might also help to explain the curvature of the first-order transition line at 7.85 T which implies that the entropy is higher in the ordered phase than that on either the high or low field sides of the phase.

What is clear though, is that any further investigations on $Sr_3Ru_2O_7$ should be wary of disorder as it is clearly very important. Magnetic field is a clean tuning parameter, ideal for tuning through the quantum critical region, and as such has been studied in great depth. Uniaxial stress is another clean and continuous tuning parameter so can be used as a secondary tool to investigate quantum criticality in combination with a *c*-axis oriented magnetic field. It is suspected that the metamagnetism is related to Van Hove singularities that can be reached in an ∼8 T field. The influence of uniaxial stress might therefore be quite strong so a study of the interaction between uniaxial stress and magnetic field on the metamagnetism and the influence around quantum criticality is of interest.

The properties of the novel phase are also known to be highly susceptible to in-plane fields lifting the tetragonal symmetry. Uniaxial pressure can provide an alternative method for tuning this symmetry breaking and it can, in principle, provide a much larger strength change than the previously used in-plane magnetic fields which simultaneously detune from the QCEP as the in-plane field is increased. However, it is not easy to predict what effect uniaxial pressure might have as the band structure is much more compli-

cated in $Sr_3Ru_2O_7$ than in Sr_2RuO_4, so the initial investigations will rather be somewhat exploratory.

4.3   Experimental methods
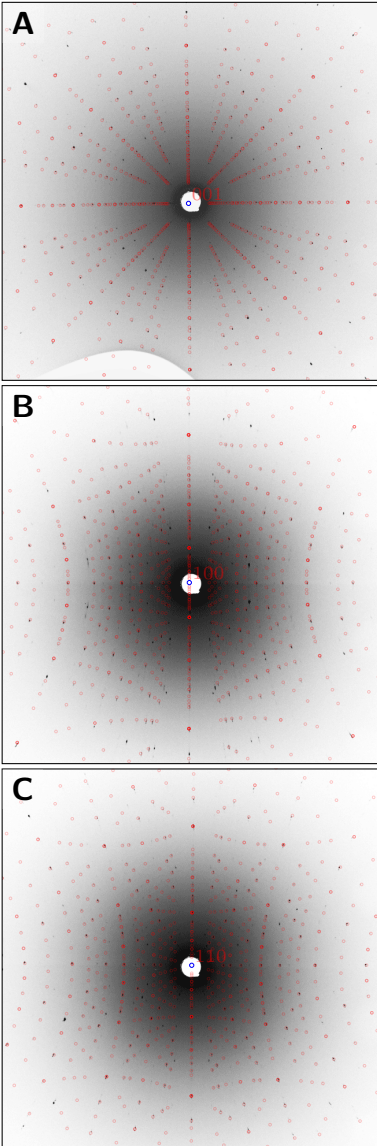
The core method used for the experiments on $Sr_3Ru_2O_7$ is the uniaxial stress technique described in chapter 2 of this thesis. In this technique the direction along which the uniaxial pressure is applied is set by the direction along which the long bar shaped sample is cut. For the remainder of this chapter I will use the tetragonal unit cell of $Sr_3Ru_2O_7$ where the a and b directions, [100] and [010], are along the Ru-O-Ru bond directions. The neutron scattering results indicate that the $\langle 100 \rangle$ directions are the principal axes of the possible C_2 symmetric order. Resistivity measurements in a fully rotatable vector magnet field also suggest this, showing strong anisotropic transport when the field has a component along [100] or [010] but very little $[110]/[1\bar{1}0]$ anisotropy when the field is at 45° to the Ru-O-Ru bond directions. Guided by these observations we chose to cut the samples along $\langle 100 \rangle$, defining the pressure axis. Only the ends of the sample are supported in the device, meaning that for instance when a compression is applied along [100], the [010] direction in the centre of the sample is free to expand according to the sample's own Poisson's ratio. The applied stress is uniaxial but the design of the device means that we can more accurately determine the applied strain along the pressurised direction.

In total four different $Sr_3Ru_2O_7$ samples were strained. The first three samples were measured in collaboration with another student, Daniel Brodsky, and the results have been published in references [236, 237]. After this first run of measurements I came back to the project to add magnetic measurements in addition to resistivity, and to also carry out a wider investigation covering more than just one temperature and going to much larger strains. In doing this, the measurements from the first three samples were necessarily repeated as part of this larger data set but since these have been described elsewhere I will only present data from this fourth sample in this thesis. I mention the other three samples to show that consistency, at least in the resistivity measurements at low strains, is observed.

4.3.1   Sample preparation

The sample was cut from a well characterised growth, C697B, from R. Perry. This batch was chosen because of its particularly low residual resistivity and low impurity content, as characterised by J.-F. Mercure [238]. The novel phase in this batch of crystals has

Fig. 4.17: **Sample alignment.** Pictures of X-ray back-reflection Laue diffraction patterns with simulated fits from OrientExpress [144] overlaid in red. **A** c-axis aligned with the X-ray beam, **B** [100] direction and **C** the [110] direction of the tetragonal unit cell.

also been extensively studied by resistivity measurements [199]. As stressed earlier in this thesis precise sample preparation is a necessity for reaching high strain. To prepare the sample, the main growth rod was first aligned using the Laue method, figure 4.17, and then transferred to a lapping saw to cut out a bar shape of roughly the required size. The sample was then finished using fine mechanical polishing on all faces to bring the sample to its final dimensions and produce the highest quality surfaces. The result can be seen in figure 4.18.

Details of the sample mounting are described in chapter 2 along with the procedure for determining the optimal dimensions of the sample and epoxy thickness to prevent sample buckling or epoxy failure. For these measurements the range of the device was not pushed to its upper limits because a thorough investigation at different temperatures and fields, all on the same sample, was more important than the absolute highest strain. I therefore decided to reduce the strain range to decrease the risk of breaking the sample or epoxy. In fact, $Sr_3Ru_2O_7$ appears to be slightly softer than Sr_2RuO_4, because no slippage of the epoxy was observed so there should be slightly less risk in going to higher strains in the future. The fact that the RuO_4 octahedra are already buckled in $Sr_3Ru_2O_7$ may be the cause of the softer in-plane modulus but the elastic tensor of $Sr_3Ru_2O_7$ has not been measured to verify this.
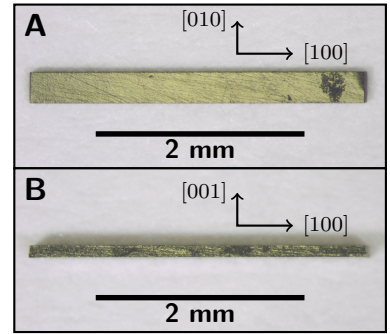
Fig. 4.18: **Cut and polished sample.** Sample before attaching electrical contacts and mounting in the rig. **A.** *ab*-face. **B.** *ac*-face. Crystallographic directions are labelled as per the tetragonal unit cell. The sample has dimensions: length 3.2 mm, width 295 μm, and thickness 110 μm.
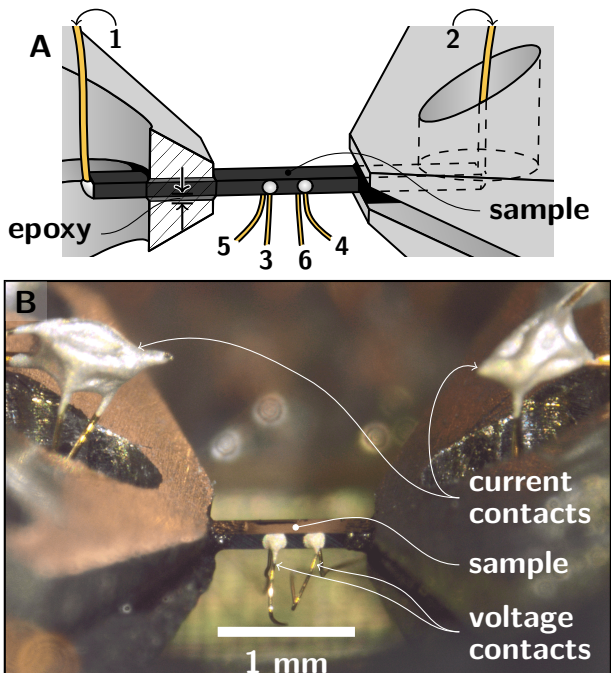
Fig. 4.19: **Mounted Sample. A.** Mounting schematic showing the epoxy holding the sample between the sample plates. The schematic is the same as that given in chapter 3 but it is included here because it defines the resistivity contact numbering. **B.** Mounted sample showing the electrical resistivity setup. The gap between the two sample plates was set to 1.1 mm and the epoxy was 25 μm thick giving a strain transmission of $\sim$70 %.

4.3.2   Resistivity measurements

The aim of these measurements was to observe the resistivity response to strain simultaneously with the magnetic response. It would also be ideal to measure both principal in-plane resistivity components and determine any nematic-like behaviour. The geometry of the sample means that measurements of the longitudinal resistivity are straightforward. The ends of the sample are accessible through holes in the sample plates for current contacts, see figure 4.19, and voltage contacts placed in the central region of the sample can measure the voltage drop in the homogeneously strained region of the sample. From this an accurate measurement of ρ_{xx} can be made were x is the direction along which the pressure is applied.

Measurements of the transverse resistivity can also be made using only the four contacts in the centre of the sample. Making reference to figure 4.19, instead of passing current along the bar between contacts 1 and 2, current can be passed between contacts 3 and 5 measuring the voltage drop between contacts 4 and 6. This measured voltage is not independent of the longitudinal resistivity ρ_{xx}, which sets the distance that the current stream lines spread out along the length of the sample, but with precise enough information on the contact geometry finite element simulations should be able to disentangle the different resistivity components. The measured voltage at contacts 4 and 6 decreases exponentially with their distance from the current contacts 3 and 5. It is therefore best for the transverse measurement to have the contacts on the sides of the sample close together, however, the measured longitudinal voltage decreases linearly with the contact separation so a balance between the two must be made. As in the study reported in chapter 3 for Sr_2RuO_4, for this $Sr_3Ru_2O_7$ sample the contacts were placed approximately 300 μm apart, making their overall placement approximately square as a compromise between the two.

To prevent buckling the sample must be relatively thick. This, in combination with the close proximity of the contacts to facilitate the transverse measurement, means that the resistance of the measured part of the sample is very small. At low temperatures it is approximately 45 $\mu\Omega$. Driving a current though the sample and back into ground through the long resistive wires on the cryostat insert leads to a large common mode voltage beyond the maximum rejection ratio of standard preamplifiers. To prevent this common mode signal artificially leaking into the differential measurement I used the balanced dual end current source which I designed and built for the resistivity measurements on Sr_2RuO_4. The details of this can be found in appendix A. The key point is that by using a balanced current source with active feedback the common mode can be reduced to less than $\sim$0.5 % of the signal compared to the

residual resistivity and the effects of common mode voltage can then be ignored.

An absolute measurement of the transverse voltage is needed before attempting any sort of finite element analysis but so far all the transverse measurements published in [236] had an extrinsic field dependent background that dominated the signal. I managed to remove the source of this background by identifying wire vibration as its source and taking much more care when wiring up the sample. I made all the wires as direct and as short as possible, removing the possibility of any large oscillatory modes which could vibrate in the strong magnetic field. All the contacts also had twisted pairs for both measurement geometries, doubling the amount of wiring required for the experiment, but achieving the best noise levels.

4.3.2.1 Finite element simulations

A finite element simulation of the resistivity to extract ρ_{yy} from the measured transverse voltage needs to include the effects of magnetic field and anisotropic resistivity. This is something that is not always included with simple software packages so to facilitate this analysis I programmed a complete finite element simulation myself. Chapter 2 of this thesis provides a basic introduction to the finite element technique but with the aim of solving elastic deformation problems. The basic principles of a resistivity simulation are the same but the partial differential equation that needs to be solved is different.

From classical electrostatics we known that the electric potential, ϕ, at any point within the sample can be calculated from the electric field, $\boldsymbol{E}$, by

$$\boldsymbol{E} = -\nabla\phi\,. \tag{4.11}$$

The current density at any point within the sample, assuming we are in a linear transport regime, only depends on the conductivity tensor $\boldsymbol{\sigma}$

$$\boldsymbol{J} = \boldsymbol{\sigma}\boldsymbol{E}\,, \tag{4.12}$$

where the conductivity of an anisotropic material is expressed as

$$\boldsymbol{\sigma} = \begin{pmatrix} \rho_{xx} & -\rho_{xy} & -\rho_{xz} \\ \rho_{xy} & \rho_{yy} & -\rho_{yz} \\ \rho_{xz} & \rho_{yz} & \rho_{zz} \end{pmatrix}^{-1}. \tag{4.13}$$

The off-diagonal terms are the field dependent Hall terms which, if the Hall effect is linear, can be written

$$\rho_{ij} = B_k R_{\mathrm{H},ij}\,, \tag{4.14}$$

where B_k is the perpendicular component of magnetic field. Charge

conservation necessitates that

$$\nabla \cdot \boldsymbol{J} = -\frac{\partial \rho_q}{\partial t}\,, \qquad (4.15)$$

but for a steady state solution the charge density, ρ_q, is constant so the differential equation we need to solve over the volume of the sample, Ω, is

$$\nabla \cdot (\boldsymbol{\sigma} \nabla \phi) = 0\,. \qquad (4.16)$$

Neumann boundary conditions are imposed on the surfaces of the sample, $\partial \Omega$,

$$\boldsymbol{J}_\perp = (-\boldsymbol{\sigma} \nabla \phi) \cdot \boldsymbol{n}(\boldsymbol{x}) = f(\boldsymbol{x}) \quad \forall \boldsymbol{x} \in \partial \Omega \qquad (4.17)$$

where $\boldsymbol{n}(\boldsymbol{x})$ is the normal to the samples surface at $\boldsymbol{x}$ and the scalar function $f(\boldsymbol{x})$ is zero everywhere except at the current contacts where it equals the applied current density. The formalism from here on in is as per the standard finite element approach: the partial differential equation is rephrased in its weak form, the geometry discretised, and the electric potential solved numerically.

My original aim was to measure ρ_{xx} and V_{46}/I_{35} then use finite element simulations to calculate ρ_{yy} across the whole phase diagram as a function of temperature, field and strain. This information can provide important insights into the nature of phase transitions and can be used to calculate several components of the elastoresistivity tensor [239], a fourth-rank tensor relating normalised resistivity changes with applied strain,

$$m_{ij,kl} = \left.\frac{\partial(\Delta\rho/\rho)_{ij}}{\partial\varepsilon_{kl}}\right|_{\boldsymbol{\varepsilon}=0}\,, \qquad (4.18)$$

which therefore incorporates more information than the resistivity tensor alone. Anomalies in the resistivity in regular transport measurements do not in general help when trying to identify the type of symmetry breaking at a phase transition but the elastoresistivity tensor is a probe for this and can be used as a direct measure of thermodynamic susceptibilities. However in order to test specific symmetry breaking susceptibilities an experimental probe of the same symmetry is required. In-plane anisotropic strain is one such probe and would be of a great importance here as it can be used as a direct probe of nematic susceptibility and electronic nematic phase transitions.

Unfortunately this complete nematic susceptibility analysis was not possible for $Sr_3Ru_2O_7$ with the current experimental setup, because of the large ρ_c/ρ_a resistive anisotropy. Layered materials with large resistivity anisotropies are known to be particularly problematic for measuring the in-plane resistivity accurately, because it is easy to accidentally incorporate a component of ρ_c into the

Fig. 4.20: **Finite element electrical resistivity simulations. A.** Finite element simulation of the longitudinal resistivity setup. Real sample dimensions from figure 4.18 were used and the room temperature resistivity tensor. At zero field the components are $\rho_{aa} = \rho_{bb} = 232\ \mu\Omega$ cm and $\rho_{cc} \approx 8.5\ m\Omega$ cm [188]. The simulations are with an applied current of 1 mA. **B and C.** A simulation of the transverse resistivity setup showing the electric potential and current density stream lines.

measurement. For longitudinal resistivity measurements this problem is generally solved by taking meticulous care when painting the silver paste contacts at the ends of the sample, making sure to short out all the planes over the thickness of the sample. The long length of the sample is enough to compensate for any slight variations in contact resistance across the contact and a good in-plane resistivity measurement can be made. For the transverse resistivity measurement I also made sure the silver paste contacts covered the full height of the sample but it appears that the current flow still had a small c-axis component which is almost unavoidable when trying to keep the contact area as small as possible. The effect is additionally amplified by the short width of the sample in this direction. At room temperature where the resistive anisotropy is not so high, $\sim$40, the measured transverse voltage is in good agreement with finite element simulations. However at low temperatures where the resistive anisotropy is substantially higher, in excess of 500 [188] (but this has not been measured for the purest samples so it may be higher still as was seen in Sr_2RuO_4 [6]), there is a large discrepancy between the measured voltage and the simulations, with the measured voltage being over a factor of two larger than the prediction. Correspondingly, the measured residual resistivity ratios for the longitudinal and transverse measurements show the same discrepancy. If a small offset is made to the position of the contacts in the simulation, moving the contacts up on one side of the sample and down on the other, the contacts only need to be displaced as little as 4 μm to induce this difference. For a sample that is 100 μm thick it is entirely possible that slight variations in the contact quality can account for this.

In light of this, the data presented here will not be converted from measured transverse voltage to resistivity as the uncertainty in exact contact geometry means the contributions from ρ_{zz} and ρ_{yy} cannot be fully disentangled. When the measurement is described as transverse it refers only to the predominant current direction being transverse to the pressure axis but it does not imply that the current flow is purely within the ab-plane of the sample. The data published on the first three samples also have contributions of a similar nature, but these samples were more than twice as thin (sufficient when not aiming for such high strains), so the unwanted c-axis contribution is slightly smaller. In future, accurate measurements of the elastoresistivity tensor are still highly desirable, but whether this is ultimately achieved just by screening many samples to find one with more symmetrical contacts or by something much more sophisticated such as using a focused ion beam to produce samples with a well defined geometry is still to be determined. This is certainly a key direction to pursue, by whichever route works best.

4.3.3   Magnetic measurements

One of the main aims of this work was to combine magnetic measurements with those of resistivity for a direct measure of how the metamagnetism responds to strain. However, the space around the sample in the strain device is very limited. Whilst AC susceptibility has been used previously for measuring superconducting transitions, measuring normal state magnetic susceptibility is far more challenging. For example, the strongest metamagnetic peak in $Sr_3Ru_2O_7$ with the field aligned along the *c*-axis (Grigera *et al.* measuring at 300 mK [178]) is 50 times smaller than the susceptibility signal of a perfect diamagnet. In order to be sensitive to this small change some improvement in the technique was required. I decided to simulate various coil geometries to work out how to best utilise the available space.

A simulation with an arbitrary coil geometry, number of turns, sample size and alignment, etc, is relatively straightforward using the principles of reciprocity and superposition. After approximating both the excitation and pick-up coils as stacks of single-turn circular current loops, the field at any arbitrary point can be calculated analytically using, for instance, the work of Simpson *et al.* [240]. The sample is also divided up into many small finite elements and the moment of each element can be calculated from its volume, the material's susceptibility and the field at the centre of the element due to the sum of the fields from each of the segments of the excitation coil. For an AC excitation current the AC moment of each finite element induces an AC voltage across the pick-up coils. Calculating the flux threading through each of the pick-up coils due to the sample's moment is quite computationally intensive so a better tactic is to use the principle of reciprocity. The flux threading the coil from the moment is the same as the flux at the moment if the current was in the pick-up coil, this is to say the mutual inductance between the two is identical. The field generated at the position of the sample by unit current in the pick-up coil can be used to calculate the mutual inductance, then from the moment of the sample the induced voltage in the pick-up coil can be calculated without any additional laborious integration steps. This is repeated for all the finite elements of the sample and all the pick-up coils, summing the voltage each time, to find the total signal

$$V_{\mathrm{ac}} = 2\pi f \int\limits_{\mathrm{sample}} \sum_i^{\mathrm{pick\text{-}up}} \left(\frac{\boldsymbol{B_i}(\boldsymbol{x})}{|\hat{I}_i|} \cdot \left(\sum_j^{\mathrm{excitation}} \frac{\chi \boldsymbol{B_j}(\boldsymbol{x})}{\mu_0} \right) \right) dV \, .$$

(4.19)

Here, f is the AC driving frequency, $\boldsymbol{B_i}(\boldsymbol{x})$ is the magnetic field at position $\boldsymbol{x}$ due to unit current $|\hat{I}_i|$ in pick-up coil i, χ is the volume

magnetic susceptibility of the sample and $\boldsymbol{B_j}(\boldsymbol{x})$ is the field at position $\boldsymbol{x}$ in the sample from the excitation current flowing around excitation coil j. When the coils are not compensated this is the additional voltage due to the sample, on top of the background signal from the mutual inductance between the excitation and pick-up coils. Typically the background is much larger than the signal from the sample; it can be calculated using Babic's formula [241]. Demagnetisation effects from the sample's geometry are not included in this simple model but as a first approximation it can provide an adequate comparison of different coil geometries. The code to run these simulations is not very long but may be useful to other groups measuring susceptibility, so it is included in full in appendix D.

The chosen coil geometry is shown in figure 4.21. Superconducting NbTi wire was used for the excitation coil because it enables a large field to be produced without requiring a large number of turns which would take up valuable space; a relatively large current can be used without causing unmanageable heating. With 15 turns of 50 μm wire starting from an internal diameter of 500 μm and making three layers, the field at centre of the coil is ∼9 G with a current of 30 mA (RMS). The pick-up coil diameter was maximised to fill the space inside the excitation coil and was made using 50 turns of 15 μm copper wire. I decided to couple the pick-up coil to a low temperature transformer mounted inside the vacuum can at 4 K. For susceptibility measurements the signal-to-noise ratio can be increased by increasing the driving frequency but because I was wary of finite frequency effects [242, 178] this time I opted for a low temperature transformer with a limited frequency range but capable of achieving a better noise level of ∼40 pV/$\sqrt{\text{Hz}}$. I was only interested in the additional susceptibility signal due to the metamagnetism, so a slowly varying background signal was subtracted from all the data sets using a 3rd-degree polynomial fit to the susceptibility data away from the regions of metamagnetism. This background includes both the background signal from the coils and the normal paramagnetic response of the sample. The coils are not calibrated, so changes in susceptibility are quoted in arbitrary units in all the figures. However the relative amplitude at different strains can still be directly compared since for all the measurements the excitation current and frequency, and all the measurement electronics, remained the same.

4.3.4 Strain transmission

As described in chapter 2, a finite element simulation must be used to estimate how much of the displacement measured by the device is transmitted to the sample through the softer epoxy. Using a
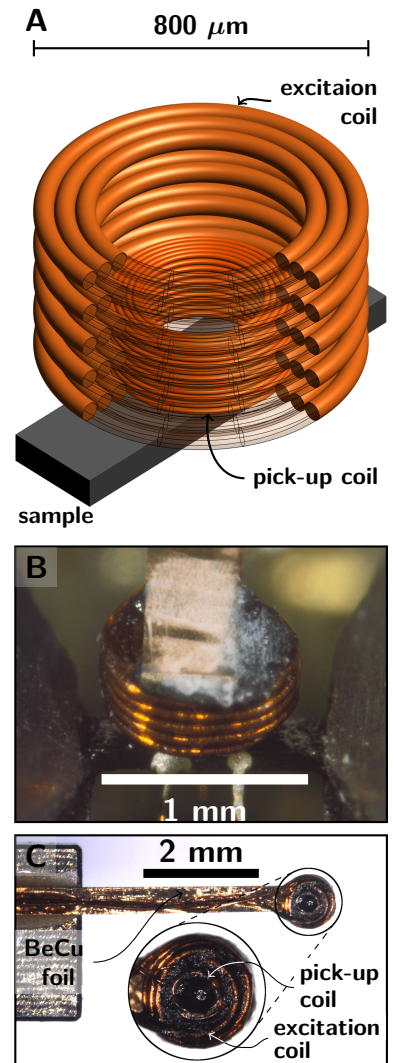
Fig. 4.21: **Susceptibility Coils. A.** Model of the susceptibility coils used in the simulation. The excitation coil has 15 turns of 50 μm wire wound in three layers with diameters 550, 650 and 750 μm. The pick-up coil fits within the excitation coil and consists of 50 turns of 15 μm wire in five layers with diameters from 315 to 435 μm. The pick-up coil rests on the surface of the sample which is 250 μm wide and 80 μm thick. **B and C.** The actual susceptibility setup. The coils are mounted on a flexible cantilever so they can be easily positioned above the sample.

4 K
IVC
flange

Low T
transformer

Sorb

1 K
Pot

³He
Pot

Uniaxial
Stress
cell
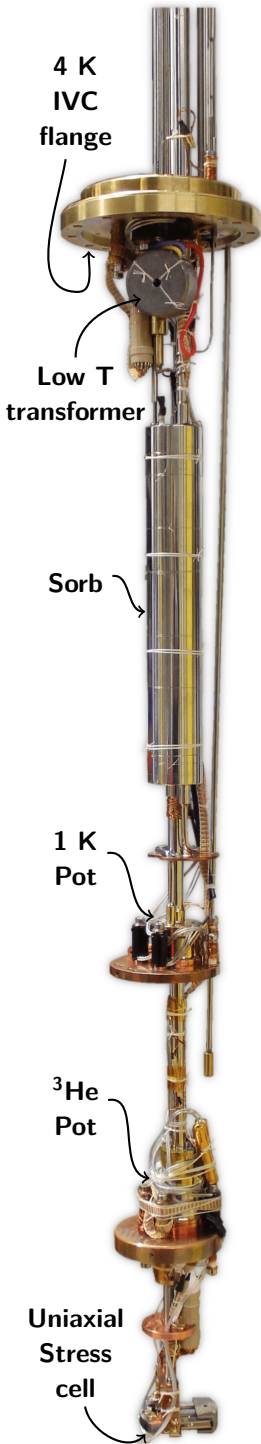
Fig. 4.22: **Low temperature cryostat.**
Business end of a ^{3}He sample in vacuum cryostat. This cryostat has a large 75 mm internal diameter bore to accommodate large uniaxial stress cells.

shear modulus of 6 GPa for the epoxy and the elastic modulus of Sr_2RuO_4 [68] in the absence of a measurement for $Sr_3Ru_2O_7$, the strain at the centre of the sample is approximately 70 % of that calculated using the actual gap between the sample plates (the dimensions of the sample are given in figure 4.18). This is perhaps a slight under estimate as $Sr_3Ru_2O_7$ may well be softer than Sr_2RuO_4 but uncertainty in the exact properties of the epoxy at low temperatures mean all strains are quoted with a 20 % uncertainty, a systematic error affecting all measured strains equally.

4.3.5   Low temperature cryostat

To reach the temperatures needed to observe the novel phase a ^{3}He cryostat was used. The inside of the vacuum can is pictured in figure 4.22. This cryostat, which we specified, ordered and commissioned for this project, has a particularly large bore sample space, 75 mm diameter, providing enough space to have the large strain rig perpendicular to the magnetic field and the magnetic field along the sample's *c* axis. The requirement of the large bore means the maximum field of this system is 10 T. The ^{3}He part of the cryostat is a closed system which can operate down to 270 mK in single-shot mode or in a higher temperature mode up to ∼50 K. The basic principles of the two modes of operation are shown schematically in figure 4.23.

For low temperature operation a regular 1 K pot pumping on ^{4}He from the main reservoir of the cryostat is used to reach ∼1.4 K. This is used as a cold source to condense a small amount of liquid ^{3}He. Heating up the sorb above 25 K causes it to outgas, releasing the adsorbed ^{3}He which then condenses in the column through the centre of the 1 K pot collecting in the lower ^{3}He pot. After about 45 minutes with the sorb at 45 K all the ^{3}He is condensed into the ^{3}He pot, but the temperature is still the same as the 1 K pot. Allowing the sorb to cool starts to pump on the liquid ^{3}He as the ^{3}He vapour is adsorbed back onto the sorb's large surface area, evaporatively cooling the ^{3}He pot. Using ^{3}He much lower temperatures can be reached from evaporative cooling than for ^{4}He. Superfluidity limits the ultimate base temperature and since ^{3}He is a fermion this develops at lower temperatures than in ^{4}He. In this cryostat a base temperature of 270 mK can be reached when the sorb is cooled back to 1.5 K. By varying the temperature of the sorb and/or in combination with resistive heaters at the sample stage the temperature can be controlled precisely between 270 mK and 1.5 K. The sorb continues to pump on the ^{3}He pot until all the ^{3}He has evaporated and the ^{3}He must be recondensed to continue operation. In our cryostat the run time for a single condensing cycle gives us more than 100 continuous hours at 270 mK. After a few
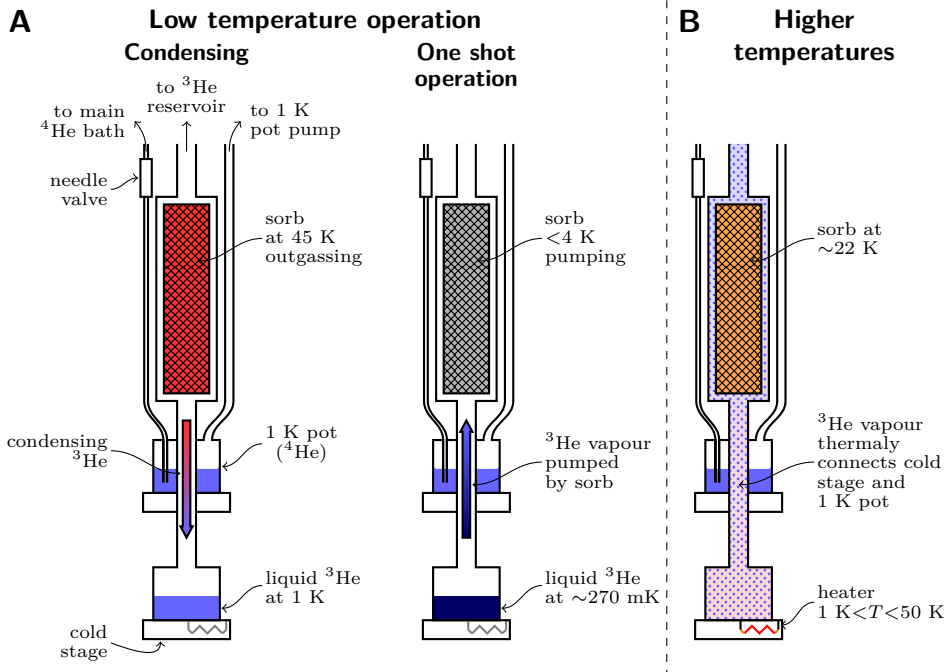
Fig. 4.23: **Principle of operation of the ³He refrigerator. A and B.** To reach temperatures below 1 K the condensing cycle begins by warming up the sorb to 45 K, outgassing the adsorbed helium-3 which then condenses through the 1 K pot into the lower helium-3 pot. Once the sorb is cooled back down it also acts as a pump, evaporatively cooling the ³He pot by readsorbing the helium-3 gas. **C.** To operate at higher temperatures the sorb is held at 22–25 K maintaining a small pressure of helium-3 gas which provides a heat link between the 1 K pot and the sample stage which is heated using a resistive heater. See text for further details.

modifications to accommodate the strain rigs, the additional wires required increase the heat load and limit the base temperature to ∼320 mK. During operation with excitation currents for all the different measurements and a sweeping magnetic field the system warms up a little more to ∼350 mK. To keep the temperature stable throughout the measurement I decided to use a heater at the sample stage running off a PID loop which warms the sample stage up a further 20 mK. The PID control can keep the temperature constant to within ±1 mK while ramping the field up and down to 10 T.

When operating at higher temperatures no liquid ³He remains in the pot. Instead the sorb is held at approximately 20–25 K to provide a small pressure of ³He gas in the system providing a heat link between the sample stage and the 1 K pot. Restive heaters at the sample stage are then used to heat against the cooling power of the 1 K pot and temperatures up to approximately 50 K can be safely reached. It is possible to transition between these the two regimes but while ramping the temperature from 50 K to 300 mK

a stop at 1.5 K must be made to recondense the ^{3}He.

Before starting these measurements I installed and set up the cryostat, measurement rack and computer control for all the instruments. The details of this computer program are described in section 3.3. A key feature of the software was the automation of nearly all measurement routines. This meant the cryostat could be left unattended for several days at a time continuing to record data and, importantly, the control software was capable of automatically recondensing ^{3}He once the pot became empty and then continuing the measurements once the stable base temperature was reached again. The main human interaction needed during the course of this essentially autonomous measurement run was to refill the main helium bath of the cryostat.

4.4   Results and discussions

I will start by presenting the results from the resistivity measurements under strain first and then show the susceptibility data for comparison.

4.4.1   Magnetoresistance

The longitudinal resistivity ρ_{xx} for the strained sample at 370 mK and a series of applied ε_{xx} strains is shown in figure 4.24A. The origin of the strain scale was determined from a number of factors. First, the measurement nearest zero strain should preserve the overall shape that is seen in strain free samples mounted on flexible wires, see for example figure 4.13. Secondly, but less subjective, the transition fields and temperatures of the region of enhanced resistivity should coincide at zero strain for the longitudinal and transverse measurements. Determining these transition fields and temperatures is described later on, see figure 4.36. We estimate the error in identifying zero strain for these measurements to be ± 0.02 %. For the field ramps plotted here the strain was incremented between each field ramp at 10 T, outside the field range, at least initially, of phase formation. This is important because if the phase does involve spontaneous symmetry breaking, increasing the strain within the region of phase formation may lead to metastable domain configurations.

A small lattice distortion has a dramatic effect on the resistivity. In an unstrained sample the resistivity increases by almost 100 % upon entry to the phase with field at low temperatures, but when the sample is compressed to only 0.1 % this enhancement is increased by almost a factor of two. The extent of the field range showing enhanced ρ_{xx} also increases with strain, albeit not so substantially at low strains, and perhaps one of the most striking features is the
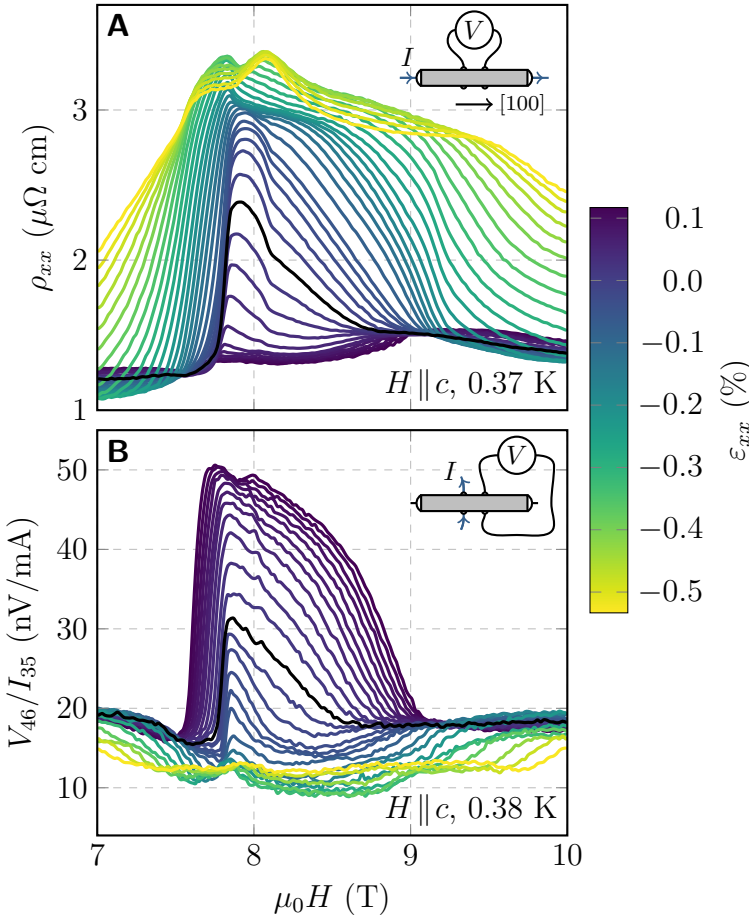
Fig. 4.24: **Magnetoresistance. A.** Longitudinal resistivity ρ_{xx} against c-axis magnetic field for a series of applied strains at 370 mK. **B.** Transverse resistivity measurement against c-axis magnetic field for the same sample and strains. The measurement configuration is depicted in the upper right corner, contact numbers are as per figure 4.19. V_{46} is the voltage difference between contacts 4 and 6 when current I_{35} is passed between contacts 3 and 5. The transverse measurements were at 380 mK. The black curves in both panels are the measurements closest to zero strain.

vast growth of the B region, which at zero strain is only a tail on the high field side of the main A phase between 8.1 and 8.5 T As the strain is increased its visibility grows, becoming comparable in magnitude to that of the A region. Above about 0.2 % compression the breadth of the region of enhanced resistivity in field starts to grow substantially faster to both lower and higher fields, covering almost the whole of the measured field window. This can be seen most clearly in an alternative representation of the data in figure 4.25A as a contour map. Under tension the resistivity enhancement is rapidly suppressed. 0.07 % tension is already enough to almost completely eliminate any resistivity enhancement.

The results of the transverse measurements are shown in panel B of figures 4.24 and 4.25. The effect is the mirror of the longitudinal response. Under ε_{xx} compression the phase-induced enhancement in the transverse response is suppressed whereas tension strengthens the enhancement. The approximate mirroring of the longitudinal and transverse responses is also clearly evident in the contour maps in figure 4.25 and in 3D surface plots of the resistivity in figures 4.26 and 4.27. As discussed earlier, the transverse measurement
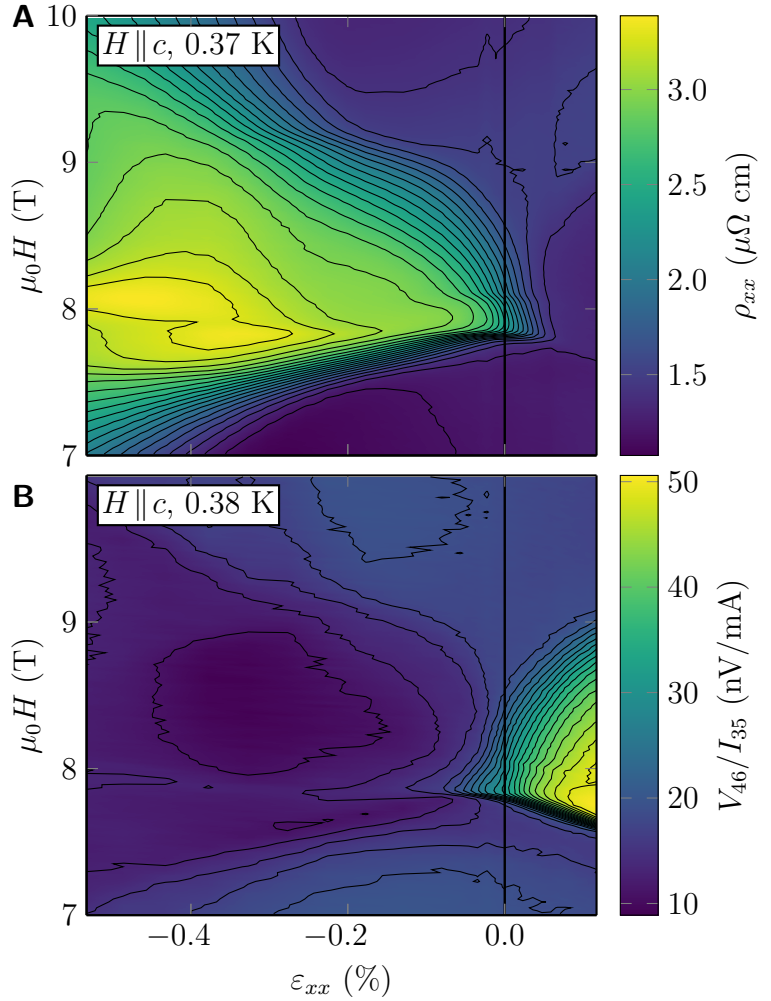
Fig. 4.25: **Magnetoresistance contour plots.** Contour plots of the longitudinal (**A**) and transverse (**B**) resistivities from figure 4.24 as a function of c-axis magnetic field and applied strain.

is likely not a measure of only the in-plane resistivity ρ_{yy}; some component of ρ_{zz} is mixed in. If the current was directed completely within the ab-plane and the contacts aligned as a perfect square, the voltage measured in the transverse geometry at zero strain should be an exact scaled copy of the longitudinal response. The shape observed here, even at zero strain, is quite different. This discrepancy might be due to the additional component of c-axis resistivity, however the c-axis magnetoresistance of $Sr_3Ru_2O_7$ has not been well studied so no quantitative comparison can be made. Preliminary investigations by Perry [188] show that the c-axis resistivity is influenced by the metamagnetism but a study of how the novel phase formation affects the c-axis magnetoresistance has not been undertaken. Before analysing the transverse measurements in too much detail, characterisation of the c-axis resistivity would be desirable.

Misalignment of the magnetic field with respect to the crystalline
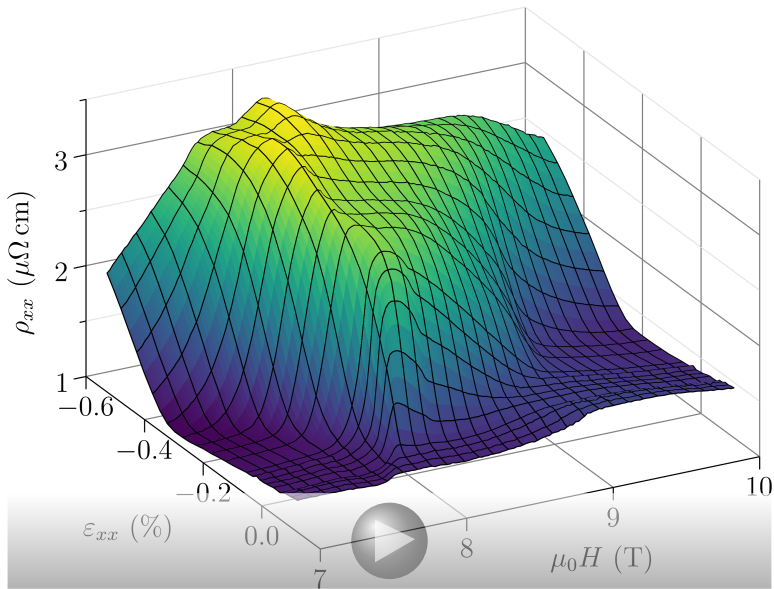
Fig. 4.26: **Magnetoresistance.** Surface plot of the longitudinal resistivity ρ_{xx} against *c*-axis magnetic field and applied strain at 370 mK.
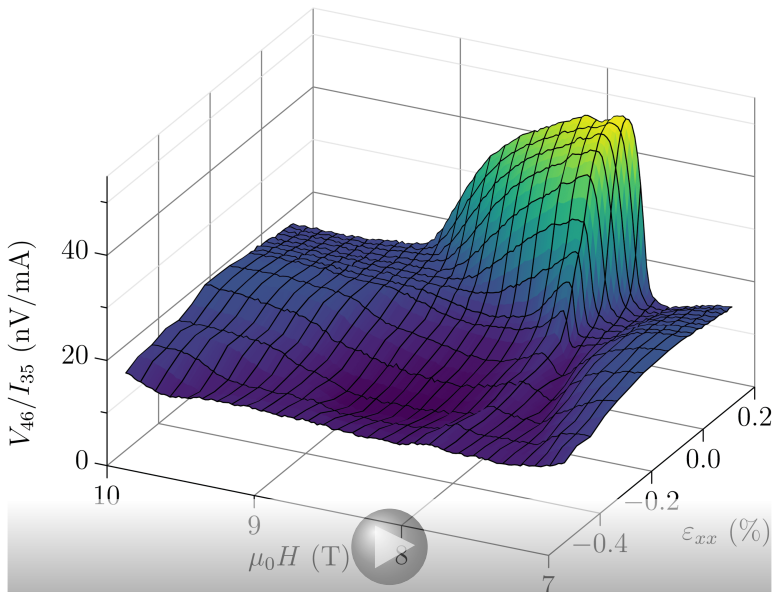
Fig. 4.27: **Transverse magnetoresistance.** Surface plot of the transverse resistivity against *c*-axis magnetic field and applied strain at 380 mK. See figure 4.24 for the measurement configuration.

c-axis could also influence the shape of the resistivity enhancement. The rig is mounted horizontally in the bore of the magnetic and the holder attaching the rig fixes this alignment. Here the alignment should be better than ±3°. However the sample can also be slightly misaligned with the rig as its orientation is not held rigidly while the epoxy cures. The two ends of the samples are fixed at the same height in the rig but there is the possibility for the sample to rotate about its long axis as the epoxy cures since the gap between the sample plates sandwiching the ends of the sample is larger than the thickness of the sample. When curing the epoxy the pre-attached voltage wires were positioned to try and prevent the sample from rotating but a small misalignment might still occur. Any misalignment of the field will be noticeable as a change in the onset field of the phase; rotating the field off axis decreases both field boundaries of the phase [199]. By comparison to data from Bruin [199] who used a vector magnet with very precise control of the field alignment, the onset field we observe here suggests the sample is aligned better than ±3° from axis. At the moment we cannot definitively identify the cause of the different shape observed in the transverse response and it would be best to repeat these measurements on more samples and also perhaps carry out a dedicated more accurate study of the *c*-axis resistivity which would now be possible using the precision of a Focus Ion Beam (FIB) to fabricate samples of the correct geometries.

4.4.2   Metamagnetism

Figure 4.28 shows the AC susceptibility measurements after the smoothly varying background subtraction described in section 4.3. What is left is the additional susceptibility due to the metamagnetism. As a reminder, at zero strain susceptibility measurements show three metamagnetic jumps, see for example figure 4.13. The first at 7.5 T is a broad crossover, the second is the largest in magnitude and signifies the transition into the A phase at ∼7.8 T and the third at ∼8.1 T occurs at the transition between the A and B phases. At 370 mK the transitions at 7.5 T and 8.1 T are very weak. They are still observable above the background at zero strain but under both compression and tension they quickly become lost in the background. Without being able to follow these transitions to lower temperatures I will mainly be concerned with the metamagnetic transition at the entrance to the A phase. The susceptibility behaviour under compression and tension is in stark contrast to the approximate mirroring of the longitudinal and transverse resistivity between compression and tension. Under tension the peak in the real part of the susceptibility moves to lower fields without changing in magnitude significantly. At zero strain this
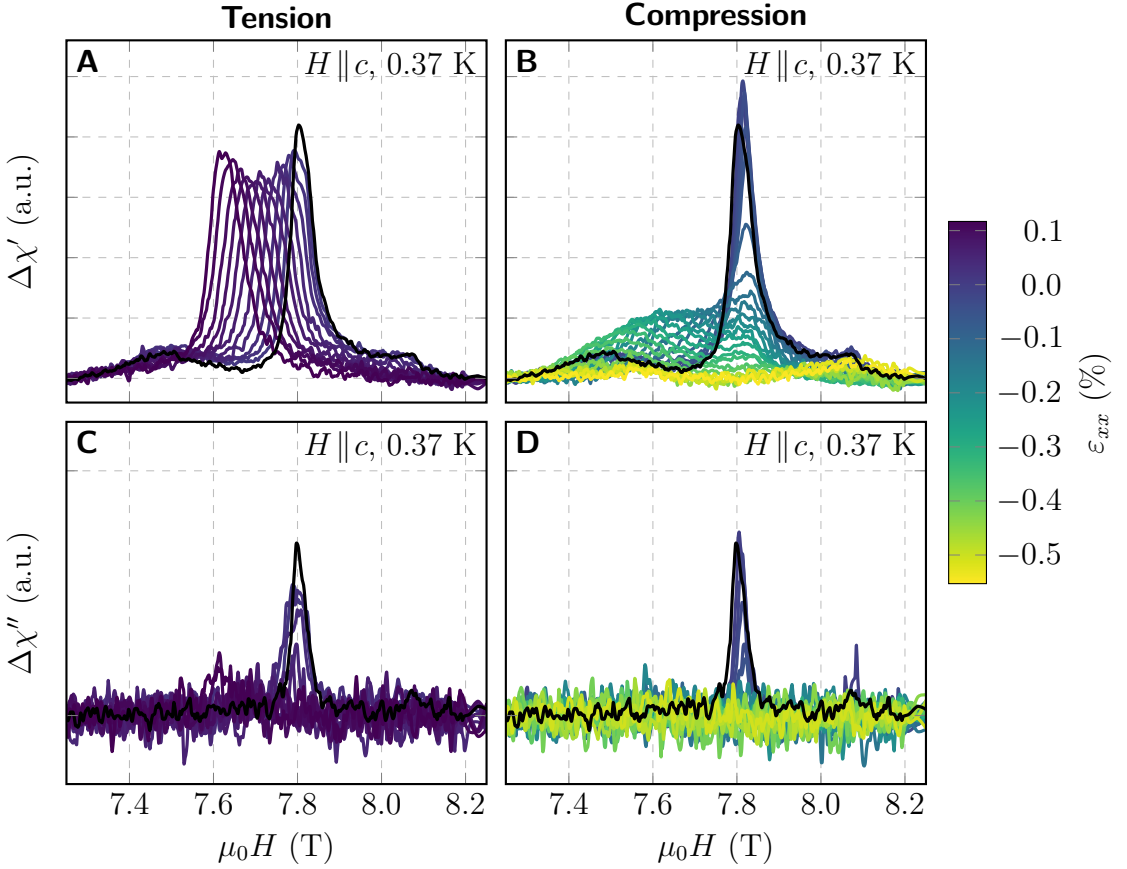
Fig. 4.28: **Susceptibility against field. A and B.** Real part of the AC susceptibility χ against c-axis magnetic field for a series of applied strains at 370 mK. The black curves are the measurement closest to zero strain. **A** shows measurements under tensioned and **B** compression. All measurements are of increasing field sweeps and are quoted as $\Delta\chi$ because of a background subtraction procedure detailed in the text. **C and D.** The imaginary part of the susceptibility for the same measurements. The susceptibility is expressed in arbitrary units but the scale divisions for the real and imaginary susceptibilities are the same.

transition is first-order and a peak in the imaginary part of the susceptibility is observed due to hysteresis-related dissipation [178]. This peak in the imaginary part of the susceptibility can be seen for the strained sample too, albeit with a low signal-to-noise ratio. However, unlike the corresponding peak in χ' it does not seem to move to lower fields with tensile strain rather it very quickly dies out and stays centred on approximately the same field value.

Under compression something different occurs. The main peak stays at approximately the same field but changes magnitude initially, then as it is decreasing in magnitude a shoulder starts to protrude on the lower field side. This develops into a second weaker peak before also becoming lost into the background by ~0.4 %

Fig. 4.29: **Susceptibility contour plots.** Contour plots of the AC susceptibility measurements from figure 4.28 as a function of *c*-axis magnetic field and applied strain. The dashed white line is the H_1 line of the anomalous phase from the loci of maxima in $d\rho_{xx}/dH$. The dotted white line is the equivalent maxima in the transverse resistivity measurement.
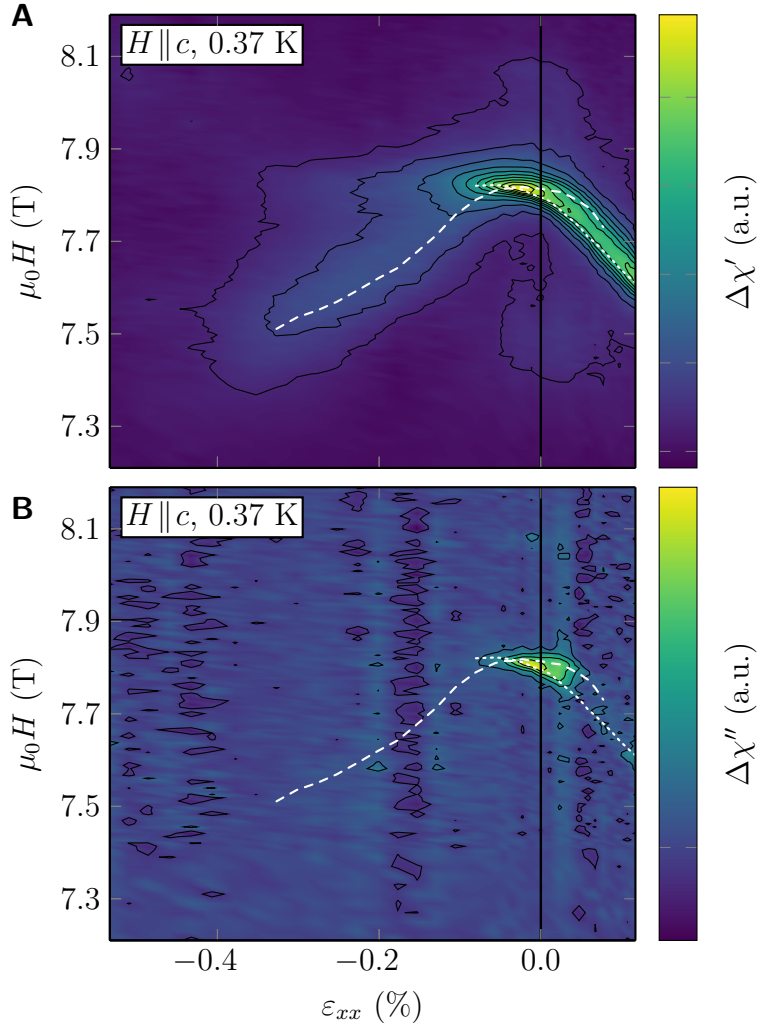
compression. The peak in χ'' also disappears with only a small amount of compressive strain. As a better comparison with the resistivity, figure 4.29 shows a contour plot of the susceptibility with the lower field boundary of the A phase, H_1, as identified by the maximum slope in the magnetoresistance, overlaid on top. The H_1 line from the magnetoresistance tracks well with the peak in susceptibility and loses definition at a similar strain as that at which the peak in susceptibility can no longer be resolved. From this plot it might appear that zero strain is wrongly identified and the sample is really under slight tension at what we are calling zero strain. However, this is still an open question and it will be addressed again when the temperature ramp data is presented.

To help visualise how the susceptibility changes with strain, the data is also plotted as 3D surfaces in figures 4.30 and 4.31.
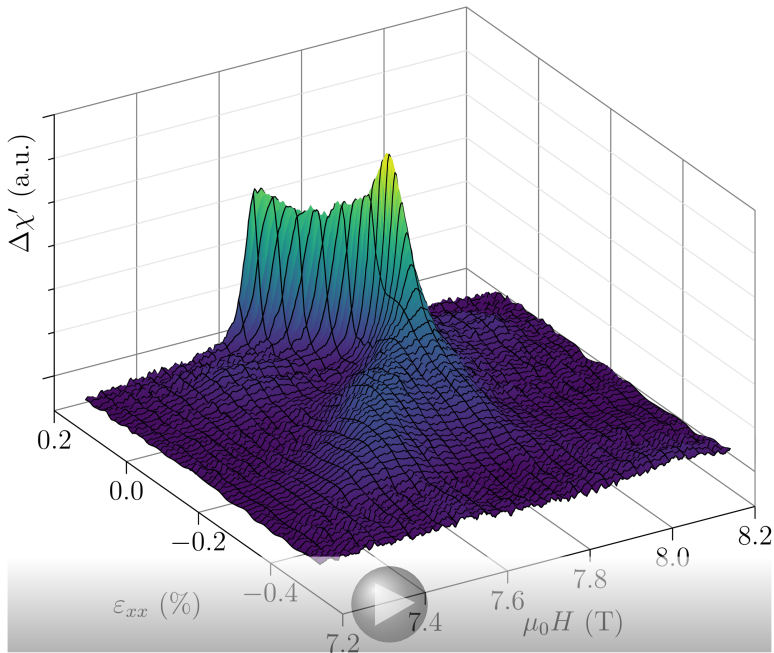
Fig. 4.30: **Susceptibility.** Surface plot of the real part of the AC susceptibility χ against c-axis magnetic field and applied strain at 370 mK.
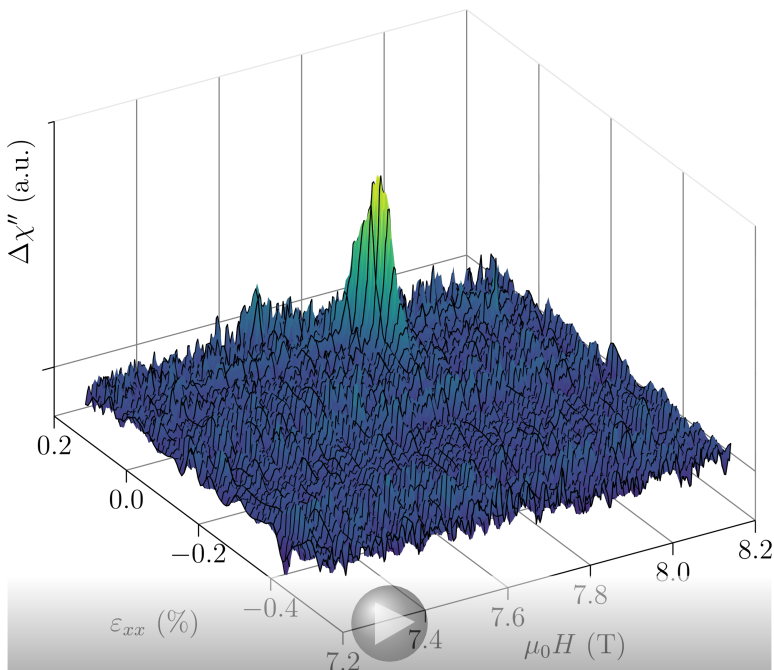
Fig. 4.31: **Susceptibility.** Surface plot of the imaginary part of the AC susceptibility χ against c-axis magnetic field and applied strain at 370 mK.

4.4.3   Strain ramps

So far all the data presented were recorded while ramping the magnetic field. It is also possible to traverse phase space in an orthogonal direction, sweeping the strain at fixed field and temperature. Figure 4.32 shows a series of strain ramps at fixed fields covering the field range of the novel phase. Outside the region of phase formation there is no measurable hysteresis between increasing and decreasing strain runs and the data overlap with the data recorded during the field ramps. However, in the field range of the phase, some hysteresis is observed at high compression but close to zero strain almost no measurable hysteresis is detected at any field.

To investigate the effect of strain over a wider field range a series of short strain ramps spanning zero strain were carried out at fields between 0 and 10 T both at 370 mk and 4.5 K. The elastoresistance (also known as the gauge factor), determined from the slope of these
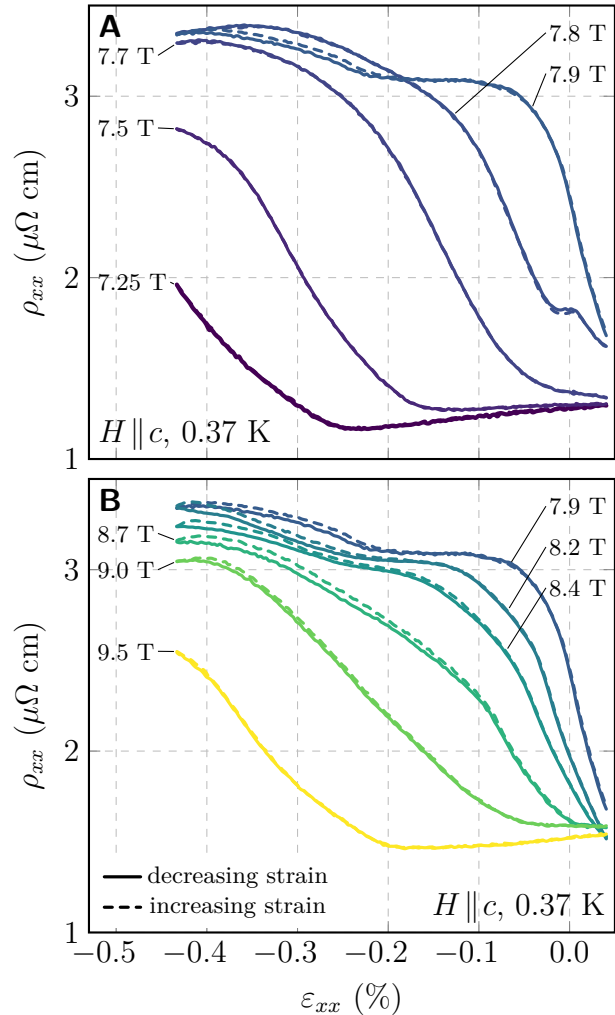
Fig. 4.32: **Resistivity against strain.** Longitudinal resistivity ρ_{xx} at a series of constant *c*-axis magnetic fields and constant temperature as the strain is swept through the anomalous phase. **A.** Fields up to 7.9 T. **B.** Fields above 7.9 T. Solid lines for decreasing strain sweeps (towards higher compression) and dashed lines for increasing strain (towards tension).
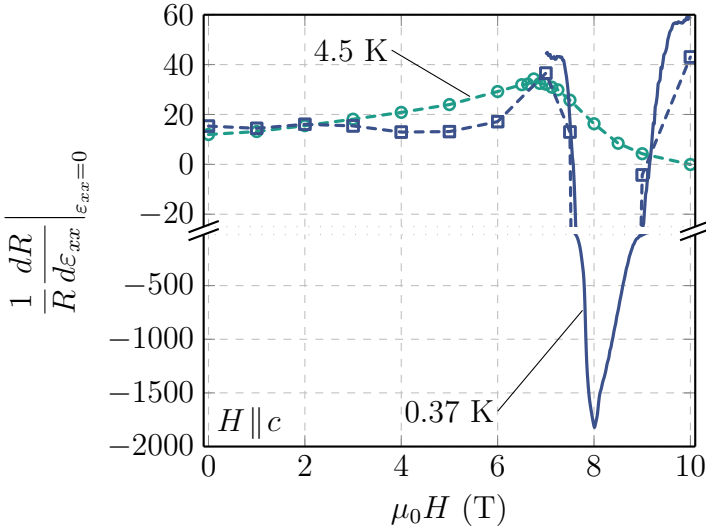
Fig. 4.33: **Elastoresistance.** Gauge factor against *c*-axis magnetic field at 4.5 K and 370 mK. The gauge factor is highly nonlinear with strain and is evaluated at zero strain from the derivative of the elastoresistance $(1/R)dR/d\varepsilon_{xx}|_{\varepsilon_{xx}=0}$. The circle and square points are calculated from short strain sweeps through zero strain at fixed field and temperature. The solid line is calculated by interpolating between different field sweeps at fixed strain and temperature but at fine enough strain spacing to accurately capture the slope at zero strain.

measurements at zero strain is plotted in figure 4.33. Even if the resistivity of a material is unaffected by strain, the elastoresistance still includes a contribution from the geometrical change of the sample. For an isotropic material with a Poisson's ratio ν this contribution is $1 + 2\nu$, which in a normal metal is about 2, and is typically the dominant contribution. In a correlated system, however, the changes in hopping strength with applied strain can have a much larger effect on the resistivity. For $Sr_3Ru_2O_7$ at zero field the gauge factor is $\sim$15, not a surprising result due to its known strong correlations and narrow bandwidth. The gauge factor increases towards the critical field but is cut off by the formation of the phase which shows a dramatically large and negative response. At 8 T the gauge factor is close to -2000. For comparison the gauge factor of another nematic material, $BaFe_2As_2$, peaks at $\sim$$-90$ at the nematically driven structural transition [51]. At 4.5 K, above the temperature for phase formation, the gauge coefficient for $Sr_3Ru_2O_7$ remains positive at all fields and peaks at $\sim$7 T with a value of $\sim$35.

4.4.4 Higher temperatures

Up until now the main measurements of $Sr_3Ru_2O_7$ under strain have been carried out at base temperature. Mapping out the complete boundary of the phase in temperature as well as strain and field is an important experimental task but a formidable one. The data already presented cover a cut through phase space in the field-strain plane, so a sensible start for investigating the wider phase space is a cut in the temperature-strain plane. A field of 7.95 T was chosen, right in the centre of the A phase, and a series of temperature and strain ramps was performed.

Fig. 4.34: **Resistivity against temperature. A.** Longitudinal resistivity against temperature at 7.95 T for a series of applied strains. The upturn in resistivity marks the onset of the anomalous phase. The transition temperature is identified by the maximum in $d^2\rho/dT^2$ and is shown by the dashed line. A second transition is seen at lower temperatures for compressions above ~ -0.1 % and the second dashed line follows the corresponding extremum in the second derivative. The inset shows the resistivity temperature exponent at high temperatures calculated from a fit of the form $\rho = \rho_0 + AT^\alpha$ above 3 K. **B.** Transverse resistivity measurement against temperature at 7.95 T for a series of applied strains. See figure 4.24 for the measurement configuration. The dashed line marks the maximum in the second derivative with temperature.

Figure 4.34 shows the longitudinal and transverse resistivity between 400 mK and 7 K for a series of applied strains. This field is very close to the QCEP at 7.9 T and the effect on the resistivity is clearly apparent. Above the temperature of phase formation at zero strain the resistivity is almost linear in temperature for the whole measurement range. At higher compression the exponent of the temperature dependent part of the resistivity increases. The inset to panel A of the figure shows this exponent extracted from a $\rho = \rho + AT^\alpha$ fit of the resistivity between 3 and 8 K. Slightly puzzlingly the exponent keeps decreasing under slight tension. It would be interesting to attempt to reach higher tensile strains to see at what point the exponent saturates or starts to increase again. In resistivity the entrance into the novel phase with temperature is marked by a saturation or slight upturn [224, 199]. This can be identified in both the longitudinal and transverse measurements. To identify the transition temperature in a fully consistent manner, the peak in the second derivative of the resistivity minus the high temperature fit with respect to temperature was used. An example

Fig. 4.35: **Resistivity against strain. A.** Longitudinal resistivity against strain at 7.95 T for a series of fixed temperatures. The resistivity is largest in the anomalous phase and the transition is identified by the maximum in $d^2\rho/d\varepsilon_{xx}^2$. The dashed line follows this maximum in the second derivative. **B.** Transverse resistivity measurement against strain at 7.95 T for a series of fixed temperatures. The transition to the high resistivity phase is identified in the same manner.

is shown in figure C.2A in the appendix. The dashed black line in the figure shows the position of this peak in the second derivative. At high compressions a second feature appears at a lower temperature and can also be identified by a corresponding extremum in the second derivative.

Strain sweeps at a selection of temperatures, all at 7.95 T, are shown in figure 4.35. Here the strain range is smaller than before and no hysteresis was observed between the increasing and decreasing strain runs. The boundary of enhanced resistivity is not as sharp in strain ramps as in temperature ramps, but a weak peak in the second derivative with strain can still be seen, see figure C.2B. The calculated strain values coincide well with those from the temperature ramps suggesting some validity to this analysis.

From the temperature and strain ramps at 7.95 T an empirical phase boundary can be drawn defining the regions of enhanced longitudinal and transverse resistivity. The field ramps described earlier can also be used to identify this phase boundary but this time in the strain-field plane at 0.37 K. Guided by the analysis of

Fig. 4.36: **Boundaries of enhanced ρ_{xx} and transverse resistivity.** Empirical phase diagrams for the boundaries of enhanced longitudinal and transverse resistivity in **A** the field-strain plane at 0.37 K and **B** the temperature-strain plane at 7.95 T. The boundaries are identified through both resistivity and susceptibility measurements. Left triangles are the loci of the peak in χ', upright triangles are the loci of maxima in $d\rho/dH$, and these mark the H_1 line. The resistive transition features are shown in the inset. H_2 marked by right triangles and H_3 by inverted triangles are the loci of maxima in $d^2\rho/dH^2$. The boundary is also identified by maxima in $d^2\rho/d\varepsilon_{xx}^2$ from strain sweeps and marked with squares. Open symbols are from measurements of the longitudinal resistivity and closed symbols the transverse resistivity. The roof of the phase is identified by temperature ramps and more strain ramps. Diamonds mark the loci of maxima in $d^2\rho/dT^2$ and circles the loci of maxima in $d^2\rho/d\varepsilon_{xx}^2$. Above ~ -0.1 % compression a second transition is observed at lower temperatures and is marked by stars following the loci of a maxima in $|d^2\rho/dT^2|$.

Fig. 4.37: **Boundaries of enhanced ρ_{xx} and transverse resistivity.** An empirical phase diagram for the bounding surfaces of enhanced longitudinal and transverse resistivity, in blue and red respectively, based on the resistivity and susceptibility measurements presented in figures 4.24, 4.28, 4.34 and 4.35. The symbols are the loci of peaks in susceptibility or maxima in derivatives of the resistivities with respect to temperature, field or strain as follows: $\triangle$ $d\rho/dH$, $\triangledown$ $d^2\rho/dH^2$, $\square$ and $\circ$ $d^2\rho/d\varepsilon_{xx}^2$, $\diamond$ $d^2\rho/dT^2$ and $\triangleleft$ peaks in χ'. Open symbols are from measurements of the longitudinal resistivity and closed symbols the transverse resistivity. The shaded surfaces are guides to the eye only. The region encloses both the A and B phases with the boundary between them H_2 drawn with $\triangleright$ symbols only while it can be identified from the corresponding feature in $d^2\rho/dH^2$. The solid lower bounding lines are H_1 and H_3.

Grigera *et al.* [180] the field defining the entry to the phase, H_1, coincides with a maximum in $d\rho/dH$, the same field as that at which the peak in susceptibility is seen. Here I make the assertion that the transition between the A and B phase, H_2, and the upper line of the B phase, H_3, can be identified by peaks in the second derivative $d^2\rho/dH^2$, i.e. where the slope of the magnetoresistance changes. Both the first and second derivatives of an example magnetoresistance curve are shown in figure C.1 in the appendix along with the identified fields H_1, H_2 and H_3. The accumulation of all these points is presented as an empirical phase diagram in figures 4.37 and 4.36.

4.4.5 Discussion

The measurements presented here reveal the rather complex development of the novel phase of $Sr_3Ru_2O_7$ with strain. As with small in-plane magnetic fields, small orthorhombic lattice distortion also reveals the large susceptibility of magnetotransport to

Fig. 4.38: **Phase diagram of a two-component vector order parameter.** The Landau free energy for a two-component order parameter, where each component is C_2 symmetric. The phase diagram of temperature (T) against h, a C_2 symmetric field, shows (**A**) a bicritical point (BP) when $u_a u_b < u_{ab}^2$ and (**B**) a tetra-critical point (TP) when $u_a u_b > u_{ab}^2$. The double line marks a first-order transition, all other transition lines are second-order. Reproduced from [243].

Landau free energy:
$$F = a(T - T_c)(|\Delta_a|^2 + |\Delta_b|^2) + u_a|\Delta_a|^4 + u_b|\Delta_b|^4 + 2u_{ab}|\Delta_a|^2|\Delta_b|^2 - h(|\Delta_a|^2 - |\Delta_b|^2)$$
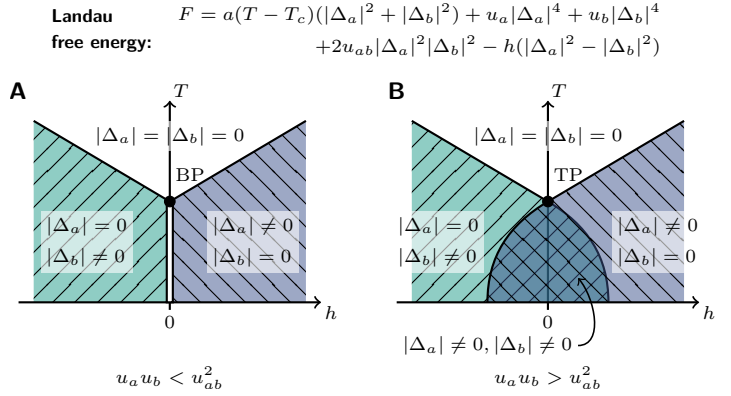
C_2-symmetric fields. The complex nature of the novel phase is not understood theoretically to date, and as such an in-depth analysis of the influence of strain on all aspects of the phase is not yet manageable. There are however some key points we can draw from these measurements and these should be useful for constraining further theoretical investigations.

The first question we address is the symmetry of the novel phase. It was suspected that much of the unusual behaviour observed in magnetotransport could be explained by domains of spontaneous C_2-symmetric order. The 100 % increase in resistivity as the phase is entered suggests an additional scattering channel which could be domain walls, additionally small in-plane fields induce a strong resistive anisotropy suggesting reorientation of either the order or domain walls. However, despite detailed investigations searching for definitive signatures of domains and domain wall movement, no conclusive evidence has been discovered. In light of the new results from uniaxial pressure tuning we now also discuss the possibility of a ground state with a large albeit finite susceptibility towards C_2-symmetry and overall C_4-symmetry. In terms of a Landau free energy for a multicomponent order parameter, say x- and y-oriented density waves, we are asking the question of whether the two components can microscopically coexist or whether the development of one precludes the condensation of the other, thus resulting in a lowering of rotational symmetry of the ground state. The Landau free energy for the two scenarios is shown in figure 4.38. When the prefactors satisfy $u_a u_b < u_{ab}^2$, a first order phase transition separates the states of orthogonal polarisation and at zero C_2-symmetry breaking field, i.e. strain or in-plane field, domains of both polarisations are expected. When $u_a u_b > u_{ab}^2$, the two order parameters are not in direct competition and they can microscopically coexist over a region of applied C_2-symmetry breaking field.

It is not clear from the neutron scattering work whether the scattering peaks that correspond to orthogonally oriented spin

density waves arise from separate domains of a single density wave or from their microscopic coexistence. Thermodynamic measurements establish some form of symmetry breaking through the second-order roof of the phase [180, 244, 245] but this could be the translational symmetry breaking of the density waves or the possible lowering of rotational symmetry C_4 to C_2, or both.

The results that put the strongest constrains on possible domain formation are from a series of resistivity measurements in a fully rotatable vector magnetic field by Bruin and Borzi [199, 237]. The vector magnet's unique capabilities allow both the field orientation and strength to be changed precisely and smoothly without, for instance, affecting the sample temperature. By rotating the in-plane field slowly through 90° they could follow how the hard and easy transport axes are exchanged. In the scenario of domains the naive expectation is a sharp jump in the resistance as the orientation of the order flips when the field is rotated. It was found, however, that the in-plane resistances vary smoothly as the field direction is rotated. If there were many small domains one might expect a series of much smaller steps, however, no such jumps or excess noise from domain reorientation were resolvable at all above the background noise level of the measurements.

If domain reorientation were also responsible for the large C_2-symmetric susceptibility, hysteresis might be expected when the applied field is varied. To test for this Bruin and Borzi started with the field applied along the sample's c-axis and then rotated the field far enough off axis to exit phase and then re-enter with the strongest possible in-plane field. In their measurements they could not resolve any hysteresis and the same conclusion was made when comparing clockwise and anticlockwise field rotations. They observed that when the magnetic field is tilted off axis there is still a region of overlap where both ρ_a and ρ_b are enhanced and this region extends out to at least 1.7 T.

In the uniaxial pressure measurements presented here there is also an absence of hysteresis at small strains when crossing from the regions of enhanced longitudinal to transverse resistance and vice versa. The large overlap in strain of both enhanced longitudinal to transverse resistance is also clear. In both these measurements the region of phase formation was repeatedly entered and exited in the presence of non-zero C_2 field. Approaching the phase in this way should mean that any domain formation is at or at least very close to its ground state configuration with respect to the applied C_2 field. This means that for the resistive properties of $Sr_3Ru_2O_7$ to still be explainable in terms of domains, the formation of domains must be energetically favourable up to at least the upper limits of the overlap regions; ∼1.7 T for in-plane field and ∼0.08 % strain. Given that the associated lattice distortion in the presence of an

in-plane field component is only $\sim 4 \cdot 10^{-6}$ [246] and the size of the largest metamagnetic jump is only 0.008 T [244], domain formation stabilised by long-range elastic or magnetic interactions up to the required limits seems naively rather unlikely. Disorder could extend the region of domain formation, be it from local sample defects or inhomogeneously applied strain, but the observed broadening of the transitions is not more than the width of the overlap region. The data do not appear like they could be the result of a disorder broadened transition at zero C_2 field but rather it seems more likely there is a real transition at a small but finite C_2 field.

The key point of the discussion so far is that any domains must result in extremely weak hysteresis, below the resolution of the measurements, but if domains are the origin of the large C_2-symmetric susceptibility they must also be robust against substantial C_2 fields. In general these requirements will not be satisfied simultaneously and the data seem to suggest that the measured resistivity is intrinsic to the phase. If this is the case then the data is most naturally explained by a multi-component order parameter with microscopic coexistence of [100]- and [010]-oriented components at low applied C_2 fields.

The close connection between the intensity of spin density wave scattering peaks in neutron scattering and the resistivity adds some validity to this interpretation and suggests the two components of the order parameter are associated with the orthogonal spin density waves. Their microscopic coexistence could take on many forms. The simplest would be when both orthogonal density waves coexist within each layer but the two components could also exist spatially separated with the direction of the density wave rotating 90° between the layers within each bilayer or between the bilayers themselves.

Even though spontaneous C_2-symmetry breaking now seems unlikely the particularly large susceptibility of the C_4-symmetric ground state to C_2-symmetric fields is striking and deserves further investigation. It may be a result of fine-tuning or only weakly stabilised density waves but this is an interesting avenue for further measurements.

After excluding domains, explaining the origin of the resistive enhancement remains a considerable challenge. At high strains the ratio of the resistivity along the hard and easy axes is ~ 2.5. This is particularly large. For comparison, in another spin-density wave system, elemental chromium, a three-dimensional spin-density wave induces a maximum resistive anisotropy of only 8 % [247,248]. In Cr, a spin density wave matching a nesting vector of the Fermi surface opens a gap on those parts of the Fermi surface, but in $Sr_3Ru_2O_7$, a multiband material, the number of states that must be gapped away to realise the large resistive anisotropy seems unrealistic.

Thermodynamic measurements also show that the entropy and specific heat are highest in the region of phase formation, directly arguing against widespread gapping. To further our understanding of $Sr_3Ru_2O_7$ it is of great importance to determining the origin of the large changes in resistivity and this should be a key focus for future investigations.

The addition of magnetic measurements allowed me to measure the influence of strain on the metamagnetic quantum criticality directly. Pressure along the *c*-axis is known to rapidly suppress the transition fields but these measurements show the effect of in-plane pressure is much weaker. Simultaneous measurements of the resistivity and susceptibility confirm that the onset of enhanced resistivity under strain tracks the metamagnetic transition, and that the phase is still bounded by a metamagnetic transition, at least on the low field side. In-plane strain lowers the field of the metamagnetic transition at $\sim$7.8 T at a maximum rate of 1.6 T/%, something of the order of 1 T/GPa. It is suspected that the metamagnetism is related to a Van Hove singularity in close enough proximity to the Fermi surface that can be reached by the Zeeman splitting of an $\sim$8 T field. Since the metamagnetic fields change very little under strain, the effect of in-plane anisotropic strain on the part of the Fermi surface close the Van Hove singularity must be weak, or else a vastly different metamagnetic field might be expected.

The positions of the susceptibility peak and the onset of enhanced resistivity track together well under strain but there is no good connection between the strength of the peak in χ and the magnitude of the resistivity enhancement. The susceptibility peak, which relates to some $q=0$ physics, becomes weaker with strain, by either measure of its height or area, whereas the enhancement in ρ increases. It is often assumed that the metamagnetism in $Sr_3Ru_2O_7$ is associated with a peak in the density of states that can satisfy the Stoner criterion once sampled by the Zeeman splitting of an applied field. If the peak in the density of states occurs along the *x*- and *y*-directions in the band structure, anisotropic strain could naturally lead to a weakening of the associated metamagnetism. Under the application of anisotropic strain the bandwidth would increase along one direction and decrease along the perpendicular direction, changing the energy of the peaks in the density of states. Under applied field the density of states at the Fermi energy would therefore peak at a different energies due to the now non-equivalent peaks along the *x*- and *y*-directions. Depending on the strength of the peaks two scenarios can be imagined. If neither peak alone provides a strong enough divergence of the density of states the Stoner criterion may only remain satisfied at low strain while there is a large enough overlap from both peaks and at higher strains

the metamagnetism might then be expected to reduce to a smooth crossover. If, however, the peaks are strong enough alone to satisfy the Stoner criterion metamagnetism at two separate fields might be expected, but each smaller in magnitude than at zero strain. To address these scenarios in any more detail better knowledge of the band structure and how it changes under both applied field and strain would be necessary.

In $Sr_3Ru_2O_7$ the physical property that shows the most dramatic change is the resistivity. In spite of this, the new phases/phase transitions that appear or disappear with strain and magnetic field all lead to a resistivity of very similar order of magnitude. Either this implies only small changes to the Fermi surface are ever being induced, or that the mechanism by which the resistivity is being increases is always the same.

4.5   Conclusions

In this work I have applied in-plane uniaxial stress to $Sr_3Ru_2O_7$, reaching more than a factor of two higher strain than that in the previous study. Additionally, by significantly improving the resolution of magnetic susceptibility measurements under strain, I could measure the magnetic response directly, simultaneously with resistivity.

The strong susceptibility of the novel phase to in-plane magnetic fields is also found for in-plane anisotropic strain. The magnetic susceptibility measurements show that the novel phase under strain is still bounded by a metamagnetic transition, at least on the low field side. The entrance to the phase, H_1, moves to lower fields with either compression or tension but at high compression the signature of the metamagnetic transition in susceptibility loses definition. This occurs at a similar strain to that at which the jump in resistivity at the entrance to the novel phase also starts to broaden more rapidly. At the highest strains measured in this work, the region of enhanced resistivity covers almost the entire measured field window from 7 T to 10 T and more detailed structure also appears to develop.

Close to zero strain we can identify a clear region of overlap where both the longitudinal and transverse resistivity are enhanced. The extent of this region puts strong bounds on the energetics of any possible domain formation. In addition, with the absence of any hysteresis at low strains, the phase diagram that these uniaxial pressure measurements reveal is most easily explained by a state that does not involve any spontaneous symmetry reduction and rather only a large but finite susceptibility to in-plane symmetry breaking fields.

These measurements show the importance of using external

probes to selectively break underlying symmetries when investigating novel physics, and these techniques should be applicable to a wide range of other materials. The evidence against spontaneous symmetry breaking in $Sr_3Ru_2O_7$ also strongly motivates the need for a better understanding of the origin of the resistive enhancement in the region of novel phase formation, something that will be of paramount importance for future investigations of $Sr_3Ru_2O_7$. Completing the phase diagram in the rest of field-temperature-strain space would be a formidable task but some select cuts may prove to be useful, for instance to investigate the resistivity temperature exponent at high compression and tension in more detail. The combination of both vector-magnetic field and uniaxial stress simultaneously may also provide important information of how these two symmetry breaking fields compete or interact, and whether they have the same underlying effect on the novel phase.

Conclusions and Outlook

<div style="text-align: right;">

5

</div>

I hope that during the course of this thesis I have demonstrated that the new uniaxial stress technique that I describe is now coming out of its infancy. The first successful adaptation of the device by another group has now been reported, and used by Stern *et al.* [249] to study SmB_6 under strain. I know that a number of other groups world-wide are also working on implementing the technique, and versions of the Hicks design are now being sold commercially by Razorbill Instruments.

I would like to conclude by summarising how the uniaxial stress technique has developed and what I envision for the future; what physics it can help tackle and some key directions for further technical development. For the scientific conclusions regarding Sr_2RuO_4 and $Sr_3Ru_2O_7$, the reader is referred back to the conclusions at the end of each of the respective chapters.

The work in this thesis has hopefully demonstrated that the device as it stands now is already a powerful tool for condensed matter physics research. Two of its key uses have been demonstrated; its brute force is useful for Van Hove singularity tuning, and its fine precision is useful for controlled symmetry breaking. I would like to reiterate once more the significance of the energy changes possible with this technique. We are now quite routinely able to reach strains of 1 %, but to put it in perspective it is useful to compare to more common energy scales. Roughly, one can say that a strain of 1 % can change the Fermi level by approximately 1 % of the band width. For Sr_2RuO_4 the band width of the γ band along the [100] direction is $\sim$3 eV, so a 1 % change of strain along the [100] direction is equivalent to a temperature change of $\sim$300 K or the Zeeman splitting from a magnetic field of $\sim$600 T.

I have looked mainly at ruthenates using both resistivity and magnetic susceptibility but this uniaxial stress technique is applicable in principle to a far wider range of materials and experimental techniques. As outlined in chapter 2, techniques such as heat capacity, thermal conductivity, Seebeck and Nernst effect, nuclear magnetic resonance (NMR), and many more, are all in principle possible. Additionally, since the upper face of the sample remains exposed, even techniques like angle-resolved photoemission spectroscopy (ARPES) and scanning tunnelling microscopy (STM) may be possible. Even if experiment specific restraints impose a smaller strain range, quite significant changes have still been demonstrated at lower strains, and integrating these techniques with uniaxial

stress will open up a whole host of new experimental possibilities.

Much novel physics will benefit from the new perspective of uniaxial stress. For example, in the high temperature cuprate superconductors the proximity of a Van Hove singularity to the Fermi level is well-established [250–253]. If possible, tuning through this Van Hove singularity with uniaxial pressure may provide a novel way to explore the phase diagram with more control and less disorder than chemical doping. Uniaxial pressure may also be useful for more direct investigations into the superconductivity and competing instabilities. It is well-established in certain regions of the phase diagram that charge order is stabilised [254, 255], and nematic fluctuations are reported in certain regions of the phase diagram too [256, 226, 257]. Both these phenomena may have a strong coupling to uniaxial pressure and thus could reveal further insights into the cuprates. For example, in rare-earth doped $La_{2-x}Sr_xCuO_4$, a system with an analogous stripe phase to $x=1/8$ doped $La_{2-x}Ba_xCuO_4$, uniaxial pressure applied at a 45° to the Cu-O-Cu bond direction has been demonstrated to rapidly enhance T_c by almost a factor of 2, and was attributed to a suppression of the competition with stripe ordering [42, 258].

Many other novel superconductors would also be suitable for uniaxial stress measurements. The multiple superconducting phases of UPt_3 are known to respond differently and anisotropically under uniaxial stress [259–261]. A reinvestigation with higher homogeneity, precision and range could be quite fruitful. So too could investigations on another possible time-reversal symmetry-breaking superconductor $PrOs_4Sb_{12}$ [262], and on the strongly nematic iron-based superconductors [227, 56].

Other puzzles such as the hidden order parameter in URu_2Si_2 might also be amenable to study under high uniaxial pressure, but hopefully this technique can find uses across a far wider range of fields than the quite closely related examples suggested here.

As already discussed, we are now routinely capable of reaching 1 % level strains. The yield strain of some materials, however, can be much higher still and a key direction for future developments will be to see how much higher we can push this. Single crystal silicon and several other silicon containing ceramics have yield strains greater than 3 % [263] and *ab initio* calculations for pristine silicon nitride suggest this could even be in excess of 10 % for higher purity samples [264]. As part of this development process, two key aspects should be the development of controlled stress rather than controlled strain devices and miniaturisation.

Currently the largest uncertainty in determining the sample strain comes from the epoxy. This rather imprecise strain scale means it is not possible to compare subtle differences between many samples. In a device where stress rather than strain is applied and

controlled, the relatively softer epoxy does not hinder the accuracy, since all the force applied to the epoxy must also be transmitted through the sample. Controlling the applied stress is beneficial for other reasons too. It simplifies identifying zero strain and eliminates the complications that arise from differential thermal expansion in the controlled strain devices. Additionally the range of materials that can be measured is expanded. Materials which undergo structural changes involving a large change in lattice constant between the mounting temperature and measuring temperature would now be suitable for study, avoiding the complications that could arise when the sample length is held constant in a controlled strain device.

For a truly controlled stress device the spring constant of the device must be lower than that of the sample. Inherently this requires the device to produce a much larger displacement in order to apply the force to the sample, for instance, by pushing on one end of a soft spring. To facilitate this a purely mechanical solution may be needed or perhaps some form of mechanical amplification for the piezo actuators.

Miniaturisation would also be useful on many fronts. Currently there are rather stringent requirements on sample size, with a minimum sample length of approximately 1 mm. For many interesting samples it is simply not possible to grow samples big enough for this method and routes to expand the capability, for instance by mounting samples to a platform that is then strained, should be explored. The upper limits of strain will also be limited by the quality of the sample's surface. Currently all samples are prepared with mechanical cutting and polishing but more pristine surfaces and geometries may be possible using new fabrication techniques such as xenon plasma or liquid gallium focused ion beam milling. However, restrictions on reasonable cutting time limit the overall size of samples that can be prepared in this way. In the current device the achievable strain range is also limited by the strength of the epoxy holding the sample between the sample plates. By reducing the thickness of the sample, the force required and therefore the shear stress in the epoxy can also be reduced. However, the length of the sample must also be reduced proportionally for the same buckling limit to be maintained. The highest ultimate strain may therefore come by utilising a combination of these ideas.

Overall we are still at an early stage in terms of the expected development of the uniaxial pressure technique, and there is still plenty of room for advancement as well as exciting opportunities for measurements to come. I hope then that the work presented in this thesis provides strong motivation for tackling these new challenges and experimental frontiers.

Bibliography

[1] K. Yamada. *Electron Correlation in Metals.* Cambridge University Press, 2004. ISBN 9780521572323. . on page 1.

[2] R. B. Laughlin and D. Pines. The Theory of Everything. *Proceedings of the National Academy of Sciences*, **97** 1 28–31, (2000). . . . . on page 1.

[3] N. W. Ashcroft and N. D. Mermin. *Solid State Physics.* Saunders College Publishing, 1976. ISBN 9780030839931. on pages 2, 4, 6, and 56.

[4] C. Kittel. *Introduction to Solid State Physics.* Wiley, eighth edition, 2004. ISBN 9780471415268. . . . . on pages 2 and 3.

[5] J. Singleton. *Band Theory and Electronic Properties of Solids.* Oxford University Press, 2001. ISBN 9780198506447. on pages 2, 3, 4, and 5.

[6] C. Bergemann, A. P. Mackenzie, S. R. Julian, D. Forsythe, and E. Ohmichi. Quasi-two-dimensional Fermi liquid properties of the unconventional superconductor Sr_2RuO_4. *Advances in Physics*, **52** 7 639–725, (2003). . on pages 4, 37, 39, 41, 42, 44, 54, 56, 71, and 113.

[7] P. A. Cox. *Transition Metal Oxides: An Introduction to Their Electronic Structure and Properties.* Oxford University Press, 2010. ISBN 9780199588947. . . . . on page 4.

[8] L. D. Landau. The Theory of a Fermi Liquid. *Zhurnal Experimental'noi i Teoreticheskoi Fiziki*, **30** 6 1058–1064, (1956). . . . . on page 6.

[9] L. D. Landau. Oscillations in a Fermi Liquid. *Zhurnal Experimental'noi i Teoreticheskoi Fiziki*, **32** 1 59–66, (1957). on page 6.

[10] L. D. Landau. On the Theory of the Fermi Liquid. *Zhurnal Experimental'noi i Teoreticheskoi Fiziki*, **8** 35 97–103, (1958). . . . . on page 6.

[11] D. Pines and P. Nozières. *The Theory of Quantum Liquids.* Westview Press, 1999. ISBN 9780738202297. . . on page 6.

[12] A. J. Schofield. Non-Fermi liquids. *Contemporary Physics*, **40** 2 95–115, (1999). . . . . on pages 6, 7, and 8.

[13] L. D. Landau and I. Pomeranchuk. On the properties of metals at very low temperatures. *Zhurnal Experimental'noi i Teoreticheskoi Fiziki*, **7** 379, (1937). . . . . on page 8.

[14] W. G. Baber. The Contribution to the Electrical Resistance of Metals from Collisions between Electrons. *Proceedings of the Royal Society of London A: Mathematical, Physical and Engineering Sciences*, **158** 894 383–396, (1937). on page 8.

[15] P. H. Frings, J. J. M. Franse, F. R. de Boer, and A. Menovsky. Magnetic properties of U_xPt_y compounds. *Journal of Magnetism and Magnetic Materials*, **31** 240–242, (1983). on page 9.

[16] G. R. Stewart, Z. Fisk, J. O. Willis, and J. L. Smith. Possibility of Coexistence of Bulk Superconductivity and Spin Fluctuations in UPt_3. *Physical Review Letters*, **52** 8 679–682, (1984). . . . . on pages 9 and 11.

[17] L. Taillefer and G. G. Lonzarich. Heavy-fermion quasiparticles in UPt_3. *Physical Review Letters*, **60** 15 1570–1573, (1988). . . . . on page 9.

[18] G. J. McMullan, P. M. C. Rourke, M. R. Norman, A. D. Huxley, N. Doiron-Leyraud, J. Flouquet, G. G. Lonzarich, A. McCollam, and S. R. Julian. The Fermi surface and f-valence electron count of UPt_3. *New Journal of Physics*, **10** 5 053029, (2008). . . . . on page 9.

[19] H. K. Onnes. The resistance of pure mercury at helium temperatures. *Commun. Phys. Lab. Univ. Leiden*, **12** 120, (1911). . . . . on pages 11 and 44.

[20] W. L. McMillan. Transition Temperature of Strong-Coupled Superconductors. *Physical Review*, **167** 2 331–344, (1968). on page 11.

[21] J. G. Bednorz and K. A. Müller. Possible High T_c Superconductivity in the Ba-La-Cu-O System. *Zeitschrift für Physik B: Condensed Matter*, **64** 2 189–193, (1986). . on page 11.

[22] A. Schilling, M. Cantoni, J. D. Guo, and H. R. Ott. Superconductivity above 130 K in the Hg-Ba-Ca-Cu-O system. *Nature*, **363** 6424 56–58, (1993). . . . . on page 11.

[23] F. Steglich, J. Aarts, C. D. Bredl, W. Lieke, D. Meschede, W. Franz, and H. Schäfer. Superconductivity in the Presence of Strong Pauli Paramagnetism: $CeCu_2S_2$. *Physical Review Letters*, **43** 25 1892–1896, (1979). . . . . on page 11.

[24] H. R. Ott, H. Rudigier, Z. Fisk, and J. L. Smith. UBe$_{13}$: An Unconventional Actinide Superconductor. *Physical Review Letters*, **50** 20 1595–1598, (1983). . . . . on page 11.

[25] Y. Kamihara, H. Hiramatsu, M. Hirano, R. Kawamura, H. Yanagi, T. Kamiya, and H. Hosono. Iron-Based Layered Superconductor: LaOFeP. *Journal of the American Chemical Society*, **128** 31 10012–10013, (2006). . . . . on page 11.

[26] Y. Kamihara, T. Watanabe, M. Hirano, and H. Hosono. Iron-Based Layered Superconductor La[O$_{1-x}$F$_x$]FeAs (x = 0.05–0.12) with T_c = 26 K. *Journal of the American Chemical Society*, **130** 11 3296–3297, (2008). on page 11.

[27] Z.-A. Ren, G.-C. Che, X.-L. Dong, J. Yang, W. Lu, W. Yi, X.-L. Shen, Z.-C. Li, L.-L. Sun, F. Zhou, and Z.-X. Zhao. Superconductivity and phase diagram in iron-based arsenic-oxides ReFeAsO$_{1-\delta}$ (Re = rare-earth metal) without fluorine doping. *EPL (Europhysics Letters)*, **83** 1 17002, (2008). on page 11.

[28] M. Rotter, M. Tegel, and D. Johrendt. Superconductivity at 38 K in the Iron Arsenide (Ba$_{1-x}$K$_x$)Fe$_2$As$_2$. *Physical Review Letters*, **101** 10 107006, (2008). . . . . . . on page 11.

[29] N. Doiron-Leyraud, C. Proust, D. LeBoeuf, J. Levallois, J.-B. Bonnemaison, R. Liang, D. A. Bonn, W. N. Hardy, and L. Taillefer. Quantum oscillations and the Fermi surface in an underdoped high-T_c superconductor. *Nature*, **447** 7144 565–568, (2007). . . . . on page 11.

[30] E. A. Yelland, J. Singleton, C. H. Mielke, N. Harrison, F. F. Balakirev, B. Dabrowski, and J. R. Cooper. Quantum Oscillations in the Underdoped Cuprate YBa$_2$Cu$_4$O$_8$. *Physical Review Letters*, **100** 4 047003, (2008). . . . . on page 11.

[31] A. F. Bangura, J. D. Fletcher, A. Carrington, J. Levallois, M. Nardone, B. Vignolle, P. J. Heard, N. Doiron-Leyraud, D. LeBoeuf, L. Taillefer, S. Adachi, C. Proust, and N. E. Hussey. Small Fermi Surface Pockets in Underdoped High Temperature Superconductors: Observation of Shubnikov-de Haas Oscillations in YBa$_2$Cu$_4$O$_8$. *Physical Review Letters*, **100** 4 047004, (2008). . . . . on page 11.

[32] A. P. Drozdov, M. I. Eremets, I. A. Troyan, V. Ksenofontov, and S. I. Shylin. Conventional superconductivity at 203 kelvin at high pressures in the sulfur hydride system. *Nature*, **525** 7567 73–76, (2015). . . . . on page 11.

[33] C. W. Hicks, D. O. Brodsky, E. A. Yelland, A. S. Gibbs, J. A. N. Bruin, M. E. Barber, S. D. Edkins, K. Nishimura, S. Yonezawa, Y. Maeno, and A. P. Mackenzie. Strong Increase of T_c of Sr_2RuO_4 Under Both Tensile and Compressive Strain. *Science*, **344** 6181 283–285, (2014). on pages 11, 22, 40, 54, 60, 68, and 70.

[34] C. W. Hicks, M. E. Barber, S. D. Edkins, D. O. Brodsky, and A. P. Mackenzie. Piezoelectric-based apparatus for strain tuning. *The Review of Scientific Instruments*, **85** 6 065003, (2014). . . . . on pages 11, 23, and 30.

[35] J. N. Reddy. *An Introduction to the Finite Element Method*. McGraw-Hill, third edition, 2006. ISBN 9780071267618. on pages 14 and 15.

[36] R. D. Cook, D. S. Malkus, M. E. Plesha, and R. J. Witt. *Concepts and Applications of Finite Element Analysis*. Wiley, fourth edition, 2001. ISBN 9780471356059.   on page 15.

[37] The MathWorks, Inc., Natick, Massachusetts, United States. *MATLAB 8.5*. . . . . on pages 17 and 32.

[38] C. Meingast, O. Kraut, T. Wolf, H. Wühl, A. Erb, and G. Müller-Vogt. Large *a-b* Anisotropy of the Expansivity Anomaly at T_c in Untwinned $YBa_2Cu_3O_{7-\delta}$. *Physical Review Letters*, **67** 12 1634–1637, (1991). . . . . on page 18.

[39] O. Kraut, C. Meingast, G. Bräuchle, H. Claus, A. Erb, G. Müller-Vogt, and H. Wühl. Uniaxial pressure dependence of T_c of untwinned $YBa_2Cu_3O_x$ single crystals for x=6.5– 7. *Physica C: Superconductivity*, **205** 1 139–146, (1993). on page 18.

[40] R. J. Wijngaarden, E. N. Van Eenige, J. J. Scholtz, and R. Griessen. High temperature superconductors under pressure: Experimental review and test on the RVB model. *High Pressure Research*, **3** 1–6 105–107, (1990). . . . on page 19.

[41] R. Küchler, T. Bauer, M. Brando, and F. Steglich. A compact and miniaturized high resolution capacitance dilatometer for measuring thermal expansion and magnetostriction. *The Review of Scientific Instruments*, **83** 9 095102, (2012). on page 19.

[42] N. Takeshita, T. Sasagawa, T. Sugioka, Y. Tokura, and H. Takagi. Gigantic Anisotropic Uniaxial Pressure Effect on Superconductivity within the CuO_2 Plane of $La_{1.64}Eu_{0.2}Sr_{0.16}CuO_4$: Strain Control of Stripe Criticality. *Journal of the Physics Society Japan*, **73** 5 1123–1126, (2004). . . . . on pages 19, 20, and 140.

[43] S. D. Johnson, R. J. Zieve, and J. C. Cooley. Nonlinear effect of uniaxial pressure on superconductivity in $CeCoIn_5$. *Physical Review B*, **83** 14 144510, (2011). . . . on pages 19 and 20.

[44] U. Welp, M. Grimsditch, S. Fleshler, W. Nessler, J. Downey, and G. W. Crabtree. Effect of Uniaxial Stress on the Superconducting Transition in $YBa_2Cu_3O_7$. *Physical Review Letters*, **69** 14 2130–2133, (1992). . . . . on page 20.

[45] O. M. Dix, A. G. Swartz, R. J. Zieve, J. Cooley, T. R. Sayles, and M. B. Maple. Anisotropic Dependence of Superconductivity on Uniaxial Pressure in $CeIrIn_5$. *Physical Review Letters*, **102** 19 197001, (2009). . . . . . . on page 20.

[46] S. Arumugam and N. Mori. A simple uniaxial high pressure cell for electrical resistivity measurements. *Physica C: Superconductivity*, **341** 1559–1560, (2000). . . . on page 20.

[47] D. S. Jin, A. Husmann, T. F. Rosenbaum, T. E. Steyer, and K. T. Faber. Controlled Symmetry Breaking in Super-conducting UPt_3. *Physical Review Letters*, **78** 9 1775–1778, (1997). . . . . on page 20.

[48] N. Aso, Y. Uwatoko, H. Kimura, Y. Noda, Y. Yoshida, S.-I. Ikeda, and S. Katano. A uniaxial pressure cell for neutron diffraction investigation and its use in studying the single- crystalline $Sr_3Ru_2O_7$ compound. *Journal of Physics: Condensed Matter*, **17** 40 S3025, (2005). . . . . . on page 20.

[49] F. Bourdarot, N. Martin, S. Raymond, L.-P. Regnault, D. Aoki, V. Taufour, and J. Flouquet. Magnetic properties of URu_2Si_2 under uniaxial stress by neutron scattering. *Physical Review B*, **84** 18 184430, (2011). . . . . on page 20.

[50] M. Shayegan, K. Karrai, Y. P. Shkolnikov, K. Vakili, E. P. De Poortere, and S. Manus. Low-temperature, *in situ* tunable, uniaxial stress measurements in semiconductors using a piezoelectric actuator. *Applied Physics Letters*, **83** 25 5235–5237, (2003). . . . . on pages 20 and 21.

[51] J.-H. Chu, H.-H. Kuo, J. G. Analytis, and I. R. Fisher. Divergent Nematic Susceptibility in an Iron Arsenide Superconductor. *Science*, **337** 6095 710–712, (2012). on pages 20, 21, and 127.

[52] PI Ceramic GmbH. *PICMA® Stack Multilayer Piezo Ac-tuators*, 2015. `http://www.piceramic.com/download/PI_Datasheet_P-882_-_P-888_20150123.pdf`. . . on page 20.

[53] PI Ceramic GmbH. *Catalog: Piezoelectric Actuators*, 2014. `http://www.piceramic.com/download/CAT128E_R2_Piezoelectric_Actuators.pdf`. . on pages 21 and 25.

[54] A. M. Simpson and W. Wolfs. Thermal expansion and piezoelectric response of PZT Channel 5800 for use in low-temperature scanning tunneling microscope designs. *Review of Scientific Instruments*, **58** 11 2193–2195, (1987). on pages 21 and 25.

[55] H.-H. Kuo, M. C. Shapiro, S. C. Riggs, and I. R. Fisher. Measurement of the elastoresistivity coefficients of the underdoped iron arsenide $Ba(Fe_{0.975}Co_{0.025})_2As_2$. *Physical Review B*, **88** 8 085113, (2013). . . . . on page 21.

[56] H.-H. Kuo, J.-H. Chu, J. C. Palmstrom, S. A. Kivelson, and I. R. Fisher. Ubiquitous signatures of nematic quantum criticality in optimally doped Fe-based superconductors. *Science*, **352** 6288 958–962, (2016).   on pages 22 and 140.

[57] M. C. Shapiro, A. T. Hristov, J. C. Palmstrom, J.-H. Chu, and I. R. Fisher. Measurement of the B_{1g} and B_{2g} components of the elastoresistivity tensor for tetragonal materials via transverse resistivity configurations. *Review of Scientific Instruments*, **87** 6 063902, (2016). . . . . on page 22.

[58] Z. H. Ni, T. Yu, Y. H. Lu, Y. Y. Wang, Y. P. Feng, and Z. X. Shen. Uniaxial Strain on Graphene: Raman Spectroscopy Study and Band-Gap Opening. *ACS Nano*, **2** 11 2301–2305, (2008). . . . . on page 22.

[59] F. Guinea, M. I. Katsnelson, and A. K. Geim. Energy gaps and a zero-field quantum Hall effect in graphene by strain engineering. *Nature Physics*, **6** 1 30–33, (2010). on page 22.

[60] J.-P. Locquet, J. Perret, J. Fompeyrine, E. Mächler, J.W. Seo, and G. Van Tendeloo. Doubling the critical temperature of $La_{1.9}Sr_{0.1}CuO_4$ using epitaxial strain. *Nature*, **394** 6692 453–456, (1998). . . . . on page 22.

[61] A. P. Mackenzie and Y. Maeno. The superconductivity of Sr_2RuO_4 and the physics of spin-triplet pairing. *Reviews of Modern Physics*, **75** 2 657–712, (2003). . on pages 22, 44, 49, 50, and 52.

[62] M. Sigrist and K. Ueda. Phenomenological theory of unconventional superconductivity. *Reviews of Modern Physics*, **63** 2 239–311, (1991). . . . . on pages 23 and 54.

[63] M. B. Walker and P. Contreras. Theory of elastic properties of Sr2RuO4 at the superconducting transition temperature. *Physical Review B*, **66** 21 214508, (2002). ... on pages 23 and 54.

[64] J. Ekin. *Experimental Techniques for Low-Temperature Measurements: Cryostat Design, Material Properties and Superconductor Critical-Current Testing.* Oxford University Press, 2006. ISBN 9780198570547. .... on page 24.

[65] C. W. Hicks. private communication, 2013. .. on page 27.

[66] C. E. Ojeda, E. J. Oakes, J. R. Hill, D. Aldi, and G. A. Forsberg. Temperature effects on adhesive bond strengths and modulus for commonly used spacecraft stuctural adhesives. Technical report, Jet Propulsion Laboratory, Pasadena, CA, USA, 2011. .... on pages 28 and 29.

[67] T. Hashimoto and A. Ikushima. Mechanical properties of Stycast-1266 at low temperatures. *Review of Scientific Instruments*, **51** 3 378–379, (1980). .... on page 28.

[68] J. Paglione, C. Lupien, W. A. MacFarlane, J. M. Perz, L. Taillefer, Z. Q. Mao, and Y. Maeno. Elastic tensor of Sr_2RuO_4. *Physical Review B*, **65** 22 220506, (2002). on pages 28, 66, 71, and 116.

[69] W. van de Camp, M. M. J. Dhallé, W. A. J. Wessel, L. Warnet, B. Atli-Veltin, S. van der Putten, J. A. M. Dam, and H. J. M. ter Brake. Cryogenic fatigue and stress-strain behavior of a fibre metal laminate. *Physics Procedia*, **67** 1043–1048, (2015). .... on pages 29 and 36.

[70] C. Geuzaine and J.-F. Remacle. Gmsh: A 3-D finite element mesh generator with built-in pre- and post-processing facilities. *International Journal for Numerical Methods in Engineering*, **79** 11 1309–1331, (2009). .... on page 32.

[71] American Institute of Steel Construction. *Steel Construction Manual.* American Institute of Steel Construction, fourteenth edition, 2011. ISBN 9781564240606. ... on page 35.

[72] EPOXY TECHNOLOGY, INC. *EPO-TEK® H74 Technical Data Sheet*, 2010. http://www.epotek.com/site/administrator/components/com_products/assets/files/Style_Uploads/H74.pdf. .... on page 36.

[73] EPOXY TECHNOLOGY, INC. *EPO-TEK® H20E Technical Data Sheet*, 2015. http://www.epotek.com/site/administrator/components/com_products/assets/files/Style_Uploads/H20E.pdf. .... on page 36.

[74] Huntsman Advanced Materials GmbH. *Araldite® Technical Data Sheet*, 2015. . . . . on page 36.

[75] Master Bond Inc. *MasterBond® EP29LPSP Technical Data Sheet*, 2015. . . . . on page 36.

[76] M. Lei, J. L. Sarrao, W. M. Visscher, T. M. Bell, J. D. Thompson, A. Migliori, U. W. Welp, and B. W. Veal. Elastic constants of a monocrystal of superconducting $YBa_2Cu_3O_{7-\delta}$. *Physical Review B*, **47** 10 6154–6156, (1993). . . . . on page 37.

[77] Y. Maeno, H. Hashimoto, K. Yoshida, S. Nishizaki, T. Fujita, J. G. Bednorz, and F. Lichtenberg. Superconductivity in a layered perovskite without copper. *Nature*, **372** 6506 532–534, (1994). . . . . on page 39.

[78] D. Forsythe, S. R. Julian, C. Bergemann, E. Pugh, M. J. Steiner, P. L. Alireza, G. J. McMullan, F. Nakamura, R. K. W. Haselwimmer, I. R. Walker, S. S. Saxena, G. G. Lonzarich, A. P. Mackenzie, Z. Q. Mao, and Y. Maeno. Evolution of Fermi-Liquid Interactions in Sr_2RuO_4 under Pressure. *Physical Review Letters*, **89** 16 166402, (2002). on page 39.

[79] N. Kikugawa, C. Bergemann, A. P. Mackenzie, and Y. Maeno. Band-selective modification of the magnetic fluctuations in Sr_2RuO_4: A study of substitution effects. *Physical Review B*, **70** 13 134520, (2004). on pages 39, 58, and 59.

[80] K. M. Shen, N. Kikugawa, C. Bergemann, L. Balicas, F. Baumberger, W. Meevasana, N. J. C. Ingle, Y. Maeno, Z. X. Shen, and A. P. Mackenzie. Evolution of the Fermi Surface and Quasiparticle Renormalization through a van Hove Singularity in $Sr_{2-y}La_yRuO_4$. *Physical Review Letters*, **99** 18 187001, (2007). . . . . on pages 39, 56, 58, and 71.

[81] B. Burganov, C. Adamo, A. Mulder, M. Uchida, P.D.C. King, J.W. Harter, D.E. Shai, A.S. Gibbs, A.P. Mackenzie, R. Uecker, M. Bruetzam, M.R. Beasley, C.J. Fennie, D.G. Schlom, and K.M. Shen. Strain Control of Fermiology and Many-Body Interactions in Two-Dimensional Ruthenates. *Physical Review Letters*, **116** 19 197003, (2016). on pages 39 and 59.

[82] O. Chmaissem, J. D. Jorgensen, H. Shaked, S. Ikeda, and Y. Maeno. Thermal expansion and compressibility of Sr_2RuO_4. *Physical Review B*, **57** 9 5067–5070, (1998). on page 41.

[83] A. P. Mackenzie, S. R. Julian, A. J. Diver, G. J. McMullan, M. P. Ray, G. G. Lonzarich, Y. Maeno, S. Nishizaki, and T. Fujita. Quantum Oscillations in the Layered Perovskite Superconductor Sr_2RuO_4. *Physical Review Letters*, **76** 20 3786–3789, (1996). . . . . on pages 41, 42, 43, and 44.

[84] A. Damascelli, D. H. Lu, K. M. Shen, N. P. Armitage, F. Ronning, D. L. Feng, C. Kim, and Z.-X. Shen. Fermi Surface, Surface States, and Surface Reconstruction in Sr_2RuO_4. *Physical Review Letters*, **85** 24 5194–5197, (2000). . . . . on page 42.

[85] C. Bergemann, S. R. Julian, A. P. Mackenzie, S. NishiZaki, and Y. Maeno. Detailed Topography of the Fermi Surface of Sr_2RuO_4. *Physical Review Letters*, **84** 12 2662–2665, (2000). . . . . on page 42.

[86] Y. Yoshida, A. Mukai, R. Settai, K. Miyake, Y. Inada, Y. Onuki, K. Betsuyaku, H. Harima, T. D. Matsuda, Y. Aoki, and H. Sato. Fermi Surface Properties in Sr_2RuO_4. *Journal of the Physical Society of Japan*, **68** 9 3041–3053, (1999). . . . . on page 42.

[87] Y. Yoshida, R. Settai, Y. Onuki, H. Takei, K. Betsuyaku, and H. Harima. Fermi Surface and Yamaji Effect in Sr_2RuO_4. *Journal of the Physical Society of Japan*, **67** 5 1677–1681, (1998). . . . . on page 42.

[88] E. Ohmichi, H. Adachi, Y. Mori, Y. Maeno, T. Ishiguro, and T. Oguchi. Angle-dependent magnetoresistance oscillation in the layered perovskite Sr_2RuO_4. *Physical Review B*, **59** 11 7263–7265, (1999). . . . . on page 42.

[89] Y. Maeno, K. Yoshida, H. Hashimoto, S. Nishizaki, S.-I. Ikeda, M. Nohara, T. Fujita, A. P. Mackenzie, N. E. Hussey, J. G. Bednorz, and F. Lichtenberg. Two-Dimensional Fermi Liquid Behavior of the Superconductor Sr_2RuO_4. *Journal of the Physical Society of Japan*, **66** 5 1405–1408, (1997). . . . . on page 42.

[90] K. Ishida, Y. Kitaoka, K. Asayama, S. Ikeda, S. Nishizaki, Y. Maeno, K. Yoshida, and T. Fujita. Anisotropic pairing in superconducting Sr_2RuO_4: Ru NMR and NQR studies. *Physical Review B*, **56** 2 R505–R508, (1997).   on page 42.

[91] E. Ohmichi, Y. Maeno, S. Nagai, Z. Q. Mao, M. A. Tanatar, and T. Ishiguro. Magnetoresistance of Sr_2RuO_4 under high magnetic fields parallel to the conducting plane. *Physical Review B*, **61** 10 7101–7107, (2000).   on pages 43 and 94.

[92] N. E. Hussey, A. P. Mackenzie, J. R. Cooper, Y. Maeno, S. Nishizaki, and T. Fujita. Normal-state magnetoresistance of Sr_2RuO_4. *Physical Review B*, **57** 9 5505–5511, (1998). on page 43.

[93] D. Shoenberg. *Magnetic oscillations in metals*. Cambridge University Press, 1984. ISBN 9780521224802.   on page 43.

[94] V. L. Ginzburg and L. D. Landau. On the theory of superconductivity. *Zhurnal Experimental'noi i Teoreticheskoi Fiziki*, **20** 1064, (1950). . . . . on page 44.

[95] J. Bardeen, L. N. Cooper, and J. R. Schrieffer. Microscopic Theory of Superconductivity. *Physical Review*, **106** 1 162–164, (1957). . . . . on page 44.

[96] J. F. Annett. *Superconductivity, Superfluids and Condensates*. Oxford University Press, 2004. ISBN 9780198507567. on pages 44 and 47.

[97] S. J. Blundell. *Superconductivity: A Very Short Introduction*. Oxford University Press, 2009. ISBN 9780199540907. on page 46.

[98] P. Townsend and J. Sutton. Investigation by Electron Tunneling of the Superconducting Energy Gaps in Nb, Ta, Sn, and Pb. *Physical Review*, **128** 2 591–595, (1962). on page 48.

[99] A. P. Mackenzie, R. K. W. Haselwimmer, A. W. Tyler, G. G. Lonzarich, Y. Mori, S. Nishizaki, and Y. Maeno. Extremely Strong Dependence of Superconductivity on Disorder in Sr_2RuO_4. *Physical Review Letters*, **80** 1 161–164, (1998). . . . . on page 49.

[100] P. W. Anderson. Knight Shift in Superconductors. *Physical Review Letters*, **3** 7 325–326, (1959). . . . . on page 49.

[101] T. M. Rice and M. Sigrist. Sr_2RuO_4: an electronic analogue of ^{3}He? *Journal of Physics: Condensed Matter*, **7** 47 L643–L648, (1995). . . . . on page 50.

[102] Y. Maeno, S. Kittaka, T. Nomura, S. Yonezawa, and K. Ishida. Evaluation of Spin-Triplet Superconductivity in Sr_2RuO_4. *Journal of the Physical Society of Japan*, **81** 1 011009, (2012). . . . . on page 50.

[103] C. Kallin. Chiral p-wave order in Sr_2RuO_4. *Reports on Progress in Physics*, **75** 4 042501, (2012). . . . . on page 50.

[104] Y. Liu and Z.-Q. Mao. Unconventional superconductivity in Sr$_2$RuO$_4$. *Physica C: Superconductivity and its Applications*, **514** 339–353, (2015). . . . . on page 50.

[105] K. Ishida, H. Mukuda, Y. Kitaoka, K. Asayama, Z. Q. Mao, Y. Mori, and Y. Maeno. Spin-triplet superconductivity in Sr$_2$RuO$_4$ identified by ^{17}O Knight Shift. *Nature*, **396** 6712 658–660, (1998). . . . . on page 50.

[106] J. A. Duffy, S. M. Hayden, Y. Maeno, Z. Mao, J. Kulda, and G. J. Mcintyre. Polarized-Neutron Scattering Study of the Cooper-Pair Moment in Sr$_2$RuO$_4$. *Physical Review Letters*, **85** 25 5412–5415, (2000). . . . . on page 50.

[107] K. D. Nelson, Z. Q. Mao, Y. Maeno, and Y. Liu. Odd-Parity Superconductivity in Sr$_2$RuO$_4$. *Science*, **306** 5699 1151–1154, (2004). . . . . on page 50.

[108] J. A. Sauls, Z. Zou, and P. W. Anderson. Josephson Tunneling between Superconductors with Different Spin and Space Symmetries. Unpublished 1985. . . . . on page 51.

[109] V. B. Geshkenbein and A. I. Larkin. The Josephson effect in superconductors with heavy fermions. *JETP Letters*, **43** 6 306–309, (1986). . . . . on page 51.

[110] R. Balian and N. R. Werthamer. Superconductivity with Pairs in a Relative *p* Wave. *Physical Review*, **131** 4 1553–1564, (1963). . . . . on page 51.

[111] G. M. Luke, Y. Fudamoto, K. M. Kojima, M. I. Larkin, B. Nachumi, Y. J. Uemura, J. E. Sonier, Y. Maeno, Z. Q. Mao, Y. Mori, and D. F. Agterberg. Unconventional superconductivity in Sr$_2$RuO$_4$. *Physica B: Condensed Matter*, **289-290** 373–376, (2000). on page 52.

[112] G. M. Luke, Y. Fudamoto, K. M. Kojima, M. I. Larkin, J. Merrin, B. Nachumi, Y. J. Uemura, Y. Maeno, Z. Q. Mao, Y. Mori, H. Nakamura, and M. Sigrist. Time-reversal symmetry-breaking superconductivity in Sr$_2$RuO$_4$. *Nature*, **394** 6693 558–561, (1998). . . . . on page 52.

[113] A. Kapitulnik, J. Xia, E. Schemm, and A. Palevski. Polar Kerr effect as probe for time-reversal symmetry breaking in unconventional superconductors. *New Journal of Physics*, **11** 5 055060, (2009). . . . . on page 52.

[114] T. Tamegai, K. Yamazaki, M. Tokunaga, Z. Mao, and Y. Maeno. Search for spontaneous magnetization in Sr$_2$RuO$_4$. *Physica C: Superconductivity*, **388-389** 499–500, (2003). . . . . on page 53.

[115] P. G. Björnsson, Y. Maeno, M. E. Huber, and K. A. Moler. Scanning magnetic imaging of Sr_2RuO_4. *Physical Review B*, **72** 1 012504, (2005). . . . . on page 53.

[116] J. R. Kirtley, C. Kallin, C. W. Hicks, E.-A. Kim, Y. Liu, K. A. Moler, Y. Maeno, and K. D. Nelson. Upper limit on spontaneous supercurrents in Sr_2RuO_4. *Physical Review B*, **76** 1 014526, (2007). . . . . on page 53.

[117] C. W. Hicks, J. R. Kirtley, T. M. Lippman, N. C. Koshnick, M. E. Huber, Y. Maeno, W. M. Yuhasz, M. B. Maple, and K. A. Moler. Limits on superconductivity-related magnetization in Sr_2RuO_4 and $PrOs_4Sb_{12}$ from scanning SQUID microscopy. *Physical Review B*, **81** 21 214501, (2010). . . . . on page 53.

[118] J. Xia, Y. Maeno, P. T. Beyersdorf, M. M. Fejer, and A. Kapitulnik. High Resolution Polar Kerr Effect Measurements of Sr_2RuO_4: Evidence for Broken Time-Reversal Symmetry in the Superconducting State. *Physical Review Letters*, **97** 16 167002, (2006). . . . . on page 53.

[119] S. NishiZaki, Y. Maeno, and Z. Mao. Changes in the Superconducting State of Sr_2RuO_4 under Magnetic Fields Probed by Specific Heat. *Journal of the Physical Society of Japan*, **69** 2 572–578, (2000). . . . . on page 53.

[120] K. Izawa, H. Takahashi, H. Yamaguchi, Y. Matsuda, M. Suzuki, T. Sasaki, T. Fukase, Y. Yoshida, R. Settai, and Y. Onuki. Superconducting Gap Structure of Spin-Triplet Superconductor Sr_2RuO_4 Studied by Thermal Conductivity. *Physical Review Letters*, **86** 12 2653–2656, (2001). . . . . on page 53.

[121] M. A. Tanatar, S. Nagai, Z. Q. Mao, Y. Maeno, and T. Ishiguro. Thermal conductivity of superconducting Sr_2RuO_4 in oriented magnetic fields. *Physical Review B*, **63** 6 064505, (2001). . . . . on page 53.

[122] M. A. Tanatar, M. Suzuki, S. Nagai, Z. Q. Mao, Y. Maeno, and T. Ishiguro. Anisotropy of Magnetothermal Conductivity in Sr_2RuO_4. *Physical Review Letters*, **86** 12 2649–2652, (2001). . . . . on page 53.

[123] K. Ishida, H. Mukuda, Y. Kitaoka, Z. Mao, Y. Mori, and Y. Maeno. Anisotropic Superconducting Gap in the Spin-Triplet Superconductor Sr_2RuO_4: Evidence from a Ru-NQR Study. *Physical Review Letters*, **84** 23 5387–5390, (2000). . . . . on page 53.

[124] I. Bonalde, B. D. Yanoff, M. B. Salamon, D. J. Van Harlingen, E. M. E. Chia, Z. Q. Mao, and Y. Maeno. Temperature Dependence of the Penetration Depth in Sr_2RuO_4: Evidence for Nodes in the Gap Function. *Physical Review Letters*, **85** 22 4775–4778, (2000). .... on page 53.

[125] M. A. Hein, R. J. Ormeno, and C. E. Gough. The microwave surface impedance of ultra-pure superconducting metals. *Journal of Physics: Condensed Matter*, **13** 4 L65, (2001). .... on page 53.

[126] C. Lupien, W. A. Macfarlane, C. Proust, L. Taillefer, Z. Q. Mao, and Y. Maeno. Ultrasound Attenuation in Sr_2RuO_4: An Angle-Resolved Study of the Superconducting Gap Function. *Physical Review Letters*, **86** 26 5986–5989, (2001). on page 53.

[127] R. C. Morris, R. V. Coleman, and R. Bhandari. Superconductivity and Magnetoresistance in $NbSe_2$. *Physical Review B*, **5** 3 895–901, (1972). .... on page 54.

[128] K. Deguchi, M. A. Tanatar, Z. Mao, T. Ishiguro, and Y. Maeno. Superconducting Double Transition and the Upper Critical Field Limit of Sr_2RuO_4 in Parallel Magnetic Fields. *Journal of the Physical Society of Japan*, **71** 12 2839–2842, (2002). .... on page 54.

[129] I. Zutić and I. Mazin. Phase-Sensitive Tests of the Pairing State Symmetry in Sr_2RuO_4. *Physical Review Letters*, **95** 21 217004, (2005). .... on page 54.

[130] M. Leijnse and K. Flensberg. Introduction to topological superconductivity and Majorana fermions. *Semiconductor Science and Technology*, **27** 12 124003, (2012). .. on page 55.

[131] C. W. J. Beenakker. Search for Majorana Fermions in Superconductors. *Annual Review of Condensed Matter Physics*, **4** 1 113–136, (2013). .... on page 55.

[132] L. Van Hove. The Occurrence of Singularities in the Elastic Frequency Distribution of a Crystal. *Physical Review*, **89** 6 1189–1193, (1953). .... on page 55.

[133] I. M. Lifshitz. Anomalies of Electron Characteristics of a Metal in the High Pressure Region. *Zhurnal Experimental'noi i Teoreticheskoi Fiziki*, **38** 5 1569–1576, (1960). on page 57.

[134] L. D. Landau. On the theory of phase transitions. *Zhurnal Experimental'noi i Teoreticheskoi Fiziki*, **7** 1 19–32, (1937). on page 57.

[135] X.-G. Wen. *Quantum Field Theory of Many-Body Systems.* Oxford University Press, 2004. ISBN 9780198530947. on page 57.

[136] B. G. Lazarev, L. S. Lazareva, and V. I. Makarov. Some Singularities of the Behavior of the Superconducting Transition Temperature of Thallium Under Pressure. *Zhurnal Experimental'noi i Teoreticheskoi Fiziki*, **44** 2 481–482, (1963). .... on page 58.

[137] V. I. Makarov and V. G. Bar'yakhtar. Anomalies in the Superconducting Transition Temperature under Pressure. *Zhurnal Experimental'noi i Teoreticheskoi Fiziki*, **48** 6 1717–1722, (1965). .... on page 58.

[138] P. M. Holtham. A pseudopotential calculation of the effect of pressure on the Fermi surface and superconducting transition temperature of thallium. *Journal of Physics F: Metal Physics*, **3** 7 1361–1372, (1973). .... on page 58.

[139] C. W. Chu, T. F. Smith, and W. E. Gardner. Study of Fermi-Surface Topology Changes in Rhenium and Dilute Re Solid Solutions from T_c Measurements at High Pressure. *Physical Review B*, **1** 1 214–221, (1970). ...... on page 58.

[140] V. V. Struzhkin, Y. A. Timofeev, R. J. Hemley, and H.-K. Mao. Superconducting T_c and Electron-Phonon Coupling in Nb to 132 GPa: Magnetic Susceptibility at Megabar Pressures. *Physical Review Letters*, **79** 21 4262–4265, (1997). .... on page 58.

[141] S. Benhabib, A. Sacuto, M. Civelli, I. Paul, M. Cazayous, Y. Gallais, M.-A. Méasson, R. D. Zhong, J. Schneeloch, G. D. Gu, D. Colson, and A. Forget. Collapse of the Normal-State Pseudogap at a Lifshitz Transition in the $Bi_2Sr_2CaCu_2O_{8+\delta}$ Cuprate Superconductor. *Physical Review Letters*, **114** 14 147001, (2015). ...... on page 58.

[142] D. LeBoeuf, N. Doiron-Leyraud, B. Vignolle, M. Sutherland, B. J. Ramshaw, J. Levallois, R. Daou, F. Laliberté, O. Cyr-Choinière, J. Chang, Y. J. Jo, L. Balicas, R. Liang, D. A. Bonn, W. N. Hardy, C. Proust, and L. Taillefer. Lifshitz critical point in the cuprate superconductor $YBa_2Cu_3O_y$ from high-field Hall effect measurements. *Physical Review B*, **83** 5 054506, (2011). .... on page 58.

[143] N. Kikugawa, A. P. Mackenzie, C. Bergemann, R. A. Borzi, S. A. Grigera, and Y. Maeno. Rigid-band shift of the Fermi level in the strongly correlated metal: $Sr_{2-y}La_yRuO_4$. *Physical Review B*, **70** 6 060508, (2004). .... on page 58.

[144] J. Laugier and A. Filhol. An interactive program for the interpretation and simulation of Laue patterns. *Journal of Applied Crystallography*, **16** 2 281–283, (1983).   on pages 60 and 108.

[145] H. Taniguchi, K. Nishimura, S. K. Goh, S. Yonezawa, and Y. Maeno. Higher-T_c Superconducting Phase in Sr_2RuO_4 Induced by In-Plane Uniaxial Pressure. *Journal of the Physical Society of Japan*, **84** 1 014707, (2015). . . . on page 69.

[146] Y. A. Ying, N. E. Staley, Y. Xin, K. Sun, X. Cai, D. Fobes, T. J. Liu, Z. Q. Mao, and Y. Liu. Enhanced spin-triplet superconductivity near dislocations in Sr_2RuO_4. *Nature Communications*, **4** 2596, (2013). . . . . on page 69.

[147] A. Steppke, L. Zhao, M. E. Barber, T. Scaffidi, F. Jerzembeck, H. Rosner, A. S. Gibbs, Y. Maeno, S. H. Simon, A. P. Mackenzie, and C. W. Hicks. Strong peak in T_c of Sr_2RuO_4 under uniaxial pressure. *Science*, **355** 6321, (2017). . . . . on pages 71, 73, 74, 75, and 81.

[148] Y.-C. Liu, F.-C. Zhang, T. M. Rice, and Q.-H. Wang. Theory of the Evolution of Superconductivity in Sr_2RuO_4 under Anisotropic Strain. arXiv:1604.06666, Unpublished 2016. . . . . on pages 72 and 79.

[149] L. Lyard, P. Samuely, P. Szabo, T. Klein, C. Marcenat, L. Paulius, K. H. P. Kim, C. U. Jung, H.-S. Lee, B. Kang, S. Choi, S.-I. Lee, J. Marcus, S. Blanchard, A. G. M. Jansen, U. Welp, G. Karapetrov, and W. K. Kwok. Anisotropy of the upper critical field and critical current in single crystal MgB_2. *Physical Review B*, **66** 18 180502, (2002). . . . . on page 73.

[150] A. Gurevich. Limits of the upper critical field in dirty two-gap superconductors. *Physica C: Superconductivity and its Applications*, **456** 1-2 160–169, (2007). . . . . on page 73.

[151] S. Kittaka, T. Nakamura, Y. Aono, S. Yonezawa, K. Ishida, and Y. Maeno. Angular dependence of the upper critical field of Sr_2RuO_4. *Physical Review B*, **80** 17 174514, (2009). on page 73.

[152] A. Ramires and M. Sigrist. Identifying detrimental effects for multiorbital superconductivity: Application to Sr_2RuO_4. *Physical Review B*, **94** 10 104501, (2016). . . . . on page 75.

[153] A. Ramires and M. Sigrist. A note on the upper critical field of Sr_2RuO_4 under strain. arXiv:1606.08709, Unpublished 2016. . . . . on page 75.

[154] Y. Maeno, T. Ando, Y. Mori, E. Ohmichi, S. Ikeda, S. NishiZaki, and S. Nakatsuji. Enhancement of Superconductivity of Sr_2RuO_4 to 3 K by Embedded Metallic Microdomains. *Physical Review Letters*, **81** 17 3765–3768, (1998). . . . . on page 75.

[155] H. Yaguchi, M. Wada, T. Akima, Y. Maeno, and T. Ishiguro. Interface superconductivity in the eutectic Sr_2RuO_4-Ru: 3-K phase of Sr_2RuO_4. *Physical Review B*, **67** 21 214519, (2003). . . . . on page 75.

[156] S. Kittaka, T. Nakamura, H. Yaguchi, S. Yonezawa, and Y. Maeno. Spatial Development of Superconductivity in the Sr_2RuO_4-Ru Eutectic System. *Journal of the Physical Society of Japan*, **78** 6 064703, (2009). . . . . on page 75.

[157] Y. A. Ying, Y. Xin, B. W. Clouser, E. Hao, N. E. Staley, R. J. Myers, L. F. Allard, D. Fobes, T. Liu, Z. Q. Mao, and Y. Liu. Suppression of Proximity Effect and the Enhancement of p-Wave Superconductivity in the Sr_2RuO_4-Ru System. *Physical Review Letters*, **103** 24 247004, (2009). on page 75.

[158] P. J. Ford and J. A. Mydosh. Electrical resistivity of noble-metal-host-3d solute spin-glass alloys. *Physical Review B*, **14** 5 2057–2070, (1976). . . . . on page 82.

[159] S. A. Hartnoll, R. Mahajan, M. Punk, and S. Sachdev. Transport near the Ising-nematic quantum critical point of metals in two dimensions. *Physical Review B*, **89** 15 155130, (2014). . . . . on page 83.

[160] D. L. Maslov, V. I. Yudson, and A. V. Chubukov. Resistivity of a Non-Galilean–Invariant Fermi Liquid near Pomeranchuk Quantum Criticality. *Physical Review Letters*, **106** 10 106403, (2011). . . . . on page 83.

[161] H. K. Pal, V. I. Yudson, and D. L. Maslov. Resistivity of non-Galilean-invariant Fermi- and non-Fermi liquids. *Lithuanian Journal of Physics*, **52** 2 142–164, (2012). on page 83.

[162] F. M. Grosche, C. Pfleiderer, G. J. McMullan, G. G. Lonzarich, and N. R. Bernhoeft. Critical behaviour of $ZrZn_2$. *Physica B: Physics of Condensed Matter*, **206–207** 20–22, (1995). . . . . on page 83.

[163] S. R. Julian, C. Pfleiderer, F. M. Grosche, N. D. Mathur, G. J. McMullan, A. J. Diver, I. R. Walker, and G. G. Lonzarich. The normal states of magnetic d and f transition

metals. *Journal of Physics: Condensed Matter*, **8** 48 9675, (1996). .... on page 83.

[164] C. Pfleiderer, G. J. McMullan, S. R. Julian, and G. G. Lonzarich. Magnetic quantum phase transition in MnSi under hydrostatic pressure. *Physical Review B*, **55** 13 8330–8338, (1997). .... on page 83.

[165] C. Pfleiderer, S. R. Julian, and G. G. Lonzarich. Non-Fermi-liquid nature of the normal state of itinerant-electron ferromagnets. *Nature*, **414** 6862 427–430, (2001). on page 83.

[166] P. G. Niklowitz, F. Beckers, G. G. Lonzarich, G. Knebel, B. Salce, J. Thomasson, N. Bernhoeft, D. Braithwaite, and J. Flouquet. Spin-fluctuation-dominated electrical transport of Ni_3Al at high pressure. *Physical Review B*, **72** 2 024424, (2005). .... on page 83.

[167] F. M. Grosche, S. R. Julian, N. D. Mathur, and G. G. Lonzarich. Magnetic and superconducting phases of $CePd_2Si_2$. *Physica B: Condensed Matter*, **223** 50–52, (1996). .... on page 83.

[168] F. M. Grosche, I. R. Walker, S. R. Julian, N. D. Mathur, D. M. Freye, M. J. Steiner, and G. G. Lonzarich. Superconductivity on the threshold of magnetism in $CePd_2Si_2$ and $CeIn_3$. *Journal of Physics: Condensed Matter*, **13** 12 2845–2860, (2001). .... on page 83.

[169] D. Moroni-Klementowicz, M. Brando, C. Albrecht, W. J. Duncan, F. M. Grosche, D. Grüner, and G. Kreiner. Magnetism in $Nb_{1-y}Fe_{2+y}$: Composition and magnetic field dependence. *Physical Review B*, **79** 22 224410, (2009). on page 83.

[170] M. Brando, W. J. Duncan, D. Moroni-Klementowicz, C. Albrecht, D. Grüner, R. Ballou, and F. M. Grosche. Logarithmic Fermi-Liquid Breakdown in $NbFe_2$. *Physical Review Letters*, **101** 2 026401, (2008). .... on page 84.

[171] B. P. Neal, E. R. Ylvisaker, and W. E. Pickett. Quantum criticality in $NbFe_2$ induced by zero carrier velocity. *Physical Review B*, **84** 8 085133, (2011). ..... on page 84.

[172] J. R. Klauder and J. E. Kunzler. Higher Order Open Orbits and the Interpretation of Magnetoresistance and Hall-Effect Data for Copper. In *The Fermi Surface*, page 125. John Wiley & Sons, New York, 1960. .... on page 85.

[173] A. B. Pippard. *Magnetoresistance in metals*. Cambridge University Press, 1989. ISBN 9780521326605. on page 85.

[174] A.P. Mackenzie, N.E. Hussey, A.J. Diver, S.R. Julian, Y. Maeno, S. Nishizaki, and T. Fujita. Hall effect in the two-dimensional metal Sr_2RuO_4. *Physical Review B*, **54** 10 7425–7429, (1996). . . . . on pages 86 and 88.

[175] N.P. Ong. Geometric interpretation of the weak-field Hall conductivity in two-dimensional metals with arbitrary Fermi surface. *Physical Review B*, **43** 1 193–201, (1991). on page 86.

[176] N. Kikugawa, A.P. Mackenzie, C. Bergemann, and Y. Maeno. Low-temperature Hall effect in substituted Sr_2RuO_4. *Physical Review B*, **70** 17 174501, (2004). on page 88.

[177] S.-I. Ikeda, Y. Maeno, S. Nakatsuji, M. Kosaka, and Y. Uwatoko. Ground state in $Sr_3Ru_2O_7$: Fermi liquid close to a ferromagnetic instability. *Physical Review B*, **62** 10 R6089–R6092, (2000). . . . . on pages 93, 95, and 96.

[178] S. A. Grigera, R. A. Borzi, A. P. Mackenzie, S. R. Julian, R. S. Perry, and Y. Maeno. Angular dependence of the magnetic susceptibility in the itinerant metamagnet $Sr_3Ru_2O_7$. *Physical Review B*, **67** 21 214427, (2003). . . . on pages 93, 100, 114, 115, and 123.

[179] Y. Tokiwa, M. McHalwat, R. S. Perry, and P. Gegenwart. Multiple Metamagnetic Quantum Criticality in $Sr_3Ru_2O_7$. *Physical Review Letters*, **116** 22 226402, (2016). on pages 93 and 107.

[180] S. A. Grigera, P. Gegenwart, R. A. Borzi, F. Weickert, A. J. Schofield, R. S. Perry, T. Tayama, T. Sakakibara, Y. Maeno, A. G. Green, and A. P. Mackenzie. Disorder-Sensitive Phase Formation Linked to Metamagnetic Quantum Criticality. *Science*, **306** 5699 1154–1157, (2004). on pages 93, 103, 131, 133, and 183.

[181] C. Lester, S. Ramos, R. S. Perry, T. P. Croft, R. I. Bewley, T. Guidi, P. Manuel, D. D. Khalyavin, E. M. Forgan, and S. M. Hayden. Field-tunable spin-density-wave phases in $Sr_3Ru_2O_7$. *Nature Materials*, **14** 4 373–378, (2015). on pages 93 and 105.

[182] R. A. Borzi, S. A. Grigera, J. Farrell, R. S. Perry, S. J. S. Lister, S. L. Lee, D. A. Tennant, Y. Maeno, and A. P. Mackenzie. Formation of a Nematic Fluid at High Fields in $Sr_3Ru_2O_7$. *Science*, **315** 5809 214–217, (2007). on pages 93, 103, and 104.

[183] M. Chiao, C. Pfleiderer, S. R. Julian, G. G. Lonzarich, R. S. Perry, A. P. Mackenzie, and Y. Maeno. Effect of pressure on metamagnetic $Sr_3Ru_2O_7$. *Physica B: Condensed Matter*, **312-313** 698–699, (2002). . . . . on page 94.

[184] W. Wu, A. McCollam, S. A. Grigera, R. S. Perry, A. P. Mackenzie, and S. R. Julian. Quantum critical metamagnetism of $Sr_3Ru_2O_7$ under hydrostatic pressure. *Physical Review B*, **83** 4 045106, (2011). . . . . on page 94.

[185] S.-I. Ikeda, N. Shirakawa, T. Yanagisawa, Y. Yoshida, S. Koikegami, S. Koike, M. Kosaka, and Y. Uwatoko. Uniaxial-Pressure Induced Ferromagnetism of Enhanced Paramagnetic $Sr_3Ru_2O_7$. *Journal of the Physics Society Japan*, **73** 5 1322–1325, (2004). . . . . . on pages 94 and 95.

[186] S. N. Ruddlesden and P. Popper. New compounds of the K_2NiF_4 type. *Acta Crystallographica*, **10** 8 538–539, (1957). on page 94.

[187] S. N. Ruddlesden and P. Popper. The compound $Sr_3Ti_2O_7$ and its structure. *Acta Crystallographica*, **11** 1 54–55, (1958). . . . . on page 94.

[188] R. S. Perry. PhD thesis, University of Birmingham, 2001. on pages 94, 96, 112, 113, and 120.

[189] P. B. Allen, H. Berger, O. Chauvet, L. Forro, T. Jarlborg, A. Junod, B. Revaz, and G. Santi. Transport properties, thermodynamic properties, and electronic structure of $SrRuO_3$. *Physical Review B*, **53** 8 4393–4398, (1996). on page 94.

[190] A. Kanbayasi. Magnetic properties of $SrRuO_3$ Single Crystal. *Journal of the Physical Society of Japan*, **41** 6 1876–1878, (1976). . . . . on page 94.

[191] M. Crawford, R. L. Harlow, W. Marshall, Z. Li, G. Cao, R. L. Lindstrom, Q. Huang, and J. W. Lynn. Structure and magnetism of single crystal $Sr_4Ru_3O_{10}$: A ferromagnetic triple-layer ruthenate. *Physical Review B*, **65** 21 214412, (2002). . . . . on page 94.

[192] G. Cao, L. Balicas, W. H. Song, Y. P. Sun, Y. Xin, V. A. Bondarenko, J. W. Brill, S. Parkin, and X. N. Lin. Competing ground states in triple-layered $Sr_4Ru_3O_{10}$: Verging on itinerant ferromagnetism with critical fluctuations. *Physical Review B*, **68** 17 174409, (2003). . . . . on page 94.

[193] M. Zhou, J. Hooper, D. Fobes, Z. Q. Mao, V. Golub, and C. J. OâĂŹConnor. Electronic and magnetic properties of triple-layered ruthenate $Sr_4Ru_3O_{10}$ single crystals grown by a floating-zone method. *Materials Research Bulletin*, **40** 6 942–950, (2005). . . . . on page 94.

[194] H. Shaked, J. D. Jorgensen, O. Chmaissem, S. Ikeda, and Y. Maeno. Neutron Diffraction Study of the Structural Distortions in $Sr_3Ru_2O_7$. *Journal of Solid State Chemistry*, **154** 2 361–367, (2000). . . . . on page 95.

[195] Q. Huang, J. W. Lynn, R. W. Erwin, J. Jarupatrakorn, and R. J. Cava. Oxygen displacements and search for magnetic order in $Sr_3Ru_2O_7$. *Physical Review B*, **58** 13 8515–8521, (1998). . . . . on page 95.

[196] R. Kiyanagi, K. Tsuda, N. Aso, H. Kimura, Y. Noda, Y. Yoshida, S.-I. Ikeda, and Y. Uwatoko. Investigation of the Structure of Single Crystal $Sr_3Ru_2O_7$ by Neutron and Convergent Beam Electron Diffractions. *Journal of the Physics Society Japan*, **73** 3 639–642, (2004). on page 95.

[197] R. Matzdorf, Z. Fang, Ismail, J. Zhang, T. Kimura, Y. Tokura, K. Terakura, and E. W. Plummer. Ferromagnetism Stabilized by Lattice Distortion at the Surface of the p-Wave Superconductor Sr_2RuO_4. *Science*, **289** 5480 746–748, (2000). . . . . on page 95.

[198] R. Matzdorf, Ismail, T. Kimura, Y. Tokura, and E. W. Plummer. Surface structural analysis of the layered perovskite Sr_2RuO_4 by LEED $I(V)$. *Physical Review B*, **65** 8 085404, (2002). . . . . on page 95.

[199] J. A. N. Bruin. *Transport Studies of the Itinerant Metamagnet $Sr_3Ru_2O_7$ Near its Quantum Critical Point.* PhD thesis, University of St Andrews, 2012. on pages 95, 109, 122, 128, and 133.

[200] J.-F. Mercure, A. W. Rost, E. C. T. O'Farrell, S. K. Goh, R. S. Perry, M. L. Sutherland, S. A. Grigera, R. A. Borzi, P. Gegenwart, A. S. Gibbs, and A. P. Mackenzie. Quantum oscillations near the metamagnetic transition in $Sr_3Ru_2O_7$. *Physical Review B*, **81** 23 235103, (2010). on pages 95, 96, and 100.

[201] A. Tamai, M. P. Allan, J.-F. Mercure, W. Meevasana, R. Dunkel, D. H. Lu, R. S. Perry, A. P. Mackenzie, D. J. Singh, Z.-X. Shen, and F. Baumberger. Fermi Surface and van Hove Singularities in the Itinerant Metamagnet

$Sr_3Ru_2O_7$. *Physical Review Letters*, **101** 2 026407, (2008). on pages 95, 96, and 100.

[202] R. S. Perry and Y. Maeno. Systematic approach to the growth of high-quality single crystals of $Sr_3Ru_2O_7$. *Journal of Crystal Growth*, **271** 1-2 134–141, (2004).   on pages 96 and 103.

[203] R. S. Perry, L. M. Galvin, S. A. Grigera, L. Capogna, A. J. Schofield, A. P. Mackenzie, M. Chiao, S. R. Julian, S. I. Ikeda, S. Nakatsuji, Y. Maeno, and C. Pfleiderer. Metamagnetism and Critical Fluctuations in High Quality Single Crystals of the Bilayer Ruthenate $Sr_3Ru_2O_7$. *Physical Review Letters*, **86** 12 2661–2664, (2001). ...... on pages 97 and 102.

[204] E. Stryjewski and N. Giordano. Metamagnetism. *Advances in Physics*, **26** 5 487–650, (1977). .... on page 97.

[205] S. J. Blundell. *Magnetism in Condensed Matter*. Oxford University Press, 2001. ISBN 9780198505921.   on pages 97 and 105.

[206] E. C. Stoner. Collective Electron Specific Heat and Spin Paramagnetism in Metals. *Proceedings of the Royal Society of London A*, **154** 883 656–678, (1936). ...... on page 98.

[207] M. Shimizu. On the conditions of ferromagnetism by the band model: II. *Proceedings of the Physical Society*, **86** 1 147–157, (1965). .... on pages 98 and 99.

[208] M. Shimizu. Itinerant electron metamagnetism. *Journal de Physique (France)*, **43** 1 155–163, (1982). .... on page 99.

[209] E. P. Wohlfarth and P. Rhodes. Collective Electron Metamagnetism. *Philosophical Magazine*, **7** 83 1817–1824, (1962). on page 99.

[210] K. Fukamichi. *Handbook of Advanced Magnetic Materials*, chapter Itinerant-Electron Metamagnetism. Springer US, 2006. ISBN 9781402079849. .... on page 99.

[211] M. P. Allan, A. Tamai, E. Rozbicki, M. H. Fischer, J. Voss, P. D C King, W. Meevasana, S. Thirupathaiah, E. Rienks, J. Fink, D. A. Tennant, R. S. Perry, J. F. Mercure, M. A. Wang, J. Lee, C. J. Fennie, E.-A. Kim, M. J. Lawler, K. M. Shen, A. P. Mackenzie, Z.-X. Shen, and F. Baumberger. Formation of heavy d-electron quasiparticles in $Sr_3Ru_2O_7$. *New Journal of Physics*, **15** 6 063029, (2013). ... on page 100.

[212] B. Binz and M. Sigrist. Metamagnetism of itinerant electrons in multi-layer ruthenates. *Europhysics Letters*, **65** 6 816–822, (2004). . . . . on page 100.

[213] H.-Y. Kee and Y. B. Kim. Itinerant metamagnetism induced by electronic nematic order. *Physical Review B*, **71** 18 184402, (2005). . . . . on pages 100 and 104.

[214] C. Puetter, H. Doh, and H.-Y. Kee. Metanematic transitions in a bilayer system: Application to the bilayer ruthenate. *Physical Review B*, **76** 23 235112, (2007). on pages 100 and 104.

[215] H. Yamase and A. A. Katanin. Van Hove Singularity and Spontaneous Fermi Surface Symmetry Breaking in $Sr_3Ru_2O_7$. *Journal of the Physical Society of Japan*, **76** 7 073706, (2007). . . . . on pages 100 and 104.

[216] S. Raghu, A. Paramekanti, E. A. Kim, R. A. Borzi, S. A. Grigera, A. P. Mackenzie, and S. A. Kivelson. Microscopic theory of the nematic phase in $Sr_3Ru_2O_7$. *Physical Review B*, **79** 21 214402, (2009). . . . . on pages 100 and 104.

[217] W.-C. Lee and C. Wu. Theory of unconventional metamagnetic electron states in orbital band systems. *Physical Review B*, **80** 10 104438, (2009). . . on pages 100 and 104.

[218] M. H. Fischer and M. Sigrist. Effect of a staggered spin-orbit coupling on the occurrence of a nematic phase in $Sr_3Ru_2O_7$. *Physical Review B*, **81** 6 064435, (2010). on pages 100 and 104.

[219] P. Coleman and A. J. Schofield. Quantum criticality. *Nature*, **433** 7023 226–229, (2005). . . . . on pages 100 and 102.

[220] H. v. Löhneysen, T. Pietrus, G. Portisch, H. G. Schlager, A. Schröder, M. Sieck, and T. Trappmann. Non-Fermi-liquid behavior in a heavy-fermion alloy at a magnetic instability. *Physical Review Letters*, **72** 20 3262–3265, (1994). . . . . on page 101.

[221] G. R. Stewart. Non-fermi-liquid behavior in d-and f-electron metals. *Reviews of Modern Physics*, **73** 4 797–855, (2001). on page 101.

[222] S.A. Grigera, R.S. Perry, A.J. Schofield, M. Chiao, S.R. Julian, G.G. Lonzarich, S.I. Ikeda, Y. Maeno, A.J. Millis, and A.P. Mackenziel. Magnetic Field-Tunes Quantum Criticality in the Metallic Ruthenate $Sr_3Ru_2O_7$. *Science*, **294** 5541 329–332, (2001). . . . . on page 102.

[223] N. D. Mathur, F. M. Grosche, S. R. Julian, I. R. Walker, D. M. Freye, R. K. W. Haselwimmer, and G. G. Lonzarich. Magnetically mediated superconductivity in heavy fermion compounds. *Nature*, **394** 6688 39–43, (1998). on page 102.

[224] R. S. Perry, K. Kitagawa, S. A. Grigera, R. A. Borzi, A. P. Mackenzie, K. Ishida, and Y. Maeno. Multiple First-Order Metamagnetic Transitions and Quantum Oscillations in Ultrapure $Sr_3Ru_2O_7$. *Physical Review Letters*, **92** 16 166602, (2004). on pages 103 and 128.

[225] E. Fradkin. *Modern Theories of Many-Particle Systems in Condensed Matter Physics*, chapter Electronic Liquid Crystal Phases in Strongly Correlated Systems. Springer Berlin Heidelberg, 2012. ISBN 9783642104497. . . . . . on page 104.

[226] E. Fradkin, S. A. Kivelson, M. J. Lawler, J. P. Eisenstein, and A. P. Mackenzie. Nematic Fermi Fluids in Condensed Matter Physics. *Annual Review of Condensed Matter Physics*, **1** 1 153–178, (2010). . . . . . on pages 104 and 140.

[227] E. Fradkin and S. A. Kivelson. Electron Nematic Phases Proliferate. *Science*, **327** 5962 155–156, (2010). on pages 104 and 140.

[228] V. J. Emery, S. A. Kivelson, and J. M. Tranquada. Stripe phases in high-temperature superconductors. *Proceedings of the National Academy of Sciences*, **96** 16 8814–8817, (1999). . . . . on page 104.

[229] S. A. Kivelson, E. Fradkin, and V. J. Emery. Electronic liquid-crystal phases of a doped Mott insulator. *Nature*, **393** 6685 550–553, (1998). . . . . on page 104.

[230] D. F. Mross and T. Senthil. Theory of a Continuous Stripe Melting Transition in a Two-Dimensional Metal: A Possible Application to Cuprate Superconductors. *Physical Review Letters*, **108** 26 267001, (2012). . . . . . on page 104.

[231] D. F. Mross and T. Senthil. Stripe melting and quantum criticality in correlated metals. *Physical Review B*, **86** 11 115138, (2012). . . . . on page 104.

[232] I. I. Pomeranchuk. On the stability of a fermi liquid. *Soviet Physics Journal of Experimental and Theoretical Physics*, **35** 2 524–525, (1958). . . . . on page 104.

[233] J. A. N. Bruin, R. A. Borzi, S. A. Grigera, A. W. Rost, R. S. Perry, and A. P. Mackenzie. Study of the electronic

nematic phase of $Sr_3Ru_2O_7$ with precise control of the applied magnetic field vector. *Physical Review B*, **87** 16 161106, (2013). . . . . on page 106.

[234] K. Kitagawa, K. Ishida, R. S. Perry, T. Tayama, T. Sakakibara, and Y. Maeno. Metamagnetic Quantum Criticality Revealed by ^{17}O-NMR in the Itinerant Metamagnet $Sr_3Ru_2O_7$. *Physical Review Letters*, **95** 12 127001, (2005). on page 106.

[235] D. Sun, A. Rost, R. Perry, A. P. Mackenzie, and M. Brando. Low temperature thermodynamic investigation of the phase diagram of $Sr_3Ru_2O_7$. arXiv:1605.00396, Unpublished 2016. . . . . on page 107.

[236] D. O. Brodsky. *Investigation of Correlated Electron Systems under Uni-axial Strain.* PhD thesis, University of St Andrews, 2015. on pages 108 and 111.

[237] D. O. Brodsky, M. E. Barber, J. A. N. Bruin, R. A. Borzi, S. A. Grigera, R. S. Perry, A. P. Mackenzie, and C. W. Hicks. Strain and vector magnetic field tuning of the anomalous phase in $Sr_3Ru_2O_7$. *Science Advances*, **3** 2 e1501804, (2017). . . . . on pages 108 and 133.

[238] J.-F. Mercure. *The de Haas van Alphen effect near a quantum critical end point in Sr3Ru2O7.* PhD thesis, University of St Andrews, 2008. . . . . on page 108.

[239] M. C. Shapiro, P. Hlobil, A. T. Hristov, A. V. Maharaj, and I. R. Fisher. Symmetry constraints on the elastoresistivity tensor. *Physical Review B*, **92** 23 235147, (2015). on page 112.

[240] J. C. Simpson, J. E. Lane, C. D. Immer, and R. C. Youngquist. Simple Analytic Expressions for the Magnetic Field of a Circular Current Loop. *NASA Technical Report Server*, **20140002333**, (2001). . . . . . . on page 114.

[241] S. Babic, F. Sirois, C. Akyel, and C. Girardi. Mutual Inductance Calculation Between Circular Filaments Arbitrarily Positioned in Space: Alternative to Grover's Formula. *IEEE Transactions on Magnetics*, **46** 9 3591–3600, (2010). on page 115.

[242] A. J. van Duyneveldt. Differential susceptibility as a magnetic probe: Some recent applications. *Journal of Applied Physics*, **53** 11 8006–8011, (1982). . . . . on page 115.

[243] P. M. Chaikin and T. C. Lubensky. *Principles of Condensed Matter Physics.* Cambridge University Press, 2000. ISBN 9780521794503. . . . . on page 132.

[244] A. W. Rost, R. S. Perry, J.-F. Mercure, A. P. Mackenziel, and S. A. Grigera. Entropy Landscape of Phase Formation Associated with Quantum Criticality in $Sr_3Ru_2O_7$. *Science*, **325** 5946 1360–1363, (2009). . . . . . . on pages 133 and 134.

[245] C. Stingl, R. S. Perry, Y. Maeno, and P. Gegenwart. Electronic nematicity and its relation to quantum criticality in $Sr_3Ru_2O_7$ studied by thermal expansion. *Physica Status Solidi (B)*, **250** 3 450–456, (2013). . . . . on page 133.

[246] C. Stingl, R. S. Perry, Y. Maeno, and P. Gegenwart. Symmetry-Breaking Lattice Distortion in $Sr_3Ru_2O_7$. *Physical Review Letters*, **107** 2 026404, (2011). . . . on page 134.

[247] W. B. Muir and J. O. Ström-Olsen. Electrical Resistance of Single-Crystal Single-Domain Chromium from 77 to 325 K. *Physical Review B*, **4** 3 988–991, (1971). . . . . on page 134.

[248] R. K. Kummamuru and Y.-A. Soh. Electrical effects of spin density wave quantization and magnetic domain walls in chromium. *Nature*, **452** 7189 859–863, (2008). on page 134.

[249] A. Stern, M. Dzero, V. M. Galitski, Z. Fisk, and Xia J. Kondo insulator SmB_6 under strain: surface dominated conduction near room temperature. arXiv:1607.07454, Unpublished 2016. . . . . on page 139.

[250] J. Labbé and J. Bok. Superconductivity in Alcaline-Earth-Substituted La_2CuO_4: A Theoretical Model. *Europhysics Letters*, **3** 11 1225–1230, (1987). . . . . on page 140.

[251] A. Ino, C. Kim, M. Nakamura, T. Yoshida, T. Mizokawa, A. Fujimori, Z.-X. Shen, T. Kakeshita, H. Eisaki, and S. Uchida. Doping-dependent evolution of the electronic structure of $La_{2-x}Sr_xCuO_4$ in the superconducting and metallic phases. *Physical Review B*, **65** 9 094504, (2002). on page 140.

[252] M. Abrecht, D. Ariosa, D. Cloetta, S. Mitrovic, M. Onellion, X. X. Xi, G. Margaritondo, and D. Pavuna. Strain and High Temperature Superconductivity: Unexpected Results from Direct Electronic Structure Measurements in Thin Films. *Physical Review Letters*, **91** 5 057002, (2003). on page 140.

[253] J. Bok and J. Bouvier. Superconductivity and the Van Hove Scenario. *Journal of Superconductivity and Novel Magnetism*, **25** 3 657–667, (2012). . . . . on page 140.

[254] G. Ghiringhelli, M. Le Tacon, M. Minola, S. Blanco-Canosa, C. Mazzoli, N. B. Brookes, G. M. De Luca, A. Frano, D. G. Hawthorn, F. He, T. Loew, M. M. Sala, D. C. Peets, M. Salluzzo, E. Schierle, R. Sutarto, G. A. Sawatzky, E. Weschke, B. Keimer, and L. Braicovich. Long-Range Incommensurate Charge Fluctuations in $(Y,Nd)Ba_2Cu_3O_{6+x}$. *Science*, **337** 6096 821–825, (2012). on page 140.

[255] E. H. da Silva Neto, P. Aynajian, A. Frano, R. Comin, E. Schierle, E. Weschke, A. Gyenis, J. Wen, J. Schneeloch, Z. Xu, S. Ono, G. Gu, M. Le Tacon, and A. Yazdani. Ubiquitous Interplay Between Charge Ordering and High-Temperature Superconductivity in Cuprates. *Science*, **343** 6169 393–396, (2014). . . . . on page 140.

[256] M. Vojta. Lattice symmetry breaking in cuprate superconductors: stripes, nematics, and superconductivity. *Advances in Physics*, **58** 6 699–820, (2009). . . . . on page 140.

[257] E. Fradkin, S. A. Kivelson, and J. M. Tranquada. Colloquium: Theory of intertwined orders in high temperature superconductors. *Reviews of Modern Physics*, **87** 2 457–482, (2015). . . . . on page 140.

[258] T. Sasagawa, T. Sugioka, N. Takeshita, K. Kitazawa, and H. Takagi. hrefhttp://dx.doi.org/10.1023/A:1022922429634Uniaxial Pressure Control of Superconductivity via Stripe Instability in $La_{1.64}Eu_{0.2}Sr_{0.16}CuO_4$ Crystals. *Journal of Low Temperature Physics*, **131** 3-4 395–399, (2003). . . . . on page 140.

[259] M. Greiter, G. G. Lonzarich, and L. Taillefer. Effect of uniaxial stress on the onset of superconductivity in UPt_3. *Physics Letters A*, **169** 3 199–204, (1992). . . on page 140.

[260] D. S. Jin, S. A. Carter, B. Ellman, T. F. Rosenbaum, and D. G. Hinks. Uniaxial-stress Anisotropy of the Double Superconducting Transition in UPt_3. *Physical Review Letters*, **68** 10 1597–1600, (1992). . . . . on page 140.

[261] R. Joynt and L. Taillefer. The superconducting phases of UPt_3. *Reviews of Modern Physics*, **74** 1 235–294, (2002). on page 140.

[262] Y. Aoki, A. Tsuchiya, T. Kanayama, S. R. Saha, H. Sugawara, H. Sato, W. Higemoto, A. Koda, K. Ohishi, K. Nishiyama, and R. Kadono. Time-Reversal Symmetry-Breaking Superconductivity in Heavy-Fermion $PrOs_4Sb_{12}$ Detected by Muon-Spin Relaxation. *Physical Review Letters*, **91** 6 067003, (2003). . . . . on page 140.

[263] K. E. Petersen. Silicon as a mechanical material. *Proceedings of the IEEE*, **70** 5 420–457, (1982). . . . . on page 140.

[264] S. Ogata, N. Hirosaki, C. Kocer, and H. Kitagawa. An ab initio calculation of the ideal tensile strength of β-silicon nitride. *Physical Review B*, **64** 17 172102, (2001). on page 140.

[265] G. S. Pomeroy. Differential current source with active common mode reduction, 2002. Lake Shore Cryotronics, Inc. US Patent 6,501,255 B2. . . . . on page 171.

[266] M. Simmonds and P. Alesu. Differential and symmetrical current source, 2011. Quantum Design, Inc. US Patent 7,884,593 B2. . . . . on page 171.

[267] P. Horowitz and W Hill. *The Art of Electronics*. Cambridge University Press, third edition, 2015. ISBN 9780521809269. on page 172.

Appendix A

Details of the Dual End Current Source with Active Common-Mode Rejection

Common-mode voltage present on both measurement leads of a differential four point resistance measurement can lead to significant offset errors if the common-mode voltage exceeds the level at which the preamplifier or lock-in amplifier can successfully reject it. Typically preamplifiers can be sourced with common-mode rejection ratios (CMRR) up to 100–120 dB, but if the common-mode ratio is larger than this, which can happen with very conductive samples and long resistive wiring in a cryostat, the common-mode voltage itself must be reduced before a reliable measurement can be achieved. This is a known problem and companies like Lake Shore Cryotronics, Inc. and Quantum Design, Inc. incorporate symmetrical current sources in some of their products to reduce common-mode voltages and allow smaller resistances to be measured behind long resistive wires [265, 266]. The current source built for this set of measurements follows most closely the implementation from Lake Shore Cryotronics, Inc. in their model 370 and 372 resistance bridges, but with a few key modifications. As well as reducing common-mode voltage, a balanced current source also helps to reduce the effects of a noisy environment capacitively coupled to the current leads. By providing equal impedances to ground at both ends of the sample, the common-mode noise is not converted to differential noise as occurs with a single ended source. This is actually one of the main reasons why dual end current sources are incorporated into many commercial devices. In the following section I will introduce how the common-mode problem can appear, and then show the necessary steps to reduce it, before coming to our final implementation of the current source.

Lock-in amplifiers typically provide a sinusoidal output voltage at their reference frequency. Models like the SR830 from Stanford Research can also provide a few tens of milliamps on this output so, in combination with a shunt resistor, this output can be used directly as a current source for a grounded load. If the shunt resistor is chosen to be of much higher resistance than that of the sample plus wiring, the current through the sample is approximately the ratio of the output voltage and the shunt's resistance. A spare

lock-in amplifier or AC voltmeter can also be used to measure the voltage drop across the shunt and calculate the current more accurately. An improvement is to use a dedicated current source rather than voltage source plus shunt. An example that can still be driven from the sinusoidal voltage reference of the lock-in is the modified Howland bipolarity current source-sink from Horowitz and Hill p.230 [267], see figure A.1. However, when using any single ended current source to drive a grounded load there is always a common-mode voltage present at the voltage contacts of a four point resistance measurement. The common-mode voltage depends on the resistance to ground of the return current path, $V_{cm} = \frac{1}{2}(V_+ + V_-) \approx I(R_{lead} + R_{sample}/2)$. The voltage measured in an ideal four point resistance measurement depends only on the sample's resistance but the output of a real differential amplifier is better described by

$$V_{out} = G(V_+ - V_-) + \frac{G}{CMRR}\frac{1}{2}(V_+ + V_-),\qquad \text{(A.1)}$$

where G is the differential gain of the amplifier and CMRR the common-mode rejection ratio of the amplifier, normally expressed in decibels. A common-mode signal of 100 mV is only cancelled to 1 part in 10^5 by a preamplifier with a CMRR of 100 dB and so it appears as if there is still a 1 μV differential signal at the input.
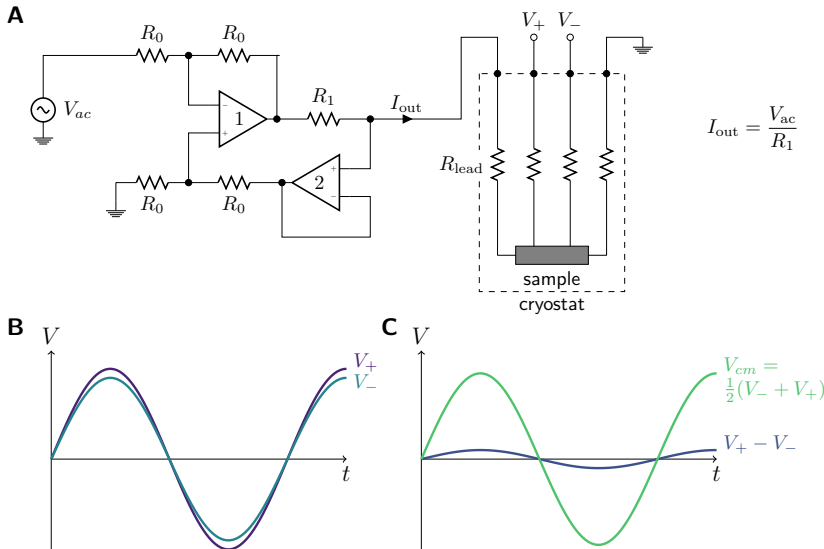
A better current source can be made by taking two of the

Fig. A.1: **A modified Howland bipolarity current source-sink. A.** Circuit diagram for a single ended voltage to current converter for driving a grounded load. **B and C.** In a four point resistance measurement with long resistive wires in the cryostat, the large lead resistance to ground produces a large common-mode voltage in addition to the normal sample voltage drop.

modified Howland current sources, inverting the input voltage for one of them, and joining their outputs together through the sample. Each half of the current source still provides the full current output but with opposite sign. This centres the load between the two current sources/sinks but a feedback mechanism must also be incorporated to keep the current sources centred around ground, reducing any DC offset at the sample. The average DC voltage at the output of the current sourcing op-amps can be calculated by two slow integrators and then fed back to the non-inverting inputs of each of the op-amps, driving the output back towards ground.

In the ideal case, when the two halves are identical, the load remains centred between the two current sources. However, if the sample is not exactly the centre of the load, i.e. the current leads or contacts have unequal resistance, or if the two halves of the current source are not strictly identical then there will still be a small but finite common-mode voltage in the measurement. Our current source can sense this common-mode voltage and it uses additional active feedback to drive this back towards zero. We sense the common-mode voltage directly between two of the voltage contacts of the four point resistance measurement. This ensures that exactly the central point of the sample is held at ground, not the central point of the wires plus contacts and sample which would be the case if the current contacts were used instead. The common-mode voltage is first amplified and then used as the reference point for the two integrators. Feeding back in this way causes each half of the current source to move in an opposite direction when there is a common-mode voltage present, thus driving the common-mode voltage back towards zero.

A simplified circuit diagram is pictured in figure A.2. The complete design includes a few additional features to expand its functionality and I will describe them here. The output current is set by the combination of the input voltage and the resistor R. So that currents over many orders of magnitude can be sourced using the same 0–5 V reference from a lock-in amplifier, a switch was included to select R from a range of resistors providing currents from <100 nA to ∼20 mA at frequencies between ∼10 Hz and ∼10 kHz. The active common-mode rejection can also be disabled so that the current source can still be used to drive a grounded load. With the common-mode rejection disabled, each side of the current source can operated independently. The final modification allows switching of the common-mode feedback from the voltage leads to the current leads. The inverting-inputs of the second op-amps in each of the modified Howland current sources are summed to give the common-mode voltage. This provides a further option in case the feedback mechanism influences the phase sensitive measurement or the voltage contacts cannot be easily accessed.
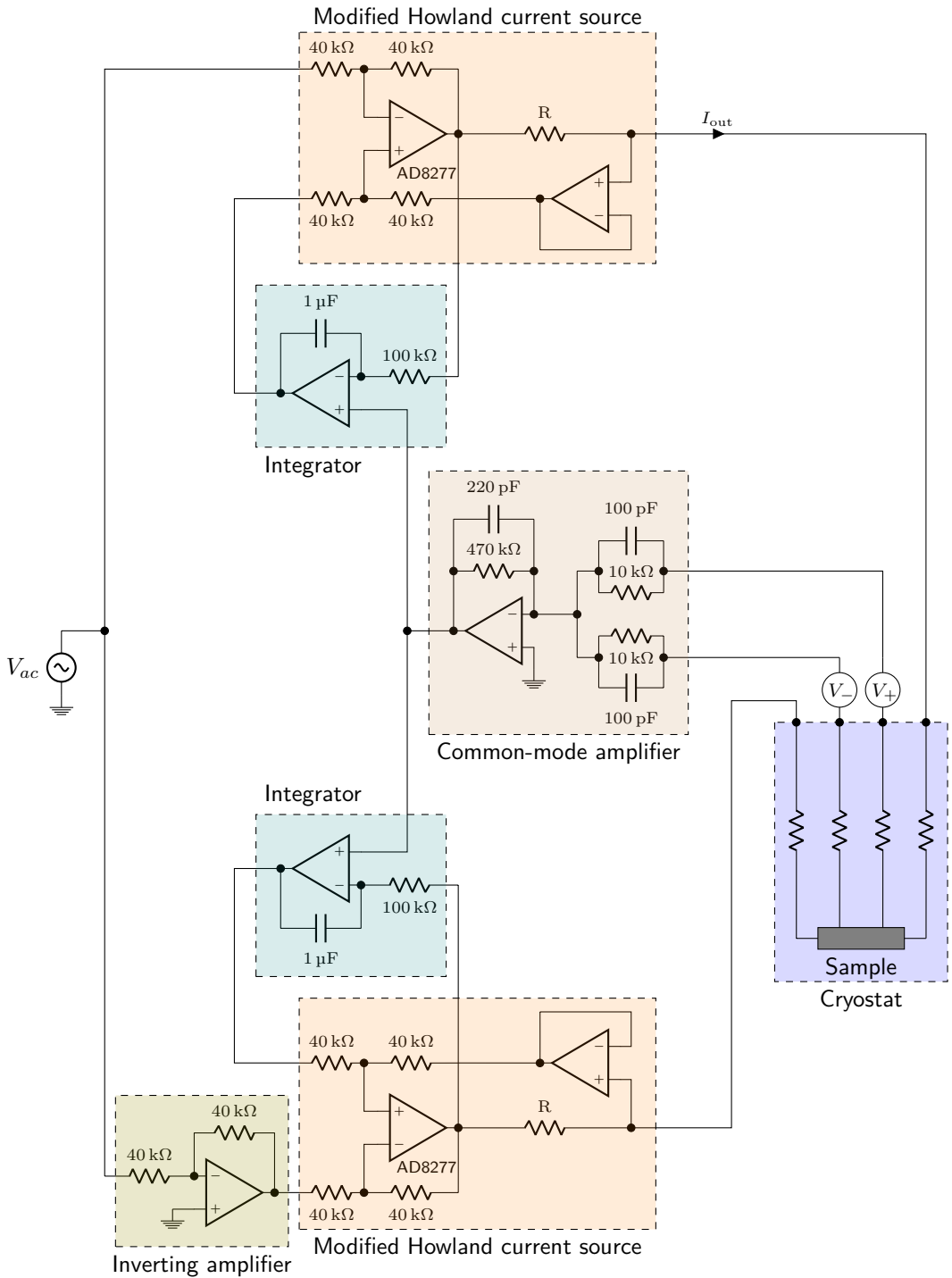
Fig. A.2: **Dual End Current Source with Active Common-Mode Rejection.** Schematic with constituent parts labelled. See text for a description of the operating principle.

Appendix B

Supplementary Materials for Sr_2RuO_4 Under Strain

In the main body of this thesis most of the experimental results presented were from one sample, namely sample 3, to avoid unwanted repetition of essentially similar results. For completeness the remaining data sets from the first two samples are presented in this appendix.

To begin with, the susceptibility data for samples 1 and 2 at a series of strains is presented in figures B.1 and B.2. Figure B.3
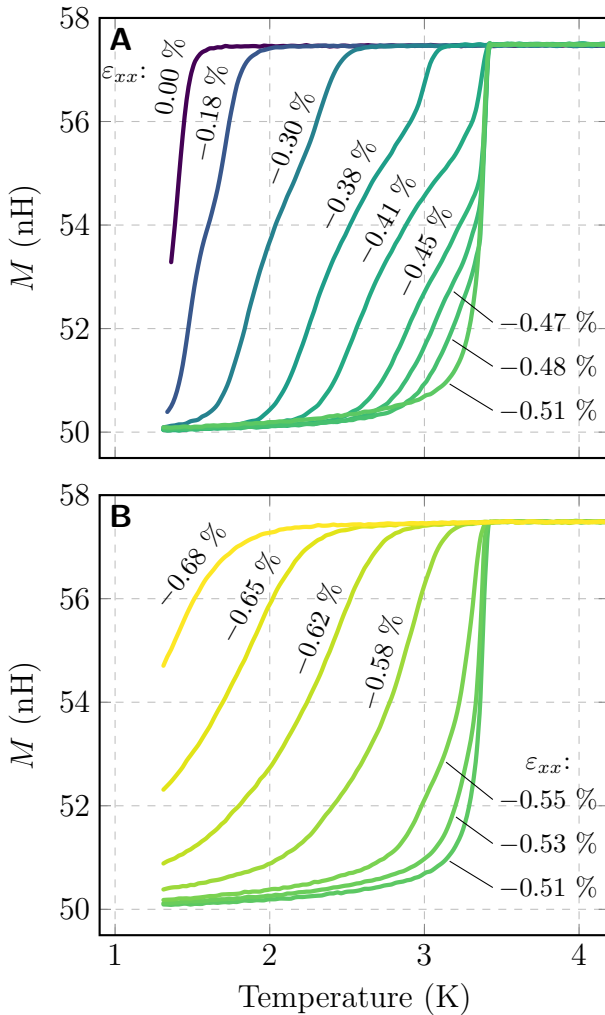

Fig. B.1: **Susceptibility against temperature.** Real part of the susceptibility χ for sample 1 against temperature. **A** Strains below the peak T_c, **B** above the peak. No normalisation or offsets are applied to the curves. The y axis is the mutual inductance between the two coils of the susceptibility sensor.

Fig. B.2: **Susceptibility against temperature.** Real part of the susceptibility χ for sample 2 against temperature. **A** Strains below the peak T_c, **B** above the peak. No normalisation or offsets are applied to the curves. The y axis is the mutual inductance between the two coils of the susceptibility sensor.
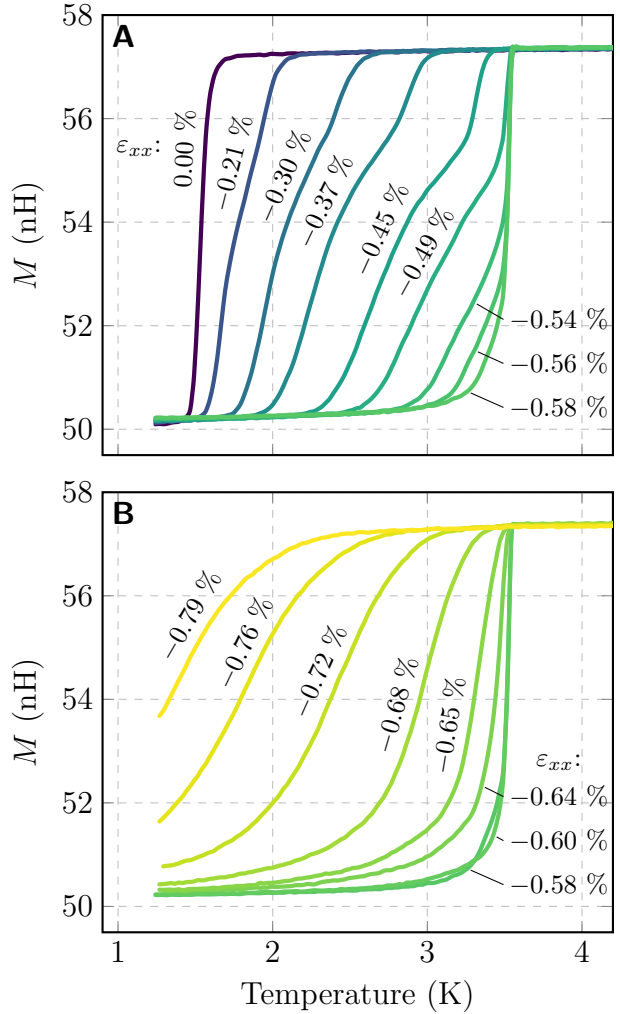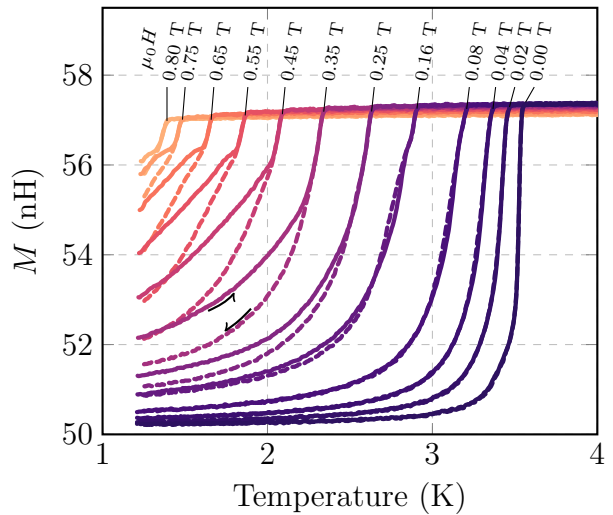

Fig. B.3: **Susceptibility measured at the peak in T_c at various applied fields $H \parallel c$.** Real part of the susceptibility χ measured as the temperature is swept up and down for sample 2. The y axis is the mutual inductance between the two coils of the susceptibility sensor. The field was incremented at the bottom of each temperature ramp, in the superconducting phase. This disrupts the vortex lattice and is responsible for the apparent hysteresis.

shows the susceptibility measurements made at the peak in T_c for sample 2 with various c-axis applied fields used for determining $H_{c2\|c}(T)$ presented in the main text in figure 3.28.

The resistivity measurements on sample 2 are presented in full in figure B.4 and as a colour map of the logarithmic derivative with respect to temperature in figure B.5, highlighting the change in temperature exponent. Figure B.6 shows the Hall effect measurements on sample 2.
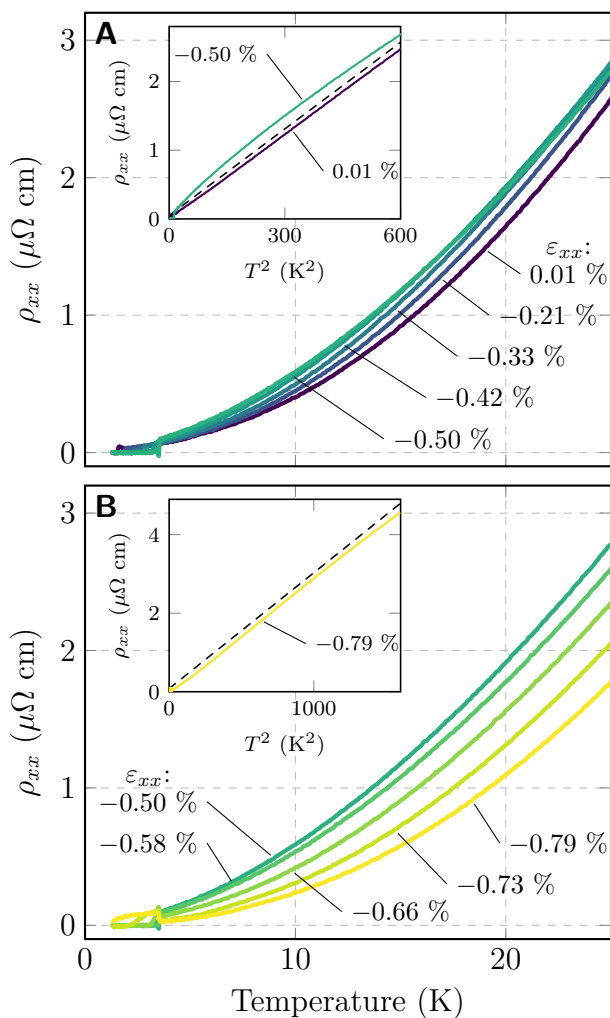

Fig. B.4: **Resistivity against temperature. A** Longitudinal resistivity against temperature at strains below the peak in resistivity for sample 2. The inset shows the resistivity plotted against T^2 at zero strain, highlighting the Fermi liquid behaviour with a straight line as a guide to the eye, and for the strain where the lowest temperature exponent is observed. **B** At strains above the maximum in the resistivity, T^2 behaviour is recovered at high compression. The inset shows the larger extent of the T^2 region for the highest strain measured.

Fig. B.5: **Resistivity temperature exponent.** The resistivity exponent, α, for sample 2 plotted against temperature and strain. ρ_0 was first extracted from fits of the type $\rho = \rho_0 + AT^\alpha$ and then α was calculated as a function of temperature by $d\ln(\rho - \rho_0)/d\ln T$. The figure is cut off below 4 K, due to percolating superconducting paths that can affect the resistivity strongly.
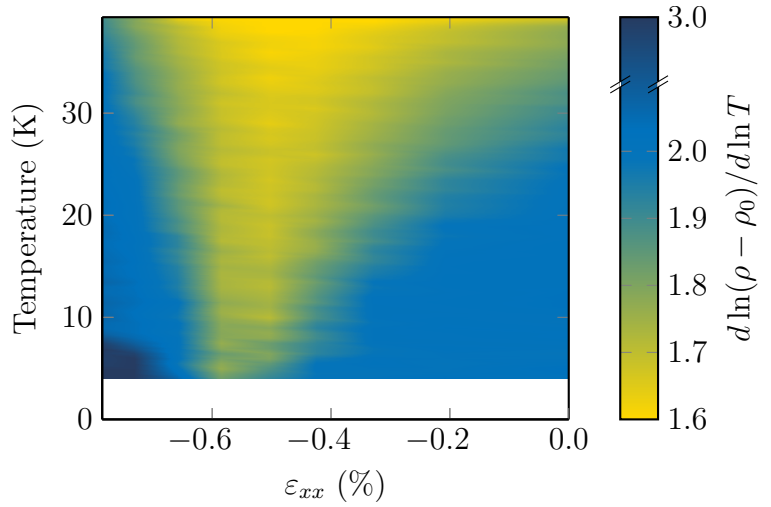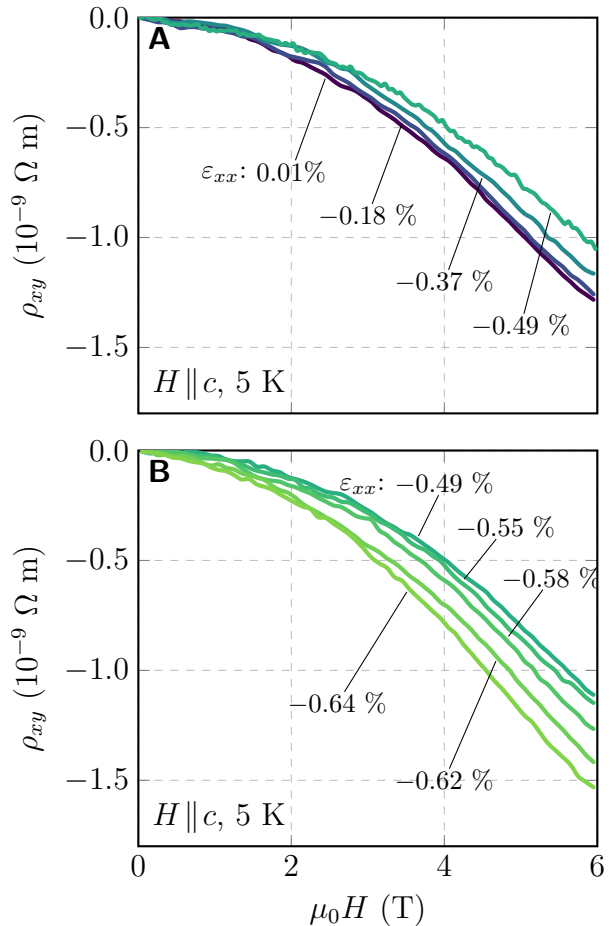

Fig. B.6: **Hall Effect. A** Hall effect measurements at strains below the peak in resistivity for sample 2. **B** The same measurements at strains above the peak in resistivity.

B.1   Resistivity temperature exponent analysis

As noted in the main text, we are in the unique situation of being able to tune continuously through a Lifshitz transition in a multiband and exquisitely clean system. To see how much physical significance can be assigned to the changes in the temperature dependence of the resistivity, it is worthwhile examining the quality of the fit used for extracting the exponent presented in figure 3.36.

Figure B.7 shows a fit of the form $a + bT^c$ through the data in the range 4 to 12 K at -0.49% strain. The fit rapidly deviates from the data above $\sim$10 K but even below 10 K the residual plot indicates that the trial form is not a satisfactory fit. The green trace in figure B.7C seems to deviate systematically from zero by more than its random error.

A better fit can be achieved by adding a parallel conducting channel with a fixed T^2 temperature dependence. The now larger number of fitting parameters quite rightly produces a better fit, but to determine if this is physically conceivable a few consistency checks can be carried out. The Lifshitz transition opens up the γ sheet whereas the shape of the α and β bands are mostly unaffected by the applied strain. If there is complete decoupling of the three bands the relative weight that each band adds to the conductivity must be consistent. At zero strain a simple estimate for the conductivity contributed by each band can be calculated from the Fermi surface properties. In the limit of isotropic scattering time τ, the conductivity for a circular Fermi surface is proportional to $\tau k_F^2/m^*$. Making this assumption for Sr_2RuO_4, the γ band should carry $\sim$30 % of the total conductivity. The conductivity could then decrease by only as much as $\sim$30 % and the resistivity increase by as much as $1/0.7 \sim 40$ %. This is at the low end of what was observed, see figure 3.34, but in an isotropic scattering length approximation, applicable at very low temperatures, the conductivity is proportional to ℓk_F and a larger change could be expected, as much as an 80 % increase in the resistivity.

As well as the overall resistivity enhancement being affected by the weight each band contributes to the resistivity in an idealised completely decoupled picture, the temperature dependence of the resistivity captured by the extended fitting function with one T^2 term and one free power should match with the relative weights of each band. Although the fit is much better with this extended function, the fitting parameters for the two halves of the fit are not consistent with the overall resistivity enhancement discussed above, and a better explanation for the systematic deviations of the first fit comes from considering the influence of strain inhomogeneity.

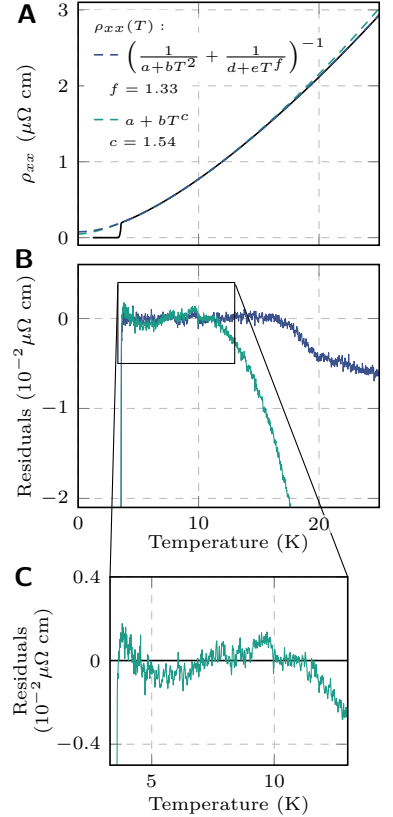Strain inhomogeneity can arise for instance through imperfec-

Fig. B.7: **Resistivity fitting.** Two fits to the temperature dependence of the resistivity at -0.49% strain, see text for discussion. The colour coding is the same for all panels.
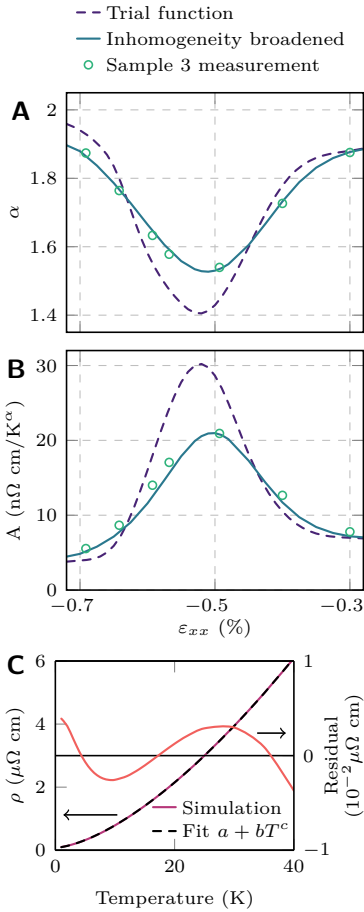
Fig. B.8: **Simulation for the effect of strain inhomogeneity. A and B.** Simulation results for the effect of strain inhomogeneity on the measured resistivity as discussed in the text. The trial functions $A(\varepsilon)$ and $\alpha(\varepsilon)$ are used to calculate the resistivity of a sample with a Gaussian strain distribution centred at the nominally applied strain with a FHWM that depends on the applied strain as $(0.05\ \% + 0.2\varepsilon_{\mathrm{applied}})$. The open circles are the values extracted from the measured resistivity curves, the purple curve the assumed intrinsic resistivity, and the blue curve the result after inhomogeneity broadening. **C.** The simulated data at $-0.49\ \%$ strain and the residual once refitted with a $a + bT^c$ fit.

tions in the sample mounting which can cause the sample to bend once strained, therefore creating a strain gradient through the sample. With a range of strains present throughout the thickness of the sample any sharp features, such as the lowest power reached at the Lifshitz transition, will be rounded out. A qualitative analysis of this effect can be seen in a rudimentary simulation.

Making the simplest assumption about the strain inhomogeneity variation we can look at an example where the strain only varies over the thickness of the sample but not across its width or length and the variation over the thickness is described by a Gaussian distribution centred at the nominally applied strain. The measured resistance for a sample with this strain distribution is given by the integral over the strain distribution with the resistivities added in parallel

$$\frac{1}{R(\varepsilon, T)} = \frac{wt}{L} \int\limits_{-\infty}^{\infty} f(x|\varepsilon, \sigma) \frac{dx}{\rho(x, T)} \ . \tag{B.1}$$

Here $f(x|\varepsilon, \sigma)$ is a Gaussian distribution with mean ε and standard deviation σ setting the level of strain inhomogeneity. $\rho(\varepsilon, T)$ is the intrinsic resistivity at a strain of ε and temperature T. Some assumption must be made about how the intrinsic resistivity changes with strain. Here we pick the form

$$\rho(\varepsilon, T) = \rho_0 + A(\varepsilon)T^{\alpha(\varepsilon)} \tag{B.2}$$

not based particularly on any physical reasoning but a useful example and one that is simple to calculate. $A(\varepsilon)$ and $\alpha(\varepsilon)$ are two trial functions that are picked by hand to make the broadened result match the measured data. In figure B.8 A and B they are the two dashed purple curves. The result of this calculation once refitted with a $a + bT^c$ fit shows quite a similar systematic deviation of the residual around zero to that seen in the data.

Since already the most simple assumptions about the strain inhomogeneity variation can reproduce qualitative similar discrepancies when trying to fit the exponent, it seems that it could at least be possible that this, or some other slightly more complicated strain variation, could be affecting the measurements, and complicating the extraction of the real exponent.

This analysis suggests that the observed power is only an upper limit on the real power which could only be observed if true homogeneity is achieved. It is difficult to infer exactly how much lower the power might be without a quantitative measure of the inhomogeneity. A trial form with a much lower power but subject to a larger inhomogeneity could produce qualitatively similar results to a higher power with lower sample inhomogeneity. The suggested inhomogeneity from the width of the susceptibility curves implies

the inhomogeneity could be as large as 20 %, but probably not all accountable to a depth variation of strain. Using this level of inhomogeneity and the trial forms for $A(\varepsilon)$ and $\alpha(\varepsilon)$ shown in figure B.8, a temperature exponent as low as 1.4 is still consistent with the measured results. Therefore, because of the presence of these uncertainties, at present I do not believe that we can put an uncertainty better than 0.1 on the exponent close to the suspected Lifshitz transition.

Strain inhomogeneity may also account for some of the discrepancy between the resistivity and T_c peaks, see figure 3.35. The resistivity measurement is an average over the whole sample whereas the susceptibility measurement can be influenced by the exact nature of the inhomogeneity. If for instance the top part of the sample close to the coil has a higher T_c than the bulk, then this part of the sample will screen the magnetic field from the rest of the sample and will lead to a higher T_c measurement than the average T_c. In future local probe techniques and better characterisation of the devices will be useful for quantifying the amount of inhomogeneity actually introduced by the device when straining the sample.

Appendix C

Phase boundaries from the derivatives of resistivity in $Sr_3Ru_2O_7$
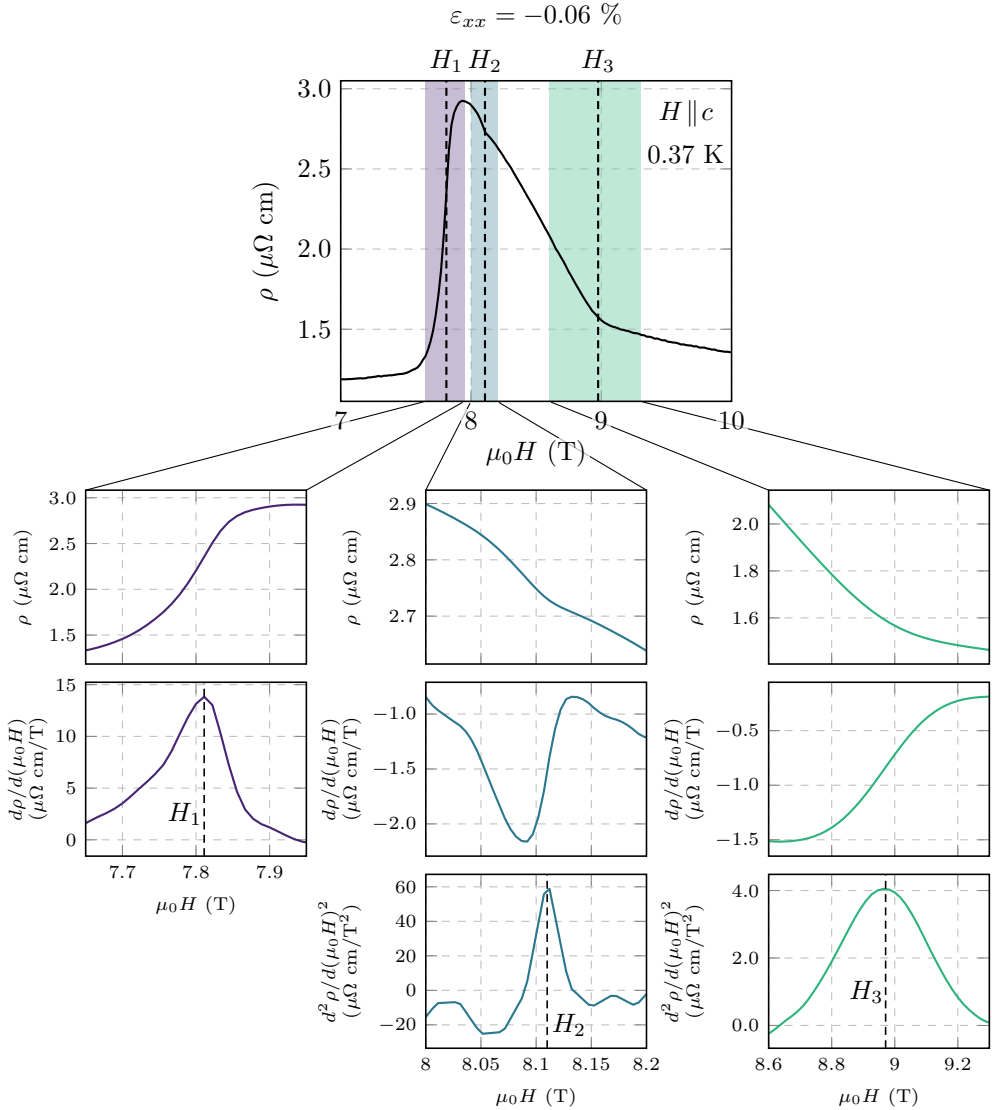
Fig. C.1: **Phase boundaries from field ramps.** A method for identifying the boundaries of the A and B phases from magnetoresistance measurements. H_1, the entrance to the A phase, is identified with the maximum slope of the magnetoresistance, i.e. a peak in the first derivative as introduced by Grigera *et al.* [180]. Transitions H_2 and H_3 are identified by changes in slope of the magnetoresistance, i.e. a peak in the second derivative.
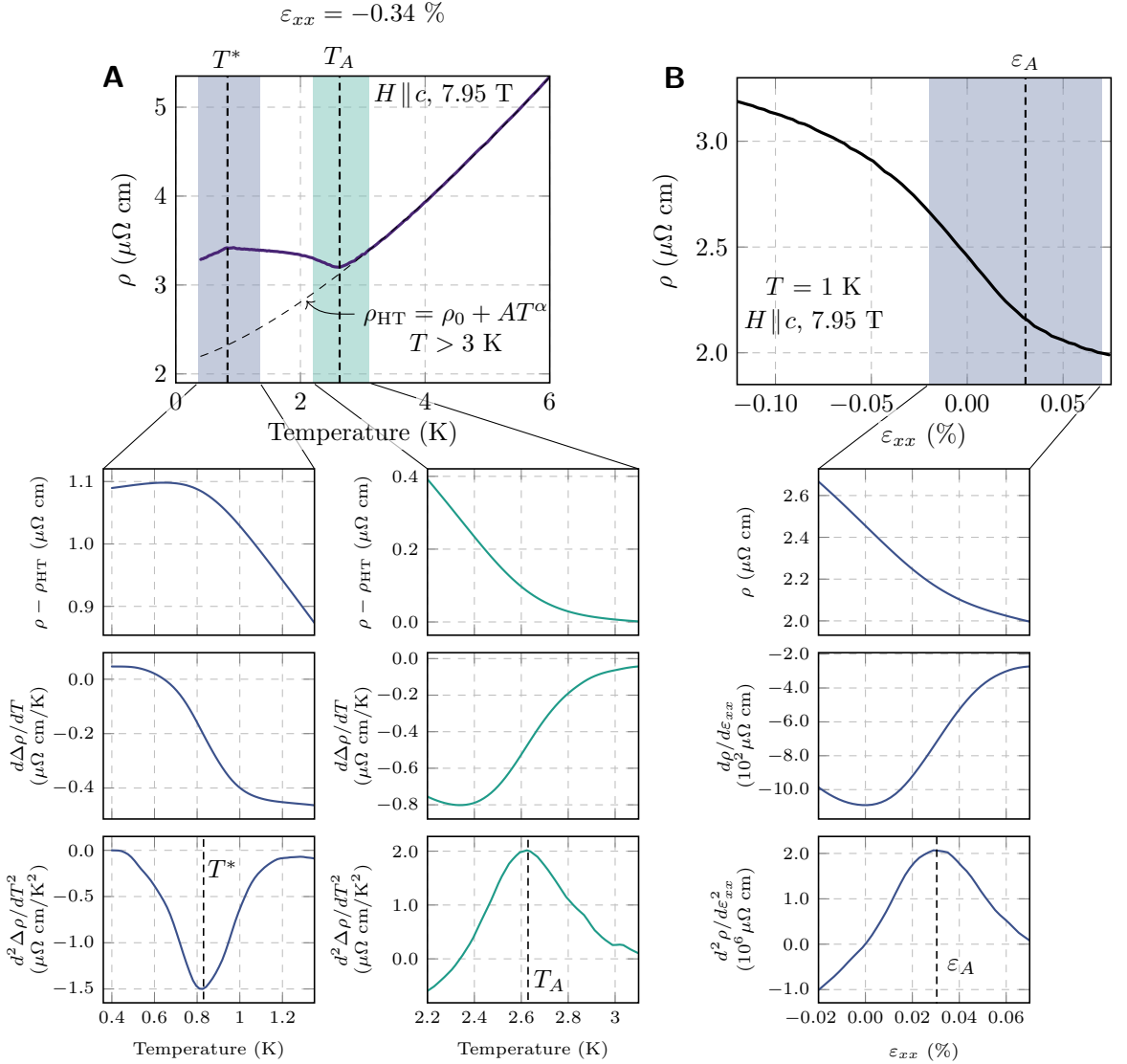
Fig. C.2: **Phase boundaries from temperature and strain ramps. A** The transition into the A phase through the roof with temperature, T_a, was identified from the point at which the slope of the resistivity deviates from a high temperature power law fit, i.e. a peak in the second derivative. A second feature, T^*, was observed at lower temperatures and high strains and was also identified by an extremum in the second derivative. **B** The entry into the phase with strain is the least sharp of all the observed features in the data, but it could also be identified from a change in slope of ρ vs. ε_{xx}; a peak in the second derivative of ρ with respect to ε_{xx}.

Appendix D

AC susceptibility coils simulation

```
1   function Signal=ACSusceptibilitySimulation(ExcitationCoils,IExcitation,IFreq,PickupCoils,X,Y,Z,Chi)
2   %ACSUSCEPTIBILITYSIMULATION Susceptibility signal simulation
3   %   This simulation returns two voltages: one the voltage induced across
4   %   the pick-up coil of the susceptibility setup due to the sample in the
5   %   presence of an oscillating magnetic field from the excitation coils and
6   %   secondly the voltage due to only the mutual inductance between the
7   %   excitation and pick-up coils, the empty coils background signal.
8   %
9   %   Input parameters:
10  %   ExcitationCoils: Cell of position, size and orientation of excitation
11  %   coils in meters
12  %      Position  Radius  Orientation (coil normal)
13  %      { [x,y,z],    r,    [nx,ny,nz];
14  %        [x,y,z],    r,    [nx,ny,nz];
15  %               ...                  }
16  %
17  %   IExcitation: Excitation coil current in Amperes
18  %
19  %   IFreq: Excitation frequency in Hertz
20  %
21  %   PickupCoils: Cell of position, size and orientation of pickup
22  %   coils in meters
23  %      Position  Radius  Orientation (coil normal)
24  %      { [x,y,z],    r,    [nx,ny,nz];
25  %        [x,y,z],    r,    [nx,ny,nz];
26  %               ...                  }
27  %
28  %   X,Y, Z: Mesh grid of the sample elements in meters
29  %
30  %   Chi: Dimensionless volume susceptibility of the sample
31
32  muzero=4*pi()*1e-7; % H/m
33
34  Voltage=0;
35
36  % Loop over the size of the sample
37  for i=1:(size(X,1)-1)
38      for j=1:(size(X,2)-1)
39          for k=1:(size(X,3)-1)
40              % Find centre of this element
41              Xcentre=0.5*(X(i,j,k)+X(i+1,j+1,k+1));
42              Ycentre=0.5*(Y(i,j,k)+Y(i+1,j+1,k+1));
43              Zcentre=0.5*(Z(i,j,k)+Z(i+1,j+1,k+1));
44
45              % Find the volume of this element
46              V=(X(i+1,j+1,k+1)-X(i,j,k))*(Y(i+1,j+1,k+1)-Y(i,j,k))*(Z(i+1,j+1,k+1)-Z(i,j,k));
47
48              % Find the field from the excitation coils at the centre of
49              % this element
50              BExcitation=zeros(1,3);
51              for e=1:size(ExcitationCoils,1)
52                  % Distance between element and coil
53                  XSep=Xcentre-ExcitationCoils{e,1}(1);
54                  YSep=Ycentre-ExcitationCoils{e,1}(2);
55                  ZSep=Zcentre-ExcitationCoils{e,1}(3);
```

```matlab
                        % Rotate so z-axis is along the coil normal to calculate
                        % the field
                        Orientation=ExcitationCoils{e,3}/norm(ExcitationCoils{e,3});
                        Theta=acos(Orientation(3));
                        RotationAxis=cross(Orientation,[0 0 1]);

                        R=rodriguesRotation([XSep,YSep,ZSep],RotationAxis,Theta);

                        B=coilField(ExcitationCoils{e,2},IExcitation,R(1),R(2),R(3));

                        % Rotate field back to sample orientation
                        BExcitation=BExcitation+rodriguesRotation(B,RotationAxis,-Theta);
                    end

                % Magnetisation of this element
                M=Chi*BExcitation/muzero;

                % Find the field from each of the pickup coils at the centre of
                % this element
                for p=1:size(PickupCoils,1)
                    % Distance between element and coil
                    XSep=Xcentre-PickupCoils{e,1}(1);
                    YSep=Ycentre-PickupCoils{e,1}(2);
                    ZSep=Zcentre-PickupCoils{e,1}(3);

                    % Rotate so z-axis is along the coil normal to calculate
                    % the field
                    Orientation=PickupCoils{e,3}/norm(PickupCoils{e,3});
                    Theta=acos(Orientation(3));
                    RotationAxis=cross(Orientation,[0 0 1]);

                    R=rodriguesRotation([XSep,YSep,ZSep],RotationAxis,Theta);

                    B=coilField(PickupCoils{e,2},1,R(1),R(2),R(3));

                    % Rotate field back to sample orientation
                    Voltage=Voltage+2*pi()*dot(M,rodriguesRotation(B,RotationAxis,-Theta))*V;
                end
            end
        end
end

Signal(1)=Voltage*IFreq;

Voltage=0;
for e=1:size(ExcitationCoils,1)
    for p=1:size(PickupCoils,1)
        if ExcitationCoils{e,2}>=PickupCoils{p,2}
            % Seperation between the coils
            XSep=PickupCoils{p,1}(1)-ExcitationCoils{e,1}(1);
            YSep=PickupCoils{p,1}(2)-ExcitationCoils{e,1}(2);
            ZSep=PickupCoils{p,1}(3)-ExcitationCoils{e,1}(3);

            % Rotate so z-axis is along the coil normal to calculate
            % the mutual inductance
            Orientation=ExcitationCoils{e,3}/norm(ExcitationCoils{e,3});
            Theta=acos(Orientation(3));
            RotationAxis=cross(Orientation,[0 0 1]);
            R=rodriguesRotation([XSep,YSep,ZSep],RotationAxis,Theta);

            % Rotate noraml of pick-up coil
            N=rodriguesRotation(PickupCoils{p,3}/norm(PickupCoils{p,3}),RotationAxis,Theta);
```

```matlab
120                 M=Babic_24(ExcitationCoils{e,2},PickupCoils{p,2},R,N);
121             else
122                 % Seperation between the coils
123                 XSep=ExcitationCoils{e,1}(1)-PickupCoils{p,1}(1);
124                 YSep=ExcitationCoils{e,1}(2)-PickupCoils{p,1}(2);
125                 ZSep=ExcitationCoils{e,1}(3)-PickupCoils{p,1}(3);
126
127                 % Rotate so z-axis is along the coil normal to calculate
128                 % the mutual inductance
129                 Orientation=PickupCoils{p,3}/norm(PickupCoils{p,3});
130                 Theta=acos(Orientation(3));
131                 RotationAxis=cross(Orientation,[0 0 1]);
132                 R=rodriguesRotation([XSep,YSep,ZSep],RotationAxis,Theta);
133
134                 % Rotate normal of excitation coil
135                 N=rodriguesRotation(ExcitationCoils{e,3}/norm(ExcitationCoils{e,3}),RotationAxis,Theta);
136
137                 M=Babic_24(PickupCoils{p,2},ExcitationCoils{e,2},R,N);
138             end
139             Voltage=Voltage+M*IExcitation*2*pi();
140         end
141     end
142
143     Signal(2)=Voltage*IFreq;
144     end
145
146     function RRot=rodriguesRotation(R,RotationAxis,Theta)
147     %RODRIGUESROTATION Rotate vector R about axis RotationAxis Theta degrees
148     RRot=R*cos(Theta)+(cross(RotationAxis,R))*sin(Theta)+(RotationAxis*dot(RotationAxis,R))*(1-cos(Theta)
              );
149     end
150
151     function B=coilField(A,I,X,Y,Z)
152     %COILFIELD Field from a coil radius A and carrying current I at position
153     %   (X,Y,Z). The coil is in the x-y plane centred at the origin.
154     rhosqu=X.^2+Y.^2;
155     rsqu=X.^2+Y.^2+Z.^2;
156     alphasqu=A.^2+rsqu-2*A*sqrt(rhosqu);
157     beta=sqrt(A.^2+rsqu+2*A*sqrt(rhosqu));
158     ksqu=1-alphasqu/(A.^2+rsqu+2*A*sqrt(rhosqu));
159     C=4*(1e-7)*I;
160     [K,E]=ellipke(ksqu);
161     if X*Z==0
162         Bx=0;
163     else
164         Bx=((C*X*Z)/(2*alphasqu*beta*rhosqu))*((A.^2+rsqu)*E-alphasqu*K);
165     end
166     if Y*Z==0
167         By=0;
168     else
169         By=((C*Y*Z)/(2*alphasqu*beta*rhosqu))*((A.^2+rsqu)*E-alphasqu*K);
170     end
171     Bz=((C)/(2*alphasqu*beta))*((A.^2-rsqu)*E+alphasqu*K);
172     B=[Bx,By,Bz];
173     end
174
175     % Following code adapted from S. Babic et al.
176     function M=Babic_24(Rp,Rs,Pc,N)
177     %BABIC_24 Mutual inductance between two circular loops
178     %   Returns the mutual inductance between two circular loops of radius Rp
179     %   and Rs (with Rp >= Rs), whose centres are separated by a vector
180     %   pc=[xc,yc,zc], and normal to the plane of secondary loop is n=[a,b,c],
181     %   with absolute tolerance 1e-13.
182     %
```

```matlab
183  %    All dimensions must be in "meters" and angles in "radians".
184  %
185  %    The formula used in this function is the one provided by: S. Babic, F.
186  %    Sirois, C. Akyel and C. Girardi, IEEE Trans. Magn., 2010, at press.
187  %
188  %    The units have been adapted to the S.I. system.
189  %
190  %    Programmed by F. Sirois and S. Babic Ecole Polytechnique de Montreal,
191  %    June 2009.
192  Tol=1e-13;
193
194  % Recovery of parameters
195  Xc=Pc(1); Yc=Pc(2); Zc=Pc(3);
196  A=N(1); B=N(2); C=N(3);
197
198  % Preliminary computations
199  Alpha=Rs/Rp; Beta=Xc/Rp; Gamma=Yc/Rp; Delta=Zc/Rp;
200
201  % Integration, Romberg method (adaptation from author below)
202  %    Author: Martin Kacenak,
203  %            Department of Informatics and Control Engineering,
204  %            Faculty of BERG, Technical University of Kosice,
205  %            B.Nemcovej 3, 04200 Kosice, Slovak Republic
206  %    E-mail: ma.kac@post.cz
207  %    Date:   february 2001
208  Decdigs=abs(floor(log10(Tol)));
209  Rom=zeros(2,Decdigs);
210  Romall=zeros(1,(2^(Decdigs-1))+1);
211  Romall=feval('f24',0:2*pi/2^(Decdigs-1):2*pi,Alpha,Beta,Gamma,Delta,A,B,C);
212  H=2*pi;
213  Rom(1,1)=H*(Romall(1)+Romall(end))/2;
214  for i=2:Decdigs
215      Step=2^(Decdigs-i+1);
216      % trapezoidal approximations
217      Rom(2,1)=(Rom(1,1)+H*sum(Romall((Step/2)+1:Step:2^(Decdigs-1))))/2;
218      % Richardson extrapolation
219      for k=1:i-1
220          Rom(2,k+1)=((4^k)*Rom(2,k)-Rom(1,k))/((4^k)-1);
221      end
222      Rom(1,1:i)=Rom(2,1:i);
223      H=H/2;
224  end
225  M=4e-7*Rs*Rom(1,Decdigs);
226  end
227
228  % Integrand function
229  function F=f24(p,h,e,g,d,a,b,c)
230      h2=h*h; e2=e*e; g2=g*g; a2=a*a; b2=b*b; c2=c*c;
231      l2=(a*a+c2); l=sqrt(l2); L2=(l2+b*b); L=sqrt(L2); l2L2=L2*l2; lL=l*L;
232      sp=sin(p); cp=cos(p); cp2=cp.*cp; sp2=sp.*sp;
233      if l==0,
234          p1=0; p2=-g*sign(b); p3=0; p4=-e*sign(b); p5=d;
235          V=sqrt(e2+g2+h2*cp2-2*h*e*sign(b)*cp);
236      else
237          p1=g*c/l; p2=-(e*l2+g*a*b)/lL; p3=h*c/L; p4=(g*l2-e*a*b-d*b*c)/lL; p5=(d*a-e*c)/l;
238          V=sqrt((e2+g2)+h2*((1-b2*c2/l2L2)*cp2+c2/l2*sp2+a*b*c/(l2*L)*sin(2*p))-2*h/lL*(e*a*b-g*l2)*cp-
                  2*h*e*c/l*sp );
239      end
240      A=(1+e2+g2+h2+d*d)+2*h*(p4*cp+p5*sp);
241      m=4*V./(A+2*V); k=sqrt(m);
242      [K,E]=ellipke(m);
243      PSI=(1-0.5*m).*K-E;
244      F=(p1*cp+p2*sp+p3).*PSI./(k.*V.^1.5);
245  end
```